A MULTISCALE ANALYSIS OF FLOW AND TRANSPORT IN THE HUMAN PLACENTA

Igor L. Chernyavsky

Thesis submitted to The University of Nottingham
for the degree of Doctor of Philosophy

October 2011

Tributaries by Rob Gonsalves (reproduced with permission).

Abstract

The human placenta is characterised by a unique circulatory arrangement, with numerous villous trees containing fetal vessels immersed in maternal blood. Placental tissue therefore manifests a multiscale structure balancing microscopic delivery of nutrients and macroscopic flow. The aims of this study are to examine the interaction between these scales and to understand the influence of placental organisation on the effectiveness of nutrient uptake, which can be compromised in pathologies like pre-eclampsia and diabetes.

We first systematically analyse solute transport by a unidirectional flow past an array of microscopic sinks, taking up a dissolved nutrient or gas, for both regular and random sink distributions. We classify distinct asymptotic transport regimes, each characterised by the dominance of advective, diffusive or uptake effects at the macroscale, and analyse a set of simplified model problems to assess the accuracy of homogenization approximations as a function of governing parameters (Péclet and Damköhler numbers) and the statistical properties of the sink distribution. The difference between the leading-order homogenization approximation and the exact solute distribution is determined by large spatial gradients at the scale of individual villi (depending on transport parameter values) and substantial fluctuations that can be correlated over lengthscales comparable to the whole domain. In addition, we consider the nonlinear advective effects of solute-carriers, such as red blood cells carrying oxygen. Homogenization of the solute-carrier-facilitated transport introduces an effective Péclet number that depends on the slowly varying leading-order concentration, so that an asymptotic transport regime can be changed within the domain. At large Péclet and Damköhler numbers (typical for oxygen transport in the human placenta), nonlinear advection due to solute-carriers leads to a more uniform solute distribution than for a linear carrier-free transport, suggesting a "homogenizing" effect of red blood cells on placental oxygen transport.

We then use image analysis and homogenization concepts to extract the effective transport properties (diffusivity and hydraulic resistance) from the microscopic images of histological sections of the normal human placenta. The resulting two-dimensional tensor quantities allow us to assess the anisotropy of placental tissue for solute transport. We also show how the pattern of villous centres of mass can be characterised using an integral correlation measure, and identify the minimum spatial scale over which the distribution of villous branches appears statistically homogeneous.

Finally, we propose a mathematical model for maternal blood flow in a placental functional unit (a placentone), describing flow of maternal blood via Darcy's law and steady advective transport of a dissolved nutrient. An analytical method of images and computational integration along streamlines are employed to find flow and solute concentration distributions, which are illustrated for a range of governing system parameters. Predictions of the model agree with experimental radioangiographic studies of tracer dynamics in the intervillous space. The model supports the hypothesis that basal veins are located on the periphery of the placentone in order to optimise delivery of nutrients. We also explain the importance of dilatation of maternal spiral arteries and suggest the existence of an optimal volume fraction of villous tissue, which can both be involved in the placental dysfunction. Theoretical studies of this thesis thus constitute a step towards modelling-based diagnostics and treatment of placental disorders.

Acknowledgements

Verba volant, scripta manent.

I owe immense gratitude to my scientific supervisors, Prof. Oliver Jensen for the insightful guidance and friendly advice, Dr Lopa Leach for her enthusiasm and opening an interesting world of biosciences to me, and Prof. Ian Dryden for helping to navigate through the realm of statistics. It is hard to fully express my appreciation of this collaboration and the things you helped me to learn, as many scientific traditions are unspoken. I hope you enjoyed the project as much as I did.

The success of our work would not have been possible without the kind administrative and technical support of Ms Andrea Blackbourn, Ms Helen Cunliffe, Ms Hilary Lonsdale, Ms Jane Mason, and Mr Dave Parkin. And it remains for me to heartily acknowledge the generous support of the Marie Curie Fellowship through the 6th EU Research and Training Framework.

I cannot conclude without gratefully acknowledging the many obligations. My deepest thanks are to my mother and grandmother for their unparalleled understanding and support, and I am very grateful to Julia for offering a smile when it is most needed. Finally, I thank all the friends and colleagues, the full list being too long to fit the space, who made my time in Nottingham so much fulfilling.

CONTENTS

I Introduction

1.1 Basic structure and function of the human placenta

We shall start by quoting Bernard Shaw [241]: "Except during the nine months before he draws his first breath, no man manages his affairs as well as a tree does."

The human placenta (Fig. 1.1) incorporates almost all functions of the adult body, acting as the fetal lung, digestive and immune systems, to mention a few. It is therefore not surprising that many complications of the pregnancy are associated with failures of this life-support system [33], such as intrauterine growth restriction (IUGR) of the fetus, diabetes, gestational hypertension (pre-eclampsia) that manifest in more than 5% of all pregnancies [266]. Thus, it is essential to understand how the structure of the placenta influences and is influenced by its transport function: delivery of nutrients and oxygen to the fetus.

The vascular morphology of the human placenta consists of supplying *spiral arteries* and draining *decidual veins* from the maternal side, and a complex network of vessels in the *villous*

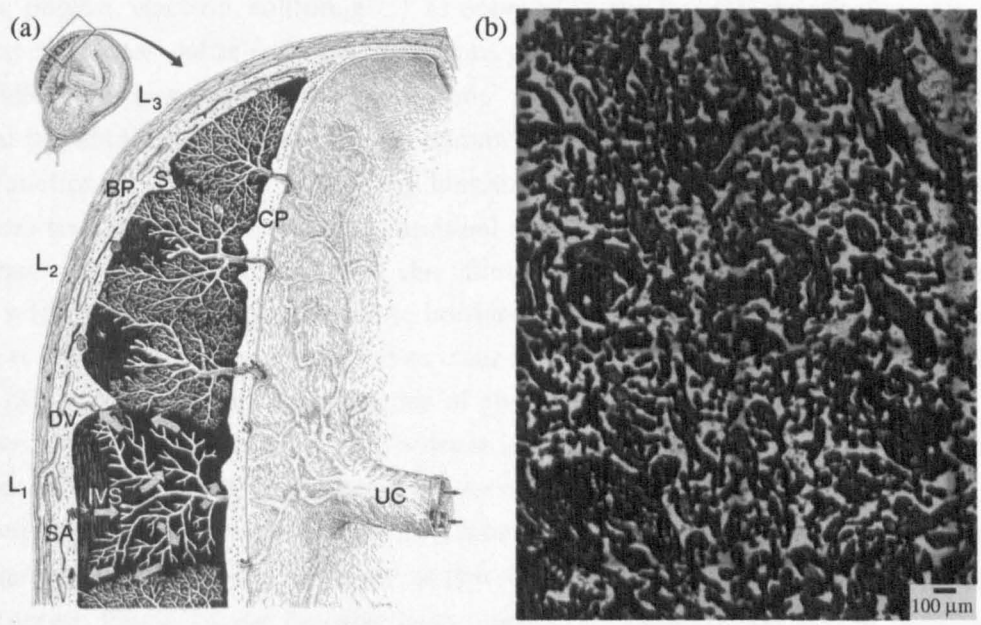

Figure 1.1. (a) Schematic diagram (modified from [33]) of the nearly mature human placenta *in situ*, composed of the chorionic plate (CP) and the basal plate (BP) surrounding the intervillous space (IVS). The villous trees containing fetal vasculature (communicating with the fetus via the umbilical cord (UC)) project from the CP into the IVS and are directly surrounded by maternal blood that emerges from spiral arteries (SA) in the BP and circulates, as indicated by arrows in lobule L_1, to leave the IVS through the decidual veins (DV); terminal branches of the chorionic villi are not shown in L_1. Note the single villous tree in the peripheral lobule L_3, demarcated by the placental septum (S), as opposed to several trees in the central lobule L_2. (b) A cross-section of a normal peripheral placental lobule showing villous branches in the IVS (section taken parallel to the BP, about 1 mm from the decidua).

trees from the fetal side. The dense terminal branches of villi (with enormous surface area of the order of 10 m^2 in a mature placenta) form an interface for metabolic exchange between the two circulatory systems. The mature placenta is subdivided into 60 to 70 villous trees (or fetal cotyledons) that are grouped in 10 to 40 lobules [33] (Fig. 1.1a).

1.2 The concept of the placentone

Our modern understanding of blood flow in the primate and human placenta is based on the pioneering studies by Freese, Ramsey, Reynolds, Wilkin and co-authors [96, 207, 216, 272, 274]. Using a combination of radioangiography and casting techniques they visualised the flow patterns of maternal blood and the morphological relationship between the uteroplacental vasculature and fetal chorionic villi. Schuhmann *et al.* confirmed the topological findings of Freese and others by demonstrating different zonal enzymatic activities in the fetal cotyledon [235]. Schuhmann also coined the term "placentone" for a functional placental circulatory unit [236].

According to Schuhmann, this term was modified by him and Wehler from "placentom", previously used to denote a placental unit in ruminants and human by Strahl and Strauss, because "the ending '-om' is widely used for tumors whereas the ending '-one' in the morphological nomenclature characterizes functional units (osteon, nephron, chondron)" [237]. However, the common semantics for a functional or structural unit in biology and physics is given by the suffix '-on' (ion, photon, electron, soliton, etc.) as opposed to the integral description of a system as a whole by the '-ome' suffix (genome, proteome, cardiome, physiome, etc.) [158]. Nevertheless, we will follow the historical name "placentone" adopted in the literature as a reference to a functional placental unit in primates and human [33].

The functional circulatory unit of the human placenta, a *placentone*, is defined as a single fetal villous tree and its corresponding decidual vessels. Maternal blood, ejected from a spiral artery, passes between the branches of the villous tree before leaving the placentone through decidual veins. Although strict anatomic borders cannot always be found between these functional units [237], this arrangement is most clear in the peripheral lobules of the mature human placenta [33]. The distinguishing features of the placentone are a central cavity of the fetal villous tree with less differentiated villi, a dense lateral portion, the functional decidual arterial opening into the central cavity, and basal venous openings near the periphery [98, 237] (Fig. 1.2).

Although this one-to-one arrangement is most clear in the peripheral lobules of the mature human placenta [33], a general tendency to pair-wise villous tree and spiral artery organisation can be observed [96, 272], and has also been reported in macaque Rhesus [98, 205]. Moreover, the fetal cotyledons without a corresponding decidual artery were found to have a considerably different shape, and it was suggested that these "artery-free" villous trees are more specialised to have a secretory rather than sorptive function [98]. It has also been shown that the number of decidual arterial openings decreases throughout the first trimester of pregnancy [197]. This may support the concept that the quantity of arterial openings at term should be comparable to the number of fetal villous trees.

An important determinant of the successful preparation of the maternal side for gestation is the dilatation and suppression of contractile activity in spiral arteries. This is believed to

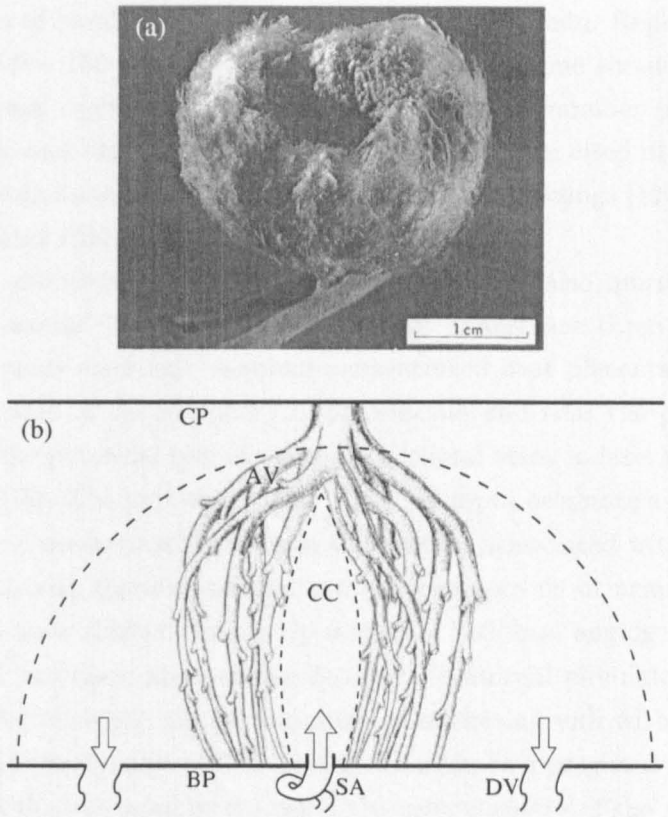

Figure 1.2. (a) A cast of a large villous tree from the human term placenta (incomplete injection), showing differences in density of villi forming a central cavity (top). Reproduced from [98]. (b) A scheme of the placentone at term, enclosed between the basal (BP) and chorionic (CP) plates. Maternal blood enters the central cavity (CC) via the spiral artery (SA) and is drained through the decidual veins (DV) at the periphery. Note the anchoring stem villi (AV) surrounding the CC and connecting the CP with the BP. The dashed lines show the central cavity and notional outer boundary of the placentone. The intermediate and terminal villi are not shown. Modified from [33].

be largely achieved through the invasion of the extravillous *trophoblast*, derived from the shell covering the villous trees [33]. It is the ability of these trophoblast cells to migrate and invade the spiral arteries, converting them into high-capacity nearly passive conduits, that contributes to their *remodelling*, pioneered by Pijnenborg and others [194, 195].

Intrauterine blood flow and the development of villous structure are addressed both in the experimental works by Kaufmann, Freese, Ramsey, *et al.* [70, 72, 99, 131, 142, 148, 207, 235] and by mathematical modelling of Erian, Longo, Power and others [86, 143, 153, 160, 211, 255]. There were long debates concerning the presence of intervillous maternal blood circulation in the first trimester [56, 65, 246, 263] and the existence of a central cavity in the fetal villous tree [97, 108, 237]. Now most investigators agree that a considerable rise in blood flow through the intervillous space happens between the 8th and 12th weeks of gestation [144, 195], and that a typical mature placentone exhibits structural and metabolic differences between its central and peripheral portions [237].

However, the problem of obtaining a quantitative statistical description of the villous structure of a placentone and of the distribution of decidual spiral arteries and veins is still open [33].

Even the total number of basal arterial openings at term is uncertain. Reported values vary from 80 – 100 [186] and 100 – 150 [163] to 25 – 320 [33, 49]. Also, one should distinguish between anatomic and functional openings of spiral arteries, since the number of observed functional openings in ultrasonic and radioangiographic studies is less than cited above [49]. Thus, Boyd and Hamilton have given an estimate of about 100 functional openings [49], which is comparable with the number of fetal villous trees in the mature placenta.

The number and distribution of basal venous orifices are also quite uncertain; the total amount varies from around 70 [49] to 50 – 200 [33]. There are three main hypotheses for the distribution of venous openings: random; concentrated near placental margins ("marginal lakes"); and concentrated in the periphery of placentones and near the placental septum [49]. Recent studies show the potential role of marginal decidual veins in lateral placental growth by trophoblast invasion [78]. The hypothesis that placental septa originate as a result of a growing venous network, and of mechanical stresses in the decidua associated with anchoring villi [48], is also more consistent with basal venous orifices being located on or near the elevated septum.

While researchers have studied separately maternal and fetal angiogenesis, the mechanism governing the spatial co-organisation of the fetal and maternal circulatory systems has been largely overlooked. For example, the arrangement of anchoring villi with respect to the spiral arteries, and especially the dynamics of anchoring throughout a pregnancy, is unclear; however, there is evidence that the villi tend to surround the central cavity of the placentone containing a spiral artery [65, 215]. The questions of whether there is random or regular architecture in the relative position of villous trees and decidual vessels, and what guides their development, if it is not random, remain open.

Based on a review of literature on the biochemistry of growth factors, and the effects of haemodynamical forces and oxygen concentration on villous development (see Appendix A), we conclude that the available data tends to support the concept that a villous tree develops around a specific spiral artery, optimising its spatial arrangement for effective metabolic exchange. As remarked by Freese [98]: "There is a nicely designed system of maternal blood flow in the intervillous space."

Having established the ordered development and the ultimate design of a placentone, one would question its implications for haemodynamics and metabolic exchange in the human placenta. Mathematical models can assist in investigating the impact of such a design on intervillous flow and solute transport.

1.3 Review of theoretical models of placental circulation and metabolic exchange

Theoretical studies of the placental circulation and metabolic exchange were started more than 40 years ago by Faber, Kirschbaum, Longo, Moll and co-workers [25, 88, 143, 160]. Nevertheless, we still do not have complete understanding of many phenomena related to intrauterine fetal growth restriction and macrosomia (abnormally large birth-size of a neonate), and it is also unclear how these pathologies are connected to placental structure, haemodynamics and regulatory activity.

The first lumped-parameter (or compartmental) models focused on oxygen and carbon dioxide exchange between the maternal and fetal circulatory systems, ignoring spatial flow patterns of maternal blood, where Fick's law was used to approximate diffusive mass transfer across the placental barrier [88, 121, 122, 143, 153]. Interestingly, one of the earliest and most cited models by Bartels and Moll [25, 179] contains an incorrect attempt to generalise the "theory of heat exchangers" to the multivillous feto-maternal vascular arrangement in the human placenta using double-exponential growth for net uptake rate, due to misinterpretation of ordinary differential equations for solute exchange. This indicates a danger of superficial compartmental modelling of placental circulation. On the other hand, Power *et al.* showed experimentally a considerable heterogeneity of maternal and fetal circulations in a cotyledon (the placentone analogue) of the sheep placenta [200].

Later approaches, such as the influential paper of Erian *et al.* [86], accounted for spatial effects and included linear and nonlinear laws for flow of maternal blood in the villous tissue described as a porous medium, which was generalised by Smith, Wilson and Duffy to include inertial effects near the spiral artery in the framework of Forchheimer's equation [248] (which will be discussed in Sec. 1.4.2 below); other models took account of the radial oxygen diffusion at the scale of a single capillary in the intervillous space [77, 109, 116], and considered blood flow and pressure in the spiral artery with a terminal expansion as a function of arterial radius using Poiseuille's law for a conical tube [57]. A brief description, and main outcome, of each relevant model is summarised in Table 1.1.

Model	Description	Main results
Kirschbaum, Shapiro (1969) [143]	Equilibrium mass transfer in the lamb placenta. A system of algebraic equations is derived from Fick's law for diffusion and Hill's law for uptake.	The influence of the placental shunts is investigated. The distribution of blood flow-rate-fraction participating in materno-fetal gas exchange is presented.
Faber (1969) [88]	Steady transfer of inert solutes is considered for concurrent, countercurrent, crosscurrent and "pool flow" arrangement of placental circulation based on a one-dimensional advection-mass transfer model. The effectiveness of solute transport with respect to the placental type and model parameters is analysed.	Three non-dimensional parameters representing placental permeability, materno-fetal blood flow rates and solute transport rates are identified. The isolines of solute transport rates are plotted for homogeneous and heterogeneous blood flows and placental barrier permeability.
Guilbeau, Reneau, Knisely (1972) [109]	Steady and unsteady oxygen transfer in a capillary-scale unit of the human placenta, which is described by a system of diffusion-convection-reaction equations in a three-layer cylinder, with the Hill equation for oxygen saturation; placental shunts are neglected.	Spatio-temporal distributions of oxygen partial pressure in maternal and fetal blood near the exchange unit are computed. The effect of time-varying velocity of maternal blood on oxygen content is explored.

Table 1.1. Mathematical models proposed for the uteroplacental blood flow and solute transport. (ODE = Ordinary differential equations).

Model	Description	Main results
Hill, Power, Longo (1973) [122]	Unsteady gas transfer in the human placenta. A system of ODEs is obtained based on Fick's law in terms of O_2 and CO_2 partial pressures, using exponential and Hill-type dissociation kinetics in red blood cells.	The time course of O_2, CO_2 partial pressures in the maternal and fetal erythrocytes and in plasma is obtained. The influence of kinetic parameters on transient processes is studied.
Lardner (1975) [153]	Steady one dimensional oxygen transfer in the human placenta. The model is described by a system of nonlinear ODEs, with combined linear and Hill-type uptake kinetics.	A set of non-dimensional parameters characterising diffusion, uptake and flow rates is proposed. The dependence of oxygen uptake and partial pressure on these parameters is given.
Erian, Corrsin, Davis (1977) [86]	Steady maternal blood flow in a single placentone of the human placenta. Darcy's law with constant, spatially non-uniform and local maternal flow-velocity-dependent hydraulic conductivity is used.	The effect of villous distortion due to maternal blood flow on flow patterns is studied. A short-circuiting of maternal blood entering the placentone is observed.
Aifantis (1978) [6]	A general scheme of haemodynamics and heat transfer in the human placenta, based on mixture theory.	A critical review of existing models is presented. A plan of future developments is proposed.
Wilbur, Power, Longo (1978) [273]	Unsteady water and solute exchange in the human placenta as a generalisation of [122]. The model is given by a system of 36 ODEs, taking account of hydrostatic and osmotic pressures as well as chemical reactions for a variety of solutes.	Steady distribution of water and solute transfer rates between mother and fetus along placental membrane is given. Reversed exchange near the end of a fetal capillary is observed. A sensitivity analysis to the model parameters is performed.
Heilmann, Grebner, Mattheck, Ludwig (1979) [116]	Unsteady radial oxygen diffusion in a human placentone, described as two-layer Krogh cylinder with different diffusion coefficients for the blood-filled intervillous space and trophoblastic tissue; no oxygen uptake and zero maternal blood flow are assumed.	The model studies the rheological effect of a sudden occlusion in the intervillous space, caused by erythrocyte aggregation. The typical time of a physiologically significant decay in oxygen partial pressure is given.
Schröder (1982) [234]	Unsteady passive transport of solutes in the guinea-pig placenta. A one-dimensional mathematical model uses a generalisation of Fick's law to take account of hydrostatic and colloid osmotic pressure differences across a placental membrane at constant arterial flow rates.	Steady distributions of concentrations, hydrostatic and osmotic pressure along a placental membrane are obtained for both concurrent and counter-current flows. The computed osmotic pressure effect on transplacental bulk water exchange is compared with experimental data.
Schmid-Schönbein (1988) [232]	A schematic analysis of steady flow of maternal blood in the intervillous space as a porous medium is presented. The Poiseuille's and Darcy's flows are compared and contrasted, using algebraic relations and the empirical Kozeny–Carman formula for placental hydraulic conductivity.	Experimental techniques to identify the phenomenological parameters are proposed. An explanation of x-ray images of radio-opaque tracer as "percolating chromatographic fronts" is given. The role of non-Newtonian blood rheology at small flow velocities is highlighted.

Table 1.1. (continued).

Model	Description	Main results
Groome (1991) [107]	Steady one-dimensional oxygen transport in the human placenta, described by a system of nonlinear ODEs with a Hill-type law for haemoglobin dissociation, and Michaelis–Menten kinetics for uptake by syncytiotrophoblast.	The effect of placental oxygen consumption, due to metabolism, on the fetal oxygenation in a microscopic uteroplacental unit is investigated. Placental vascular shunts are taken into account.
Costa, Constantino, Fumero (1992) [77]	Steady oxygen exchange in the human placenta, based on one-dimensional diffusion and uptake in an individual fetal capillary. Anatomical capillary network data is employed.	The dependence of oxygen partial pressure in fetal blood on gestational age and on thickness of the materno-fetal barrier is calculated.
Finn, Leach, Gowland, Jensen (2004) [91]	Unsteady haemodynamics and mass transfer in a single maternal lobule of the human placenta. The 2D model incorporates the fluid dynamics of almost incompressible maternal blood, solved by the lattice-Boltzmann method, and linear diffusion-reaction-uptake equation.	The spatio-temporal distributions of maternal blood pressure, flow velocity and solute concentration in a complex geometry reconstructed from histological sections. The effect of maternal blood flow pulsatility and inertia is studied.
Sengers, Please, Lewis (2010) [238]	A compartmental model for unsteady exchange of three amino-acids (serine, alanine glycine) through the placental barrier is developed, taking account of the active transporters in the syncytiotrophoblast membranes via Michaelis–Menten-type kinetics, assuming steady diffusion and uniform advection across the placenta.	The parameters of the model are fitted to *ex vivo* perfusion data. The computations reproduce experimental observations, examine the sensitivity of amino-acids to the kinetic parameters of transporters, and suggest the accumulation of considered amino-acids in the syncytiotrophoblast compartment.

Table 1.1. (continued).

The modelling of the placental transport function therefore falls into three broad groups: (i) homogeneous trans-membrane exchange and diffusion of oxygen, carbon dioxide, water, amino-acids and other species at constant maternal and fetal flow rates [77, 88, 107, 116, 122, 143, 153, 212, 238]; (ii) steady (Darcy-type) percolation of maternal blood without solute uptake [57, 86, 232], and (iii) unsteady two-dimensional flows with a linear uptake and the inertial effects [91, 248].

A shortcoming of many previous models is that they focus on metabolic exchange but assume uniform blood flow distribution across the placenta, paying little attention to the spatial solute patterns; or they consider complex flows ignoring nonlinear uptake kinetics (such as in the case of glucose transport [114]). Also, no previous model provides a systematic account of micro-geometry in the macroscopic flow and transport (see Fig. 1.3). Thus, a gap in understanding the interplay between placental circulation at macroscales and nutrient delivery at microscales is yet to be bridged.

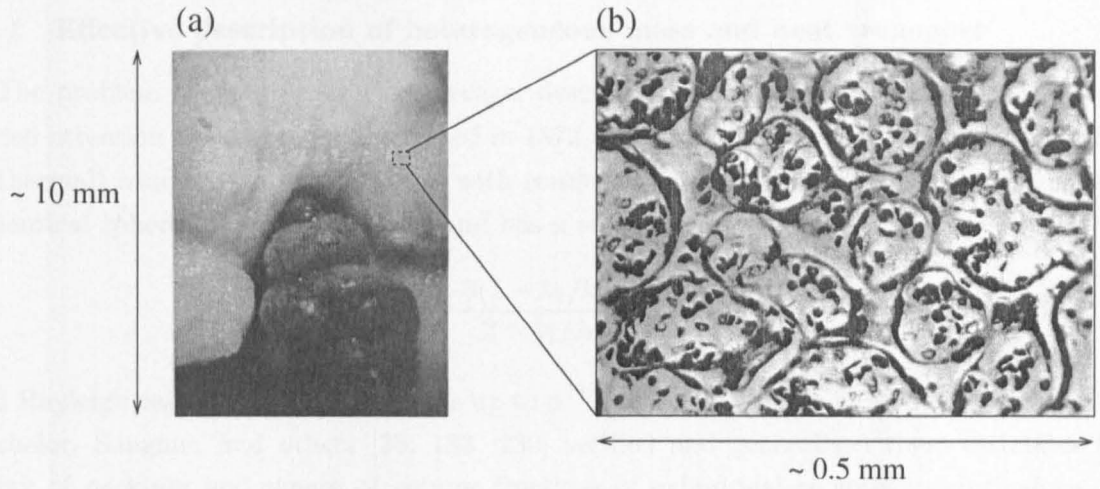

Figure 1.3. Hierarchy of scales in the human placenta: (a) spiral artery entering a mature placentone; (b) cross-sections of the terminal villi in the placentone (magnification of (b) is ca. $\times 20$ over (a)). Modified from [96, 98].

1.4 Review of theoretical studies of flow and transport across multiple scales

The *theory of homogenization* is a combination of the multiscale analysis and the averaging technique that has been successfully applied to a variety of physical, engineering and biomedical problems since it was developed by Babuška, Berdichevsky, Bakhvalov, Keller, Papanicolaou, Sánchez-Palencia, *et al.* [15, 19, 34, 36, 135, 227]. The applications are as diverse as homogenization of standard equations of mathematical physics with rapidly oscillating coefficients (on a domain with periodic microstructure) [20], homogenization of wave-propagation in fibre-reinforced poroelastic media [190], and homogenization of molecular strain energy of DNA with respect to the twist angle [165].

The homogenization method provides a convenient analytical tool for obtaining the effective macroscopic description of underlying phenomena at fine scales if a representative periodic structural unit at these scales can be devised or the assumptions of statistical homogeneity and ergodicity can be applied to the system [261]. This method is essentially based on the two-scale expansions procedure, which was put forward by Lick and others as a natural approach bringing together advantages of the method of matched asymptotic expansions and Lighthill's method of stretched coordinates [32, 159].

The original motivation and most common application of the homogenization method is the physics of composite materials [227], with much effort put to the problems of convergence of differential operators and functionals in the theory of ordinary and partial differential equations with rapidly oscillating coefficients [20, 34, 282]. However, recent interest in biomechanical applications unveils a new potential of averaging and homogenization approaches [71, 242, 275].

Below we present a brief review of homogenization and other effective description techniques.

1.4.1 Effective description of heterogeneous mass and heat transport

The problem of the effective, or average, description of heterogeneous media has long attracted attention since Maxwell suggested in 1873 analytical estimates of the effective electrical (or thermal) conductivity of a medium with conductivity k_0 that contains a dilute cubic array of identical spheres of conductivity k_1 and has a volume fraction ϕ [170]

$$\frac{k_{\text{eff}}}{k_0} \approx 1 - \frac{3(1 - k_1/k_0)}{2 + k_1/k_0}\,\phi, \quad \phi \ll 1; \tag{1.4.1}$$

Lord Rayleigh calculated the corrections up to $\phi^{13/3}$ in 1892 [208]. In subsequent works, Keller, Batchelor, Sangani, and others [28, 133, 230] verified and generalised these estimates for a variety of packings and ranges of volume fractions of cylindrical or spherical inclusions. The role of advective transport in bulk heat exchange between a conducting liquid and a fixed array of heated spheres was first investigated by Acrivos *et al.* [3] for small volume fractions and small Péclet numbers Pe (a ratio of advective to conductive heat (or diffusive mass) transport). They showed that even at small Péclet number and small but finite volume fractions ($\text{Pe}^2 \ll \phi \ll 1$), the average temperature difference depends on details of the flow. Recent progress in microfluidic devices and biomedical applications has renewed interest in these analytical and numerical results, as reviewed in [130, 279]. Below we present a short review of different approaches and results known up to date.

Transport in periodic arrays

The *successive multipole moments* approach to estimate the effective electric conductivity was suggested by Rayleigh [208], corrected by Runge [222] and experimentally verified and developed by Meredith and Tobias [178] and by McKenzie and McPhedran [174, 176]. Alternative approaches of Keller, Batchelor, Acrivos, Sangani and co-authors [28, 133, 230] established a set of comprehensive and accurate estimates of the bulk electrical or heat conductivity for small or high volume fractions of conducting or isolating spheres as the composite's constituents. Since the hydraulic conductivity (at low Reynolds number) is proportional to the effective electrical conductivity of the same porous medium composed of a non-conducting solid part and filled with a conducting liquid electrolyte [14], these results have a broad applicability.

The *spectral properties of singularities* method introduced by Bergman [37] is based on the property of an effective complex dielectric conductivity being an analytical function of the constituent-conductivities' ratio k_1/k_0, except for a finite number of simple poles at the negative real axis (see, e.g. (1.4.1)). A linear Hermitian operator based on the Green function for the Laplace operator reduces the problem of counting the poles and their magnitudes (residues) to a spectral problem for this operator. The method has been successfully applied to a systematic analysis of several composite arrangements, and has proved especially useful when k_1/k_0 is negative and near its singular value (resonance) [38]. The method has been further developed by Bergman and Milton to provide rigorous bounds of effective conductivity [39, 183].

In the framework of *homogenization and multiscale averaging* techniques, Sangani and Acrivos with co-authors have studied by a hybrid numerical-analytical approach the effect of flow at

low [3, 229] and high [264] Péclet number on heat exchange at fixed source strength; using infinite-volume homogenization (taking the limit of a large averaging volume over a heterogeneous medium, in the case of ergodicity of the medium and boundedness of the field quantities), Sangani has obtained the effective diffusivity of polymers with inclusions obeying the nonlinear Langmuir sorption law at zero Péclet number [228]; Mauri [168] considered several different scalings of Péclet and Damköhler numbers for the first-order irreversible reaction kinetics in a periodic porous medium and obtained the corresponding effective equations, which he later extended to non-reactive transport in a random velocity field (e.g. for a medium composed of solid spheroidal inclusions) [169]; and recently Mikelić *et al.* [180] and Allaire & Raphael [7] provided rigorous estimates for convergence of the homogenised solutions to an advection-diffusion-reaction problem at large macroscopic Péclet and Damköhler numbers. A homogenization of an advection-diffusion-reaction problem with evolving (time-dependent) microstructure that permits transformation to a static reference periodic domain was also briefly considered [192].

Using the framework of *generalised Taylor dispersion*, Brenner and Shapiro [51, 240] have calculated effective parameters of an advection-diffusion-reaction equation for first-order kinetics by studying the properties of statistical averages (moments) of a solute "Brownian particle" introduced into a spatially periodic porous medium.

Transport in random arrays

Estimates of the *rigorous bounds of effective material properties*, which represent the original progress in the averaged description of heterogeneous media, are due to fundamental works by Prager [202], and Hashin & Shtrikman [110, 111] based on *variational principles.* They are important because of their applicability to a wide class of composite microstructures, including irregular ones, and the possibility to obtain geometry-independent upper and lower bounds depending only on the constituents' physical properties and volume fractions [39]. The essence of the variational-bounds method is in using a trial, or reference, homogeneous composite property for an "energy" functional describing the effective medium [261]. An alternative method of looking for rigorous bounds, proposed by Bergman and Milton [39, 183], exploits *analyticity* of the effective property as a complex function of the constituents of two-phase composites. Further development is due to works by Keller, Talbot & Willis, Papanicolaou, Torquato, Berryman, and many others [41, 103, 146, 166, 219, 220, 256]. In particular, the n-point correlation (probability) functions formalism of Torquato and co-authors has largely assisted in calculating the geometry-specific bounds [41, 260].

The *stochastic homogenization* method of Papanicolaou *et al.* [34, 35] was proposed almost simultaneously with homogenization of periodic structures. In the case of statistically homogeneous and ergodic microstructure, virtually all results for periodic porous media are directly applicable here and *vice versa* [261]. Advection-diffusion in turbulent and random flow fields has also been extensively studied and is shown to be largely equivalent to convection in a periodic velocity field [89, 173, 175, 223].

The *volume averaging* method by Whitaker and others [262, 268, 283] deals with volume-averaged microscopic equations simplified by use of the Reynolds transport theorem (for volume-averaging of time-derivatives of quantities) and its spatial analogue [268, 270]; this is comple-

mented by the "closure cell problems" for perturbation over mean values, where a periodicity assumption is often employed. Recently Whitaker, Wood, *et al.* have applied this approach to find effective nonlinear reaction-diffusion in biofilms, using Michaelis–Menten-type reaction kinetics [275, 276]. Although the volume-averaging approach allows one to obtain effective transport equations and their coefficients without assuming periodicity of the medium, this requires some heuristic estimates to be made about the terms in the equations that are used to "close" the averaged problem (see [40] for more detailed discussion and comparison of homogenization and volume-averaging methods).

Recent advances in *stochastic geometry* allow one to approach non-linear time-dependent growth models (such as angiogenesis), where global scalar fields of the medium affect the geometry of the microstructure and *vice versa*, providing a feedback loop across different length-scales, as done by Capasso and co-authors by means of *mesoscale hybrid homogenization* of random branching-and-growth [62, 63]. This method involves systematic coupling of stochastic differential equations for evolution of the microstructure (e.g. a growing network of vessels) at the microscale with deterministic averaged partial differential equations for transport of the underlying scalar field (e.g. concentration of diffusible growth factors) at the macroscale [53].

1.4.2 Effective description of flow in a porous medium

Empirical and phenomenological laws of flow in a porous medium (filtration) are due to works of Darcy [79], Forchheimer [94], Brinkman [52], and Biot [43]. The mass conservation of incompressible liquids in the absence of sources and sinks is expressed by the condition

$$\nabla \cdot \mathbf{u} = 0\,,$$

and the momentum conservation equations in these models are as follows:

$$\mathbf{u} = -\tfrac{K}{\mu}\,\nabla P\,, \qquad \text{(Darcy)}$$

$$\mathbf{u}\,(1 + \tfrac{\rho}{\mu}\,\beta\,|\mathbf{u}|^{n-1}) = -\tfrac{K}{\mu}\,\nabla P\,, \qquad \text{(Forchheimer)}$$

$$\mathbf{u} = -\tfrac{K}{\mu}\,(\nabla P - \mu_b\,\nabla^2\mathbf{u})\,, \qquad \text{(Brinkman)}$$

where $\mathbf{u}$ is the superficial average (over the entire volume of a representative element of a porous medium) velocity of fluid, P is the pressure of the liquid phase, K is the superficial average hydraulic permeability of the medium, μ and ρ are the dynamic viscosity and density of the fluid, β and n are the Forchheimer drag coefficient and velocity exponent (empirically usually set to be $n = 2$), and μ_b is the Brinkman effective viscosity. Both β and μ_b are functions of K and the volume fraction ϕ of the solid phase.

The quasi-static Biot model [43] that couples Darcy's law for the fluid and linear elasticity for the solid phase, for an isotropic and homogeneous porous medium filled with incompressible

liquid in the absence of external volume forces and sources, is given, following [244], by

$$\begin{aligned} &\alpha \frac{\partial (\nabla \cdot \boldsymbol{\xi})}{\partial t} + \nabla \cdot \mathbf{u} = 0, \quad \mathbf{u} = -\tfrac{K}{\mu} \nabla P, \\ &\nabla \cdot \boldsymbol{\sigma} = 0, \quad \boldsymbol{\sigma} = -\alpha P \mathbf{I} + \lambda_1 (\nabla \boldsymbol{\xi} + \nabla \boldsymbol{\xi}^T) + \lambda_2 (\nabla \cdot \boldsymbol{\xi}) \mathbf{I}, \end{aligned} \tag{Biot}$$

where $\boldsymbol{\xi}$ is the solid matrix displacement vector, $\mathbf{u}$ is the superficial average fluid velocity *relative* to the solid deformation velocity $\partial \boldsymbol{\xi}/\partial t$, α is the Biot–Willis pressure–deformation coupling constant, λ_1 and λ_2 are the Lamé shear and dilation elasticity moduli of the porous medium, and $\mathbf{I}$ is the unit tensor. If the porous medium is assumed to be static ($\boldsymbol{\xi} = \boldsymbol{\xi}(\mathbf{x})$), the Biot system reduces to Darcy flow in a solid phase skeleton deformed according to the static elasticity problem for a given pressure field. For small deformations, or coupling constant α much less than 1, the fluid problem also decouples from the solid problem.

Although the Darcy, Biot and Forchheimer laws have been systematically obtained from microstructure by homogenization techniques, the Brinkman equation that relates Stokes flow (for volume fraction $\phi \to 0$; $K \to \infty$, $\mu_b \to \mu$) and Darcy flow (for $\phi \to 1$; $\mu_b \to 0$) is still subject to controversy [187]. For example, the velocity $\mathbf{u}$ in the non-Darcy term is thought to be an intrinsic fluid-phase average in contrast to the conventional superficial (whole volume) average [269], the Brinkman viscosity μ_b strongly depends on the microstructure of a porous medium, and the equation itself seems to be applicable only for very small volume fractions ϕ [187]. However, the Brinkman equation can be useful in handling the boundary conditions at the interfaces of a transition region between Darcy flow in a porous medium and free Stokes flow [120]. A typical matching boundary condition is due to Beavers and Joseph [30]: $u = u_p + \frac{\sqrt{K}}{\gamma} \frac{\partial u}{\partial n}$, where $\mathbf{n}$ is a unit normal to the interface, u, u_p are the tangential velocities in free flow at the interface and in a porous medium respectively, K is the hydraulic permeability, and γ is a constant characteristic of the porous medium.

Flow in periodic arrays

The *derivation of Darcy's law by homogenization* was historically one of the first applications of the newborn homogenization method by Keller, Sanches-Palencia and others [85, 136]. We shall illustrate this derivation shortly.

In the search for a theoretical justification of the *Forchheimer's account for fluid inertia*, a quadratic correction ($n = 2$) was obtained by Whitaker [269] using the volume-averaging method, and a cubic correction ($n = 3$) by Auriault and Mei within the homogenization framework [177]. The recent careful homogenization analysis and numerical calculations by Balhoff, Mikelić and Wheeler [23] show that for flow at small local Reynolds number $\mathrm{Re} \lesssim 1$ in an isotropic porous medium, the generalisation of Darcy's law consists of an infinite power series in velocities with only odd power-terms present, thereby confirming Auriault and Mei's result and questioning the capability of the volume-averaging method to account for nonlinear inertial effects at the microscale.

The *Brinkman correction* to flow in a porous medium was obtained via volume averaging [269] and by the homogenization technique for a porous medium with a pore-size comparable with a characteristic distance between two adjacent pores [12]; however, the Brinkman term is

shown to be a correction of the order of $O(\varepsilon^2)$ to Darcy's law for a macroscopically uniform and isotropic porous medium [12]. The Beavers–Joseph boundary slip condition, matching the flows near the interface between free flow and a porous medium, has been justified for a microscopic Stokes flow by Miccliić *et al.*, using the homogenization method [181].

The *Biot model of poroelasticity* was first rigorously studied by Auriault and Sanchez-Palencia [13] in the quasi-static case by homogenization, and Burridge and Keller [54] reconstructed the full dynamical Biot model from the linearised Navier-Stokes and linear elasticity equations at the microscale, also using the homogenization technique.

Estimates of effective *viscous drag* or its rigorous bounds in an array of spheres and cylinders were found by Hasimoto using the *Green function* for the Stokes equations [112], by Keller using *lubrication theory* [134], by Berdichevsky by means of *variational principle* [36], and by Sangani & Acrivos who generalised the results of Hasimoto and re-derived Keller's findings [229].

Flow in random arrays

Prager [201] was the first to obtain bounds of hydraulic permeability by a *variational principle*, expressing the lower limit of permeability via averages of two- and three-point correlation functions (describing the statistical properties of micro-geometry of a porous medium [261]).

Stochastic homogenization and rigorous bounds are generally used to obtain effective equations and coefficients, similar to the methods of studying effective transport equations and properties of random media described in Section 1.4.1. *Darcy's law* in a random porous medium has been reconstructed from microstructure by Rubinstein & Torquato [221]. However, there has been less progress on restoring the fundamental laws of filtration for a random porous medium that is not *statistically homogeneous* compared to the case of a regular medium; studies are still ongoing [137, 261], and some theoretical considerations have been given towards flow in a fractal porous medium [147, 280].

Flow and transport in tubes and channels

The first analytical treatment to the problem of convection-enhanced diffusion (dispersion) of a solute in a long and narrow tube of radius a was given by Taylor in 1953 [258, 259] and confirmed by Aris [9]:

$$D_{\text{eff}} = D\,(1 + \tfrac{\text{Pe}^2}{48})\,, \tag{1.4.2}$$

where D_{eff} is the effective coefficient of diffusion, D is the molecular diffusivity of the solute, $\text{Pe} = a\,U/D$ is the Péclet number, and U is the mean velocity of the laminar Poiseuille flow.

Since then multiple approaches have been developed that systematically recover and generalise this result: *generalised Taylor-Aris stochastic moment-matching* scheme by Brenner, Edwards, Shapiro and others [50, 51], which has been extended to the case of a suspension of actively moving inertial particles (e.g. swimming microorganisms) by Bees *et al.* [31]; *volume averaging* method by Whitaker and others [268, 270]; *homogenization* approach by Papanicolaou *et al.* [175], Horsthemke *et al.* [173, 223], Mauri [168], and Mikelić *et al.* [180].

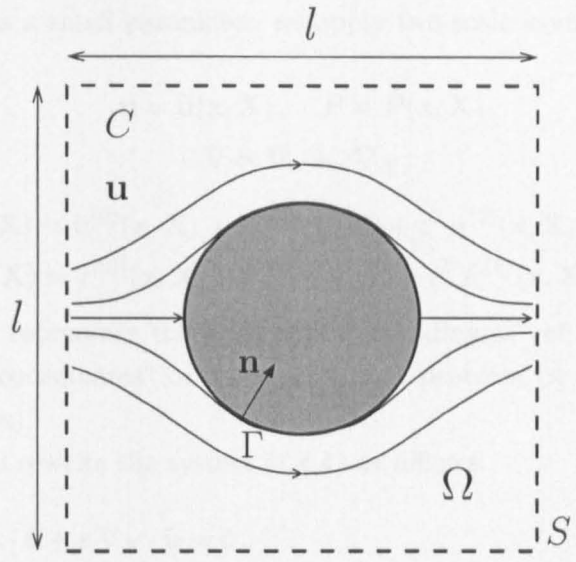

Figure 1.4. A unit cell domain Ω of size l with internal interface Γ and external boundary S. The microscopic flow velocity $\mathbf{u}$ and pressure P obey equations (1.4.3) and the solute transport is described by advection-diffusion-uptake equation (1.4.16) for solute concentration C. The inward normal to Γ is $\mathbf{n}$.

Homogenization example: derivation of the Darcy's law from the first principles

As an example of the application of homogenization technique, we derive Darcy's law of filtration, following [177]. Let us consider a medium with rigid periodic microstructure filled with an incompressible Newtonian liquid. We use Stokes flow together with incompressibility conditions to describe the flow in a representative unit cell (see Fig. 1.4) of size l small compared to the size L of the macroscopic domain of interest:

$$\nabla \cdot \mathbf{u} = 0\,, \quad \nabla P = \mu \nabla^2 \mathbf{u}\,, \tag{1.4.3}$$

where $\mathbf{u}$ and P are fluid velocity and pressure respectively, and μ is the fluid viscosity. The system of equations (1.4.3) is subject to no-slip boundary condition on Γ ($\mathbf{u}|_\Gamma = 0$), and we demand periodicity of flow and pressure fields on the external boundary S, owing to the periodicity of microstructure represented in a unit cell (Fig. 1.4).

We choose the following dimensionless variables: $\mathbf{u} = U\,\mathbf{u}'$, $P = P_0\,P'$, $\nabla = l^{-1}\nabla'$, where $P_0 = \mu U L/l^2$ (so that the pressure gradient equates local viscous dissipation), and rewrite the system of equations (1.4.3), subject to boundary conditions, in the non-dimensional form (the primes over the variables are dropped):

$$\begin{aligned} &\nabla \cdot \mathbf{u} = 0\,, \quad \nabla P = \varepsilon \nabla^2 \mathbf{u}\,, \\ &\mathbf{u}|_\Gamma = 0\,, \end{aligned} \tag{1.4.4}$$

where $\mathbf{u}$ and P are periodic on S, and $\varepsilon = l/L$ is a small parameter characterising the separation of scales ($\varepsilon \sim 10^{-2}$ for the mature human placentone, taking the size of a typical placentone $L \sim 1$ cm [98] and the average diameter of a cross-section of the villous branches in a mature placenta to be $l \sim 0.1$ mm [33, 126]).

Since the system has a small parameter, we apply two-scale asymptotic expansions to look for solutions of (1.4.4):

$$\begin{aligned} \mathbf{u} &= \tilde{\mathbf{u}}(\mathbf{x},\mathbf{X})\,, \quad P = \tilde{P}(\mathbf{x},\mathbf{X})\,, \\ \nabla &= \nabla_x + \varepsilon\nabla_X\,, \end{aligned} \tag{1.4.5}$$

$$\begin{aligned} \tilde{\mathbf{u}}(\mathbf{x},\mathbf{X}) &= \mathbf{u}^{(0)}(\mathbf{x},\mathbf{X}) + \varepsilon\,\mathbf{u}^{(1)}(\mathbf{x},\mathbf{X}) + \varepsilon^2\,\mathbf{u}^{(2)}(\mathbf{x},\mathbf{X}) + \dots\,, \\ \tilde{P}(\mathbf{x},\mathbf{X}) &= P^{(0)}(\mathbf{x},\mathbf{X}) + \varepsilon\,P^{(1)}(\mathbf{x},\mathbf{X}) + \varepsilon^2\,P^{(2)}(\mathbf{x},\mathbf{X}) + \dots\,, \end{aligned} \tag{1.4.6}$$

here $\mathbf{X} = \varepsilon\mathbf{x}$, where $\mathbf{x}$ represents the local "micro-coordinates" of the unit cell Ω, and $\mathbf{X}$ is slowly varying "macro-coordinates" of the macroscopic problem ($\mathbf{x}$ and $\mathbf{X}$ are further treated as independent variables).

Using (1.4.5) we can rewrite the system (1.4.4) as follows:

$$\begin{aligned} &\nabla_x\cdot\tilde{\mathbf{u}} + \varepsilon\,\nabla_X\cdot\tilde{\mathbf{u}} = 0\,, \\ &\nabla_x\tilde{P} + \varepsilon\,\nabla_X\tilde{P} = \varepsilon\left[\nabla_x^2\tilde{\mathbf{u}} + 2\,\varepsilon\,(\nabla_x\cdot\nabla_X)\tilde{\mathbf{u}} + \varepsilon^2\,\nabla_X^2\tilde{\mathbf{u}}\right], \\ &\tilde{\mathbf{u}}|_\Gamma = 0\,. \end{aligned} \tag{1.4.7}$$

Substituting (1.4.6) in (1.4.7) and collecting the terms at the powers of ε, we find at $O(\varepsilon^0)$ and $O(\varepsilon)$:

$$\nabla_x\cdot\mathbf{u}^{(0)} = 0\,, \quad \nabla_x\cdot\mathbf{u}^{(1)} + \nabla_X\cdot\mathbf{u}^{(0)} = 0\,, \tag{1.4.8}$$

$$\nabla_x P^{(0)} = 0\,, \quad -\nabla_x^2\mathbf{u}^{(0)} + \nabla_x P^{(1)} = -\nabla_X P^{(0)}\,, \tag{1.4.9}$$

subject to the boundary conditions $\mathbf{u}^{(i)}|_\Gamma = 0$ and $\mathbf{u}^{(i)}$, $P^{(i)}$ are periodic on S $(i = 1, 2)$.

Equation (1.4.9a) implies that the pressure field at leading order can only depend on the macro-coordinates but not on the local coordinates $\mathbf{x}$: $P^{(0)} = P^{(0)}(\mathbf{X})$.

Averaging equation (1.4.8 b) over the fluid-phase subdomain of the unit cell Ω_f, of volume $|\Omega_f|$, we obtain

$$\frac{1}{|\Omega_f|}\int\limits_{\partial\Omega_f}\mathbf{u}^{(1)}\cdot\mathbf{n}\,\mathrm{d}S_x + \nabla_X\cdot\langle\mathbf{u}^{(0)}\rangle_f = 0\,, \tag{1.4.10}$$

where $\langle\mathbf{u}^{(0)}\rangle_f = \frac{1}{|\Omega_f|}\int_{\Omega_f}\mathbf{u}^{(0)}\,\mathrm{d}\mathbf{x}$, is the *intrinsic* average of fluid velocity, $\phi = 1 - |\Omega_f|/|\Omega|$ is the volume fraction of solid skeleton in the unit cell, which is constant as we neglect the skeleton's deformations; the boundary of Ω_f is $\partial\Omega_f = S\cup\Gamma$, and $\mathbf{n}$ is the unit normal to $\partial\Omega_f$, pointing outwards from Ω_f (see Fig. 1.4)

If we take into account the no-slip flow boundary condition on Γ and the periodicity of $\mathbf{u}^{(1)}\cdot\mathbf{n}$ on S, the boundary integral in (1.4.10) vanishes to give

$$\nabla_X\cdot\langle\mathbf{u}^{(0)}\rangle_f = 0\,. \tag{1.4.11}$$

In order to get a complete system of equations, we consider a closure problem for $\mathbf{u}^{(0)}$ and $P^{(1)}$ that obey equations (1.4.8 a), (1.4.9 b) in the unit cell, subject to no-slip condition on Γ and x-periodicity on S. We observe that the source term $\nabla_X P^{(0)}$ in (1.4.9 b) depends only on the macro-variable $\mathbf{X}$, which can be treated as a parameter in each unit cell, and therefore a

solution of this linear system can be written in the following form [177]:

$$\mathbf{u}^{(0)} = -\mathsf{K} \cdot \nabla_X P^{(0)}, \tag{1.4.12a}$$

$$P^{(1)} = -\mathbf{q} \cdot \nabla_X P^{(0)} + P_0^{(1)}, \tag{1.4.12b}$$

where $\mathsf{K} = \mathsf{K}(\mathbf{x}, \mathbf{X})$ is the permeability tensor, $\mathbf{q} = \mathbf{q}(\mathbf{x}, \mathbf{X})$ is a vector, and $P_0^{(1)} = P_0^{(1)}(\mathbf{X})$ is a scalar.

Averaging of equation (1.4.12a) over the liquid phase of the unit cell Ω leads to a macroscopic relation between fluid pressure and velocity in the leading order:

$$\langle \mathbf{u}^{(0)} \rangle_f = -\langle \mathsf{K} \rangle_f \cdot \nabla_X P^{(0)}. \tag{1.4.13}$$

Substituting (1.4.12) in (1.4.8 a) and (1.4.9 b) with corresponding boundary conditions, we obtain a linear elliptic "closure" problem for K and $\mathbf{q}$ in a unit cell:

$$\begin{aligned} &\nabla_x \cdot \mathsf{K} = 0, \quad \nabla_x \mathbf{q} = \nabla_x^2 \mathsf{K} + \mathsf{I}, \quad \text{in } \Omega \\ &\mathsf{K}|_\Gamma = 0, \qquad \mathbf{q}, \mathsf{K} \text{ are periodic on } S, \end{aligned} \tag{1.4.14}$$

which completes the averaged flow equations (1.4.11) and (1.4.13).

We denote *superficial* average velocity over the whole unit cell as $\langle \mathbf{u} \rangle = (1 - \phi) \langle \mathbf{u}^{(0)} \rangle_f = \frac{1}{|\Omega|} \int_{\Omega_f} \mathbf{u}^{(0)} \, \mathrm{d}\mathbf{x}$, and fluid-phase *intrinsic* average pressure as $\langle P \rangle_f = P^{(0)} = \frac{1}{|\Omega_f|} \int_{\Omega_f} P^{(0)} \, \mathrm{d}\mathbf{x}$ to rewrite the resulting macroscopic flow problem (1.4.11), (1.4.13) as follows:

$$\nabla \cdot \langle \mathbf{u} \rangle = 0, \quad \langle \mathbf{u} \rangle = -\mathsf{K}_{\text{eff}} \cdot \nabla_X \langle P \rangle_f, \tag{1.4.15}$$

which is known as Darcy's law of flow in a porous medium, empirically found by Darcy while studying water flow through sand as an application to a fountain system [79]. Here $\mathsf{K}_{\text{eff}} = \frac{1}{|\Omega|} \int_{\Omega_f} \mathsf{K}(\mathbf{x}, \mathbf{X}) \, \mathrm{d}\mathbf{x}$ is the effective conductivity tensor given by (1.4.14), which reduces to a constant scalar for a homogeneous and isotropic medium ($(\mathsf{K}_{\text{eff}})_{ij} = k\delta_{ij}$, $k = const$) [177].

Analogous technique has been used to investigate effective macroscopic transport phenomena for a family of advection-diffusion-reaction equations, e.g.

$$\frac{\partial C}{\partial t} + \mathbf{u} \cdot \nabla C = D \nabla^2 C - \frac{\alpha C^m}{k^m + C^m}, \tag{1.4.16}$$

describing the microscopic processes [175, 228, 276]. Here C is the concentration of a solute, $\mathbf{u}$ is the flow velocity field, D is the molecular diffusion coefficient and α, k, m are reaction parameters. The effective diffusivity tensor D_{eff}, a counterpart of the conductivity tensor K_{eff} in (1.4.15), is found in these works [175, 228, 275]. The existing studies, however, have been mainly focused on either advection-diffusion in periodic and random velocity fields [89, 90] or diffusion-reaction in various media [228, 276], not addressing sufficiently the combined advection-uptake effects (see also Sec. 1.4.1).

1.5 The objectives and structure of the thesis

As has been shown in Sections 1.1 and 1.2, the human placenta is characterised by a unique circulatory arrangement, with numerous villous trees containing fetal vessels in close contact with maternal blood (Fig. 1.1a). Placental tissue thus manifests a multiscale structure balancing microscopic delivery of nutrients and macroscopic flow distribution (Fig. 1.3). Despite a long history of ultrasound diagnostics, the many complications of pregnancy associated with placental pathology can often be confidently identified only post-delivery, due to insufficient spatial resolution and specificity of ultrasound scans [113]. Recent advances in *in vivo* colour and power Doppler ultrasound and magnetic resonance imaging [26, 95, 113, 148, 205] provide a potential for modelling-aided diagnostics; however, a theoretical framework for accurate averaging of intervillous flow and transport, while preserving the key properties of fine placental structure, is urgently needed.

The aim of this study is to examine the influence of placental structure on the effectiveness of nutrient uptake, which can be compromised in pathologies like pre-eclampsia and diabetes. The study comprises a theoretical analysis of solute transport across multiple scales, a spatial statistical analysis of histological images (Fig. 1.1b), and a self-consistent mathematical model for intervillous flow and transport in a single placentone.

The thesis sets three primary goals: (i) advancing a theoretical framework for multiscale flow and transport in regular and irregular geometries, and in the presence of active solute carriers (e.g. red blood cells); (ii) developing a methodology for characterising micro-geometry of villous branches and extracting key parameters, required for effective description of the placental transport function, from histological sections and, potentially, from ultrasound scans; (iii) testing the existing physiological hypotheses concerning peripheral basal veins' distribution and of the damaging effect of failed dilatation of maternal spiral arteries.

We now briefly outline the content of the thesis.

Chapter 2 focuses on a one-dimensional model of advection-diffusion-uptake in a periodic array of point sinks, an idealised model of maternal flow past villous branches. We classify leading-order parameter regimes for the solute transport and estimate the accuracy of the homogenized description for different parameter values.

We address the stochastic nature of the placental micro-geometry in Chapter 3 by considering effective transport and the accuracy of the leading-order approximation in a disordered array of sinks, extending the model of Chapter 2 to random geometries. The magnitude and correlation properties of homogenization error are assessed for different spatial statistics of the micro-geometry.

The model of flow and transport past arrays of sinks is further developed and generalised in Chapter 4 to account for two-dimensional effects and nonlinear solute carriers, such as haemoglobin. We show, in particular, how the presence of a nonlinear advective component can dynamically change the transport regime in a parameter space, and formulate corresponding closure cell problems in linear and nonlinear cases.

Chapter 5 is devoted to the experimental imaging of a normal human placenta, which is used to systematically characterise its fine structure, complementing the developed theoretical

framework of Chapters 2–4. We test the statistical properties of villous distribution and analyse computationally a unit cell problem for the obtained villous shapes.

In Chapter 6, we develop and study a simplified three-dimensional model of flow and advective transport of a passive solute in a single placentone. This model is used to test a hypothesis concerning the location of venous openings on the basal plate, to offer a theoretical basis for radioangiographic experiments, and to quantitatively assess the role of the dilatation of decidual vasculature, impaired in certain placental pathologies.

We discuss the results and potential extensions of the study in Chapter 7.

Homogenization of Advection-Diffusion in a One-dimensional Array of Sinks

2.1 Introduction

In order to understand how the placenta functions as an organ of nutrient exchange, we here use a simple mathematical model to examine the combined effects of transport of solutes such as glucose or oxygen by maternal blood flow and uptake by the fetal circulation in villous trees. We consider competition between advection, diffusion and uptake characterised by a Péclet number Pe (relating the strength of advection to diffusion) and a Damköhler number Da (relating the rate of reaction or uptake to diffusion).

The human placenta exhibits a complex geometry formed by the villous branches where the uptake of solutes from the maternal blood takes place, with an irregular pattern of smaller terminal villi and a more regular arrangement of larger anchoring stem villi (see Figs 1.1, 1.2). This chapter aims to address the problem of classification and accuracy of effective asymptotic regimes of steady advective-diffusive transport with sorption in a regular periodic medium.

Although previous extensive studies provide numerous insights into flow and transport phenomena in porous media, it is still remains to be understood how the delicate interplay between different characteristic non-dimensional parameters, such as Péclet, Damköhler and Reynolds numbers, affects macroscopic and microscopic transport.

We start by considering a one-dimensional periodic array of sinks subjected to a uniform flow with a prescribed inlet concentration. We investigate the role of both the Péclet and Damköhler numbers on the macroscopic and microscopic concentration profiles (in Sec. 2.3 & 2.4, below), and compare the obtained map of asymptotic transport regimes against numerical simulation (Sec. 2.5, below).

We further use our idealised theoretical model to assess how governing parameters (Pe, Da) affect the accuracy of homogenization approximations (Sec. 2.6, below).

2.2 Model assumptions and problem statement

Consider a one-dimensional equispaced array of N identical point sinks of strength q_0 (Fig. 2.1). The size of the domain is L, and l is the distance between two adjacent sinks ($l \ll L$, $L = (N+1)l$). The flow field $\mathbf{u} = (u_0, 0, 0)$ is assumed to be uniform over the domain (as if driven by a constant pressure drop according to Darcy's law); the concentration C_0 at the inlet is prescribed, and the concentration at the outlet is set to be zero. The concentration field $C^*(x^*)$ is required to be non-negative, and therefore, for sufficiently strong uptake, we have to define an internal free boundary at $x^* = x_0^*$ such that $C^* > 0$ for $0 < x^* < x_0^*$, and $C^* = 0$ for $x_0^* < x^* < L$.

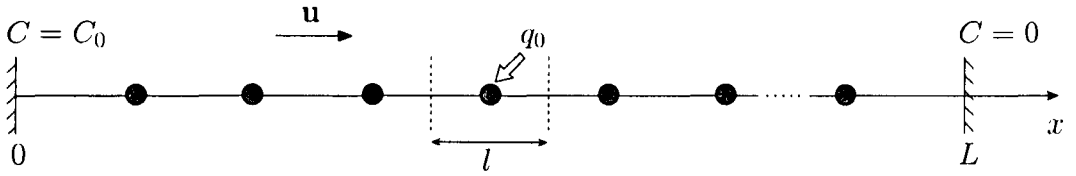

Figure 2.1. The model geometry.

The model is described by the steady advection-diffusion equation, subject to boundary conditions, as follows:

$$u_0 \frac{\mathrm{d}C^*}{\mathrm{d}x^*} = D \frac{\mathrm{d}^2 C^*}{\mathrm{d}x^{*2}} - q_0 \sum_{n=1}^{N} \delta(x^* - x_n^*), \quad 0 < x^* < L, \tag{2.2.1a}$$

$$C^*|_{x^*=0} = C_0, \tag{2.2.1b}$$

$$C^*|_{x^*=L} = 0 \quad \text{or} \quad C^*|_{x^*=x_0^*} = \left.\frac{\mathrm{d}C^*}{\mathrm{d}x^*}\right|_{x^*=x_0^*} = 0, \quad \text{for} \quad 0 < x_0^* \le L, \tag{2.2.1c}$$

where D is the diffusion coefficient, and u_0 is a flow velocity, which are both assumed constant; $x_n^* = nl\,(n = 1 \ldots N)$ are the sink locations. The no-flux boundary condition at x_0^* results from the non-negativeness constraint on concentration, i.e. if solute concentration falls to zero before reaching the outlet, it stays at zero despite all the sinks downstream.

We introduce non-dimensional variables $C^* = C_0\, C$, $x^* = l\, x$ and rewrite (2.2.1) in dimensionless form as

$$\begin{aligned} &\mathrm{Pe} \frac{\mathrm{d}C}{\mathrm{d}x} = \frac{\mathrm{d}^2 C}{\mathrm{d}x^2} - \mathrm{Da} \sum_{n=1}^{N} \delta(x - n), \quad 0 < x < \varepsilon^{-1}, \\ &C|_{x=0} = 1, \quad C|_{x=\varepsilon^{-1}} = 0 \ \text{ or } \ C|_{x=x_0} = \left.\frac{\mathrm{d}C}{\mathrm{d}x}\right|_{x=x_0} = 0, \end{aligned} \tag{2.2.2}$$

where $\mathrm{Pe} = u_0\, l/D$ and $\mathrm{Da} = q_0\, l/(D\, C_0)$ are the local Péclet and Damköhler numbers respectively, and $x_0 = x_0^*/l$.

Note that (2.2.2) can be equivalently rewritten as

$$\mathrm{Pe} \frac{\mathrm{d}C}{\mathrm{d}x} = \frac{\mathrm{d}^2 C}{\mathrm{d}x^2}, \qquad 0 < x < \varepsilon^{-1}, \quad x \neq n, \tag{2.2.3a}$$

$$C|_{x=0} = 1, \tag{2.2.3b}$$

$$C|_{x=\varepsilon^{-1}} = 0 \quad \text{or} \quad C|_{x=x_0} = \left.\frac{\mathrm{d}C}{\mathrm{d}x}\right|_{x=x_0} = 0 \ \text{ for } \ 0 < x_0 \le \varepsilon^{-1}, \tag{2.2.3c}$$

$$C|_{x=n-} = C|_{x=n+}, \quad n = 1, 2, \ldots, N;\ N = \varepsilon^{-1} - 1, \tag{2.2.3d}$$

$$\left[\frac{\mathrm{d}C}{\mathrm{d}x} - \mathrm{Pe}\, C\right]_{x=n} = \mathrm{Da}, \tag{2.2.3e}$$

where $[f]_x = f|_{x+} - f|_{x-}$ denotes a jump of function f at the point x.

The original problem (2.2.1) in dimensional variables describes an interplay between diffusive, advective and uptake concentration fluxes (or timescales), which are determined by the Péclet, Damköhler numbers and reference lengthscales. We assume that the macroscale (or

global) fluxes are characterised by a concentration drop C_0 across the domain of length L (in dimensional variables). Therefore, the reference global diffusive, advective and uptake fluxes across the macroscale domain are

$$\Phi_{\text{diff}} = \frac{D\,C_0}{L}, \quad \Phi_{\text{adv}} = u_0\,C_0, \quad \Phi_{\text{upt}} = q_0\,N \simeq \varepsilon^{-1}\,q_0\,. \tag{2.2.4}$$

Alternatively, we can characterise solute transport via local τ^l and global τ^g timescales:

$$\begin{aligned} \tau^l_{\text{diff}} &\sim \frac{l^2}{D}\,, \quad \tau^l_{\text{adv}} \sim \frac{l}{u_0}\,, \quad \tau^l_{\text{upt}} \sim \frac{C_0 l}{q_0}\,, \\ \tau^g_{\text{diff}} &\sim \frac{L^2}{D}\,, \quad \tau^g_{\text{adv}} \sim \frac{L}{u_0}\,, \quad \tau^g_{\text{upt}} \sim \frac{C_0 L}{q_0}\,, \end{aligned} \tag{2.2.5}$$

so that $\text{Pe} = \left(\tau^l_{\text{adv}}/\tau^l_{\text{diff}}\right)^{-1}$, $\text{Da} = \left(\tau^l_{\text{upt}}/\tau^l_{\text{diff}}\right)^{-1}$.

Advective and uptake fluxes approximately balance each other ($\Phi_{\text{adv}} \sim \Phi_{\text{upt}}$) when the local uptake rate at each sink matches the global advection rate ($\tau^g_{\text{adv}} \sim \tau^l_{\text{upt}}$), which is equivalent to $\text{Da} \sim \varepsilon\,\text{Pe}$. We can also identify a distinct regime of mutual balance when all three global fluxes are approximately equal

$$\Phi_{\text{uptake}} \sim \Phi_{\text{adv}} \sim \Phi_{\text{diff}}\,,$$

or (2.2.6)

$$\varepsilon^{-2}\,\text{Da} \;\sim\; \varepsilon^{-1}\,\text{Pe} \;\sim\; 1\,.$$

This defines a special "triple" point, or "organising centre", $(\text{Pe}, \text{Da}) = (O(\varepsilon), O(\varepsilon^2))$ in parameter space (see Fig. 2.2a) that is important for subsequent asymptotic analysis.

Because of the two distinct lengthscales l and L ($\varepsilon = l/L \ll 1$) present in the model, we look for solutions of (2.2.2) in the form

$$C(x) = \tilde{C}(x, X)\,, \quad X = \varepsilon\,x\,, \tag{2.2.7}$$

introducing a slowly varying spatial variable X. As ε tends to zero, x and X become independent in a sense of the weak two-scale convergence of solution of (2.2.2) to a limit (leading-order) solution $C^{(0)}(x, X)$

$$\lim_{\varepsilon\to 0} \int_0^{\varepsilon^{-1}} C(x)\,\varphi(x, \varepsilon x)\,\mathrm{d}x = \int_0^1 \mathrm{d}X \int_{-1/2}^{1/2} C^{(0)}(x, X)\,\varphi(x, X)\,\mathrm{d}x\,, \tag{2.2.8}$$

for every φ from the appropriate class of x-periodic test functions [191] (the integral on the right-hand-side is taken over a single periodic unit cell $-1/2 < x' = x - n < 1/2$ due to the translational invariance of (2.2.3a)).

The differential operators change accordingly:

$$\frac{\mathrm{d}}{\mathrm{d}x} = \frac{\partial}{\partial x} + \varepsilon\,\frac{\partial}{\partial X}\,, \quad \frac{\mathrm{d}^2}{\mathrm{d}x^2} = \frac{\partial^2}{\partial x^2} + 2\,\varepsilon\,\frac{\partial^2}{\partial x \partial X} + \varepsilon^2\,\frac{\partial^2}{\partial X^2}\,. \tag{2.2.9}$$

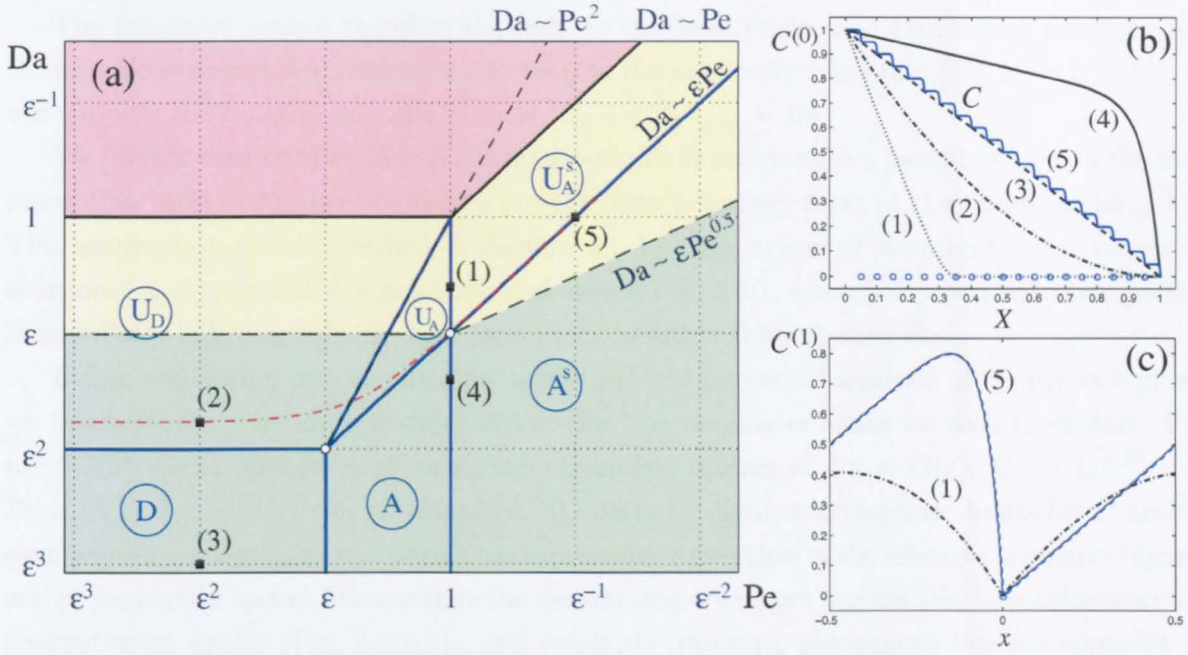

Figure 2.2. (a) Asymptotic regimes in (Pe, Da)-parameter space for transport past a periodic sink distribution with $\varepsilon = 0.05$. Solid lines demarcate six distinct regions (uptake-dominated $\mathrm{U_D}$, $\mathrm{U_A}$, $\mathrm{U_A^s}$; diffusion-dominated D; advection-dominated A, $\mathrm{A^s}$). Exact solution to (2.2.2) converges to the homogenized solution (2.3.9) strongly (in the H^1 norm) in the green region. The yellow region above the dashed lines indicates the domain of weak convergence of exact solution to the homogenization approximation (in the L_2 but not the H^1 norm); the homogenization approximation fails in the red region for large Da; the dash-dotted line indicates an approximate balance between the net solute supply and uptake, according to (2.3.10). (b) Concentration profiles (2.3.9) for points (1-5) in the parameter space (Pe $= 1, \varepsilon^2, \varepsilon^2, 1, \varepsilon^{-1}$ and Da $= \varepsilon^{0.6}, 2\varepsilon^2, \varepsilon^3, \varepsilon^{1.4}, 1$ respectively), showing the leading-order approximation $C^{(0)}$ (1-4) and the full solution (5) computed with $\varepsilon = 0.05$; circles show the locations of the 19 sinks. (c) Corrections $C^{(1)}$ given by (2.4.13) at points (1) and (5), within a unit cell with the sink at $x = 0$. (The asymptotic and numerical results in (a-c) are explained in the following sections below.)

Substituting (2.2.7) and (2.2.9) into (2.2.3), we get

$$\mathrm{Pe}\,(\tilde{C}_x + \varepsilon\,\tilde{C}_X) = \tilde{C}_{xx} + 2\varepsilon\,\tilde{C}_{xX} + \varepsilon^2\,\tilde{C}_{XX}\,, \quad 0 < x < \varepsilon^{-1},\ 0 < X < 1\,, \tag{2.2.10a}$$

$$\tilde{C}|_{X=0} = 1\,, \tag{2.2.10b}$$

$$\tilde{C}|_{X=1} = 0 \quad \text{or} \quad \tilde{C}|_{X=X_0} = \tilde{C}_X|_{X=X_0} = 0\,, \quad 0 < X_0 \le 1\,, \tag{2.2.10c}$$

$$\tilde{C}|_{x=n-} = \tilde{C}|_{x=n+}\,, \qquad n = 1, 2, \ldots, N\,, \tag{2.2.10d}$$

$$\left[\tilde{C}_x + \varepsilon\,\tilde{C}_X - \mathrm{Pe}\,\tilde{C}\right]_{x=n} = \mathrm{Da}\,, \tag{2.2.10e}$$

The transport regime therefore depends on the local Péclet and Damköhler numbers, and of the scale-separation parameter ε. As long as the continuity condition $[\tilde{C}]_{x=n} = 0$ holds, we can simplify the jump of flux at a sink as $[\tilde{C}_x + \varepsilon\,\tilde{C}_X]_{x=n} = \mathrm{Da}$.

We further assume that $\tilde{C}(x, X)$ is an x-periodic function with a period of 1 (with the scale separation valid everywhere outside a possible thin boundary layer at the outlet for large Pe). This assumption will be verified in Section 2.5 by comparison of asymptotic and numerical solutions. A representative simulation is shown in Fig. 2.2(c, case (5)) (black solid line), which is essentially indistinguishable from asymptotic solution (blue dashed line).

Before embarking into the detailed analytical and numerical analysis of transport regimes, we briefly outline the main features of the (Pe, Da) parameter space we seek to explore. Figure 2.2(a) shows how for a given ε, two organising centres at $\mathrm{Pe} = O(\varepsilon)$, $\mathrm{Da} = O(\varepsilon^2)$, and $\mathrm{Pe} = O(1)$, $\mathrm{Da} = O(\varepsilon)$ can be identified. By deriving distinct asymptotic limits for C around each organising centre, we can obtain a comprehensive overview of the effective transport regimes across parameter space. We see that the dominating transport regime affects considerably the concentration profile (Fig. 2.2(b,c)), and two-scale transport phenomena become apparent for case (5) (most relevant to the advective-dominated transport of oxygen or glucose in a placentone, as will be discussed below), where fast local oscillations are superimposed on a slowly varying global concentration profile. It is this scale-separation that we will study in more detail.

2.3 Small microscopic Péclet number transport regime

Given (2.2.6), we first consider the special case of $\mathrm{Pe} = O(\varepsilon)$ and $\mathrm{Da} = O(\varepsilon^2)$, setting $\mathrm{Pe} = \varepsilon p$, $\mathrm{Da} = \varepsilon^2 q$ and assuming $p, q = O(1)$ as $\varepsilon \to 0$.

We look for an approximate solution of (2.2.10) in the form of an asymptotic power series

$$C(x) = \tilde{C}(x, X) = C^{(0)}(x, X) + \varepsilon\,C^{(1)}(x, X) + \varepsilon^2\,C^{(2)}(x, X) + \ldots\,. \tag{2.3.1}$$

We will show that the concentration field at leading order varies only with the 'global' X (but not the 'local' x) coordinate.

Substituting (2.3.1) into (2.2.10) and collecting terms in powers of ε, we get at $O(1)$

$$C^{(0)}_{xx} = 0\,, \quad -1/2 < x < 1/2,\ 0 < X < 1\,, \tag{2.3.2a}$$

$$[C^{(0)}]_{x=0} = 0, \quad [C^{(0)}_x]_{x=0} = 0\,, \tag{2.3.2b}$$

$$C^{(0)}|_{X=0} = 1\,, \quad C^{(0)}|_{X=1} = 0 \ \text{ or } \ C^{(0)}|_{X=X_0} = C^{(0)}_X|_{X=X_0} = 0\,; \tag{2.3.2c}$$

here we limit our consideration to a single periodic unit cell $-1/2 < x' = x - n < 1/2$ (the prime on x is omitted) without loss of generality due to the translational invariance of (2.2.10a) and the assumed x-periodicity of $\tilde{C}(x, X)$.

Equations (2.3.2a,b) imply that there is no local variation of $C^{(0)}$ in each unit cell. $C^{(0)}$ is determined therefore only by the global boundary conditions (2.3.2c), so that $C^{(0)} = C^{(0)}(X)$.

Collecting the terms in (2.2.10) at $O(\varepsilon)$, then gives

$$\begin{aligned} &p\,C^{(0)}_x = C^{(1)}_{xx} + 2\,C^{(0)}_{xX}\,, \quad [C^{(1)}]_{x=0} = 0, \quad [C^{(1)}_x + C^{(0)}_X]_{x=0} = 0\,, \\ &C^{(1)}|_{X=0} = 0\,, \quad C^{(1)}|_{X=1} = 0\,, \end{aligned} \tag{2.3.3}$$

which is equivalent to

$$\begin{aligned} &C^{(1)}_{xx} = 0\,, \quad [C^{(1)}]_{x=0} = 0, \quad [C^{(1)}_x]_{x=0} = 0\,, \\ &C^{(1)}|_{X=0} = 0\,, \quad C^{(1)}|_{X=1} = 0\,. \end{aligned} \tag{2.3.4}$$

Therefore $C^{(1)} \equiv 0$.

Collecting the terms in (2.2.10) at $O(\varepsilon^2)$, we obtain

$$\begin{aligned} &p\left(C^{(1)}_x + C^{(0)}_X\right) = C^{(2)}_{xx} + 2\,C^{(1)}_{xX} + C^{(0)}_{XX}\,, \\ &[C^{(2)}]_{x=0} = 0, \quad [C^{(2)}_x + C^{(1)}_X]_{x=0} = q\,, \\ &C^{(2)}|_{X=0} = 0\,, \quad C^{(2)}|_{X=1} = 0\,, \end{aligned} \tag{2.3.5}$$

which reduces to

$$p\,C^{(0)}_X = C^{(2)}_{xx} + C^{(0)}_{XX}\,, \tag{2.3.6a}$$

$$[C^{(2)}]_{x=0} = 0, \quad [C^{(2)}_x]_{x=0} = q\,, \tag{2.3.6b}$$

$$C^{(2)}|_{X=0} = 0\,, \quad C^{(2)}|_{X=1} = 0\,. \tag{2.3.6c}$$

At this level we see competition between advection (p) and uptake (q).

Averaging (2.3.6a) over the unit cell $-1/2 < x < 1/2$, outside a small neighbourhood $(-\delta, \delta)$ of $x = 0$, leads to

$$p\,C^{(0)}_X - C^{(0)}_{XX} = \int_{-1/2}^{-\delta} C^{(2)}_{xx}\,\mathrm{d}\,x + \int_{+\delta}^{1/2} C^{(2)}_{xx}\,\mathrm{d}\,x = C^{(2)}_x|_{x=\frac{1}{2}} - C^{(2)}_x|_{x=-\frac{1}{2}} - [C^{(2)}_x]_{x=0}\,. \tag{2.3.7}$$

We assume periodicity of $C^{(2)}_x$ in a unit cell (in addition to the assumption of x-periodicity of $C^{(2)}$), use the jump condition $[C^{(2)}_x]_0 = q$, and complement equation (2.3.7) with boundary conditions (2.3.2c) to get a macroscopic averaged problem for the leading-order concentration field:

$$C^{(0)}_{XX} - p\,C^{(0)}_X = q\,, \tag{2.3.8a}$$

$$C^{(0)}|_{X=0} = 1, \quad C^{(0)}|_{X=1} = 0, \qquad 0 \le X \le 1 \quad \text{for } q \le Q(p) \tag{2.3.8b}$$

$$C^{(0)}|_{X=0} = 1, \quad C^{(0)}_X|_{X=X_0} = 0, \quad 0 \le X \le X_0 \quad \text{for } q > Q(p) \tag{2.3.8c}$$

with $q = Q(p)$ defined such that $C_X^{(0)}(1) = 0$, and X_0 defined such that $C^{(0)}(X_0) = 0$.

The solution to (2.3.8) is

$$C^{(0)}(X) = \begin{cases} \left(\frac{q}{p} - 1\right) \frac{e^{pX} - 1}{e^p - 1} - \frac{q}{p} X + 1, & q \le Q(p) \\ \frac{q}{p^2} \frac{e^{pX} - 1}{e^{pX_0}} - \frac{q}{p} X + 1, & q > Q(p) \end{cases} \tag{2.3.9}$$

where

$$Q(p) = \frac{p^2 e^p}{(p-1)e^p + 1}, \quad X_0 = -\frac{1}{p} e^{-pX_0} + \frac{q+p^2}{pq} \tag{2.3.10}$$

The macroscopic solution (2.3.9)[1] allows us to describe all asymptotic behaviour at leading order with respect to parameters $(p, q) = (\mathrm{Pe}/\varepsilon, \mathrm{Da}/\varepsilon^2)$, as shown in Fig. 2.2(a).

We now consider asymptotic limits of (2.3.9) with respect to parameters (p, q), representing (Pe, Da). First, we explore (2.3.9) near the distinguished balance of global fluxes (2.2.6), represented by the boundaries between the diffusion (D), advection (A) and uptake-dominated (U) regions (see Fig. 2.2a):

(D/A) taking the limit of (2.3.9) along the vertical line $p = O(1)$, $q \ll 1$ ($\mathrm{Pe} = O(\varepsilon)$, $\mathrm{Da} \ll \varepsilon^2$) gives $C^{(0)} \approx 1 - \frac{e^{pX}-1}{e^p-1}$, which represents the advection-diffusion balance (independent of uptake);

(D/U) taking the limit of (2.3.9) along the horizontal line $q = O(1)$, $p \ll 1$, $q \le Q(p) \approx 2$ ($\mathrm{Pe} \ll 1$, $\mathrm{Da} = O(\varepsilon^2) \le 2\varepsilon^2$) gives $C^{(0)} \approx \frac{q}{2} X^2 - \left(\frac{q}{2} + 1\right) X + 1$, which represents the diffusion-uptake balance (independent of advection);

(A/U) taking the limit of (2.3.9) along the diagonal line $q = O(p)$, $p \gg 1$, $q \le Q(p) \approx p$ ($\mathrm{Da} = O(\varepsilon \mathrm{Pe})$, $\mathrm{Pe} \gg \varepsilon$, $\mathrm{Da} \le \varepsilon \mathrm{Pe}$) gives $C^{(0)} \approx 1 - \frac{q}{p} X + \left(\frac{q}{p} - 1\right) \frac{e^{pX}-1}{e^p}$, which represents the advection-uptake balance (with a boundary layer of width $O(1/p)$ at the outlet, where diffusion balances advection locally); the composite asymptotic form for $C^{(0)}$ captures both a slow linear drop in concentration and an advective-diffusive boundary layer near the exit (as illustrated in Fig. 2.2(b), case (4)).

In addition, analysis of (2.3.8) indicates that the lengthscale $l_A \sim 1/p$ of the advective-diffusive boundary layer is comparable to the advective-uptake dominated lengthscale $l_U \sim p/q$ when $q \sim p^2$ ($\mathrm{Da} \sim \mathrm{Pe}^2$) (see case (1) in Fig. 2.2). This subdivides the uptake region U into two subdomains: $\mathrm{U_D}$ ($q \gg p^2$, $q \gg 1$), where no downstream boundary layer can be formed, and $\mathrm{U_A}$ ($p \ll q \ll p^2$), where a boundary layer with the exponential decay of solute appears downstream of the inlet. The corresponding asymptotic form of (2.3.9) is as follows:

($\mathrm{U_D/U_A}$) taking the limit of (2.3.9) along the boundary $q = O(p^2)$, $q \gg 1$, $q > Q(p)$; ($\mathrm{Da} = O(\mathrm{Pe}^2)$, $\mathrm{Da} \gg \max(\varepsilon^2, \varepsilon \mathrm{Pe})$) gives $C^{(0)} \approx 1 - \frac{q}{p} X + \frac{q}{p^2} \frac{e^{pX}-1}{e^{pX_0}}$, where $X_0 \approx \frac{2}{p}$.

Simplifying the limits of the codimension-one asymptotic expressions (D/A), (D/U), (A/U) and ($\mathrm{U_D/U_A}$) we obtain four leading-order parameter regimes in which (2.3.9) has distinct asymptotic forms:

[1] The uniqueness of the solution $0 < X_0 \le 1$ to (2.3.10b) as a fixed point is determined by the contraction mapping property [150]: $\|\varphi(X_1) - \varphi(X_2)\| \le \gamma \|X_1 - X_2\|$, $0 < \gamma < 1$ for $\varphi(X) = -\frac{1}{p} e^{-pX} + \mathrm{const}$ ($p > 0$), with $|\varphi'(X_0)| = e^{-pX_0} < 1$ for any $X_0 > 0$. The convergence thus justifies the iteration procedure $X_0^{(n+1)} = \varphi(X_0^{(n)})$.

(D) Diffusion between boundaries: taking $p \sim q \ll 1$ ($\mathrm{Pe} \ll O(\varepsilon)$, $\mathrm{Da} \ll O(\varepsilon^2)$) gives $C^{(0)} \approx 1 - X$ (linear concentration profile, as illustrated in Fig. 2.2(b), case (3));

($\mathrm{U_D}$) Uptake upstream of outlet: taking $p \ll 1$, $\max(1, p^2) \ll q \ll \varepsilon^{-2}$ ($\mathrm{Pe} \ll O(\varepsilon)$, $\max(\varepsilon^2, \mathrm{Pe}^2) \ll \mathrm{Da} \ll 1$) gives

$C^{(0)} \approx \left(1 - \frac{X}{X_0}\right)^2$, $0 \le X \le X_0$, $\varepsilon \ll X_0 = \sqrt{2/q} \ll 1$

(parabolic profile with an internal free boundary at distance of $O(1/\sqrt{q})$ from the inlet, as illustrated in Fig. 2.2(b), case (2));

($\mathrm{U_A}$) Uptake with a diffusive inner boundary layer: taking $p \gg 1$, $p \ll q \ll \min(p/\varepsilon, p^2)$ ($\mathrm{Pe} \gg O(\varepsilon)$, $\varepsilon\mathrm{Pe} \ll \mathrm{Da} \ll \min(\mathrm{Pe}, \mathrm{Pe}^2)$) gives

$C^{(0)} \approx 1 - \frac{X}{X_0} - \frac{1}{pX_0}\,\mathrm{e}^{-p(X_0 - X)}$, $0 \le X \le X_0$, $\varepsilon \ll X_0 \approx p/q \ll 1$

(linear profile stretching to the distance $O(p/q)$ with an internal boundary layer of thickness $O(1/p)$, as illustrated in Fig. 2.2(b), case (1)),

(A) Advection with a diffusive boundary layer near the outlet: taking $p \gg 1$, $q \ll p$ ($\mathrm{Pe} \gg O(\varepsilon)$, $\mathrm{Da} \ll \varepsilon\mathrm{Pe}$) gives

$C^{(0)} \approx 1 - \frac{q}{p}X - \mathrm{e}^{-p(1-X)}$

(linear profile with a boundary layer of thickness $O(1/p)$, as illustrated in Fig. 2.2(b), case (4));

Note that in the special case of $p = q$ ($\mathrm{Da} = \varepsilon\mathrm{Pe}$) the leading-order concentration profile (2.3.9) is exactly linear, showing no effect of the outlet in this case (Fig. 2.2c). We also observe that the concentration profile at leading order is generally *parabolic* in small Péclet number ($\mathrm{Pe} \ll \varepsilon$) regimes (D and $\mathrm{U_D}$), *exponential* at moderate or intermediate values $\varepsilon \ll \mathrm{Pe} \ll 1$ (A and $\mathrm{U_A}$), and *linear* at large Péclet number $\mathrm{Pe} \gg 1$ (A^s and U_2^s); here index s indicates the presence of advective "staircases" in the concentration profile due to microscale inhomogeneities (see Fig. 2.2b). However, to understand this microscale effect we need to consider the first non-vanishing correction to the leading-order solution.

To find the correction $C^{(2)}$, we substitute (2.3.8a) in (2.3.6) to get the cell problem

$$\begin{aligned} &C^{(2)}_{xx} = -q\,, \\ &[C^{(2)}]_{x=0} = 0, \quad [C^{(2)}_x]_{x=0} = q\,, \end{aligned} \tag{2.3.11}$$

which has a unique solution if we demand periodicity of $C^{(2)}$ and a calibration condition $\langle C^{(2)} \rangle = const$ in a unit cell, were $\langle f \rangle \equiv \int_{-1/2}^{1/2} f \,\mathrm{d}x$.

The solution to (2.3.11) is therefore

$$C^{(2)}(x) = \begin{cases} -\frac{q}{2}\left(x^2 + x + \frac{1}{6}\right) + \langle C^{(2)} \rangle\,, & -1/2 \le x < 0 \\ -\frac{q}{2}\left(x^2 - x + \frac{1}{6}\right) + \langle C^{(2)} \rangle\,, & 0 \le x \le 1/2\,. \end{cases} \tag{2.3.12}$$

In order for the correction $C^{(2)}$ to satisfy the global boundary conditions (2.3.6c), we observe that each border (at $X = 0, 1$) contains a half of the unit cell (see Fig. 2.1), so that

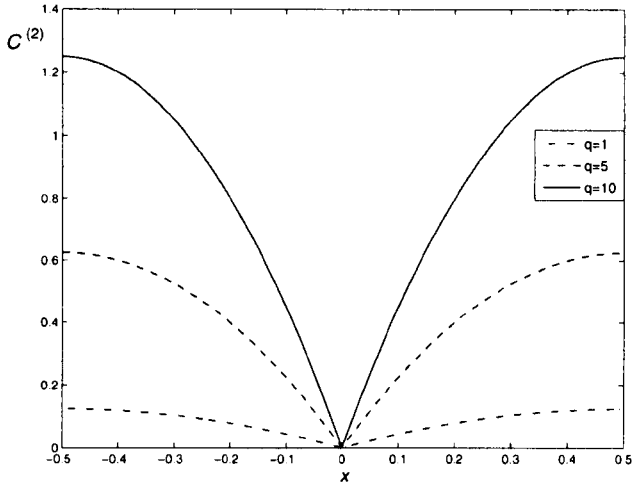

Figure 2.3. The second correction (2.3.12) in the asymptotic expansion (2.3.1) of concentration in a unit cell for different values of Damköhler number $\mathrm{Da} = \varepsilon^2 q$ ($\varepsilon = 0.05$, $\langle C^{(2)} \rangle = q/12$).

$C^{(2)}|_{x=0+} = C^{(2)}|_{x=0-} = 0$ due to (2.3.6c) and x-periodicity. The constant $\langle C^{(2)} \rangle$ is therefore identified from (2.3.12) to be $q/12$.

Fig. 2.3 shows a concentration profile of the second correction for different values of Damköhler number ($\mathrm{Da} = \varepsilon^2 q$). We compare this asymptotic correction against numerical computations below.

Relation (2.3.12) implies that $C^{(2)}$ is proportional to $\mathrm{Da}/\varepsilon^2$. One can see that when Da approaches 1, the second correction approaches ε^{-2}, and $\varepsilon^2 C^{(2)}$ becomes comparable to $C^{(0)}$ in order of magnitude, violating the convergence of the asymptotic expansion (2.3.1). Equivalently, the leading-order term $C^{(0)}$ in the solution decays considerably (of the order of $O(1)$) on lengthscale of a few sinks. This imposes a restriction for the maximal value of local Damköhler number allowing the homogenization procedure to be performed (see Fig. 2.2a).

2.3.1 Case $\mathrm{Pe} = O(\varepsilon)$, $\mathrm{Da} = O(\varepsilon^2)$: Summary

We have obtained effective macroscale equation (2.3.8) for $C^{(0)}(X)$ in case of small-to-zero microscopic Péclet numbers $\mathrm{Pe} = \varepsilon p$ and for Damköhler number scaled as $\mathrm{Da} = \varepsilon^2 q$ ($p, q = O(1)$). Equation (2.3.8) is an advection-diffusion equation with a uniform sink. Therefore, the form of the governing microscale equation (2.2.3a) is preserved at the macroscale after averaging (with microscopic boundary effects at the sinks incorporated in the uniformly distributed sink term). It can be demonstrated (see Section B.2 of Appendix B) that the effect of a finite size of the sinks (expressed by a volume fraction ϕ ($0 \le \phi < 1$) occupied by the sink in a unit cell) leads to a modified sink term $q/(1-\phi)$ on the right-hand side of (2.3.8), indicating stronger net uptake at large volume fractions, e.g. of villous tissue.

We have also shown that there is a critical relation (2.3.10) between Péclet and Damköhler numbers

$$\mathrm{Da}_{\mathrm{cr}} = \frac{\mathrm{Pe}^2 \, \mathrm{e}^{\mathrm{Pe}/\varepsilon}}{(\mathrm{Pe}/\varepsilon - 1)\, \mathrm{e}^{\mathrm{Pe}/\varepsilon} + 1},$$

so that an internal free boundary in the concentration profile develops for $\mathrm{Da} > \mathrm{Da}_{\mathrm{cr}}$. The limiting cases for this relation, $\mathrm{Da}_{\mathrm{cr}} \approx 2\varepsilon^2$ for $\mathrm{Pe} \ll \varepsilon$ and $\mathrm{Da}_{\mathrm{cr}} \approx \varepsilon\mathrm{Pe}$ for $\mathrm{Pe} \gg \varepsilon$, agree with the approximate balance of fluxes obtained from *a priori* dimensional analysis (2.2.6).

Analysis of the limiting form of (2.3.9) along the advective-uptake boundary (A/U) shows a downstream boundary layer (of thickness $1/p$) developing when $q \sim p \gg 1$ ($\mathrm{Pe} \gg \varepsilon$, $\mathrm{Da} \sim \varepsilon\mathrm{Pe}$). In the local "microscopic" coordinates, the thickness of the boundary layer is $x \sim X/\varepsilon \sim 1/(\varepsilon p)$; therefore, to capture this lengthscale, homogenization of (2.2.10) for $p = O(\varepsilon^{-1})$ ($\mathrm{Pe} = O(1)$) is required.

The first non-zero correction is of the second order in ε and is given by the diffusion problem (2.3.11) in a periodic unit cell, which provides solution (2.3.12). However, correction (2.3.12) does not depend on Péclet number and hence cannot explain the appearance of microscopic "stairs" in the concentration profile at $\mathrm{Pe} \gg \varepsilon$ (as shown in Fig. 2.2(b), case 5).

We therefore need to choose different scaling to address these questions. Correction (2.3.12) is of magnitude $\varepsilon^2 q$, becomes $O(\varepsilon)$ when $q = O(1/\varepsilon)$, motivating new regime $\mathrm{Pe} = O(1)$, $\mathrm{Da} = O(\varepsilon)$ that provides approximate balance between advective and uptake fluxes according to (2.2.6).

2.4 Regime of moderate microscopic Péclet number

We now consider the case of $\mathrm{Pe} = O(1)$ and $\mathrm{Da} = O(\varepsilon) = \varepsilon q_1$, $q_1 = O(1)$. Substituting (2.3.1) into (2.2.10) and collecting terms in powers of ε, we obtain at $O(1)$

$$\mathrm{Pe}\, C^{(0)}_x = C^{(0)}_{xx}\,, \quad [C^{(0)}]_{x=0} = 0, \quad [C^{(0)}_x]_{x=0} = 0\,, \tag{2.4.1a}$$

$$C^{(0)}|_{X=0} = 1\,, \quad C^{(0)}|_{X=1} = 0 \quad \text{or} \quad C^{(0)}|_{X=X_0} = C^{(0)}_X|_{X=X_0} = 0\,, \tag{2.4.1b}$$

which implies, analogously to (2.3.2a), $C^{(0)} = C^{(0)}(X)$.

Collecting the terms in (2.2.10) at $O(\varepsilon^1)$, we have

$$\begin{aligned} &\mathrm{Pe}\left(C^{(1)}_x + C^{(0)}_X\right) = C^{(1)}_{xx} + 2\,C^{(0)}_{xX}\,, \\ &[C^{(1)}]_{x=0} = 0, \quad [C^{(1)}_x + C^{(0)}_X]_{x=0} = q_1\,, \\ &C^{(1)}|_{X=0} = 0\,, \quad C^{(1)}|_{X=1} = 0 \quad \text{or} \quad C^{(1)}|_{X=X_0} = C^{(1)}_X|_{X=X_0} = 0\,, \end{aligned} \tag{2.4.2}$$

which reduces to

$$C^{(1)}_{xx} - \mathrm{Pe}\, C^{(1)}_x = \mathrm{Pe}\, C^{(0)}_X\,, \tag{2.4.3a}$$

$$[C^{(1)}]_{x=0} = 0\,, \qquad [C^{(1)}_x]_{x=0} = q_1\,, \tag{2.4.3b}$$

$$C^{(1)}|_{X=0} = 0\,, \qquad C^{(1)}|_{X=1} = 0 \quad \text{or} \quad C^{(0)}|_{X=X_0} = C^{(0)}_X|_{X=X_0} = 0\,. \tag{2.4.3c}$$

Averaging equation (2.4.3a) over the unit cell ($-1/2 < x < 1/2$) and assuming periodicity of $C^{(1)}$ and $C^{(1)}_x$ in a unit cell ($C^{(1)}|_{x=-1/2} = C^{(1)}|_{x=1/2}$, $C^{(1)}_x|_{x=-1/2} = C^{(1)}_x|_{x=1/2}$), we get

$$\mathrm{Pe}\, C^{(0)}_X = -\,[C^{(1)}_x]_{x=0} + \mathrm{Pe}\;[C^{(1)}]_{x=0}\,, \tag{2.4.4}$$

using the jump boundary conditions at the sink (2.4.3b) and macroscopic boundary conditions (2.4.1b), we find an averaged advection-diffusion problem

$$\mathrm{Pe}\, C^{(0)}_X = -q_1\,, \tag{2.4.5a}$$

$$C^{(0)}|_{X=0} = 1\,, \tag{2.4.5b}$$

with a linear function as a solution:

$$C^{(0)} = 1 - \frac{q_1}{\mathrm{Pe}}\, X\,, \tag{2.4.6}$$

where $q_1/\mathrm{Pe} \le 1$ if the concentration profile extends to the outlet ($X = 1$), and $q_1/\mathrm{Pe} = 1/X_0$ if the solute concentration drops to zero at $X = X_0 < 1$.

Note that (2.4.5a) allows us to satisfy only one macroscopic boundary condition, while the other ($C^{(0)}|_{X=1} = 0$ or $C^{(0)}|_{X=X_0} = C^{(0)}_X|_{X=X_0} = 0$) leads to a diffusive boundary layer of the original problem, which is not preserved in this scaling and may be too narrow (of the lengthscale $O(1/p) \sim \varepsilon/\mathrm{Pe} \ll 1$, see Sec. 2.3) to homogenize, as shown in Fig. 2.2(b), cases (1) and (4).

Equations (2.4.3a)–(2.4.3b) provide a cell problem for the first correction:

$$\begin{aligned} &C^{(1)}_{xx} - \mathrm{Pe}\, C^{(1)}_x = \mathrm{Pe}\, C^{(0)}_X\,, \\ &[C^{(1)}]_{x=0} = 0, \quad [C^{(1)}_x]_{x=0} = q_1\,. \end{aligned} \tag{2.4.7}$$

Because the source terms $C^{(0)}_X$ and q_1 in this linear problem are independent of x, it is convenient to use the superposition principle and look for a solution in the form

$$C^{(1)}(x, X) = -b(x)\,\mathrm{Pe}\, C^{(0)}_X + a(x)\, q_1\,, \tag{2.4.8}$$

where $a(x)$ and $b(x)$ are periodic with period 1 and satisfy the following cell problems:

$$\begin{aligned} &a_{xx} - \mathrm{Pe}\, a_x = 0\,, \\ &a|_{x=0-} = a|_{x=0+}, \quad (a_x)|_{x=0+} - (a_x)|_{x=0-} = 1\,, \\ &a|_{x=-1/2} = a|_{x=1/2}\,, \end{aligned} \tag{2.4.9}$$

$$\begin{aligned} &b_{xx} - \mathrm{Pe}\, b_x = -1\,, \\ &b|_{x=0-} = b|_{x=0+}, \quad (b_x)|_{x=0+} - (b_x)|_{x=0-} = 0\,, \\ &b|_{x=-1/2} = b|_{x=1/2}\,. \end{aligned} \tag{2.4.10}$$

The solutions to (2.4.9) and (2.4.10) are

$$a(x) = \begin{cases} -\frac{1}{\mathrm{Pe}}\, \dfrac{(e^{\mathrm{Pe}/2} - 1)\, e^{\mathrm{Pe}\, x}}{e^{\mathrm{Pe}/2} - e^{-\mathrm{Pe}/2}} + \frac{1}{2\,\mathrm{Pe}} + \langle a \rangle\,, & -1/2 \le x < 0 \\ -\frac{1}{\mathrm{Pe}}\, \dfrac{(e^{-\mathrm{Pe}/2} - 1)\, e^{\mathrm{Pe}\, x}}{e^{\mathrm{Pe}/2} - e^{-\mathrm{Pe}/2}} - \frac{1}{2\,\mathrm{Pe}} + \langle a \rangle\,, & 0 \le x \le 1/2\,, \end{cases} \tag{2.4.11}$$

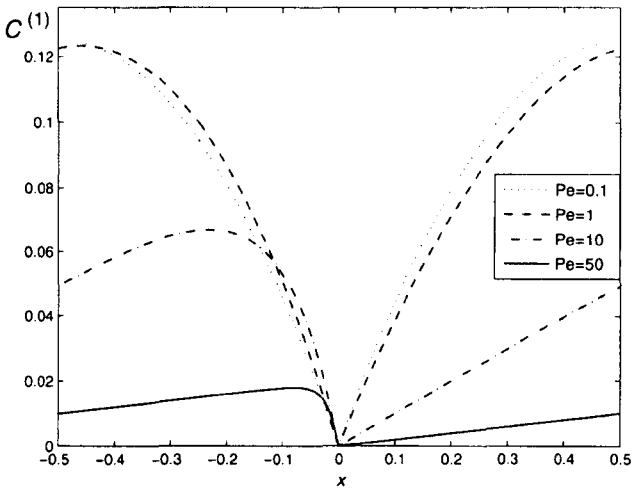

Figure 2.4. The first correction (2.4.13) in the asymptotic expansion (2.3.1) of concentration in a unit cell for Da $= \varepsilon$ ($q_1 = \varepsilon q = 1$) at different values of Péclet number ($\varepsilon = 0.05$, $\langle C^{(1)} \rangle$ is given by (2.4.14)).

$$b(x) = -\tfrac{1}{\mathrm{Pe}} \frac{e^{\mathrm{Pe}\,x}}{e^{\mathrm{Pe}/2} - e^{-\mathrm{Pe}/2}} + \tfrac{1}{\mathrm{Pe}} \left(x + \tfrac{1}{\mathrm{Pe}}\right) + \langle b \rangle\,, \quad -1/2 \le x \le 1/2\,. \tag{2.4.12}$$

We use (2.4.6) to compute the global concentration gradient $C_X^{(0)} = -\frac{q_1}{\mathrm{Pe}}$ which transforms (2.4.8) to $C^{(1)} = q_1 \left(a(x) + b(x)\right)$, and therefore (2.4.11) and (2.4.12) give

$$C^{(1)}(x) = \begin{cases} \dfrac{q_1}{\mathrm{Pe}} \left(-\dfrac{\exp\left(\mathrm{Pe}\left(x + \frac{1}{2}\right)\right)}{2\sinh(\mathrm{Pe}/2)} + x + \dfrac{2 + \mathrm{Pe}}{2\,\mathrm{Pe}} \right) + \langle C^{(1)} \rangle\,, & -1/2 \le x < 0 \\ \dfrac{q_1}{\mathrm{Pe}} \left(-\dfrac{\exp\left(\mathrm{Pe}\left(x - \frac{1}{2}\right)\right)}{2\sinh(\mathrm{Pe}/2)} + x + \dfrac{2 - \mathrm{Pe}}{2\,\mathrm{Pe}} \right) + \langle C^{(1)} \rangle\,, & 0 \le x \le 1/2\,, \end{cases} \tag{2.4.13}$$

which is plotted in Fig. 2.4.

The average of the first correction, $\langle C^{(1)} \rangle$, is identified from (2.4.13) using the global boundary conditions (2.4.3c), which are equivalent to the local condition in each unit cell: $C^{(1)}|_{x=0} = 0$ (analogous to the computations of $\langle C^{(2)} \rangle$ in (2.3.12)). Thus

$$\langle C^{(1)} \rangle = \frac{q_1}{2\mathrm{Pe}} \left(\frac{e^{\mathrm{Pe}/2}}{\sinh(\mathrm{Pe}/2)} - \frac{2 + \mathrm{Pe}}{\mathrm{Pe}} \right) = \frac{q_1}{2\mathrm{Pe}} \left(\coth(\mathrm{Pe}/2) - \frac{2}{\mathrm{Pe}} \right), \tag{2.4.14}$$

therefore $\langle C^{(1)} \rangle \approx \frac{q_1}{2\mathrm{Pe}} \left(1 - \frac{2}{\mathrm{Pe}}\right)$ at large $\mathrm{Pe} \gg 1$ and $\langle C^{(1)} \rangle \approx \frac{q_1}{12}$ at small $\mathrm{Pe} \ll 1$, in agreement with previous results of correction average (for $q_1 = \varepsilon\, q$; see Section 2.3).

One can show that, for $\mathrm{Pe} \ll 1$, (2.4.13) takes the form:

$$C^{(1)} = \begin{cases} -\frac{q_1}{2} \left(x^2 + x + \frac{1}{6}\right) + \frac{q_1}{12} + O(q_1 \mathrm{Pe})\,, & -1/2 \le x < 0 \\ -\frac{q_1}{2} \left(x^2 - x + \frac{1}{6}\right) + \frac{q_1}{12} + O(q_1 \mathrm{Pe})\,, & 0 \le x \le 1/2\,. \end{cases} \tag{2.4.15}$$

In this limiting case $C^{(1)}$ tends to $\varepsilon C^{(2)}$ from the small Péclet number regime (2.3.12) as $q_1 \mathrm{Pe}$ tends to zero, with $q_1 = \varepsilon\, q$ (see regions A and $\mathrm{U_A}$ in Fig. 2.2a).

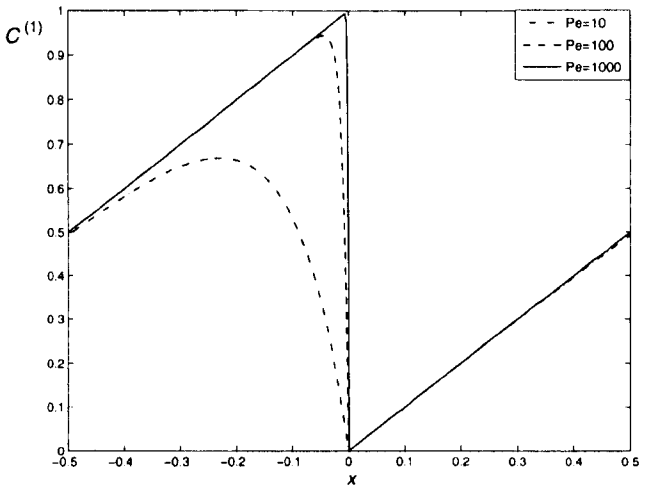

Figure 2.5. The first correction (2.4.13) to the leading-order concentration in a unit cell for $\mathrm{Da} = \varepsilon\mathrm{Pe}$ at different values of Péclet number ($\varepsilon = 0.05$, $\langle C^{(1)} \rangle$ is given by (2.4.14)).

Analogously, at large $\mathrm{Pe} \gg 1$, (2.4.13) reduces to

$$C^{(1)} \approx \begin{cases} \frac{q_1}{Pe}\left(x + \frac{1}{2} - \mathrm{e}^{-\mathrm{Pe}\,|x|}\right) + \frac{q_1}{2\mathrm{Pe}}, & -1/2 \le x < 0, \\ \frac{q_1}{Pe}\left(x - \frac{1}{2}\right) + \frac{q_1}{2\mathrm{Pe}}, & 0 \le x \le 1/2, \end{cases} \tag{2.4.16}$$

with a boundary layer of thickness $O(\mathrm{Pe}^{-1})$ upstream of the sink (see Fig. 2.5). This case corresponds to regions $\mathrm{U}_\Lambda^{\mathrm{s}}$ and A^{s} in Fig. 2.2(a). Note that this limit for $C^{(1)}$ is a discontinuous function at $x = 0$, so that the no-jump condition $[C^{(1)}]_{x=0} = 0$ is violated at each sink, leaving only the total flux $\mathrm{Pe}\,C^{(1)} - C_x^{(1)}$ to be continuous. This suggests that problem (2.2.10) becomes non-uniform at large Péclet numbers, with a diffusive inner boundary layer of width ε/Pe near each sink. We can verify this discontinuity by deriving a cell problem for (2.2.10), using an appropriate scaling for Pe and Da numbers. Homogenization analysis for $\mathrm{Pe} = O(\varepsilon^{-1})$ and $\mathrm{Da} = O(1)$ shows that the regular limit (2.4.16) of (2.4.13) is valid in this case (see Section B.4 in Appendix B for verification of this asymptotic result).

Correction (2.4.13), depicted in Figure 2.4, together with its limiting cases (2.4.15) and (2.4.16) show that microscopic "stairs" in the concentration profile occur when local Péclet number is larger than 1, thus bisecting the leading-order asymptotic regimes A and U_Λ of Fig. 2.2(a) into A & A^{s} and U_Λ & $\mathrm{U}_\Lambda^{\mathrm{s}}$ respectively. The total number of asymptotic transport regimes for problem (2.2.2) is raised to six and is summarised in Fig. 2.2(a).

It can also be shown that the second and all the successive corrections in (2.3.1) vanish (see Appendix B.3).

2.4.1 Case $\mathrm{Pe} = O(1)$, $\mathrm{Da} = O(\varepsilon)$: Summary

We have obtained an effective macroscale equation (2.4.5) for $C^{(0)}(X)$ in case of moderate microscopic Péclet numbers ($\mathrm{Pe} = O(1)$). Equation (2.4.5) is an advection-reaction equation with a uniformly distributed sink, representing the net effect of an array of point sinks. This

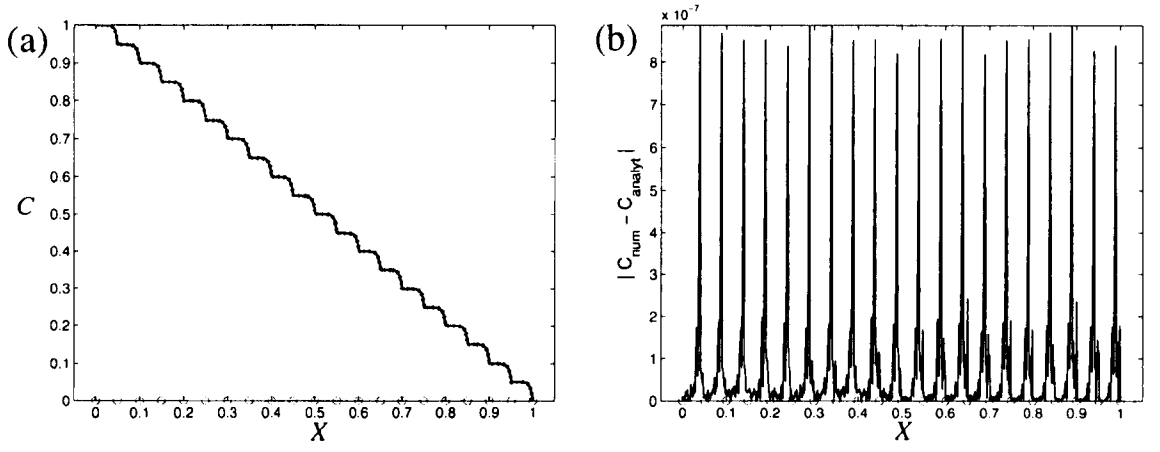

Figure 2.6. (a) a comparison of composite analytical (dots) and numerical (solid) solutions to problem (2.2.2) for Pe = 10, $N = 19$ $\varepsilon = 0.05$; (b) absolute difference between the composite analytical solution (2.5.1) computed on 400 grid points for each unit cell (with 200 uniform points per boundary layer) and numerical computation of the concentration profile on a mesh consisting of 640 elements.

equation agrees with an "advective" limit of (2.3.8) for $p = \mathrm{Pe}/\varepsilon \gg 1$.

We have found solutions of cell problems for $C^{(1)}$ and $C^{(2)}$, demonstrated that their asymptotic behaviour follow the solution obtained in Section 2.3 for $\mathrm{Pe} \ll 1$, and studied their regular limit for $\mathrm{Pe} \gg 1$.

We can also observe from (2.4.13) that the asymptotic analysis breaks down, with $\varepsilon C^{(1)}$ becoming of the same order as $C^{(0)}$ in (2.3.1), when $q_1/\mathrm{Pe} = O(\varepsilon^{-1})$, i.e. $\mathrm{Da} \sim \mathrm{Pe}$. This imposes a limit of homogenization applicability $\mathrm{Da} \ll \mathrm{Pe}$ for $\mathrm{Pe} \gtrsim 1$, and together with the result of Section 2.3 defines the overall upper "homogenization limit" for the Damköhler number:

$$\mathrm{Da} \ll \max(1, \mathrm{Pe}),$$

as shown in Fig. 2.2(a).

2.5 Comparison with numerical simulations

Preliminary tests for comparison between asymptotic and numerical solutions to the advection-diffusion-uptake problem (2.2.2) are performed using the stationary finite element solver of `COMSOL Multiphysics` with the `UMFPACK` (multi-frontal LU-factorisation) algorithm for solving sparse linear systems and sinks located at the mesh nodes.

Another hybrid analytical-numerical solution to linear problem (2.2.2) has been constructed by using the exact solution $C_i(X) = A_i\, \mathrm{e}^{\mathrm{Pe}\,(X - X_{i-1})/\varepsilon} + B_i$, and matching the concentrations and fluxes at each sink to identify the constants A_i and B_i, where X_i is the position of the i-th sink in macroscopic coordinates ($i = 1, \ldots, N$) and $X_0 = 0$, $X_{N+1} = 1$. The boundary conditions

$$C_1|_{X=0} = 1, \quad C_{N+1}|_{X=1} = 0,$$
$$C_{i+1} = C_i, \quad (C_{i+1})_X - (C_i)_X = \mathrm{Da}/\varepsilon \quad \text{at } X = X_i$$

define a composite analytical solution to (2.2.2) as follows:

$$C_i(X) = A_i\, e^{\mathrm{Pe}\,(X - X_{i-1})/\varepsilon} + B_i\,, \quad X_{i-1} \le X \le X_i,\ i = 1, \ldots, N+1\,, \tag{2.5.1a}$$

$$\begin{aligned} A_1 + B_1 &= 1, \\ e^{\mathrm{Pe}(X_i - X_{i-1})/\varepsilon} A_i - A_{i+1} &= -\tfrac{\mathrm{Da}}{\mathrm{Pe}}, \quad i = 1, \ldots, N \\ B_i - B_{i+1} &= \tfrac{\mathrm{Da}}{\mathrm{Pe}}, \\ e^{\mathrm{Pe}(1 - X_N)/\varepsilon} A_{N+1} + B_{N+1} &= 0, \end{aligned} \tag{2.5.1b}$$

where the linear system (2.5.1b) with a sparse well-conditioned matrix is solved to obtain the coefficients $A_1, \ldots, A_{N+1}$, and $B_1, \ldots, B_{N+1}$.

Numerical solution has relative inaccuracy much less than 1% (absolute inaccuracy $\max|C_{\mathrm{num}} - C_{\mathrm{analyt}}| \lesssim 10^{-6}$) for a mesh consisting of 640 elements, $\mathrm{Pe} = 10$ and $N = 19$. The maximal contribution to the error comes from the steep concentration gradient in a boundary layer developed at each sink, as shown in Figure 2.6 (where analytical and numerical solutions are essentially indistinguishable).

Figs. 2.7 and 2.8 show the numerical and asymptotic solutions in the range of small-to-moderate and moderate-to-large microscopic Péclet numbers respectively, which demonstrate a good agreement with asymptotic results of Sections 2.3 and 2.4 respectively. Note a pronounced development of "stairs" at $\mathrm{Pe} > 1$. Already at Péclet number of the order of 1, we observe that the asymptotic symmetric cell solution (2.3.12) obtained around the organising centre $(\mathrm{Pe}, \mathrm{Da}) = (O(\varepsilon), O(\varepsilon^2))$ deviates from the numerical cell solution due to the development of flow-induced asymmetry (see Fig. 2.7(c), inset). The corresponding asymptotic cell solution (2.4.13) about the second organising centre $(\mathrm{Pe}, \mathrm{Da}) = (O(1), O(\varepsilon))$ clearly agrees with the simulation (Fig. 2.8(a), inset), as anticipated from our preceding analysis.

2.6 Convergence rates and limitations of homogenization on periodic arrays

In order to consider the difference between the homogenized ($C^{(0)}(X)$) and exact (C) solutions to the original problem (2.2.1), we introduce the following measures:

$$\| f \|_{\max} = \max_{X \in [0,1]} |f|\,, \quad \| f \|_{L_2}^2 = \int_0^1 f^2 \, \mathrm{d}X\,, \quad \| f \|_{H^1}^2 = \| f \|_{L_2}^2 + \left\| \frac{\mathrm{d}f}{\mathrm{d}X} \right\|_{L_2}^2\,, \quad \langle f \rangle = \int_0^1 f \, \mathrm{d}X\,. \tag{2.6.1}$$

These are, respectively, the supremum (Chebyshev), mean-squared (L_2) and Sobolev (H^1) norms, and the mean of f.

The modes of convergence of C to $C^{(0)}$, i.e. of $f = C - C^{(0)}$ to zero, as defined in (2.6.1), are arranged in descending order in (2.6.1) with respect to their "strength" (except for the Sobolev norm), e.g. $\| C - C^{(0)} \|_{\max} \underset{\varepsilon \to 0}{\longrightarrow} 0$ implies the convergence of $\| C - C^{(0)} \|_{L_2}$, and the convergence in $\| \cdot \|_{L_2}$ implies the convergence in mean, while the converse is generally not true. Convergence in the Sobolev norm, which takes account of the first derivative, is stronger than convergence in the mean-squared norm in a sense that $\| \cdot \|_{L_2} \le \| \cdot \|_{H^1}$ (see, e.g. [191] for a more systematic treatment).

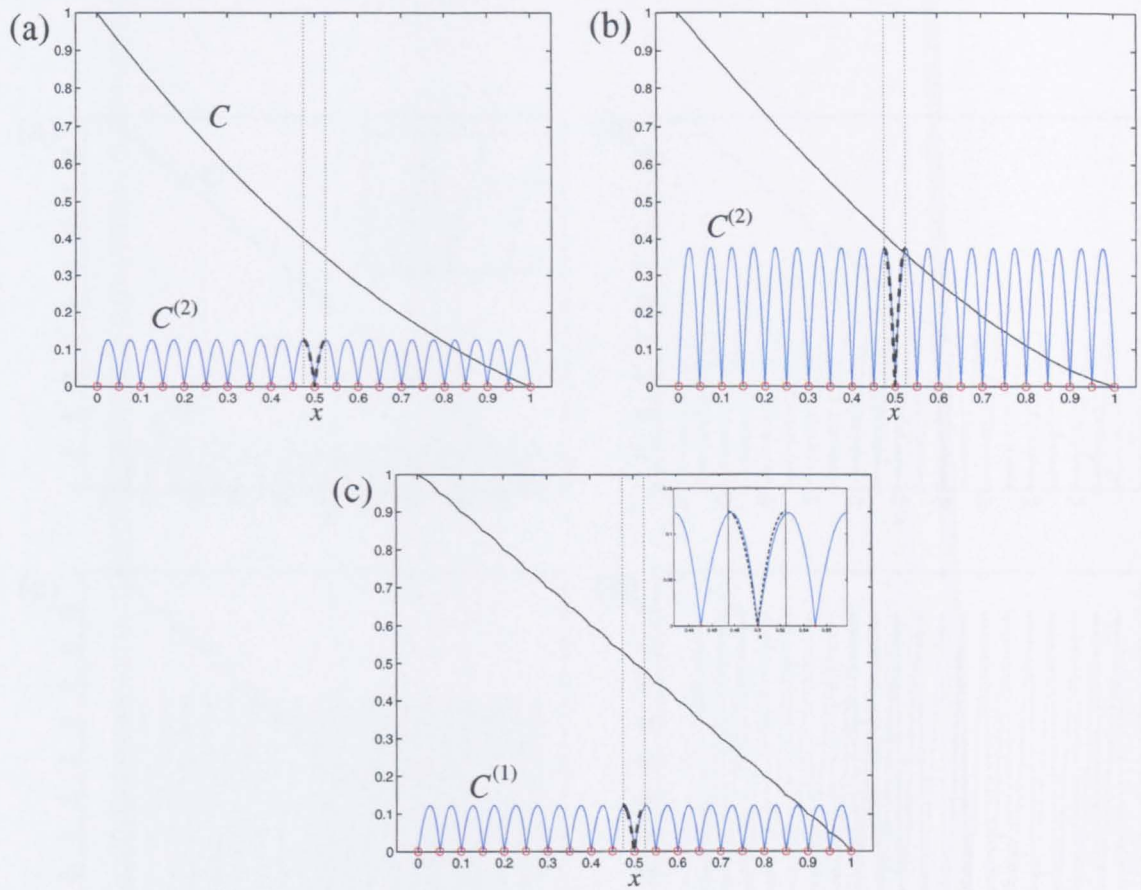

Figure 2.7. (a,b,c) Numerical solution C (solid black) to the advection-diffusion problem (2.2.2). (a,b) also show the numerical second correction $\varepsilon^{-2}\,(C - C^{(0)})$ (solid blue) computed in COMSOL and analytical second correction $C^{(2)}$ (dashed black) in a unit cell given by (2.3.12) for $\mathrm{Pe} = 0$, $\mathrm{Da} = \varepsilon^2$ (at the border $\mathrm{D/U_D}$ in the parameter space; see Fig. 2.2a) and $\mathrm{Pe} = 2\varepsilon$, $\mathrm{Da} = 3\varepsilon^2$ (about the main organising centre in Fig. 2.2a) respectively; (c) the first correction $\varepsilon^{-1}\,(C - C^{(0)})$ and its analytical estimate $\varepsilon^{-1}\,C^{(2)}$ according to (2.3.12) for $\mathrm{Pe} = 1$, $\mathrm{Da} = \varepsilon$ (at the border $\mathrm{A/U_A}$; see Fig. 2.2a). The sink positions are marked by red circles; two vertical dotted lines indicate the borders of a unit cell ($\varepsilon = 0.05$).

Observing from (2.3.1) that

$$C(x) \equiv C^{\varepsilon}(X) \approx C^{(0)}(X) + \varepsilon\, C^{(1)}(X/\varepsilon)\,, \quad C^{\varepsilon}_X \approx C^{(0)}_X + \varepsilon\, C^{(1)}_X = C^{(0)}_X + C^{(1)}_x\,, \quad \text{and}$$
$$\int_0^1 C^{(1)}(X/\varepsilon)\,\mathrm{d}X = \int_{-1/2}^{1/2} C^{(1)}(x)\,\mathrm{d}\,x \quad (\text{due to } x\text{-periodicity})\,, \tag{2.6.2}$$

where $X = \varepsilon\, x$ and the superscript $(^{\varepsilon})$ is adopted to distinguish the exact solution for a fixed epsilon from the two-scale-limit solution, we use the analytical solution (2.4.13) for the correction $C^{(1)}$ to estimate (with the aid of the computer algebra system `Maple`) the order of magnitude of the *homogenization residue*

$$r^{\varepsilon}(X) = C^{\varepsilon}(X) - C^{(0)}(X)\,. \tag{2.6.3}$$

For instance, in the case of large Péclet number with $\mathrm{Da} = \varepsilon\,\mathrm{Pe}$, by integrating (2.4.13) and

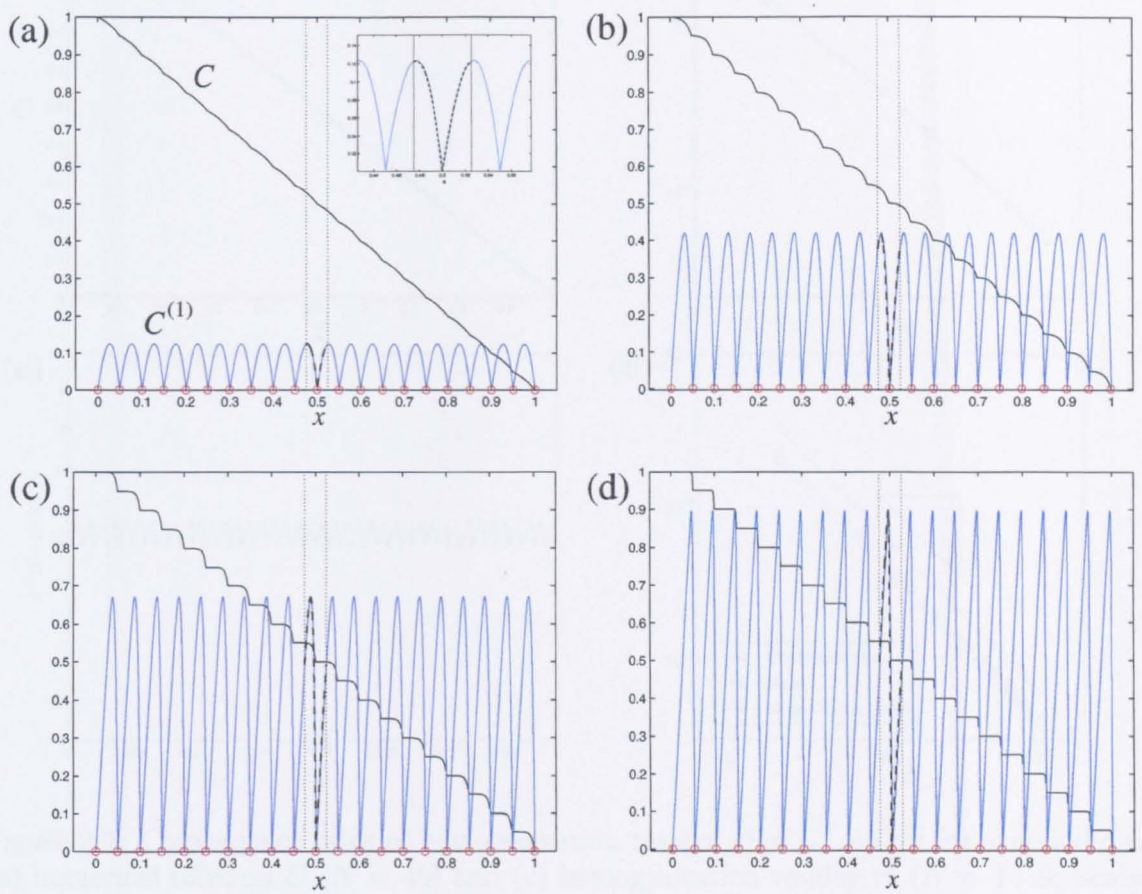

Figure 2.8. (a-d): Numerical solution C (solid black) to the advection-diffusion problem (2.2.2), numerical first correction $\varepsilon^{-1}(C - C^{(0)})$ (solid blue) and analytical correction $C^{(1)}$ given by (2.4.13) (dashed black) are plotted for $\mathrm{Pe} = 1; 4; 10; 50$ respectively and $\mathrm{Da} = \varepsilon\,\mathrm{Pe}$. The sinks' position is marked by red circles; two vertical dotted lines indicate the borders of a unit cell ($\varepsilon = 0.05$).

	$\|r^\varepsilon\|_{L^2}$	$\|r^\varepsilon_X\|_{L^2}$	$\langle r^\varepsilon \rangle$	$\langle r^\varepsilon_X \rangle$	$\max\|r^\varepsilon\|$	$\max\|r^\varepsilon_X\|$
$\mathrm{Pe} \gg 1$	$O(\varepsilon)$	$O(\sqrt{\mathrm{Pe}})$	$O(\varepsilon)$	0	$O(\varepsilon)$	$O(\mathrm{Pe})$
$\mathrm{Pe} \ll 1$	$O(\varepsilon\,\mathrm{Pe})$	$O(\mathrm{Pe})$	$O(\varepsilon\,\mathrm{Pe})$	0	$O(\varepsilon\,\mathrm{Pe})$	$O(\mathrm{Pe})$

Table 2.1. Analytical convergence rates of homogenization residue $r^\varepsilon = C^\varepsilon - C^{(0)}$ for $\mathrm{Da} = \varepsilon\,\mathrm{Pe}$.

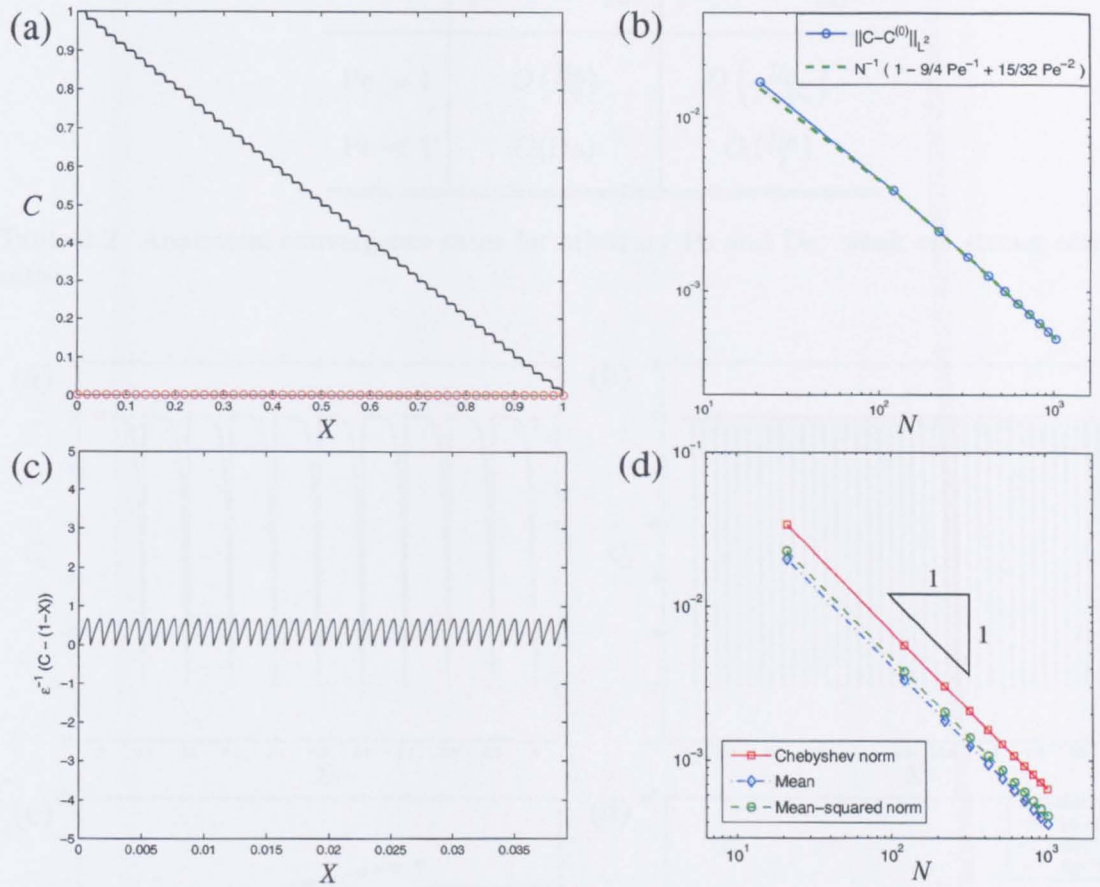

Figure 2.9. Convergence rates of homogenization residue $r^\varepsilon = C^\varepsilon - C^{(0)}$ for a periodic array: (a) numerical solution C ($N = 49$) and (c) homogenization residue r^ε ($N = 1019$; scaled by $\varepsilon^{-1} = N + 1$) for $\mathrm{Pe} = 10$, $\mathrm{Da} = \varepsilon\mathrm{Pe}$; (b) numerical (circles) and asymptotic (dashed line) convergence rates in L_2-norm *vs.* number of sinks for $\mathrm{Pe} = \varepsilon^{-1/2}$, $\mathrm{Da} = \varepsilon\mathrm{Pe}$; (d) convergence rates in Chebyshev ($\max|r^\varepsilon|$; squares) and mean-squared ($\|r^\varepsilon\|_{L_2}$; circles) norms, and in mean ($|\langle r^\varepsilon \rangle|$; diamonds) (see (2.6.1)) for $\mathrm{Pe} = 10$, $\mathrm{Da} = \varepsilon\mathrm{Pe}$.

expanding the result as a power series of $1/\mathrm{Pe}$, we find $\|C^\varepsilon - C^{(0)}\|_{L_2} = \varepsilon \|C^{(1)}\|_{L_2(x\in[-\frac{1}{2},\frac{1}{2}])} = \frac{1}{\sqrt{3}}\varepsilon\left[1 - \frac{9}{4}\mathrm{Pe}^{-1} + \frac{15}{32}\mathrm{Pe}^{-2} + O(\mathrm{Pe}^{-3})\right]$, where the equality between the residue and the correction is used due to the vanishing of all the higher order terms in the asymptotic expansion (2.3.1). The results for this and other measures in (2.6.1) are summarised in Table 2.1 (where r^ε_X denotes the derivative of the residue with respect to the global spatial coordinate). Figure 2.9 shows the numerical verification of analytical predictions for convergence rates. An example of the exact solution (for $N = 49$) is given in (Fig. 2.9a), and the corresponding residue (for $N = 1019$) is plotted in panel (c). We observe a good agreement for both high-order asymptotic approximation of $\|r^\varepsilon\|_{L_2}$ ($\mathrm{Pe} = \varepsilon^{-1/2}$; Fig. 2.9b) and for leading-order convergence rates in the Chebyshev and mean-squared norms, and in mean ($\mathrm{Pe} = 10$; Fig. 2.9d).

We see from Table 2.1 that the magnitude of the homogenization residue is typically linear in ε, while its derivative does not necessarily converge (see Fig. 2.10a,b). At the same time, the mean of r^ε_X vanishes exactly to zero, giving an example of the striking difference between "weaker" and "stronger" types of convergence. Although the results of Table 2.1 are presented for a fixed ratio $q_1/\mathrm{Pe} \equiv \mathrm{Da}/\varepsilon\mathrm{Pe} = 1$, we see from (2.4.13) that the residue scales with q_1/Pe.

	$\|C^\varepsilon - C^{(0)}\|_{L_2}$	$\|C^\varepsilon - C^{(0)}\|_{H^1}$
$\mathrm{Pe} \gg 1$	$O\left(\frac{\mathrm{Da}}{\mathrm{Pe}}\right)$	$O\left(\frac{\mathrm{Da}}{\varepsilon\sqrt{\mathrm{Pe}}}\right)$
$\mathrm{Pe} \ll 1$	$O(\mathrm{Da})$	$O\left(\frac{\mathrm{Da}}{\varepsilon}\right)$

Table 2.2. Analytical convergence rates for arbitrary Pe and Da: weak *vs.* strong convergence rates.

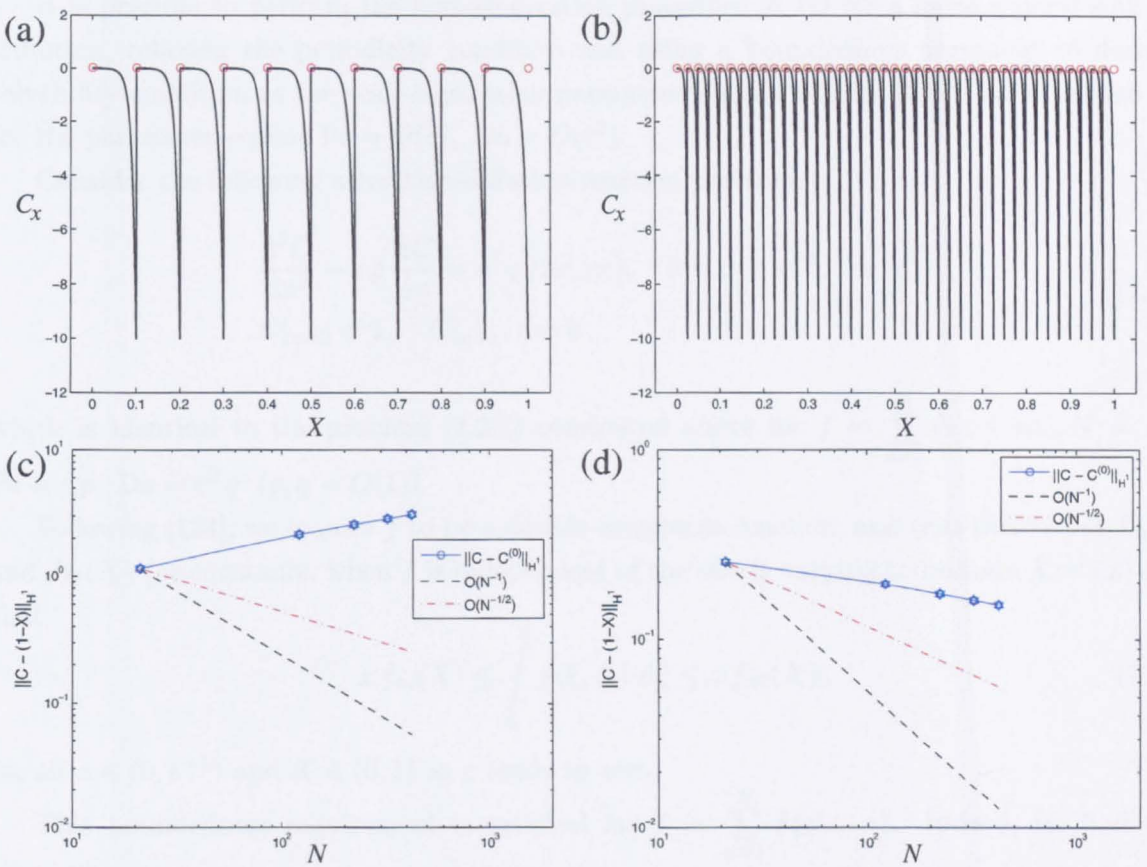

Figure 2.10. Gradient of C (equal here to $r_X^\varepsilon - 1$) for $N = 9$ (a) and $N = 39$ (b) ($\mathrm{Pe} = 10$, $\mathrm{Da} = \varepsilon\mathrm{Pe}$; yellow region of weak convergence in Fig. 2.2a) does not converge to the leading order constant $C_X^{(0)} = -1$ as $\varepsilon \sim 1/N \to 0$. Convergence rates of homogenization residue r_X^ε in H^1-norm (mean-squared with first derivative) *vs.* number of sinks for $\mathrm{Pe} = \varepsilon^{-1/2}$, $\mathrm{Da} = \varepsilon^{0.75}\sqrt{\mathrm{Pe}}$ (in the "weak-convergence" yellow region of Fig. 2.2a) (c) and for $\mathrm{Pe} = \varepsilon^{-1/2}$, $\mathrm{Da} = \varepsilon^{1.25}\sqrt{\mathrm{Pe}}$ (in the "strong-convergence" green region of Fig. 2.2a) (d).

Therefore, multiplying the entries of Table 2.1 by $\mathrm{Da}/\varepsilon\mathrm{Pe}$, we obtain weak ($\|r^\varepsilon\|_{L_2}$) and strong ($\|r^\varepsilon\|_{H^1}$) convergence rates for the homogenization residue r^ε, covering the entire parameter space, as shown in Table 2.2 and Figure 2.2(a).

We can therefore split the parameter space (Fig. 2.2a) into three regions: in the green region, there is a "strong" convergence (in the Sobolev norm); the lightly shaded (yellow) region is characterised by the loss of the convergence of derivatives, so that C^ε converges to $C^{(0)}$ only in a weak sense (in the mean-squared norm); and the darkly shaded (red) region manifests in

the complete breakdown of the two-scale analysis, with macroscopic variations in concentration at lengthscales less than the inter-sink spacing (see Fig. 2.2a). The existence of a range of parameters in problem (2.2.2) with strong convergence of the leading-order solution is unusual for homogenization approach, which typically provides only weak convergence at the leading order [34].

2.7 Homogenization for non-periodic sink distributions

It is possible to perform the homogenization procedure in 1D for a more general sink distribution, relaxing the periodicity condition and using a boundedness argument to derive a solvability condition as the scale-separation parameter ε tends to zero [124]. We illustrate this for the parameter regime $\mathrm{Pe} = O(\varepsilon)$, $\mathrm{Da} = O(\varepsilon^2)$.

Consider the following advection-diffusion-reaction problem:

$$\begin{aligned} &\frac{\mathrm{d}^2 C}{\mathrm{d}x^2} - \varepsilon p \frac{\mathrm{d}C}{\mathrm{d}x} = \varepsilon^2 q f(x, \varepsilon x), \quad 0 < x < \varepsilon^{-1}, \quad \varepsilon \ll 1 \\ &C|_{x=0} = 1, \quad C|_{x=\varepsilon^{-1}} = 0, \end{aligned} \tag{2.7.1}$$

which is identical to the problem (2.2.2) considered above for $f = \sum_{n=1}^{N} \delta(x - n)$, $N = \varepsilon^{-1}$, $\mathrm{Pe} = \varepsilon p$, $\mathrm{Da} = \varepsilon^2 q$ $(p, q = O(1))$.

Following [124], we require f to be a double-integrable function, and that there exist $f_m(X)$ and $f_M(X)$ (or constants, when f is independent of the slowly varying coordinate $X = \varepsilon x$) such that

$$x f_m(X) \leq \int_0^x f(\xi, X)\, \mathrm{d}\xi \leq x f_M(X), \tag{2.7.2}$$

for all $x \in (0, \varepsilon^{-1})$ and $X \in (0, 1)$ as ε tends to zero.

This boundedness requirement is satisfied for $f = \sum_{n=1}^{N} \delta(x - n)$. Indeed, we find that $\int_0^x \sum_{n=1}^{N} \delta(\xi - n)\, \mathrm{d}\xi = \lfloor x \rfloor$, where $\lfloor x \rfloor$ is the floor integer value of x, and there are constants $0 < \alpha \leq 1$, $\beta \geq 1$ such that $\alpha x \leq \lfloor x \rfloor \leq \beta x$.

We use the two-scale asymptotic expansion (2.3.1) and the substitution for differential operators (2.2.9) to rewrite (2.7.1) as

$$\begin{aligned} &\tilde{C}_{xx} + 2\varepsilon \tilde{C}_{xX} + \varepsilon^2 \tilde{C}_{XX} - \varepsilon p \left(\tilde{C}_x + \varepsilon \tilde{C}_X \right) = \varepsilon^2 q f(x, X), \quad 0 < x < \varepsilon^{-1}, \quad 0 < X < 1, \\ &\tilde{C}|_{X=0} = 1, \quad \tilde{C}|_{X=1} = 0. \end{aligned} \tag{2.7.3}$$

Collecting the terms in (2.7.3) at $O(1)$, we have

$$C^{(0)}_{xx} = 0, \quad C^{(0)}|_{X=0} = 1, \; C^{(0)}|_{X=1} = 0, \tag{2.7.4}$$

which gives $C^{(0)}(x, X) = \tilde{A}(X)\, x + \tilde{B}(X)$. The first term $\tilde{A}(X)\, x$ is a secular term unbounded as $x \to \infty$ $(\varepsilon \to 0)$, and therefore we require $\tilde{A} = 0$ to obtain a bounded solution in the limit of

small ε, so that

$$C^{(0)} = C^{(0)}(X)\,. \tag{2.7.5}$$

The terms in (2.7.3) at $O(\varepsilon)$ give

$$C^{(1)}_{xx} + 2C^{(0)}_{xx} - pC^{(0)}_{x} = 0, \quad C^{(1)}|_{X=0} = C^{(1)}|_{X=1} = 0\,,$$

which, according to (2.7.5), reduces to

$$C^{(1)}_{xx} = 0, \quad C^{(1)}|_{X=0} = C^{(1)}|_{X=1} = 0\,. \tag{2.7.6}$$

Then, analogously to (2.7.4), $C^{(1)} = C^{(1)}(X)$, and due to homogeneous boundary conditions in (2.7.6), we have

$$C^{(1)} \equiv 0\,. \tag{2.7.7}$$

Collecting the terms in (2.7.3) at $O(\varepsilon^2)$, we obtain

$$C^{(2)}_{xx} + 2C^{(1)}_{xX} + C^{(0)}_{XX} - p\left(C^{(1)}_{x} + C^{(0)}_{X}\right) = q\,f(x,X)\,,$$
$$C^{(2)}|_{X=0} = C^{(2)}|_{X=1} = 0\,,$$

which simplifies to

$$C^{(2)}_{xx} = -\left(C^{(0)}_{XX} - pC^{(0)}_{X}\right) + q\,f(x,X)\,, \quad 0 < x < \varepsilon^{-1},\ 0 < X < 1 \tag{2.7.8a}$$

$$C^{(2)}|_{X=0} = C^{(2)}|_{X=1} = 0\,, \tag{2.7.8b}$$

due to (2.7.5) and (2.7.7).

Integrating equation (2.7.8a) with respect to x over $(0, \varepsilon^{-1})$, we have

$$C^{(2)}_{x}|_{x=\varepsilon^{-1}} = \underbrace{-\left(C^{(0)}_{XX} - pC^{(0)}_{X}\right)\varepsilon^{-1}}_{O(\varepsilon^{-1})} + \underbrace{\int_0^{1/\varepsilon} q\,f(s,X)\,\mathrm{d}s}_{O(\varepsilon^{-1})} + A(X)\,, \tag{2.7.9}$$

$$C^{(2)}|_{x=\varepsilon^{-1}} = \underbrace{-\left(C^{(0)}_{XX} - pC^{(0)}_{X}\right)\frac{\varepsilon^{-2}}{2}}_{O(\varepsilon^{-2})} + \underbrace{\int_0^{1/\varepsilon}\mathrm{d}s\int_0^{s} q\,f(\xi,X)\,\mathrm{d}\xi}_{O(\varepsilon^{-2})} + \underbrace{A(X)\,\varepsilon^{-1}}_{O(\varepsilon^{-1})} + B(X)\,, \tag{2.7.10}$$

where we use (2.7.2) to show that $f_m(X)\,\frac{x^2}{2} \le \int_0^x \mathrm{d}s \int_0^s f(\xi,X)\,\mathrm{d}\xi \le f_M(X)\,\frac{x^2}{2}$.

To eliminate the secular terms in (2.7.10) we demand the first two terms to balance each other as $\varepsilon \to 0$ ($x \to \infty$) and impose also $A(X) \equiv 0$. The solvability condition is therefore

$$\lim_{\varepsilon\to 0}\left[\left(C^{(0)}_{XX} - pC^{(0)}_{X}\right)\frac{\varepsilon^{-2}}{2} - \int_0^{1/\varepsilon}\mathrm{d}s\int_0^{s} q\,f(\xi,X)\,\mathrm{d}\xi\right] = 0\,,$$

or, equivalently,

$$\left(C_{XX}^{(0)} - pC_X^{(0)}\right) = \bar{\bar{f}}(X), \quad \bar{\bar{f}} = \lim_{\varepsilon\to 0} 2\varepsilon^2 q \int_0^{1/\varepsilon} \mathrm{d}x \int_0^x f(s,X)\,\mathrm{d}s. \tag{2.7.11}$$

2.7.1 Examples of microstructure

Example 2.1 (periodic array):

To illustrate, we now average the source-term for a periodic array of sinks: $f = \sum_{n=1}^{N} \delta(x-n)$, $N \approx \varepsilon^{-1}$. Here $\bar{\bar{f}} = \lim_{\varepsilon\to 0} 2\varepsilon^2 \int_0^{1/\varepsilon} \mathrm{d}s \int_0^s \sum_{n=1}^{\lfloor 1/\varepsilon \rfloor} \delta(y-n)\,\mathrm{d}y$, and the inner integral equals the number of sinks between $y=1$ and $y=s$ $(s \le \varepsilon^{-1})$, i.e. $\bar{\bar{f}} = \lim_{\varepsilon\to 0} 2\varepsilon^2 \int_0^{1/\varepsilon} \lfloor s \rfloor\,\mathrm{d}s$. Since $\int_0^x \lfloor s \rfloor\,\mathrm{d}s \approx \int_0^x s\,\mathrm{d}s$ for large x, we finally have $\bar{\bar{f}} = \lim_{\varepsilon\to 0} 2\varepsilon^2 \frac{\varepsilon^{-2}}{2} = 1$, and leading-order averaged equation (2.7.11), subject to boundary conditions, takes the form identical to (2.3.8) obtained in Section 2.3 under the periodicity assumption. We consider some further examples of deterministic aperiodic microstructure in Appendix B.5.

Example 2.2 (spatially homogeneous random array):

If we allow $N \approx \varepsilon^{-1}$ sinks to be uniformly randomly distributed between $x=0$ and $x=\varepsilon^{-1}$, the source term can be written as $f(x) = \sum_{i=1}^{N} \delta(x-\xi_i)$, $\xi_i \sim \mathcal{U}(0, \varepsilon^{-1})$. Taking into account the spatial statistical homogeneity of $f(x)$, we further assume an ergodicity property for sufficiently small ε (large x), so that $\int_0^s f(y)\,\mathrm{d}y \approx \mathbb{E}[N\{\xi_i : 0 \le \xi_i \le s\}] = s$, where $\mathbb{E}$ denotes the expectation (ensemble average) of the number of sinks in the interval $[0,\, s] \subseteq [0,\, \varepsilon^{-1}]$. Ultimately, we find effective source-term $\bar{\bar{f}} = \lim_{\varepsilon\to 0} 2\varepsilon^2 \int_0^{1/\varepsilon} s\,\mathrm{d}s = 1$, which is identical to the expression in case of a periodic sink distribution. We therefore expect the same solute distribution at leading order, as ε tends to 0.

The predictions of Examples 2.1 and 2.2 are confirmed by direct simulation shown in Figure 2.11 that presents the results for periodic (dashed) and uniformly random (solid) sink distributions computed for $\varepsilon = 0.05$.

2.8 Discussion

To sum up, we have obtained the effective averaged macroscopic equations for advection-diffusion in a one-dimensional periodic array of sinks. We have considered different ranges of microscopic Péclet number ($\mathrm{Pe} = u_0\, l/D$) and Damköhler number ($\mathrm{Da} = q_0\, l/(D\, C_0)$), and have demonstrated a match of asymptotic behaviour among the solutions as well as their agreement with numerical simulations.

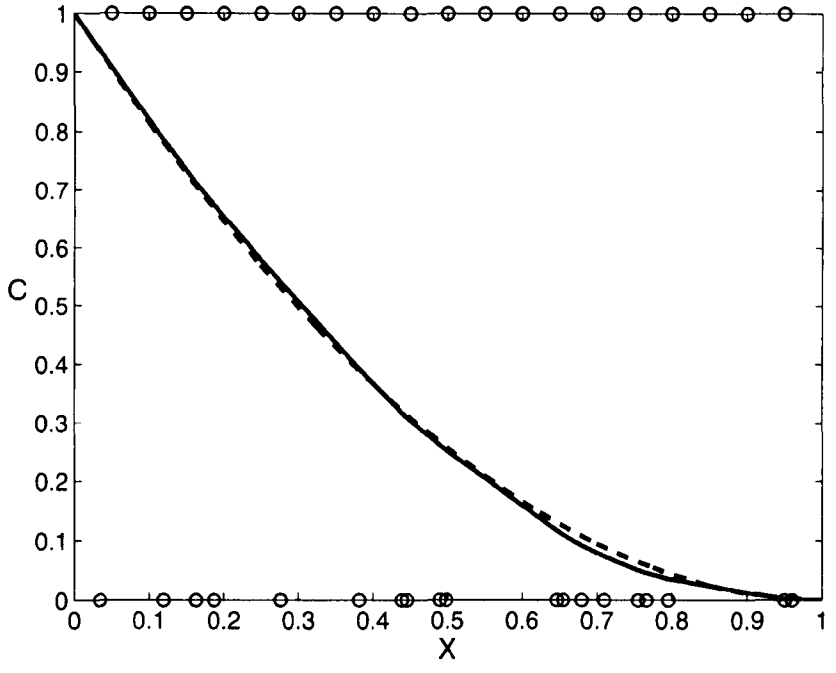

Figure 2.11. The comparison of concentration profiles on periodic (dashed) and uniformly random (solid) sink distributions, computed for D/U_D transport regime ($Pe = \varepsilon^2$, $Da = 2\varepsilon^2$ $\varepsilon = 0.05$). Bottom circles indicate the position of $N = 19$ sinks of the random array and the top circles correspond to the periodic array of the same size.

Our analysis indicates that the advection-diffusion-uptake equation for the leading-order concentration

$$\varepsilon^2 C^{(0)}_{XX} - \varepsilon \, Pe \, C^{(0)}_X = Da \tag{2.8.1}$$

gives adequate macroscopic description for a wide range of Péclet number ($0 \leq Pe \lesssim O(\varepsilon^{-1})$), where $\varepsilon = l/L$ is the scale separation parameter, providing that $Da \ll \max(Pe, 1)$. Equation (2.8.1) is also shown to be applicable to more general non-periodic sinks distributions as discussed in Section 2.7.

Solution (2.3.9) to the effective macroscopic equation (2.8.1) allows us to classify distinct regimes in (Pe, Da) parameter space. The parameter space is subdivided in three regions by relations $Pe \sim \varepsilon$, $Da \sim \varepsilon^2$ and $Da \sim \varepsilon \, Pe$ (as shown in the schematic Fig. 2.2a), each region being characterised by the dominance of advective, diffusive or uptake effects at the macroscale. In addition, dimensional analysis of equation (2.8.1) indicates that the lengthscale of diffusive boundary layer gives another relation, $Da \sim Pe^2$. Analysis of the residual (2.4.13) shows that the parameter space is further subdivided by $Pe = O(1)$ into two subregions: one with no advective effects and a smooth solution (the first non-vanishing correction to $C^{(0)}$ being of $O(\varepsilon^2)$; see Fig 2.3); and an advective region, where "staircases" are manifested at the macroscale (the first non-vanishing correction to $C^{(0)}$ is of $O(\varepsilon)$). In total, we can distinguish 6 asymptotic parameter regimes: diffusion-dominated D, advection-dominated A & A^s, and uptake-dominated U_D, U_A & U_A^s (and 6 transitional regimes of co-dimension 1 at the boundaries; see Fig. 2.2(a) and Sec. 2.3).

Our analysis also demonstrates that for given Pe, there is a critical Da (2.3.10), equivalent to

$$\mathrm{Da_{cr}(Pe)} = \frac{\mathrm{Pe}^2\, \mathrm{e}^{\mathrm{Pe}/\varepsilon}}{(\mathrm{Pe}/\varepsilon - 1)\, \mathrm{e}^{\mathrm{Pe}/\varepsilon} + 1}, \tag{2.8.2}$$

such the solute is fully absorbed within the domain (i.e. for $X \leq X_0 < 1$) for $\mathrm{Da} > \mathrm{Da_{cr}(Pe)}$. This threshold in (Pe, Da)-space asymptotes to the boundary between asymptotic regions U and $\mathrm{U_D}$ for $\mathrm{Pe} \ll \varepsilon$ (when $\mathrm{Da_{cr}} \approx 2\varepsilon^2$) and the boundary between regions A and $\mathrm{U_A}$ (and A_S and U_A^S) for $\mathrm{Pe} \gg \varepsilon$ (when $\mathrm{Da_{cr}} \approx \varepsilon \mathrm{Pe}$). Thus (2.8.2) demarcates a region where uptake by sinks can be considered optimal: for $\mathrm{Da} > \mathrm{Da_{cr}}$, all the solute is absorbed upstream of the outlet, making some sinks redundant; for $\mathrm{Da} < \mathrm{Da_{cr}}$, substantial solute escapes past the sinks to the outlet.

We can estimate the parameter regimes corresponding to the passive transport of certain solutes, such as oxygen or glucose, in the placenta. Taking the size of a typical placentone to be $L \sim 1$ cm [98] and the average diameter of a cross-section of the villous branches in a mature placenta to be $l \sim 100\ \mu$m [33, 126], we get $\varepsilon = l/L \sim 10^{-2}$. Taking the number of functional spiral arterial openings at term to be ~ 100 [33, 49] and the net flow rate of incoming blood per placenta about 500 ml/min [186], we get the flow rate per a single spiral artery (placentone) to be $Q \approx 5$ ml/min. Mass conservation implies the average velocity in a placentone to be $u_0 \sim Q/L^2 \sim 1 - 10$ cm/min (which is also consistent with the filling time ($\approx 10 - 30$ s) of the intervillous space by tracers injected into the maternal circulation [96, 205]). Assuming the molecular diffusivity (based on the values in blood plasma) for oxygen to be $D_{\mathrm{O_2}} \sim 10^{-3}$ cm^2/min [24] and for glucose to be $D_{\mathrm{gluc}} \sim 10^{-4}$ cm^2/min [217] we get a range of the local Péclet number: $\mathrm{Pe} = u_0\, l/D \sim 10 - 10^3$, or $\mathrm{Pe} = O(\varepsilon^{-1/2}) - O(\varepsilon^{-3/2})$. Placental uptake rates are harder to estimate confidently, but assuming the net oxygen uptake rate to be ~ 1 mmol/min [114, 122], which, divided by the total villous surface area ~ 10 m^2 [33], gives the uptake flux density $q_0 \sim 10^{-5}$ mmol/(cm$^2 \cdot$ min), and taking the reference arterial concentration of the dissolved oxygen C_0 to be ~ 0.1 mM $= 10^{-4}$ mmol/cm^3 [122], we get a range of the local Damköhler number: $\mathrm{Da} = q_0\, l/(D\, C_0) \sim 1 - 10$, that is $\mathrm{Da} = O(1) - O(\varepsilon^{-1/2})$, clustered about the advective-uptake balance relation $\mathrm{Da} = O(\varepsilon \mathrm{Pe})$, as expected. Therefore, placental transport of at least some passive solutes occurs at large Péclet number and likely belongs to the regime $\mathrm{A^s/U_A^s}$ in the (Pe, Da) parameter space (see, for example, Fig. 2.2(a,b), case (5)).

Finally, the upper bound for applicability of homogenization and validity of equation (2.8.1) is represented by the relations $\mathrm{Da} \lesssim \max(1, \mathrm{Pe})$. We have demonstrated that if Da fails to obey this restriction, the length of the inner diffusive boundary layer is less than the distance between two sinks in a periodic array. These restrictions are summarised in Figure 2.2(a), showing the regions of 'soft-fail' and 'hard-fail' in the accuracy of the homogenized description.

Although the homogenized leading-order concentration profile is applicable to a wide range of stationary random sink distributions, as illustrated in Fig. 2.11, it remains for us to understand the impact of stochasticity on the accuracy and convergence rate of solutions to the homogenized solution, which is particularly important for finite ε (moderate scale-separation), the case most relevant to physiological applications. This is the subject of the next chapter.

III Homogenization on Random Arrays: Error Bounds and Convergence Rates

3.1 Introduction

Alongside many naturally occurring media, the human placenta exhibits a great degree of irregularity in the arrangement of villous branches, in particular, of the terminal villi – the primary sites of solute uptake (see Figs 1.1 and 1.3).

We have indicated in Section 2.7 of Chapter 2 that the leading-order (effective) description of the advection-diffusion-uptake is applicable not only to a periodic but also to a random, statistically homogeneous distribution of sinks. However, it remains for us to understand the accuracy of the averaged homogenized description, compared to the established accuracy for a periodic medium, by looking beyond the leading-order approximation [75].

This chapter considers different random sink distributions and estimates the corresponding magnitudes and statistical properties of the homogenization residue $r^\varepsilon = C^\varepsilon - C^{(0)}(X)$.

We show, in particular, how randomness leads to large fluctuations in solute distributions that can be correlated over the distances comparable to the size of the whole domain.

3.2 Sink distribution as a spatial point process

We generalise the advection-diffusion-uptake problem (2.2.2) to allow for a random sink distribution:

$$\begin{aligned} &\frac{\mathrm{d}^2C}{\mathrm{d}x^2} - \mathrm{Pe}\frac{\mathrm{d}C}{\mathrm{d}x} = \mathrm{Da}\, f(x), \quad f = \sum_{i=1}^{N} \delta(x-\xi_i), \quad 0 < x < \varepsilon^{-1}, \\ &C|_{x=0} = 1, \quad C|_{x=\varepsilon^{-1}} = 0, \end{aligned} \tag{3.2.1}$$

where ξ_i denotes the position of the i^{th} sink ($i = 1, \ldots, N$), as illustrated in Figure 3.1.

We now consider different types of irregular arrays in order to understand the accuracy of an homogenization description in these cases. Since we deal with point objects, it is convenient to

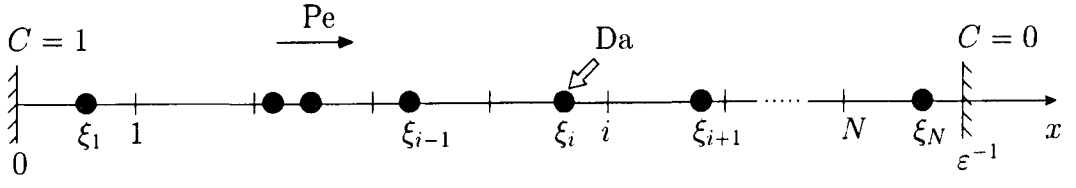

Figure 3.1. A schematic random array of N sinks (circles), located at $x = \xi_i$; ticks indicate the position of sinks in a periodic array of the same size (all variables are given in a dimensionless form).

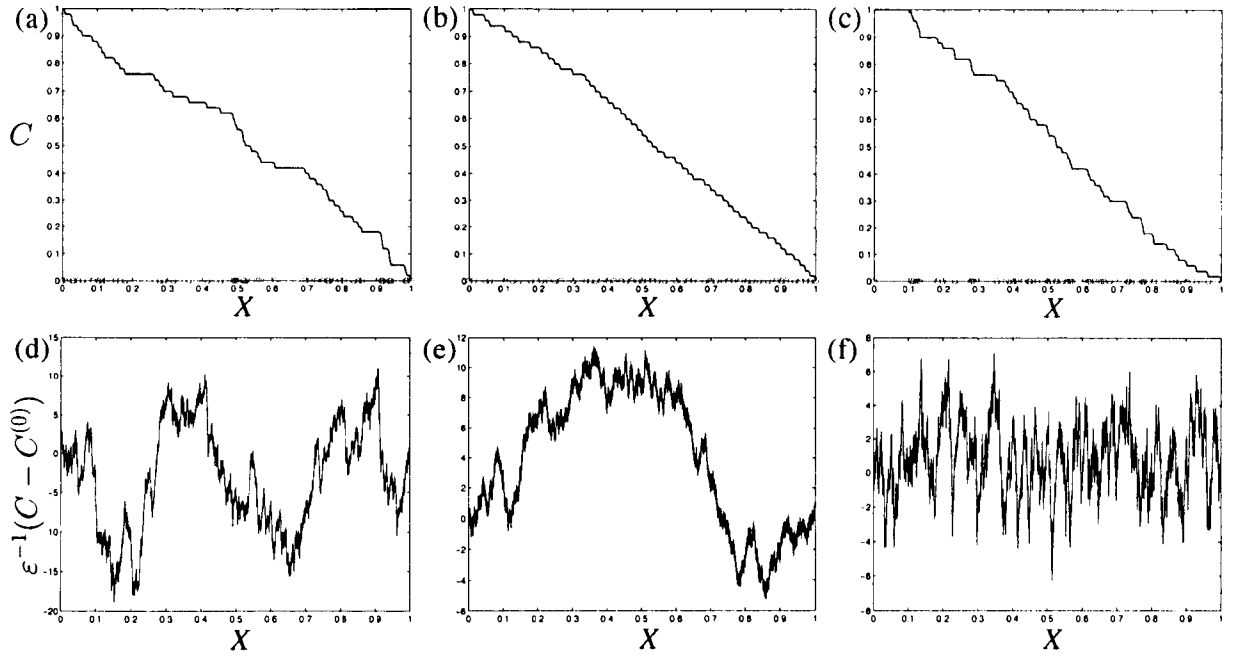

Figure 3.2. Top: Concentration profiles (2.5.1) for (a) uniformly random distribution of sinks, (b) Matérn hard-core type II process with $d = 0.65\varepsilon$ and (c) normal perturbations of a periodic array with $\sigma = 10\varepsilon$; for $N = 49$, $\varepsilon = 1/(N+1)$, $\mathrm{Pe} = 10$, $\mathrm{Da} = \varepsilon\mathrm{Pe}$. Bottom: Homogenization residue $r^\varepsilon = C - C^{(0)}$ scaled by ε^{-1} for uniformly random (d), Matérn hard-core (e) and normal perturbations (f) point processes with the same parameters (for $N = 1019$, $\mathrm{Pe} = 10$, $\mathrm{Da} = \varepsilon\mathrm{Pe}$). The corresponding correlation properties are shown in Fig. 3.4.

use standard random point processes to construct sink distributions. Apart from the uniformly random distribution of N sinks in the open interval $X \in (0,1)$ (see a single realisation of the solution C in Fig. 3.2(a) for $N = 49$ and of the homogenization residue r^ε in Fig. 3.2(d) for $N = 1019$), we use the Matérn hard-core type II (simple sequential inhibition) process that imposes a minimal allowed distance d ($0 < d < \varepsilon = (N+1)^{-1}$) between sinks (see Fig. 3.2(b,e)), making this distribution closer to applications such as the human placenta.

An algorithm for hard-core array generation is as follows: the location of each sink at $X = \varepsilon\xi_i \in (0,1)$ is sampled from a uniform distribution; a sink is accepted if it does not fall closer than a distance d (in X) to the existing sinks or boundaries; the process is continued until a given number N of sinks is reached or no gap $\geq 2d$ between two sinks is left [82]. There exists therefore a critical upper bound d_{cr} for the minimal allowed distance d, corresponding to the maximal packing density that can be achieved for all N sinks [82]. The theoretical statistical properties of this upper bound are still unknown; however, experiments with random packing of rigid spheres and numerical simulations suggest (in the sense that "many mathematicians believe and all physicists know" [253]) that the maximal volume fraction (d/ε in 1D case) does not exceed $\pi/\sqrt{18} \simeq 0.74$, at least in three dimensions [253]. For a one-dimensional Matérn hard-core distribution, $d/\varepsilon = 0$ is equivalent to a uniformly random distribution and $d/\varepsilon = 1$ represents a (generally unreachable) periodic array. A numerical estimate of the (ensemble averaged) critical minimal distance is $d_{\mathrm{cr}}/\varepsilon \simeq 0.743$ (see Appendix B.6 for the details of the estimation algorithm) for large N, which agrees with an empirical upper bound $\pi/\sqrt{18}$. This is related to the still open 18th Hilbert's problem of the densest random packing of identical

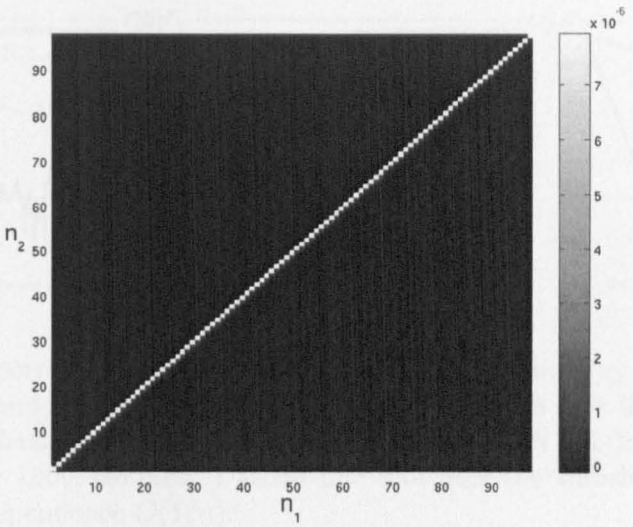

Figure 3.3. Covariance matrix $\mathbb{C}\mathrm{ov}(\Delta_{n_1}, \Delta_{n_2})$ of inter-sink distance Δ_n for a hard-core point process ($N = 99$, $d = 0.65\varepsilon$, computed for an ensemble of 5×10^5 arrays).

spheres [119].

Another random distribution considered is the normal perturbation of a periodic array (also called *normal perturbations*), where each sink is displaced normally (with a given standard deviation σ) about its position in a periodic array (shown in Fig. 3.2(c,f)). According to the properties of a normal distribution, we expect 99% of sinks to remain in their original unit cells for $0 \leq \sigma \leq \varepsilon/6$. In the limit of small standard deviations ($\sigma \to 0$), the normally-perturbed array tends to an unperturbed periodic array, and a normally-perturbed array approaches a uniformly random distribution as σ/ε becomes $\gg 1$ (with periodic boundary conditions imposed upon sinks falling out the domain). As σ increases, the sinks start swapping their unit cells and sorting of their new positions has to be applied.

Therefore, we consider three stochastic forms of the source term $f = \sum_{i=1}^{N} \delta(x - \xi_i)$ in (3.2.1):

(i) $f = f_u$: a uniformly-random distribution, where ξ_i are independent ordered values drawn from $\mathcal{U}[0, \varepsilon^{-1}]$;

(ii) $f = f_h(d)$: a Matérn hard-core type-II distribution, where $\xi_i \sim \mathcal{U}[\varepsilon^{-1}d, \varepsilon^{-1}(1-d)]$ $(0 \leq d < \varepsilon)$, provided that $|\xi_i - \xi_j| \geq d/\varepsilon$ for any $i \neq j$;

(iii) $f = f_n(\sigma)$: a normally-perturbed periodic distribution satisfying $\xi_i \sim \mathcal{N}(i, (\sigma/\varepsilon)^2)$, for some variance σ^2.

where ξ_i denotes the position of the i^{th} sink in local coordinates (see Fig. 3.1).

Figure 3.3 shows a reference covariance matrix $\mathbb{C}\mathrm{ov}(\Delta_{n_1}, \Delta_{n_2}) \equiv \mathbb{E}\big[(\Delta_{n_1} - \mathbb{E}[\Delta_{n_1}])(\Delta_{n_2} - \mathbb{E}[\Delta_{n_2}])\big]$ for the inter-sink distance $\Delta_n = \xi_{n+1} - \xi_n$ $(n = 1, \ldots, N-1)$ of a hard-core point process (f_h), where the strong diagonal dominance of the matrix indicates the absence of a long-range correlation between sinks' position. The other two random sink distributions (f_u and f_n) exhibit the same property.

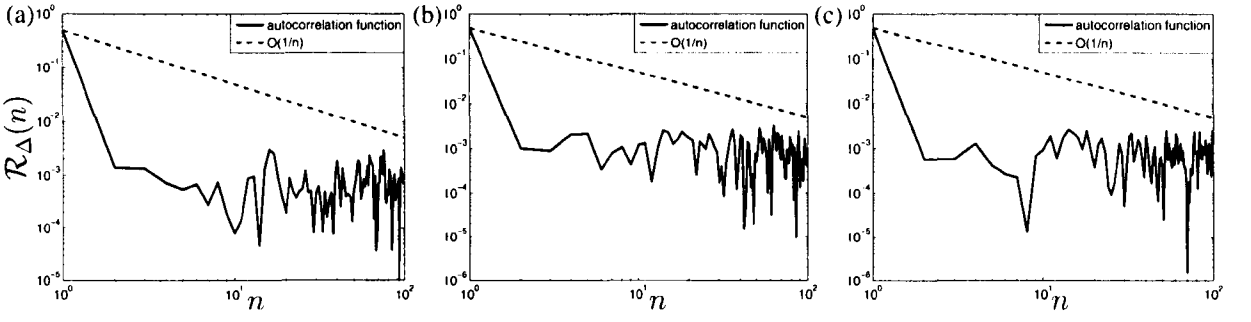

Figure 3.4. Top: Autocorrelation function $\mathcal{R}(n)$ of inter-sink distances *vs.* discrete shifting index n for (a) uniformly random, (b) Matérn hard-core type II with $d = 0.65\varepsilon$ sink distributions and (c) normal perturbations with $\sigma = 10\varepsilon$ ($N = 1019$, $\varepsilon = 1/(N+1)$); solid black line shows ensemble average over 1000 samples; Dashed line indicates the threshold long-to-short-term memory asymptotic dependence $O(1/n)$.

Another important characteristic of a random process is the autocorrelation function, showing the degree of correlation (or "memory") between spatial points separated by a given distance. We consider an autocorrelation function for the inter-sink distance Δ_i:

$$\mathcal{R}(n) = \frac{\mathbb{E}[\,(\Delta_i - \mathbb{E}[\Delta_i])\,(\Delta_{i+n} - \mathbb{E}[\Delta_{i+n}])\,]}{\mathbb{V}\mathrm{ar}[\Delta_i]}\,, \quad \Delta_i = \xi_{i+1} - \xi_i\,, \tag{3.2.2}$$

where stationarity of the corresponding discrete random process is assumed. The autocorrelation function is plotted in Figure 3.4 for different random sink distributions.

The asymptotic behaviour of the "tail" of an autocorrelation function is classified as follows:

$$\mathcal{R}(\tau) \sim \tau^{-\alpha}, \quad \text{for large } \tau \qquad \begin{cases} \alpha > 1 & \text{(short-term memory)}\,, \\ 0 < \alpha < 1 & \text{(long-term memory)}\,, \end{cases} \tag{3.2.3}$$

where α is the correlation or *mixing* factor [21, 47].

Figure 3.4 shows that the ensemble mean of the autocorrelation function for all three random sink distributions (f_u, f_h and f_n) does not jump above the short-term-memory threshold $O(1/n)$, at least for $n \lesssim 10^2$, as expected from their properties.

3.3 Statistical measures of convergence

In order to investigate the convergence rates for the homogenization residue $r^\varepsilon(X) = C^\varepsilon(X) - C^{(0)}(X)$ of the solution to (3.2.1) on a random array ($C^\varepsilon \equiv \tilde{C}(X/\varepsilon, X)$), we need to introduce statistical modes of convergence, generalising the deterministic measures (2.6.1) defined in Chapter 2, by taking expectation $\mathbb{E}$ and other statistical operators of deterministic norms for a spatial random process. In particular, we consider

$$
\begin{aligned}
&F_\varepsilon\Big(\|C^\varepsilon - C^{(0)}\|\Big) \underset{\varepsilon\to 0}{\longrightarrow} F\Big(\|C - C^{(0)}\|\Big), && \text{(convergence in distribution)}\\
&\mathbb{E}\Big[\,\|C^\varepsilon - C^{(0)}\|\,\Big] \to 0, \quad \mathbb{E}\Big[\,\|C^\varepsilon - C^{(0)}\|^2\,\Big]^{1/2} \to 0, && \text{(convergence in mean)}\\
&\mathbb{V}\mathrm{ar}\Big[\,C^\varepsilon(X) - C^{(0)}(X)\,\Big] \to 0, && \text{(pointwise convergence in variance)}
\end{aligned}
\tag{3.3.1}
$$

where F_ε is the continuous distribution function of $\|r^\varepsilon\|$ (from (2.6.1)) as a random variable for finite ε, and F is the limiting distribution. The measures in (3.3.1) are sorted from the "weakest" to the "strongest" in the same sense as in (2.6.1) [106] (here we use the term "weaker" with reference to a hierarchy of inequalities between the corresponding norms, and not as convergence in the space of linear functionals or two-scale convergence (see, e.g [191])).

We now verify the rate of convergence of solution $C^\varepsilon(X)$ to the leading-order solution $C^{(0)}(X)$ of problem (3.2.1) by means of the numerical simulation for a varying number of sinks N, $\varepsilon = 1/(N+1)$. The measures of convergence used are the Chebyshev norm $\mathbb{E}[\max(r^\varepsilon)]$, the mean $\mathbb{E}[\langle r^\varepsilon\rangle]$ ($\langle r^\varepsilon\rangle \equiv \int_0^1 r^\varepsilon\,\mathrm{d}X$), the mean-squared norm $\mathbb{E}[\|r^\varepsilon\|_{L_2}]$ and the pointwise standard deviation $\{\mathbb{V}\mathrm{ar}[r^\varepsilon(X=\frac{1}{2})]\}^{1/2}$ (see also the definitions (2.6.1)). All integrals are approximated with trapezium quadrature. The results are summarised in Figure 3.5.

Computations show that the convergence rate of the exact to the homogenized solution is $O(\sqrt{\varepsilon})$ ($\varepsilon \sim N^{-1}$) for both uniformly random and Matérn hard-core sink distributions (Fig. 3.5(a,b)). However, the solution on a normally-perturbed periodic array has convergence rate $O(\varepsilon)$ for large N (Fig. 3.5c), even with $\sigma = 10\varepsilon$, implying strong mixing of sinks. Only in a "weak" sense, in mean, do all three distributions have the same rate of convergence $O(\varepsilon)$ (Fig. 3.5(d-f)).

Furthermore, according to the Corollary to Theorem 2.1.2 by Lukacs [162], the convergence of series $\sum_{N=1}^{\infty}\mathbb{E}[|U_N - U|^2]$ implies the almost sure convergence of a random variable U_N to U: $\mathrm{Prob}(\lim_{N\to\infty} U_N = U) = 1$. Taking $U_N = r^\varepsilon(X=\frac{1}{2})$, where $\varepsilon \sim N^{-1}$, we observe that pointwise variance $\mathbb{V}\mathrm{ar}[U_N] \equiv \mathbb{E}[|U_N - \mathbb{E}[U_N]|^2]$ is $O(1/N)$ for f_u and f_h and $O(1/N^2)$ for f_n (see Fig. 3.5(a-c)). Therefore, noting that in this case $U \equiv \mathbb{E}[U_N]$, we conclude that the homogenization residue r^ε converges pointwise and almost surely to $\mathbb{E}[r^\varepsilon]$ for a normally-perturbed array (at least for the parameter values considered in Fig. 3.5), but cannot prove the almost sure convergence of r^ε for a uniformly-random or hard-core distributions.

We now investigate further the correlation properties of r^ε for all three random processes (f_u, f_h and f_n) and test their dependence on the distribution parameters σ and d.

3.4 Correlation properties and parameter dependence of homogenization residue

In order to study the spatial correlation of the homogenization residue r^ε, apart from pointwise variance $\mathbb{V}\mathrm{ar}[r^\varepsilon(X)]$ and covariance $\mathbb{C}\mathrm{ov}(r^\varepsilon(X), r^\varepsilon(Y))$, we adopt the *transverse covariance*

$$
\mathbb{C}\mathrm{ov}_{\mathrm{T}}(r^\varepsilon) \equiv \mathbb{C}\mathrm{ov}(r^\varepsilon(X), r^\varepsilon(1-X)) = \mathbb{E}\big[\,(r^\varepsilon(X) - \mathbb{E}[r^\varepsilon(X)])\,(r^\varepsilon(1-X) - \mathbb{E}[r^\varepsilon(1-X)])\,\big],
\tag{3.4.1}
$$

which characterises the degree to which fluctuations are correlated across the domain.

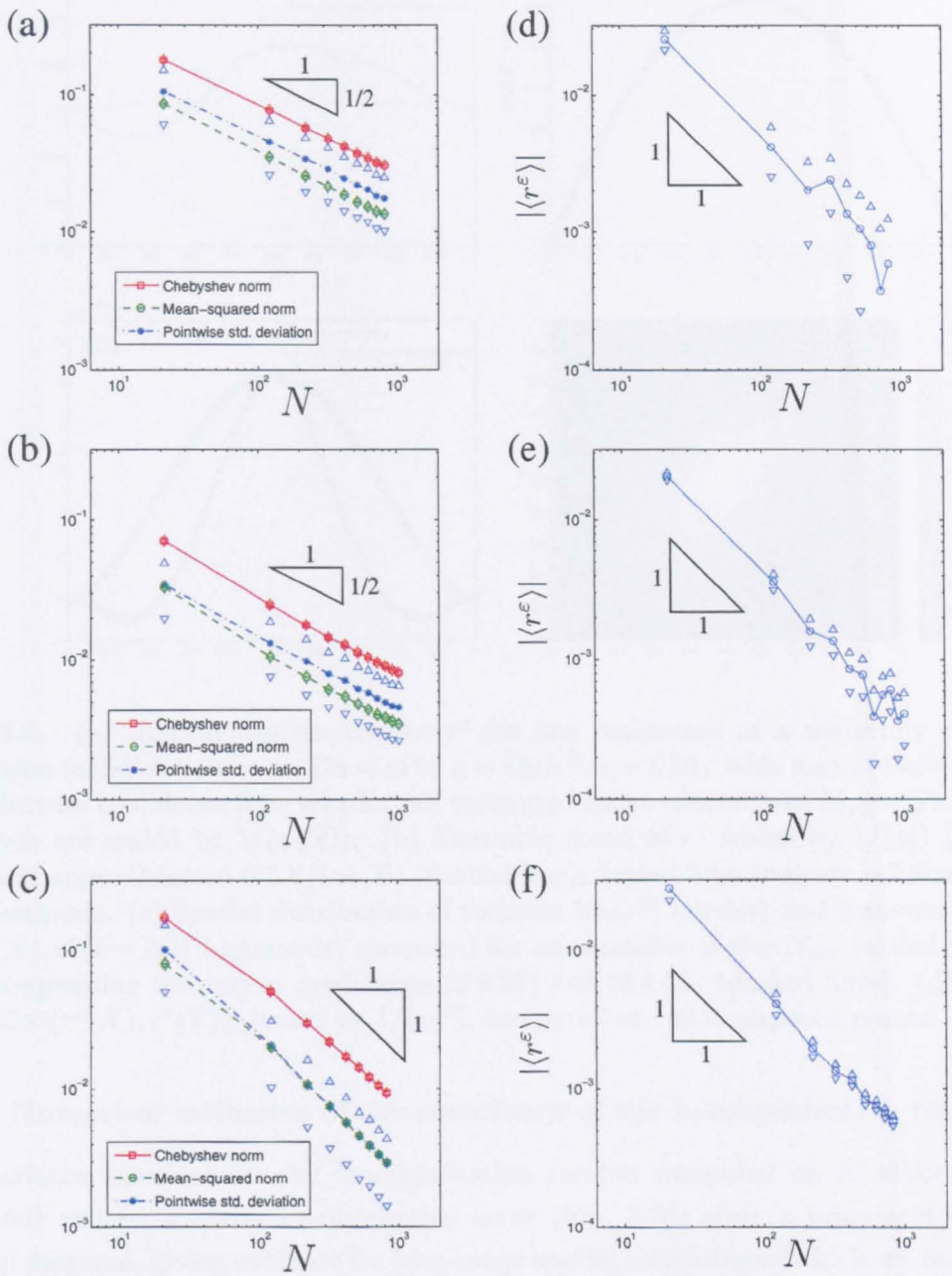

Figure 3.5. Convergence rates of the homogenization residue $r^\varepsilon = C^\varepsilon - C^{(0)}$ for different types of random arrays as a function of the number of sinks N (Pe = 10, Da = εPe, $\varepsilon = 1/(N+1)$): (a) uniformly random distribution; (b) Matérn hard-core type II ($d = 0.65\varepsilon$); (c) normal perturbations of a periodic array ($\sigma = 10\varepsilon$). Convergence of r^ε in mean for uniformly random (d), Matérn hard-core (e), and normal perturbation (f) for the same set of parameters. (Ensemble average over 1000 realisations for uniformly random and hard-core, and over 500 for normal perturbations; triangular markers denote the 95% confidence interval (±2 standard errors) of the pointwise standard deviation (confidence intervals of the other two measures are too small to be visible); see the text for the definition of measures of convergence.)

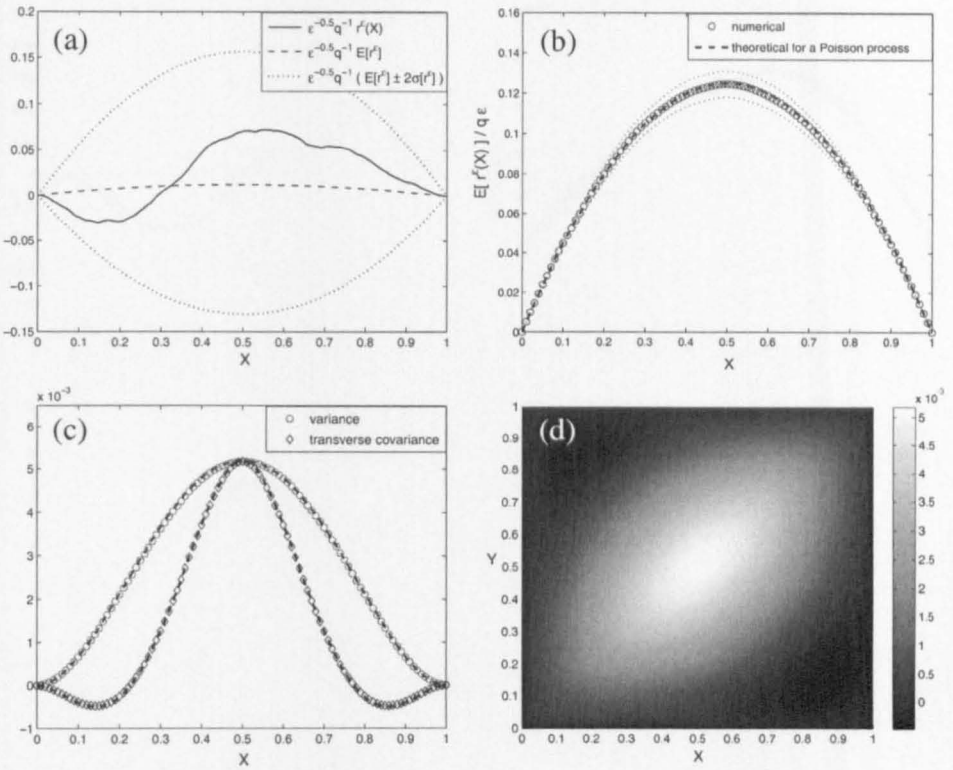

Figure 3.6. (a) Homogenization residue r^ε for one realisation of a uniformly random sink distribution (solid) for $\mathrm{Pe} = \varepsilon^2$, $\mathrm{Da} = \varepsilon\mathrm{Pe}$, $q = \mathrm{Da}/\varepsilon^2$, $\varepsilon = 0.01$, with mean (dashed) and 95%-level pointwise confidence interval (dotted) computed for an ensemble of $N_{\mathrm{ens}} = 5 \times 10^4$ samples (all curves are scaled by $1/(q\sqrt{\varepsilon})$). (b) Ensemble mean of r^ε scaled by $1/(\varepsilon q)$ (circles) and theoretical approximation $0.5X(1-X)$ (dashed line); dotted lines indicate ± 2 standard errors for the estimate. (c) Spatial distribution of variance $\mathbb{V}\mathrm{ar}[r^\varepsilon]$ (circles) and transverse covariance $\mathbb{C}\mathrm{ov}(r^\varepsilon(X), r^\varepsilon(1-X))$ (diamonds) computed for an ensemble of size N_{ens} (scaled by $1/(\varepsilon q^2)$), and corresponding theoretical predictions (3.4.27) and (3.4.28) (dashed lines). (d) Covariance matrix $\mathbb{C}\mathrm{ov}(r^\varepsilon(X), r^\varepsilon(Y))$, scaled by $1/(\varepsilon q^2)$, computed at 100 equispaced points.

3.4.1 Numerical estimates of the covariance of the homogenization residue

Covariance matrices for the homogenization residue computed on a uniformly random (Fig. 3.6d) and on a hard-core-distributed array (Fig. 3.7d) show a prominent cloud about the main diagonal, giving evidence for long-range spatial correlations (which are investigated in more detail in Figs 3.6(c) and 3.7(c) respectively). In the case of a normally-perturbed periodic array, however (3.8d), we observe a thinner band about the main diagonal, suggesting a weaker long-range correlation. The computed variances and transverse covariances for f_u, f_n are in very good agreement with theoretical predictions, which will be obtained below. Panel (a) in Figures 3.6–3.8 summarise the statistical properties of the homogenization residue r^ε by plotting an individual realisation of $r^\varepsilon(\mathrm{X})$ (solid line) together with a 95%-confidence interval (± 2 standard errors (SE), $\mathrm{SE} = \sqrt{\mathbb{V}\mathrm{ar}[r^\varepsilon]/N_{\mathrm{ens}}}$; dotted lines) and the ensemble mean $\mathbb{E}[r^\varepsilon]$ (dashed lines; the ensemble mean is shown in more detail in Figs 3.6–3.8(b)).

We investigate further the correlation properties by considering the case of locally balanced advection-diffusion ($\mathrm{Pe} = O(1)$), plotted in Figure 3.9, and the advection-dominated case

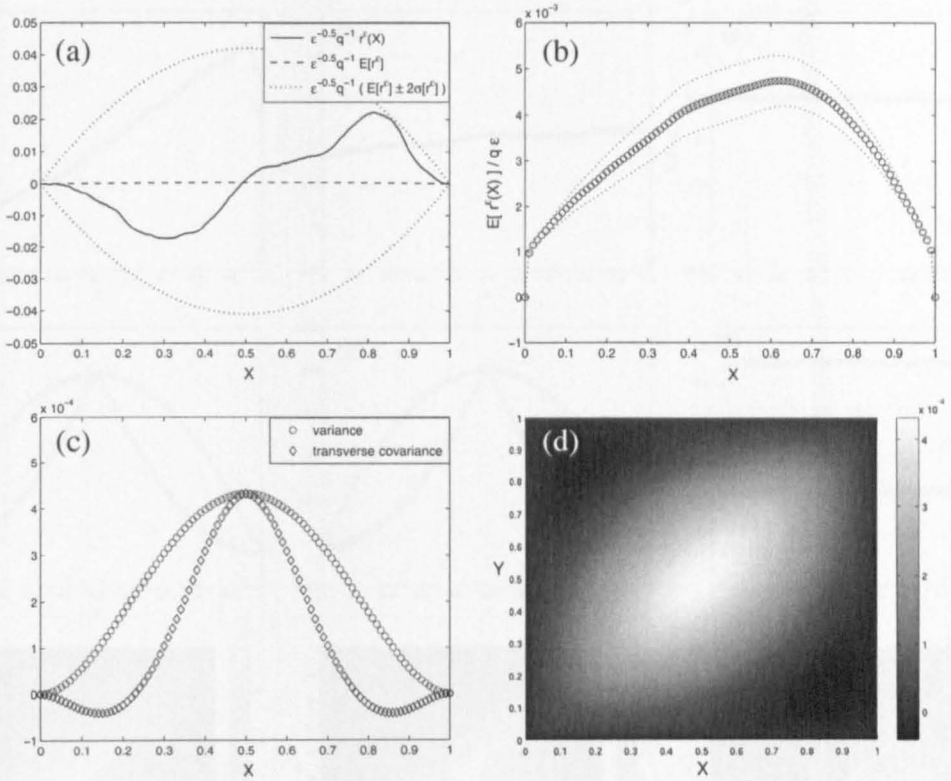

Figure 3.7. Statistical properties of the homogenization residue for a hard-core point process ($d = 0.65\varepsilon$, $\mathrm{Pe} = \varepsilon^2$, $\mathrm{Da} = \varepsilon\mathrm{Pe}$; see the Caption of Fig. 3.6 for more details).

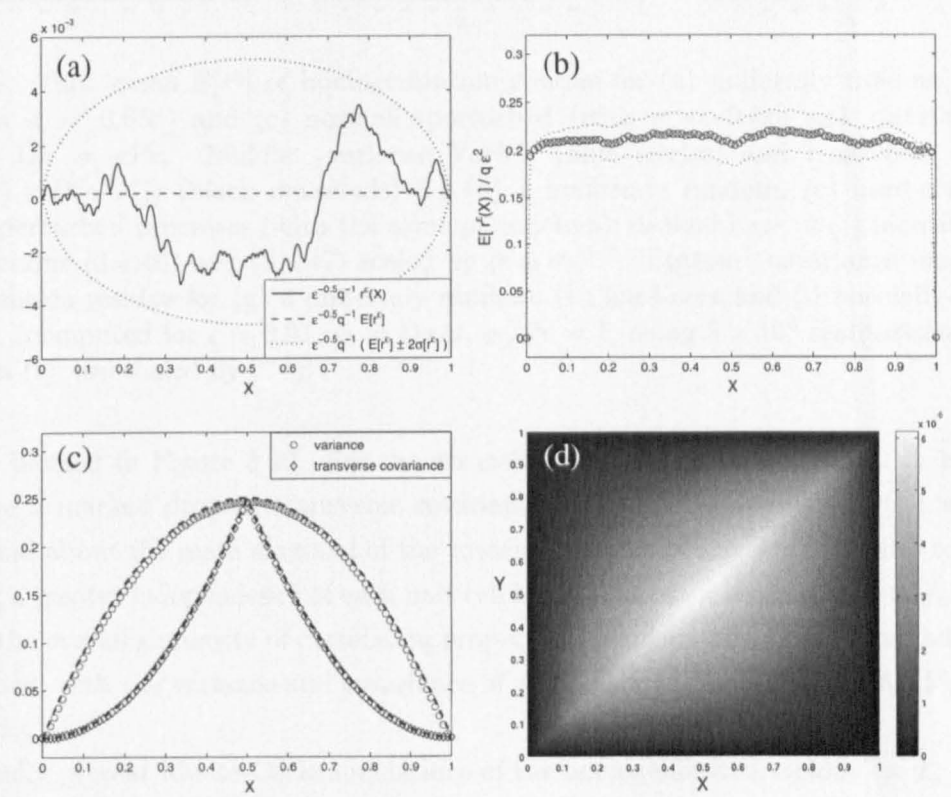

Figure 3.8. Statistical properties of the homogenization residue for normal perturbations ($\sigma_0 = \sigma/\varepsilon = 0.5$, $\mathrm{Pe} = \varepsilon^2$, $\mathrm{Da} = \varepsilon\mathrm{Pe}$; plot (c) is scaled by $(\varepsilon^3 q^2 \sigma_0^2)^{-1}$, with theoretical variance and transverse covariance given by (3.4.18) and (3.4.19); see also the caption of Fig. 3.6).

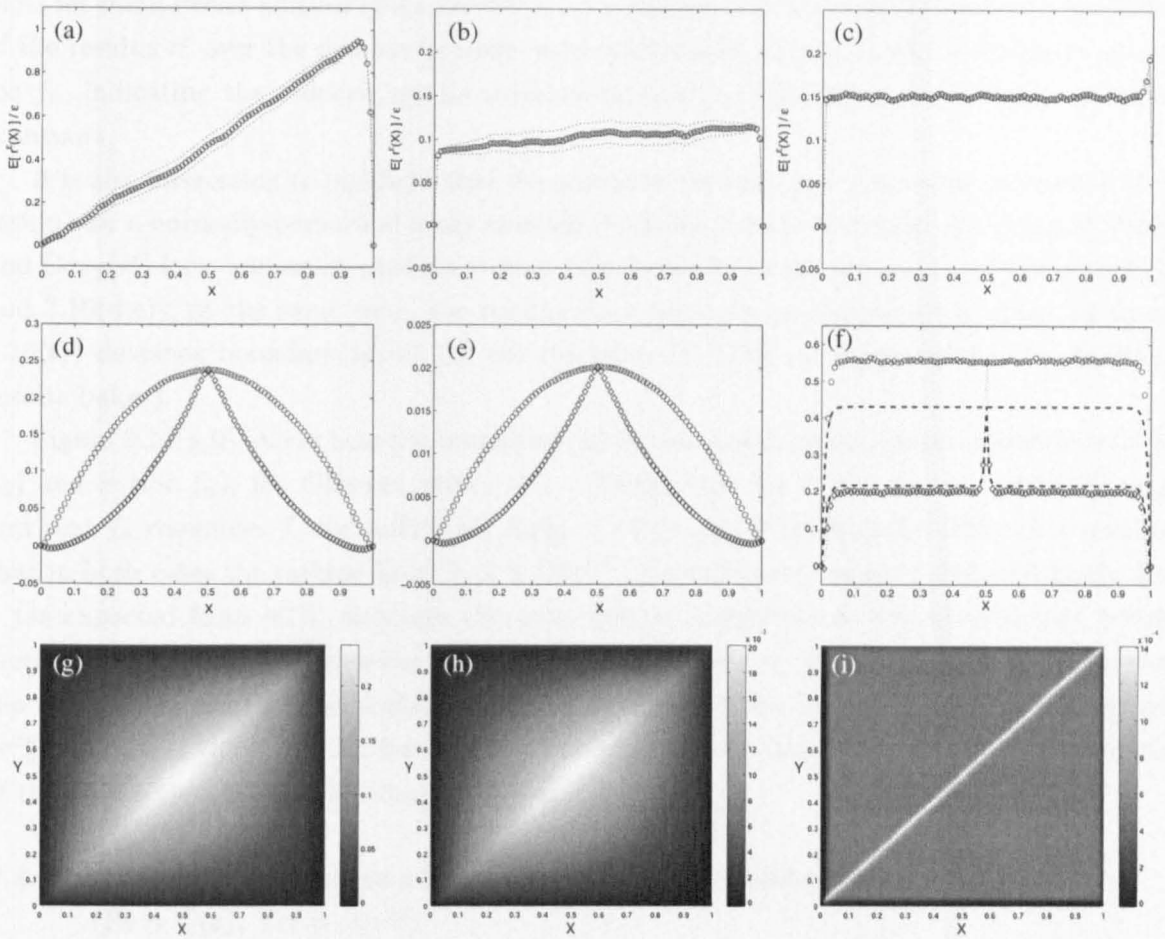

Figure 3.9. Top: mean $\mathbb{E}[r^\varepsilon]$ of homogenization residue for (a) uniformly random, (b) hard-core (with $d = 0.65\varepsilon$) and (c) normally-perturbed (with $\sigma = 0.5\varepsilon$) sink distributions for $\mathrm{Pe} = 1$, $\mathrm{Da} = \varepsilon\mathrm{Pe}$. Middle: variance $\mathbb{V}\mathrm{ar}[r^\varepsilon]$ (blue circles) and transverse covariance $\mathbb{C}\mathrm{ov}(r^\varepsilon(X), r^\varepsilon(1-X))$ (black diamonds) for (d) a uniformly random, (e) hard-core and (f) normally-perturbed processes (with the same parameters); dashed lines in (f) indicate theoretical predictions (3.4.46) and (3.4.47) scaled by $(\varepsilon\, q_1\, \sigma_0)^{-2}$. Bottom: covariance matrix of the homogenization residue for (g) a uniformly random, (h) hard-core and (i) normally-perturbed processes. (computed for $\varepsilon = 0.01$, $q_1 = \mathrm{Da}/\varepsilon$, $q_1/\mathrm{Pe} = 1$, using 5×10^4 realisations; all plots, apart from (f), are scaled by ε^{-1}).

($\mathrm{Pe} \gg 1$), plotted in Figure 3.10. For the normally-perturbed distribution f_p, in both cases, we observe a marked drop in transverse covariance (see Figs 3.9(f) and 3.10(f)) and a very narrow band about the main diagonal of the covariance matrix (Fig. 3.9(i), similar to Fig. 3.3), indicating a greater independence of each unit cell in the case of f_n as compared to f_u or f_h. We also note the overall similarity of correlation properties for the uniformly-random and hard-core distributions, with the variance and covariance of f_h being a scaled version of f_u (Figs 3.9(d,e) and 3.10(d,e)).

We finally present Monte-Carlo simulations of the homogenization residue for f_u, f_h and f_n sink distributions at large Péclet number. Figure 3.10(a-c) combines representative fluctuations of the residue (solid line) with the ensemble mean (dashed) and 95%-confidence interval (dotted; based on the corresponding variances shown in Fig. 3.10(d-f)). Comparing with the analogous

plots for small Péclet number (Figs 3.6–3.8(a)), we observe that the distribution of the amplitude of the residue r^ε over the domain becomes more uniform for f_u and f_h and essentially constant for f_n, indicating the reduced spatial correlations in r^ε in the presence of stronger advective transport.

It is also interesting to highlight that the parabolic variance and transverse covariance of the residue for a normally-perturbed array at small Pe (3.8(c)) closely resemble the shape of $\mathbb{V}\mathrm{ar}[r^\varepsilon]$ and $\mathbb{C}\mathrm{ov}_\mathrm{T}[r^\varepsilon]$ for a uniformly-random or hard-core arrays for moderate-to-large Pe (Figs 3.9(d,e) and 3.10(d,e)); at the same time, the residue for a normally-perturbed array (Figs 3.9(f) and 3.10(f)) develops boundary layers (of the thickness $O(\varepsilon/\mathrm{Pe})$, as suggested by our analytical results below).

Figure 3.10(g,h) shows how the magnitude of the homogenization residue depends on d (for f_h) and σ (for f_n), for different values of ε. (Recall that for $d = 0$, f_h is equivalent to f_u, and that f_n resembles f_u for sufficiently large σ.) Collapse of the data for different ε indicates that in both cases the residue $\mathbb{E}(\|r^\varepsilon\|_{L_2})$ is $O(\varepsilon^{1/2})$ for sufficiently small d and sufficiently large σ (as expected from [47]), although the error falls in magnitude as the distributions become more regular (either by increasing d towards d_{cr} or reducing σ close to zero). Indeed for $\sigma = 0$ the residue has exactly the scaling predicted by asymptotics for the periodic sinks, namely $\|r^\varepsilon\|_{L_2} \approx 0.451\varepsilon$ (for $\mathrm{Pe} = 10$, $\mathrm{Da} = \varepsilon\mathrm{Pe}$). The magnitude of the residue approaches the value of the uniformly-random distribution for $\sigma \gtrsim 0.3$.

3.4.2 Analytical estimates of covariance in the diffusion-dominated case ($\mathrm{Pe} = O(\varepsilon)$, $\mathrm{Da} = O(\varepsilon^2)$)

We now focus on the corrections to the leading order solution $C^{(0)}$ in the case of uniformly-random or normally-perturbed sink distributions for $\mathrm{Pe} = O(\varepsilon)$, $\mathrm{Da} = O(\varepsilon^2)$ (again writing $\mathrm{Pe} = \varepsilon p$ and $\mathrm{Da} = \varepsilon^2 q$). By using the statistical properties of these distributions and an exact solution for a cell problem we can estimate analytically the mean and covariance of the homogenization residue.

When sinks are distributed non-periodically we can derive the homogenized approximation of (3.2.1) as follows. We initially use

$$C^\varepsilon = \tilde{C}(x, X) = C^{(0)}(x, X) + \varepsilon C^{(1)}(x, X) + \dots\,, \qquad \frac{\mathrm{d}C^\varepsilon}{\mathrm{d}x} = \frac{\partial \tilde{C}}{\partial x} + \varepsilon \frac{\partial \tilde{C}}{\partial X}\,, \tag{3.4.2}$$

to rewrite (3.2.1) as

$$\begin{aligned} &\tilde{C}_{xx} + 2\varepsilon \tilde{C}_{xX} + \varepsilon^2 \tilde{C}_{XX} - \varepsilon p \left(\tilde{C}_x + \varepsilon \tilde{C}_X\right) = \varepsilon^2 q f, \quad (0 < x < \varepsilon^{-1},\, 0 < X < 1), \\ &\tilde{C}|_{X=0} = 1, \quad \tilde{C}|_{X=1} = 0. \end{aligned} \tag{3.4.3}$$

(For brevity we assume here that $\tilde{C}$ does not fall to zero upstream of $X = 1$). We allow $C^{(1)}$ and $C^{(2)}$ to have fluctuations, assuming that these are not large enough to disrupt the proposed expansion. At leading order, $C^{(0)}_{xx} = 0$, $C^{(0)}|_{X=0} = 1$ and $C^{(0)}|_{X=1} = 0$. Thus $C^{(0)}(x, X) = \tilde{A}(X)x + \tilde{B}(X)$. The first term must be suppressed to avoid secular growth, so that $C^{(0)} = C^{(0)}(X)$. Likewise at the following order we find that $C^{(1)} = C^{(1)}(X)$. Collecting

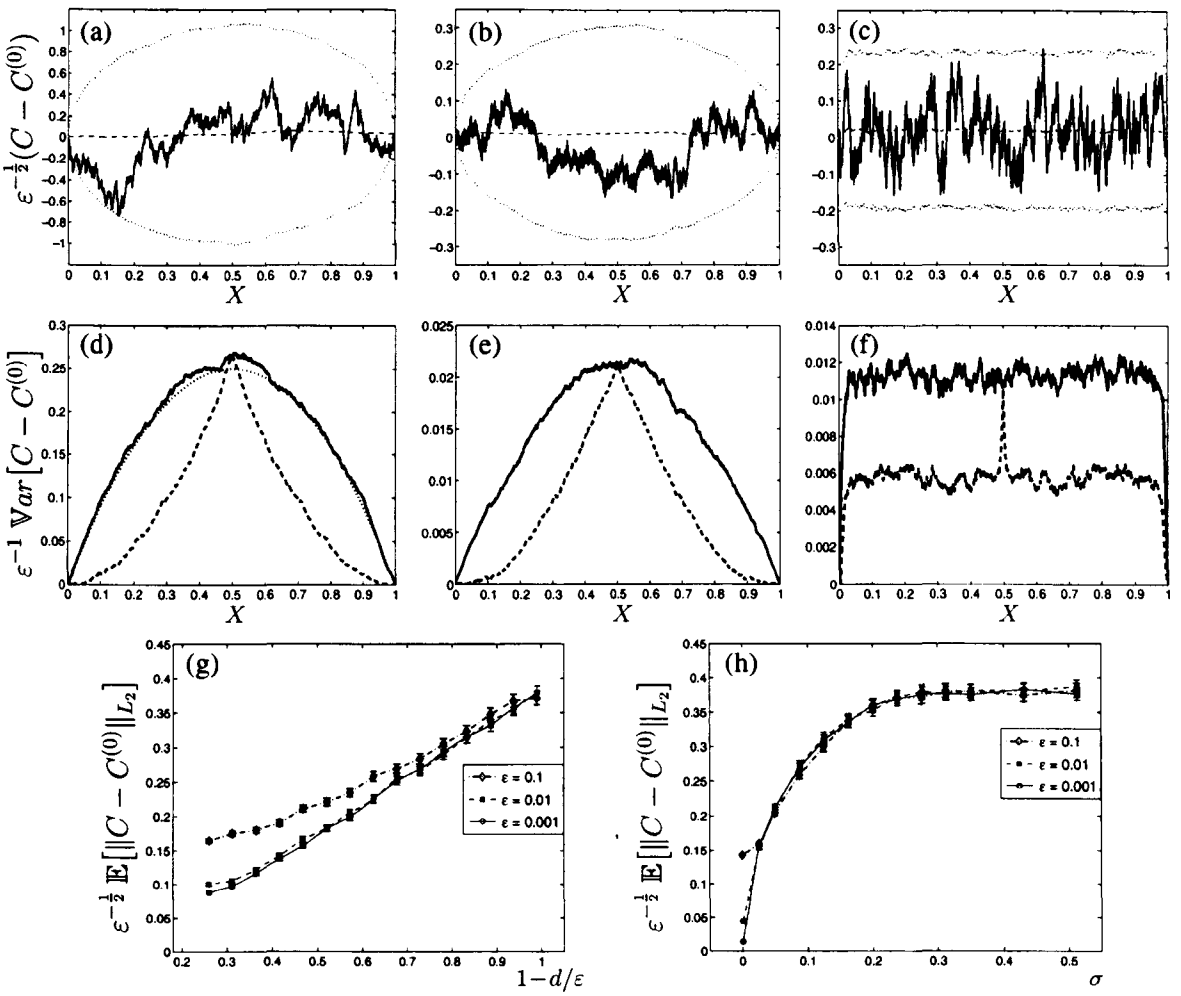

Figure 3.10. (a–c) Homogenization residue $r^\varepsilon = C - C^{(0)}$ (solid) scaled by $\varepsilon^{-1/2}$ for (a) uniformly random, (b) hard-core ($d = 0.65\varepsilon$) and (c) normally-perturbed ($\sigma = 10\varepsilon$) point processes for $\varepsilon = 0.001$, Pe $= 10$, Da $= \varepsilon$Pe. Dashed line shows population mean from $N_{\text{ens}} = 1000$ samples, dotted line shows mean $\pm$ two standard deviations. (d–f) Variance (solid) and transverse covariance (3.2.2) (dashed), scaled with ε^{-1}, corresponding to (a–c) (the dotted line shows $X(1-X)$ in (d)). (g,h) Dependence of homogenization error (estimated from $n = 1000$ samples) on the minimal inter-sink distance d for $f = f_h$ (g) and on the standard deviation σ for $f = f_n$ (h) (scaled by $\varepsilon^{-1/2}$ for $\varepsilon = 0.1, 0.01, 0.001$; Pe $= 10$, Da $= \varepsilon$Pe). Error bars are ± 2 standard errors (SE), where SE $= \sqrt{\mathbb{V}\text{ar}[\|r^\varepsilon\|_{L_2}]/N_{\text{ens}}}$, calculated using a standard unbiased estimate.

the terms in (3.4.3) at $O(\varepsilon^2)$, we obtain

$$C^{(2)}_{xx} = q(f - F), \quad \text{where} \quad qF(X) \equiv C^{(0)}_{XX} - pC^{(0)}_{X}, \tag{3.4.4}$$

with $f = \sum_{i=1}^{N} \delta(x - \xi_i)$. This is to be solved subject to $C^{(1)} = C^{(2)} = 0$ at $x = 0$ and $x = \varepsilon^{-1}$. Thus in $\xi_i < x < \xi_{i+1}$, for $i = 0, 1, 2, \ldots, N$, treating x and X as independent,

$$C^{(2)} = -\tfrac{1}{2}qF(x - \xi_i)^2 + \alpha_i(x - \xi_i) + \beta_i \tag{3.4.5}$$

for some α_i, β_i, taking $\xi_0 = 0$ and $\xi_{N+1} = \varepsilon^{-1}$. We define $\Delta_i \equiv \xi_i - \xi_{i-1}$ and $(R_i, S_i, T_i, U_i) \equiv \sum_{j=1}^{i}(\xi_j, \Delta_j^2, \xi_j\Delta_j, \xi_j^2)$ so that $\xi_i \equiv \sum_{j=1}^{i} \Delta_j$ and we note the following identities:

$$\sum_{j=1}^{i} \xi_j\xi_{j-1} \equiv U_{i-1} + \tfrac{1}{2}(\xi_i^2 - S_i), \quad \sum_{j=1}^{i} \Delta_j(j-1) \equiv (T_i - R_i) - T_{i-1} = i\xi_i - R_i. \tag{3.4.6}$$

Integrating (3.4.4) across the ith sink's location $x = \xi_i$ gives $C^{(2)}|_{\xi_i+} = C^{(2)}|_{\xi_i-}$ and $C^{(2)}_x|_{\xi_i+} - C^{(2)}_x|_{\xi_i-} = q$ for $i = 1, 2, \ldots, N$, so (3.4.5) provides the following recurrence relations:

$$\alpha_i = \alpha_{i-1} + q\,(1 - F\Delta_i)\,, \tag{3.4.7a}$$

$$\beta_i = \beta_{i-1} - \tfrac{1}{2}qF\Delta_i^2 + \alpha_{i-1}\Delta_i. \tag{3.4.7b}$$

We take $\beta_0 = 0$ to satisfy $C^{(2)} = 0$ at $x = 0$. From (3.4.7), assuming F is independent of i to leading order (verified *a posteriori*), for $i = 1, 2, \ldots, N$,

$$\alpha_i = \alpha_0 + q(i - F\xi_i), \tag{3.4.8a}$$

$$\beta_i = -\tfrac{1}{2}qFS_i + \alpha_0\,\xi_i + q\sum_{j=1}^{i} \Delta_j(j - 1 - F\xi_{j-1}). \tag{3.4.8b}$$

Substituting (3.4.8) into (3.4.5), expanding and using (3.4.6) gives, after some algebra,

$$C^{(2)} = -\tfrac{1}{2}qFx^2 + \alpha_0 x + q\,[ix - R_i]\,, \quad \text{for} \quad \xi_i < x < \xi_{i+1},\ i = 1, 2, \ldots, N\,. \tag{3.4.9}$$

Imposing $C^{(2)} = 0$ at $x = \varepsilon^{-1} \equiv N + 1$ gives $\alpha_0 = \tfrac{1}{2}qF\varepsilon^{-1} - q\,[N - \varepsilon R_N]$, and so, for $\xi_i < x < \xi_{i+1}$,

$$C^{(2)} = \tfrac{1}{2}qFx(\varepsilon^{-1} - x) + q\,[(\varepsilon x R_N - R_i) + x\,(i - N)]\,, \quad i = 1, 2, \ldots, N\,. \tag{3.4.10}$$

This expression relates solute fluctuations directly to sink distributions.

We note that all terms but $\varepsilon x R_N - R_i \equiv X R_N - R_i$ (setting $x = X/\varepsilon$) in (3.4.10) are deterministic, and therefore

$$C^{(2)} - \mathbb{E}[C^{(2)}] = q\,(X\mathring{R}_N - \mathring{R}_i)\,, \quad \mathring{R}_i \equiv R_i - \mathbb{E}[R_i],\ i = 1, \ldots, N,\ (\xi_i < x < \xi_{i+1})\,. \tag{3.4.11}$$

Likewise $\mathbb{C}\mathrm{ov}(C^{(2)}(X), C^{(2)}(Y)) = q^2\,\mathbb{C}\mathrm{ov}\big(XR_N - R(X),\, YR_N - R(Y)\big)$, where $X, Y \in (0,1)$, $R(X) = \sum_{j=1}^{\lfloor \varepsilon^{-1}X\rfloor}\xi_j$ $(i = \lfloor \varepsilon^{-1}X\rfloor\ i = 1,\dots,N)$, so that $R(1-X) = \sum_{j=1}^{N-\lfloor \varepsilon^{-1}X\rfloor}\xi_j$ (due to $\lfloor \varepsilon^{-1}(1-X)\rfloor \approx N - \lfloor \varepsilon^{-1}X\rfloor = N - i$), and therefore we have $\mathbb{C}\mathrm{ov}(C^{(2)}(X), C^{(2)}(1-X)) = q^2\,\mathbb{C}\mathrm{ov}\big(XR_N - R_i,\, (1-X)R_N - R_{N-i}\big)$. The choice of $N-i$ instead of $N+1-i$ does not affect the results at leading-order, owing to large $N \gg 1$ and smooth X-dependence of the variance and the transverse covariance, as will be shown below.

Thus, by applying the definition (3.4.1) to (3.4.11), the variance and the transverse covariance of the correction are expressed in terms of the partial sums $R_i = \sum_{j=1}^{i}\xi_j$ of the sink distribution ξ_i as follows:

$$\mathbb{V}\mathrm{ar}[C^{(2)}] = q^2\,\mathbb{E}\big[(X\mathring{R}_N - \mathring{R}_i)^2\big] = q^2\left\{X^2\mathbb{V}\mathrm{ar}[R_N] - 2X\mathbb{C}\mathrm{ov}(R_i, R_N) + \mathbb{V}\mathrm{ar}[R_i]\right\}, \quad (3.4.12a)$$

$$\begin{aligned}\mathbb{C}\mathrm{ov}_{\mathrm{T}}[C^{(2)}] &= q^2\,\mathbb{E}\big[\,\{X\mathring{R}_N - \mathring{R}_i\}\,\{(1-X)\mathring{R}_N - \mathring{R}_{N-i}\}\,\big] = \\ &= q^2\big\{X(1-X)\mathbb{V}\mathrm{ar}[R_N] - (1-X)\mathbb{C}\mathrm{ov}(R_i, R_N) - X\mathbb{C}\mathrm{ov}(R_{N-i}, R_N) + \\ &\qquad + \mathbb{C}\mathrm{ov}(R_i, R_{N-i})\,\big\}.\end{aligned} \quad (3.4.12b)$$

Our task therefore reduces to finding the corresponding variances and covariances of the partial sums R_i for a specific sink distribution.

The case of a normally-perturbed sink distribution

When $f = f_n$, then, denoting $\sigma_0 \equiv \sigma/\varepsilon$, we have $\xi_i \sim \mathcal{N}(i, \sigma_0^2) \sim i + \sigma_0\mathcal{N}(0,1)$. Therefore (owing to the independence of ξ_i for small σ_0)

$$R_i \sim \sum_{j=1}^{i}\mathcal{N}(j, \sigma_0^2) \sim \mathcal{N}\Big(\tfrac{i(i+1)}{2}, i\sigma_0^2\Big)\,, \quad (3.4.13)$$

where we used the linearity property of expectation $\mathbb{E}\left[\sum_{j=1}^{i}\xi_j\right] = \sum_{j=1}^{i}\mu_j = i(i+1)/2$ and the property of a non-central χ^2 distribution with one degree of freedom: $\mathbb{E}[\xi_j^2] = \mu_j^2 + \sigma_0^2$, $\mu_j \equiv j$ in this case.

It remains to obtain $\mathbb{C}\mathrm{ov}(R_k, R_p) \equiv \mathbb{E}[R_kR_p] - \mathbb{E}[R_k]\,\mathbb{E}[R_p]$ for $k \neq p$. The independence of ξ_j and ξ_l, i.e. $\mathbb{C}\mathrm{ov}(\xi_j, \xi_l) = 0$, for $j \neq l$, assuming that σ_0 is small enough for sinks not to swap places and $k \leq p$, gives

$$\begin{aligned}\mathbb{C}\mathrm{ov}(R_k, R_p) &= \sum_{j=1}^{k}\sum_{l=1}^{p}\big\{\mathbb{E}[\xi_j\,\xi_l] - \mathbb{E}[\xi_j]\,\mathbb{E}[\xi_l]\big\} = \sum_{j=1}^{k}\sum_{l=1}^{k}\big\{\mathbb{E}[\xi_j\,\xi_l] - \mathbb{E}[\xi_j]\,\mathbb{E}[\xi_l]\big\} + \\ &+ \sum_{j=1}^{k}\sum_{\substack{l=k+1\\(l\neq j)}}^{p}\mathbb{C}\mathrm{ov}(\xi_j, \xi_l) = \mathbb{E}\left[\sum_{j=1}^{k}\sum_{l=1}^{k}\xi_j\,\xi_l\right] - \mathbb{E}\left[\sum_{j=1}^{k}\xi_j\right]\mathbb{E}\left[\sum_{l=1}^{k}\xi_l\right] = \mathbb{V}\mathrm{ar}[R_k]\,,\end{aligned} \quad (3.4.14)$$

reducing the covariance (for $k \leq p$) to the corresponding variance.

From (3.4.13) and (3.4.14) we therefore have

$$\mathbb{E}[R_k] = \frac{k(k+1)}{2}, \quad \mathbb{V}\mathrm{ar}[R_k] = \mathbb{C}\mathrm{ov}(R_k, R_p) = k\,\sigma_0^2\,, \quad (k \leq p)\,. \quad (3.4.15)$$

Thus (3.4.12) simplifies to

$$\mathbb{V}\mathrm{ar}[C^{(2)}] = q^2\left\{X^2\mathbb{V}\mathrm{ar}[R_N] + (1-2X)\mathbb{V}\mathrm{ar}[R_i]\right\},\ (X<1,\ i\le N), \tag{3.4.16a}$$

$$\mathbb{C}\mathrm{ov}_{\mathrm{T}}[C^{(2)}] = q^2\left\{X(1-X)\mathbb{V}\mathrm{ar}[R_N] + X\,\mathbb{V}\mathrm{ar}[R_i] - X\,\mathbb{V}\mathrm{ar}[R_{N-i}]\right\},\ (X<\tfrac{1}{2},\ i\le \tfrac{N}{2}). \tag{3.4.16b}$$

Note that by setting $i=(i-x)+\varepsilon^{-1}X$ and $N=\varepsilon^{-1}-1$, we obtain from (3.4.15), $\mathbb{E}[XR_N - R_i] = \frac{1}{2}XN(N+1) - \frac{1}{2}i(i+1) = \varepsilon^{-2}\frac{1}{2}X(1-X) - \frac{1}{2}(x+i)(i+1-x)$. Substituting this into (3.4.10), we get an expectation of the correction in the case of normal perturbations:

$$\mathbb{E}(C^{(2)}) = \varepsilon^{-2}\,\tfrac{1}{2}\,q\,(F-1)X(1-X) + \tfrac{1}{2}\,q\,(x-i)(i+1-x). \tag{3.4.17}$$

To ensure the original expansion is asymptotic, we must take $F=1$ at $O(\varepsilon^{-2})$, yielding from (3.4.4) the periodic leading-order equation (2.3.8a) for $C^{(0)}$ and recovering the parabolic cell solution (2.3.12), obtained in Chapter 2. Simulations indicate that the contribution at $O(\varepsilon^{-1})$ (and hence $C^{(1)}$) vanishes (Fig. 3.8b); however, simulations also show that a further correction to $\mathbb{E}[r^\epsilon]$ of the order of ε^2 is present, presumably involving a closure condition for the correction at higher order.

Substituting the variance and covariance of the partial sums R_i (3.4.15) into (3.4.16), setting $i=\varepsilon^{-1}X+\gamma$ ($\gamma\equiv i-x=O(1)$) and $N=\varepsilon^{-1}-1$, and retaining the leading-order term in powers of ε, we find, after some algebra, that (3.4.16a) gives

$$\mathbb{V}\mathrm{ar}[C^{(2)}] = \varepsilon^{-1}\,q^2\,\sigma_0^2\,X(1-X) + O(1), \tag{3.4.18}$$

and using (3.4.16b) for $0\le X\le\frac{1}{2}$, $i\le N-i$ (owing to the symmetry of the covariance) gives

$$\mathbb{C}\mathrm{ov}_{\mathrm{T}}[C^{(2)}] = \begin{cases} \varepsilon^{-1}\,q^2\,\sigma_0^2\,X^2 + O(1), & 0\le X\le\frac{1}{2}\,, \\ \varepsilon^{-1}\,q^2\,\sigma_0^2\,(1-X)^2 + O(1), & \frac{1}{2}<X\le 1\,, \end{cases} \tag{3.4.19}$$

in a good agreement with simulations (Fig. 3.8c). Thus while $C^{(2)}$ has $O(1)$ mean, r^ϵ is dominated by fluctuations of relative magnitude $O(\varepsilon^{3/2})$. This approximation holds as long as sinks do not exchange places, which can be expected once σ_0 becomes sufficiently large. Because $\mathbb{V}\mathrm{ar}[C^{(2)}]$ scales with σ_0, (3.4.18) suggests that the fluctuations in the case of stronger mixing of perturbed sink locations will be larger than $O(\varepsilon^{3/2})$.

The case of a uniformly random sink distribution

When $f=f_u$, we turn to Matuswana [167], who determined the distribution of linear combinations of order statistics drawn from $\mathcal{U}(0,1)$ (i.e. combinations of $\hat{\xi}_1,\ldots,\hat{\xi}_N$, where $\hat{\xi}_i\equiv\varepsilon\xi_i$) as a mixture of scaled Beta distributions.

Let us consider $\hat{\xi}_i$, $i=1,\ldots,N$ to be the ordered values from a sample of N independent uniformly distributed random variables on $[0,1]$, where $\hat{\xi}_i<\hat{\xi}_j$ for $i<j$, and also set $\hat{\xi}_0=0$ and $\hat{\xi}_{N+1}=1$ to account for the boundary conditions. Let $V_i=\hat{\xi}_i-\hat{\xi}_{i-1}$, $i=1,\ldots,N+1$ and so

$(V_1, \ldots, V_{N+1})$ has a Dirichlet distribution with $(N+1)$-vector of parameters $(1, 1, \ldots, 1)$ [167]. From the properties of the Dirichlet distribution we know that

$$\mathbb{E}[V_i] = \frac{1}{N+1}, \quad \mathbb{V}\mathrm{ar}[V_i] = \frac{N}{(N+1)^2(N+2)}, \quad \mathbb{C}\mathrm{ov}(V_i, V_j) = \frac{-1}{(N+1)^2(N+2)}, \tag{3.4.20}$$

where $i \neq j$, $i, j = 1, \ldots, N$.

Consider the partial sums of order statistics $\hat{\xi}_i$

$$L_k = \sum_{j=1}^{k} b_j V_j, \quad T_p = \sum_{q=1}^{p} c_q V_q, \tag{3.4.21}$$

where b_j, c_q are given deterministic weights. Then, from (3.4.20) and the linearity property of expectation we have

$$\mathbb{E}[L_k] = \sum_{j=1}^{k} b_j \mathbb{E}[V_j] = \frac{\sum_{j=1}^{k} b_j}{N+1}, \tag{3.4.22a}$$

$$\mathbb{V}\mathrm{ar}[L_k] = \sum_{j=1}^{k}\sum_{l=1}^{k} b_j b_l \mathbb{C}\mathrm{ov}(V_j, V_l) = \frac{\sum_{j=1}^{k} b_j^2}{(N+1)(N+2)} - \frac{\sum_{j=1}^{k}\sum_{l=1}^{k} b_j b_l}{(N+1)^2(N+2)}, \tag{3.4.22b}$$

$$\mathbb{C}\mathrm{ov}(L_k, T_p) = \sum_{j=1}^{k}\sum_{q=1}^{p} b_j c_q \mathbb{C}\mathrm{ov}(V_j, V_q) = \frac{\sum_{j=1}^{k}\sum_{q=1}^{p} b_j c_q \{(N+1)\delta_{jq} - 1\}}{(N+1)^2(N+2)}, \tag{3.4.22c}$$

where $k, p = 1, \ldots, N$, $k \leq p$ and δ_{jq} is the Kronecker delta-function.

We now consider expressions for the mean, variance and covariance of the partial sums R_k of the order statistics:

$$R_k \equiv \varepsilon^{-1} \sum_{j=1}^{k} \hat{\xi}_j \equiv \sum_{j=1}^{k} (k - j + 1) V_j, \quad R_p \equiv \varepsilon^{-1} \sum_{q=1}^{p} \hat{\xi}_q \equiv \sum_{q=1}^{p} (p - q + 1) V_q, \tag{3.4.23}$$

with coefficients of (3.4.21) being

$$b_j = k - j + 1, \quad c_q = p - q + 1, \quad (k, j, p, q = 1, \ldots, N). \tag{3.4.24}$$

We also note the following identities for (3.4.24):

$$\begin{aligned} &\sum_{j=1}^{k} b_j \equiv \frac{k(k+1)}{2}, \quad \sum_{j=1}^{k} b_j^2 \equiv \frac{k(k+1)(2k+1)}{6}, \\ &\sum_{j=1}^{k} b_j c_j \equiv \frac{k(k+1)(2k+1)}{6} + \frac{k(k+1)(p-k)}{2}. \end{aligned} \tag{3.4.25}$$

Hence, from (3.4.22), (3.4.23) and (3.4.25), using $\varepsilon^{-1} \equiv N + 1$, we get the mean, variance

and covariance of R_k:

$$\mathbb{E}[R_k] \equiv \varepsilon^{-1}\mathbb{E}[L_k] = \frac{k(k+1)}{2}, \tag{3.4.26a}$$

$$\mathbb{V}\mathrm{ar}[R_k] \equiv \varepsilon^{-2}\mathbb{V}\mathrm{ar}[L_k] = \frac{k(k+1)(2k+1)(N+1)}{6(N+2)} - \frac{(\mathbb{E}[R_k])^2}{N+2}, \tag{3.4.26b}$$

$$\mathbb{C}\mathrm{ov}(R_k, R_p) \equiv \varepsilon^{-2}\mathbb{C}\mathrm{ov}(L_k, T_p) = \frac{k(k+1)(2k+1)(N+1)}{6(N+2)} + \frac{k(k+1)(p-k)(N+1)}{2(N+2)} - \\ - \frac{\mathbb{E}[R_k]\,\mathbb{E}[R_p]}{N+2}, \quad k \le p. \tag{3.4.26c}$$

By using (3.4.26a), which is identical to $\mathbb{E}[R_i]$ for the normally-perturbed distribution (3.4.15), we thereby again recover (3.4.17) from (3.4.10), requiring that $F = 1 + O(\varepsilon)$, so once more $C^{(0)}$ satisfies the leading-order equation for a periodic array (2.3.8a).

Substituting (3.4.26(b,c)) into (3.4.12) and again writing $i = \varepsilon^{-1}X + (i - x)$ (taking $|i - x| = O(1)$), we find to leading order in ε (using `Maple`) the variance and the transverse covariance of the correction for the case of a uniformly random sink distribution:

$$\mathbb{V}\mathrm{ar}[C^{(2)}] = \varepsilon^{-3} q^2 \tfrac{1}{12} X^2 (1-X)^2 + O(\varepsilon^{-2}), \tag{3.4.27}$$

$$\mathbb{C}\mathrm{ov}_{\mathrm{T}}[C^{(2)}] = \begin{cases} -\varepsilon^{-3} q^2 \tfrac{1}{12} X^2 (1 - 6X + 7X^2) + O(\varepsilon^{-2}), & 0 \le X \le \tfrac{1}{2}, \\ -\varepsilon^{-3} q^2 \tfrac{1}{12} (1-X)^2 (2 - 8X + 7X^2) + O(\varepsilon^{-2}), & \tfrac{1}{2} < X \le 1, \end{cases} \tag{3.4.28}$$

which are in an excellent agreement with numerical solutions shown in Figure 3.6(c).

Furthermore, assuming $\mathbb{V}\mathrm{ar}[C^{(1)}] = 0$, we obtain $\mathbb{V}\mathrm{ar}[r^\varepsilon] = \varepsilon\, q^2 \frac{1}{12} X^2 (1-X)^2$ to leading order in ε, consistent with simulations (see Fig. 3.6c)). The fluctuations about $C^{(0)}$ are thus $O(\varepsilon^{1/2})$, which is significantly larger than $O(\varepsilon^2)$ error for homogenization on periodic arrays (see e.g. Table 2.1 of Chapter 2, for $\mathrm{Pe} = O(\varepsilon)$).

Simulations also show that $\mathbb{E}[r^\varepsilon] \approx \frac{1}{2}\varepsilon\, q\, X(1-X)$ (see Fig. 3.6b), suggesting a contribution from $C^{(1)}$ which presumably must be determined by a closure condition at higher order.

3.4.3 Analytical estimates of covariance for the case of balanced advection-diffusion ($\mathrm{Pe} = O(1)$, $\mathrm{Da} = O(\varepsilon)$)

It remains to establish the statistical properties of the homogenization residue in the case of moderate-to-large local Péclet numbers $\mathrm{Pe} = O(1)$, $\mathrm{Da} = O(\varepsilon) = \varepsilon^2 q_1$, $q_1 = O(1)$), when (3.2.1) transforms to the following problem:

$$\tilde{C}_{xx} + 2\varepsilon \tilde{C}_{xX} + \varepsilon^2 \tilde{C}_{XX} - \mathrm{Pe}\left(\tilde{C}_x + \varepsilon \tilde{C}_X\right) = \varepsilon q_1 f, \quad f = \sum_{i=1}^{N} \delta(x - \xi_i)$$
$$\tilde{C}|_{X=0} = 1, \quad \tilde{C}|_{X=1} = 0. \tag{3.4.29}$$

(again assuming here, without loss of generality, that $\tilde{C}$ does not fall to zero upstream of $X = 1$). At $O(\varepsilon^0)$, we get $C^{(0)}_{xx} - \mathrm{Pe}\, C^{(0)}_x = 0$, $C^{(0)}|_{X=0} = 1$ and $C^{(0)}|_{X=1} = 0$. Thus $C^{(0)}(x, X) = \tilde{a}(X)\mathrm{e}^{Pe\, x} + \tilde{b}(X)$, $\tilde{a}, \tilde{b}$ being arbitrary constants of X. The first term must be suppressed to

avoid secular growth (since $x = \varepsilon^{-1} \to \infty$ as $\varepsilon \to 0$), so that again $C^{(0)} = C^{(0)}(X)$.

Collecting the terms in (3.4.29) at $O(\varepsilon)$, we obtain

$$C^{(1)}_{xx} - \mathrm{Pe}\, C^{(1)}_x = q_1(f(x) - F(X)), \quad \text{where} \quad q_1 F(X) \equiv -\mathrm{Pe}\, C^{(0)}_X . \tag{3.4.30}$$

This is to be solved between each two sinks ξ_i and ξ_{i+1} ($i = 0, \ldots, N$, taking again $\xi_0 = 0$ and $\xi_{N+1} = \varepsilon^{-1}$), subject to $C^{(1)} = 0$ at $x = 0$ and $x = \varepsilon^{-1}$. Thus

$$C^{(2)} = \tfrac{q_1}{\mathrm{Pe}} F(x - \xi_i) + \tilde{\alpha}_i \mathrm{e}^{\mathrm{Pe}(x - \xi_i)} + \tilde{\beta}_i, \quad \xi_i < x < \xi_{i+1} \text{ for } i = 0, \ldots, N, \tag{3.4.31}$$

with some $\tilde{\alpha}_i$, $\tilde{\beta}_i$ to be determined.

Integrating (3.4.30) across $x = \xi_i$ gives the balance of concentrations and fluxes: $C^{(1)}|_{\xi_i +} = C^{(1)}|_{\xi_i -}$ and $C^{(1)}_x|_{\xi_i +} - C^{(1)}_x|_{\xi_i -} = q_1$, which (using (3.4.31) for $\xi_i < x < \xi_{i+1}$ and $\xi_{i-1} < x < \xi_i$) allows us to obtain the following recurrence relations:

$$\alpha_i = \alpha_{i-1} \mathrm{e}^{\mathrm{Pe}\Delta_i} + \tfrac{q_1}{\mathrm{Pe}}, \tag{3.4.32a}$$

$$\beta_i = \beta_{i-1} + \tfrac{q_1}{\mathrm{Pe}}(F\,\Delta_i - 1), \tag{3.4.32b}$$

where $\Delta_i = \xi_i - \xi_{i-1}$, for $i = 1, 2, \ldots, N$.

Summing (3.4.32b), taking the product of (3.4.32a) for $j = 1, 2, \ldots, i$, and assuming that F is independent of i to leading order, we find

$$\alpha_i = \mathrm{e}^{\mathrm{Pe}\,\xi_i}\Big(\alpha_0 + \tfrac{q_1}{\mathrm{Pe}} \sum_{j=1}^{i} \mathrm{e}^{-\mathrm{Pe}\,\xi_j}\Big), \tag{3.4.33a}$$

$$\beta_i = \beta_0 + \tfrac{q_1}{\mathrm{Pe}}(F\,\xi_i - i), \tag{3.4.33b}$$

where we again used the identity $\sum_{j=1}^{i} \Delta_j \equiv \xi_i$.

We define

$$Q_i \equiv \sum_{j=1}^{i} \mathrm{e}^{-\mathrm{Pe}\,\xi_j} \tag{3.4.34}$$

and substitute (3.4.33) into (3.4.31) to find

$$C^{(1)} = \tfrac{q_1}{\mathrm{Pe}}(Fx - i) + \big(\tilde{\alpha}_0 + \tfrac{q_1}{\mathrm{Pe}} Q_i\big) \mathrm{e}^{\mathrm{Pe}\,x} + \tilde{\beta}_0 \quad \xi_i < x < \xi_{i+1},\ i = 0, \ldots, N. \tag{3.4.35}$$

Imposing $C^{(2)} = 0$ at $x = 0$ ($i = 0$) and $x = \varepsilon^{-1}$ ($i = N$) to satisfy the global boundary conditions, gives $\tilde{\alpha}_0 = -\tilde{\beta}_0 = -\frac{q_1}{\mathrm{Pe}}[F\varepsilon^{-1} - N + Q_N \mathrm{e}^{\mathrm{Pe}\,\varepsilon^{-1}}]/(\mathrm{e}^{\mathrm{Pe}\,\varepsilon^{-1}} - 1)$, and so, after some algebra, we obtain

$$C^{(1)} = \frac{q_1}{\mathrm{Pe}}\left[(Fx - i) - (F\varepsilon^{-1} - N)\frac{\mathrm{e}^{\mathrm{Pe}\,x} - 1}{\mathrm{e}^{\mathrm{Pe}/\varepsilon} - 1}\right] - \tag{3.4.36}$$

$$- \frac{q_1/Pe}{1 - \mathrm{e}^{-\mathrm{Pe}/\varepsilon}}\left[(\mathrm{e}^{\mathrm{Pe}\,x} - 1)\,Q_N - \mathrm{e}^{\mathrm{Pe}\,x}(1 - \mathrm{e}^{-\mathrm{Pe}/\varepsilon})\,Q_i\right], \quad \xi_i < x < \xi_{i+1},\ i = 0, \ldots, N.$$

This expression again relates solute fluctuations directly to sink distributions.

Analogously to Section 3.4.2, we observe that statistical properties of the correction $C^{(1)}$,

and thus homogenization residue $r^\varepsilon \approx C - C^{(1)}$, are entirely defined by the combination of exponential partial sums Q_i and Q_N in the second term of (3.4.36).

Therefore (setting $x = X/\varepsilon$) in (3.4.10), we have

$$C^{(1)} - \mathbb{E}[C^{(1)}] = -\frac{q_1/Pe}{1-e^{-Pe/\varepsilon}}\left[(e^{Pe\,X/\varepsilon}-1)\,\mathring{Q}_N - e^{Pe\,X/\varepsilon}(1-e^{-Pe/\varepsilon})\,\mathring{Q}_i\right], \qquad (3.4.37)$$

$$\mathring{Q}_i \equiv Q_i - \mathbb{E}[Q_i],\ i = 1,\dots,N.$$

Applying the definition of variance and transverse covariance (3.4.1) to (3.4.37), expanding and taking the expectation, we express $\mathbb{V}\mathrm{ar}[C^{(1)}]$ and $\mathbb{C}\mathrm{ov}_{\mathrm{T}}[C^{(1)}]$ in terms of the partial sums Q_i of a sink distribution ξ_i as follows:

$$\begin{aligned}\mathbb{V}\mathrm{ar}[C^{(1)}] &= \left(\frac{q_1/Pe}{1-e^{-Pe/\varepsilon}}\right)^2 \mathbb{E}\left[\left\{(e^{Pe\,X/\varepsilon}-1)\,\mathring{Q}_N - e^{Pe\,X/\varepsilon}(1-e^{-Pe/\varepsilon})\,\mathring{Q}_i\right\}^2\right] \\ &= \left(\frac{q_1/Pe}{1-e^{-Pe/\varepsilon}}\right)^2 \Big\{ \left(e^{Pe\,X/\varepsilon}-1\right)^2 \mathbb{V}\mathrm{ar}[Q_N] - \\ &\quad - 2e^{Pe\,X/\varepsilon}\left(e^{Pe\,X/\varepsilon}-1\right)\left(1-e^{-Pe/\varepsilon}\right)\mathbb{C}\mathrm{ov}(Q_i,Q_N) + e^{2Pe\,X/\varepsilon}\left(1-e^{-Pe/\varepsilon}\right)^2 \mathbb{V}\mathrm{ar}[Q_i]\Big\},\end{aligned} \qquad (3.4.38)$$

$$\begin{aligned}\mathbb{C}\mathrm{ov}_{\mathrm{T}}[C^{(1)}] &= \left(\frac{q_1}{\eta\,Pe}\right)^2 \mathbb{E}\Big[\left\{(e^{Pe\,X/\varepsilon}-1)\,\mathring{Q}_N - \eta\,e^{Pe\,X/\varepsilon}\,\mathring{Q}_i\right\} \\ &\qquad \left\{(e^{Pe\,(1-X)/\varepsilon}-1)\,\mathring{Q}_N - \eta\,e^{Pe\,(1-X)/\varepsilon}\,\mathring{Q}_{N-i}\right\}\Big] = \\ &= \left(\frac{q_1}{\eta\,Pe}\right)^2 \Big\{ \left(1 - e^{Pe\,X/\varepsilon} - e^{Pe\,(1-X)/\varepsilon} + e^{Pe/\varepsilon}\right)\mathbb{V}\mathrm{ar}[Q_N] + \\ &\quad + \eta\left(e^{Pe\,X/\varepsilon} - e^{Pe/\varepsilon}\right)\mathbb{C}\mathrm{ov}(Q_i,Q_N) + \eta\left(e^{Pe\,(1-X)/\varepsilon} - e^{Pe/\varepsilon}\right)\mathbb{C}\mathrm{ov}(Q_{N-i},Q_N) + \\ &\quad + \eta^2 e^{Pe/\varepsilon}\,\mathbb{C}\mathrm{ov}(Q_i,Q_{N-i})\Big\},\end{aligned} \qquad (3.4.39)$$

where $\eta = 1 - e^{-Pe/\varepsilon}$.

Our task once again is in finding the corresponding variances and covariances of the partial sum (3.4.34) for a specific sink distribution.

The normally-perturbed sink distribution

Consider $f = f_n$, then, for $\sigma_0 \equiv \sigma/\varepsilon$, we have $\xi_i \sim \mathcal{N}(i,\sigma_0^2)$ $(\mathbb{E}[\xi_i] \equiv \mu_i = i,\ \mathbb{V}\mathrm{ar}[\xi_i] = \sigma_0^2)$, $i = 1,\dots,N$.

Assuming small standard deviation $\sigma_0/\mu_i \ll 1$, we can find the corresponding expectation, variance and covariance for $g(\xi_i) = e^{-Pe\,\xi_i}$ by expanding it about the mean μ_i:

$$\mathbb{E}[g(\mu_i + (\xi_i - \mu_i))] \approx g_i + \tfrac{1}{2}\,g_i''\,\mathbb{V}\mathrm{ar}[\xi_i] + \tfrac{1}{24}\,g_i''''\,\mathbb{E}[(\xi_i-\mu_i)^4] + \dots, \quad g_i \equiv g(\mu_i)\,. \qquad (3.4.40)$$

For a normally distributed ξ_i with $\mathbb{E}[(\xi_i - \mu_i)^4] = 3\,\sigma_0^4$, (3.4.40) gives

$$\mathbb{E}[Q_i] \equiv \sum_{j=1}^{i} \mathbb{E}[g(\xi_j)] \approx \left[1 + \tfrac{1}{2}\,\mathrm{Pe}^2\sigma_0^2 + \tfrac{1}{8}\,\mathrm{Pe}^4\sigma_0^4\right] \sum_{j=1}^{i} \mathrm{e}^{-\mathrm{Pe}\,j} = \left[1 + \tfrac{\mathrm{Pe}^2\sigma_0^2}{2} + \tfrac{\mathrm{Pe}^4\sigma_0^4}{8}\right] \frac{1 - \mathrm{e}^{-\mathrm{Pe}\,i}}{\mathrm{e}^{\mathrm{Pe}} - 1}\,, \tag{3.4.41}$$

where we used the geometric progression $\sum_{j=1}^{n} s^j = s(s^n - 1)/(s - 1)$ to compute the sum.

Analogously

$$\mathbb{V}\mathrm{ar}[g(\xi_i)] \equiv \mathbb{E}[g(\xi_i)^2] - (\mathbb{E}[g(\xi_i)])^2 \approx (g_i')^2\,\mathbb{V}\mathrm{ar}[\xi_i] + \left(\tfrac{1}{3}\,g_i'\,g_i''' + \tfrac{1}{6}\,(g_i'')^2\right)\mathbb{E}[(\xi_i - \mu_i)^4]\,, \tag{3.4.42}$$

and since $\mathbb{V}\mathrm{ar}[Q_i] = \sum_{j=1}^{i}\sum_{k=1}^{i}\{\mathbb{E}[g(\xi_j)g(\xi_k)] - \mathbb{E}[g(\xi_j)]\,\mathbb{E}[g(\xi_k)]\} = \sum_{j=1}^{i}\mathbb{V}\mathrm{ar}[g(\xi_j)]$ due to the independence of ξ_j and ξ_k, i.e. $\mathbb{C}\mathrm{ov}(g(\xi_i), g(\xi_k)) = 0$, for $j \neq k$ and small σ_0, we get from (3.4.42) the variance

$$\mathbb{V}\mathrm{ar}[Q_i] \approx \mathrm{Pe}^2\sigma_0^2\left[1 + \tfrac{3}{2}\,\mathrm{Pe}^2\sigma_0^2\right] \sum_{j=1}^{i} \mathrm{e}^{-2Pe\,j} = \mathrm{Pe}^2\sigma_0^2\left[1 + \tfrac{3}{2}\,\mathrm{Pe}^2\sigma_0^2 + O(\sigma_0^4)\right] \frac{1 - \mathrm{e}^{-2\mathrm{Pe}\,i}}{\mathrm{e}^{2\mathrm{Pe}} - 1}\,. \tag{3.4.43}$$

It remains to find the covariance $\mathbb{C}\mathrm{ov}(Q_i, Q_k) = \mathbb{E}[Q_i Q_k] - \mathbb{E}[Q_i]\,\mathbb{E}[Q_k]$ for $i \neq k$. We denote $\mathring{g}_i \equiv g(\xi_i) - \mathbb{E}[g(\xi_i)]$, so that $\mathbb{E}[\mathring{g}_i] = 0$ and $\mathbb{E}[\mathring{g}_i^2] = \mathbb{V}\mathrm{ar}[g(\xi_i)]$. Then, for $i \leq k$,

$$\begin{aligned} \mathbb{C}\mathrm{ov}(Q_i, Q_k) &= \sum_{j=1}^{i}\sum_{l=1}^{k} \mathbb{E}[\mathring{g}_j\mathring{g}_l] = \sum_{j=1}^{i} \mathbb{E}[\mathring{g}_j^2] + \sum_{j=1}^{i}\sum_{\substack{l=1 \\ (l\neq j)}}^{k} \mathbb{E}[\mathring{g}_j\mathring{g}_l] = \\ &= \sum_{j=1}^{i} \mathbb{V}\mathrm{ar}[g(\xi_j)] + \sum_{j=1}^{i}\sum_{\substack{l=1 \\ (l\neq j)}}^{k} \mathbb{C}\mathrm{ov}(g(\xi_i), g(\xi_k))\,, \end{aligned} \tag{3.4.44}$$

with the first sum on the right-hand side of (3.4.44) being equal to (3.4.43) and the second sum vanishing due to the independence of $g(\xi_j)$ and $g(\xi_l)$, i.e. $\mathbb{C}\mathrm{ov}(g(\xi_i), g(\xi_k)) = 0$ $(j \neq l)$, for sufficiently small σ_0, providing the covariance

$$\mathbb{C}\mathrm{ov}(Q_i, Q_k) = \mathbb{V}\mathrm{ar}[Q_i] \approx \mathrm{Pe}^2\sigma_0^2\left[1 + \tfrac{3}{2}\,\mathrm{Pe}^2\sigma_0^2\right] \frac{1 - \mathrm{e}^{-2\mathrm{Pe}\,i}}{\mathrm{e}^{2\mathrm{Pe}} - 1}\,, \quad i \leq k\,. \tag{3.4.45}$$

Substituting (3.4.43), (3.4.45), $i \sim \varepsilon^{-1}X$ and $N \sim \varepsilon^{-1}$ into (3.4.38) and (3.4.39), after some algebra, we find

$$\mathbb{V}\mathrm{ar}[C^{(1)}] \approx 2\,\varepsilon^2\,q_1^2\,\sigma_0^2\,(1 + \tfrac{3}{2}\,\sigma_0^2\,\mathrm{Pe}^2)\,\frac{\left(\mathrm{e}^{\frac{\mathrm{Pe}}{\epsilon}X} + \mathrm{e}^{\frac{\mathrm{Pe}}{\epsilon}(1-X)} - \mathrm{e}^{\frac{\mathrm{Pe}}{\epsilon}(1+X)} - \mathrm{e}^{\frac{\mathrm{Pe}}{\epsilon}(2-X)} + \mathrm{e}^{2\frac{\mathrm{Pe}}{\epsilon}} - 1\right)}{\left(\mathrm{e}^{2\mathrm{Pe}} - 1\right)\left(\mathrm{e}^{\frac{\mathrm{Pe}}{\epsilon}} - 1\right)^2}\,, \tag{3.4.46}$$

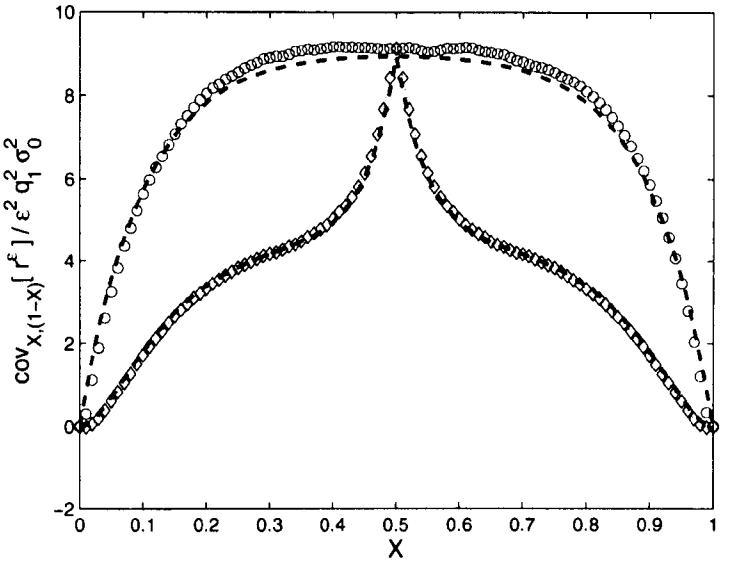

Figure 3.11. Monte-Carlo estimates of variance $\mathbb{V}\mathrm{ar}[r^\varepsilon]$ (blue circles) and transverse covariance $\mathbb{C}\mathrm{ov}(r^\varepsilon(X), r^\varepsilon(1-X))$ (black diamonds) for a normally-perturbed random process with $\sigma = 0.5\,\varepsilon$, computed for $\mathrm{Pe} = \varepsilon^{1/2}$, $q_1 \equiv \mathrm{Da}/(\varepsilon \mathrm{Pe}) = 1$, $\varepsilon = 0.01$, using 5×10^4 realisations; the dashed lines indicate the corresponding theoretical predictions (3.4.46) and (3.4.47). All data are scaled by $(\varepsilon\, q_1\, \sigma_0)^{-2}$.

$$\mathbb{C}\mathrm{ov}_{\mathrm{T}}[C^{(1)}] \approx \varepsilon^2\, q_1^2\, \sigma_0^2\, (1 + \tfrac{3}{2}\,\sigma_0^2\,\mathrm{Pe}^2)\, \left(\mathrm{e}^{2\mathrm{Pe}} - 1\right)^{-1} \left(\mathrm{e}^{\frac{\mathrm{Pe}}{\varepsilon}} - 1\right)^{-2} \left(2\mathrm{e}^{\frac{\mathrm{Pe}}{\varepsilon}X} + 2\mathrm{e}^{\frac{\mathrm{Pe}}{\varepsilon}(1-X)} + \right.$$

$$\left. + \mathrm{e}^{\frac{\mathrm{Pe}}{\varepsilon}2(1-X)} + \mathrm{e}^{\frac{\mathrm{Pe}}{\varepsilon}(1+2X)} - 2\mathrm{e}^{\frac{\mathrm{Pe}}{\varepsilon}(1+X)} - 2\mathrm{e}^{\frac{\mathrm{Pe}}{\varepsilon}(2-X)} - \mathrm{e}^{\frac{\mathrm{Pe}}{\varepsilon}(1-2X)} - \mathrm{e}^{\frac{\mathrm{Pe}}{\varepsilon}2X} + \mathrm{e}^{2\frac{\mathrm{Pe}}{\varepsilon}} - 1 \right),$$

$$0 \le X \le \tfrac{1}{2}, \tag{3.4.47}$$

where $\mathbb{C}\mathrm{ov}_{\mathrm{T}}[C^{(1)}]$ for $\frac{1}{2} < X \le 1$ corresponds to substituting X with $1 - X$ in (3.4.47), owing to the symmetry of the covariance.

By taking the limit of (3.4.46) and (3.4.47) for small $\mathrm{Pe} \ll O(\varepsilon)$, we find at leading order $\mathbb{V}\mathrm{ar}[C^{(1)}] \simeq \varepsilon^{-1}\, q_1^2\, \sigma^2\, X(1-X)$ and $\mathbb{C}\mathrm{ov}_{\mathrm{T}}[C^{(1)}] \simeq \varepsilon^{-1}\, q_1^2\, \sigma^2\, X^2$, which are identical to the variance (3.4.18) and transverse covariance (3.4.19) respectively (with $q_1 = \varepsilon\, q$).

Theoretical predictions (3.4.46), (3.4.47) agree very well with simulations at transient Péclet number $\mathrm{Pe} = \varepsilon^{1/2}$ ($O(\varepsilon) \ll \mathrm{Pe} \ll O(1)$), as shown in Figure 3.11; however, they differ by a factor of ca. 1.3 for $\mathrm{Pe} = O(1)$ (Fig. 3.9f), which can be attributed in part to neglecting the $O(\mathrm{Pe})$ terms, compared to the leading-order $O(\mathrm{Pe}/\varepsilon)$, in the exponents of (3.4.46) and (3.4.47).

In order to estimate the magnitude of the fluctuations, we take the Chebyshev norm $\|r^\varepsilon\|_C^2 \equiv \max_X \mathbb{V}\mathrm{ar}[r^\varepsilon] \approx \varepsilon \mathbb{V}\mathrm{ar}[C^{(1)}]|_{X=1/2}$ as a conservative measure (being an upper bound of the other norms defined in (2.6.1)). Then (3.4.46) gives (after some algebra)

$$\|r^\varepsilon\|_C^2 \approx \frac{2\,\varepsilon^4\, q_1^2\, \sigma_0^2\, (1 + \frac{3}{2}\,\sigma_0^2\,\mathrm{Pe}^2)}{\mathrm{e}^{2\mathrm{Pe}} - 1} \frac{1 - \mathrm{e}^{-\frac{1}{2}\frac{\mathrm{Pe}}{\varepsilon}}}{1 + \mathrm{e}^{-\frac{1}{2}\frac{\mathrm{Pe}}{\varepsilon}}}, \quad q_1 = \mathrm{Da}/\varepsilon\,. \tag{3.4.48}$$

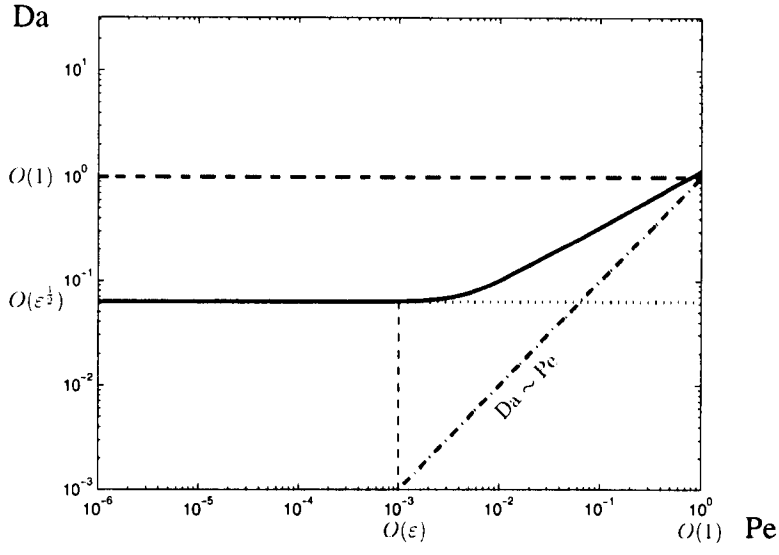

Figure 3.12. Approximate asymptotic upper bound (3.4.49) (solid) for the applicability of homogenization in the case of a normally-perturbed sink distribution (plotted for $\varepsilon = 0.001$, $\sigma_0 = \sigma/\varepsilon = 1$). The dashed and dash-dotted lines indicate the periodic (mean) upper bounds Da = 1 and Da = Pe respectively; the dotted line marks the theoretical upper bound Da = $2\varepsilon^{1/2}/\sigma_0$ of random fluctuations for small Péclet number.

When $\|r^\varepsilon\|_C = O(1)$, the homogenization fails, defining the critical Damköhler number

$$\mathrm{Da}_{\mathrm{cr}} \approx \left\{ \frac{\mathrm{e}^{2\mathrm{Pe}} - 1}{2\sigma_0^2\,(1 + \frac{3}{2}\sigma_0^2\,\mathrm{Pe}^2)} \, \frac{1 + \mathrm{e}^{-\frac{1}{2}\frac{\mathrm{Pe}}{\varepsilon}}}{1 - \mathrm{e}^{-\frac{1}{2}\frac{\mathrm{Pe}}{\varepsilon}}} \right\}^{1/2}, \tag{3.4.49}$$

which is plotted in Figure 3.12. We can therefore divide the (Pe, Da) parameter space into two regions: for $\mathrm{Pe} \lesssim O(\varepsilon)$, $\mathrm{Da}_{\mathrm{cr}} \simeq O(\sigma_0^{-1}\,\varepsilon^{1/2})$ and for $O(\varepsilon) \ll \mathrm{Pe} \ll O(1)$, $\mathrm{Da}_{\mathrm{cr}} \simeq O(\sigma_0^{-1}\,\sqrt{\mathrm{Pe}})$.

By repeating the calculations (3.4.40)–(3.4.43) up to $O(\sigma_0^6)$, taking into account that $1/\sqrt{2\pi}\int_{-\infty}^{\infty} t^6\,\mathrm{e}^{-t^2/2}dt = 15$ and hence $\mathbb{E}[(\xi_i - \mu_i)^6] = 15\,\sigma_0^6$, we find, after some algebra, that $\mathbb{V}\mathrm{ar}[Q_i] \sim \mathrm{Pe}^2\sigma_0^2\,[1 + \frac{3}{2}\,\mathrm{Pe}^2\sigma_0^2 + \frac{7}{6}\,\mathrm{Pe}^4\sigma_0^4 + O(\sigma_0^6)] \simeq \mathrm{e}^{\mathrm{Pe}^2\sigma_0^2}(\mathrm{e}^{\mathrm{Pe}^2\sigma_0^2} - 1)$, which is related to the variance of the log-normal distribution of $\mathrm{e}^{-\mathrm{Pe}\,\xi_i}$ [150]. Since this series becomes exponentially large for $\sigma_0\mathrm{Pe} > 1$, the approximation (3.4.48) is not applicable for large $\mathrm{Pe} \gg 1$. However, the simulations (see e.g. Fig. 3.5c) indicate that for a normally-perturbed array with small standard deviation σ_0, the stochastic part of the homogenization residue at large Péclet number becomes comparable or even less in magnitude than the deterministic (mean) part, leaving the upper bound $\mathrm{Da}_{\mathrm{cr}} \simeq O(\mathrm{Pe})$ of the periodic case unperturbed.

3.4.4 Correlation properties of the homogenization residue: Summary

In this Section, we have obtained and verified the theoretical predictions of Sections 3.4.2 and 3.4.3 for the diffusion-dominated case and for locally-balanced advection-diffusion ($\mathrm{Pe} \ll 1$ and $\mathrm{Pe} = O(1)$ respectively), and provided numerical estimates of the homogenization residue in the case of large local Péclet numbers ($\mathrm{Pe} \gg 1$).

Despite the fact that the individual sinks in all three considered random point processes

	$\mathcal{U}(0,1)$	Hard-core	$\mathcal{N}(i,\sigma_0^2)$	Periodic (mean)
$\mathrm{Pe} \ll 1$	$O(q\sqrt{\varepsilon})$	$O(q\sqrt{\varepsilon})$	$O(q\sigma_0\varepsilon^{3/2})$	$O(q\varepsilon^2)$
$\mathrm{Pe} \gtrsim 1$	$O(\frac{q_1}{\mathrm{Pe}}\sqrt{\varepsilon})$	$O(\frac{q_1}{\mathrm{Pe}}\sqrt{\varepsilon})$	$O(\frac{q_1}{\mathrm{Pe}}\sigma_0\varepsilon)$	$O(\frac{q_1}{\mathrm{Pe}}\varepsilon)$

Table 3.1. Asymptotic convergence rates of homogenization residue $\max_X |r^\varepsilon|$ or $\|r^\varepsilon\|_{L_2}$ for periodic and random arrays ($q = \mathrm{Da}/\varepsilon^2$, $q_1 = \mathrm{Da}/\varepsilon$, $\sigma_0 = \sigma/\varepsilon$). The estimates for $\mathrm{Pe} \ll 1$ are based on rigorous analytical results of Sec. 3.4.2; the estimates for $\mathrm{Pe} \gtrsim 1$ are suggested by the analysis of Sec. 3.4.3 and direct simulations (see Figs 3.5(a-c), 3.10(h,g) and 3.13(c,d)) and therefore remain a conjecture.

	$\mathcal{U}(0,1)$	Hard-core	$\mathcal{N}(i,\sigma_0^2)$	Periodic (mean)
$\mathrm{Pe} \ll 1$	$O(q\sqrt{\varepsilon})$	$O(q\sqrt{\varepsilon})$	$O(q\varepsilon)$	$O(q\varepsilon)$
$\mathrm{Pe} \gtrsim 1$	$O(\frac{q_1}{\mathrm{Pe}}\sqrt{\mathrm{Pe}})$	$O(\frac{q_1}{\mathrm{Pe}}\sqrt{\mathrm{Pe}})$	$O(\frac{q_1}{\mathrm{Pe}}\sqrt{\mathrm{Pe}})$	$O(\frac{q_1}{\mathrm{Pe}}\sqrt{\mathrm{Pe}})$

Table 3.2. Asymptotic convergence rates of homogenization residue in the Sobolev norm (mean-squared with the first derivative) $\|r^\varepsilon\|_{H^1}$ for periodic and random arrays. See also Table 3.1.

f_u, f_h and f_n appearing to be uncorrelated (see Sec. 3.2), the homogenization residue r^ε for uniformly-random and hard-core processes, as well as for normally-perturbed arrays with small Pe or large σ, exhibits distinctly long-range correlations (see Figs 3.6–3.10). Moreover, the amplitude of variations in the residue r^ε (as a random process) seems to be directly related to the degree of cross-correlations in r^ε, quantified by the transverse covariance.

We now combine the results to survey the accuracy of the stochastic homogenization in the (Pe, Da) parameter space.

3.5 Applicability and accuracy of homogenization on random arrays

Based on the analytical and numerical results of Sections 3.4.1, 3.4.2 and 3.4.3 we can generalise the error bounds of the solute transport homogenization (the magnitude of the residue r^ε), given in Sec. 2.6 of Chapter 2 for periodic arrays, to the case of disordered media. We also note that the fluctuations for f_n and f_u-distributed sinks (3.4.18) and (3.4.27) are polynomial in X and do not depend on the local coordinate x at leading order; therefore, $\mathbb{V}\mathrm{ar}[r^\varepsilon_X]$ has the same order of magnitude as $\mathbb{V}\mathrm{ar}[r^\varepsilon]$, facilitating the estimation of the strong norm $\|r^\varepsilon\|_{H^1}$. Tables 3.1 and 3.2 summarise the findings.

The regions of convergence for uniformly-random (f_u) or hard-core (f_h) sink distributions are illustrated in Figure 3.13(a) and the corresponding map for a normally-perturbed periodic array (f_n) is shown in Figure 3.13(b). The effect of the stochasticity on the convergence rates

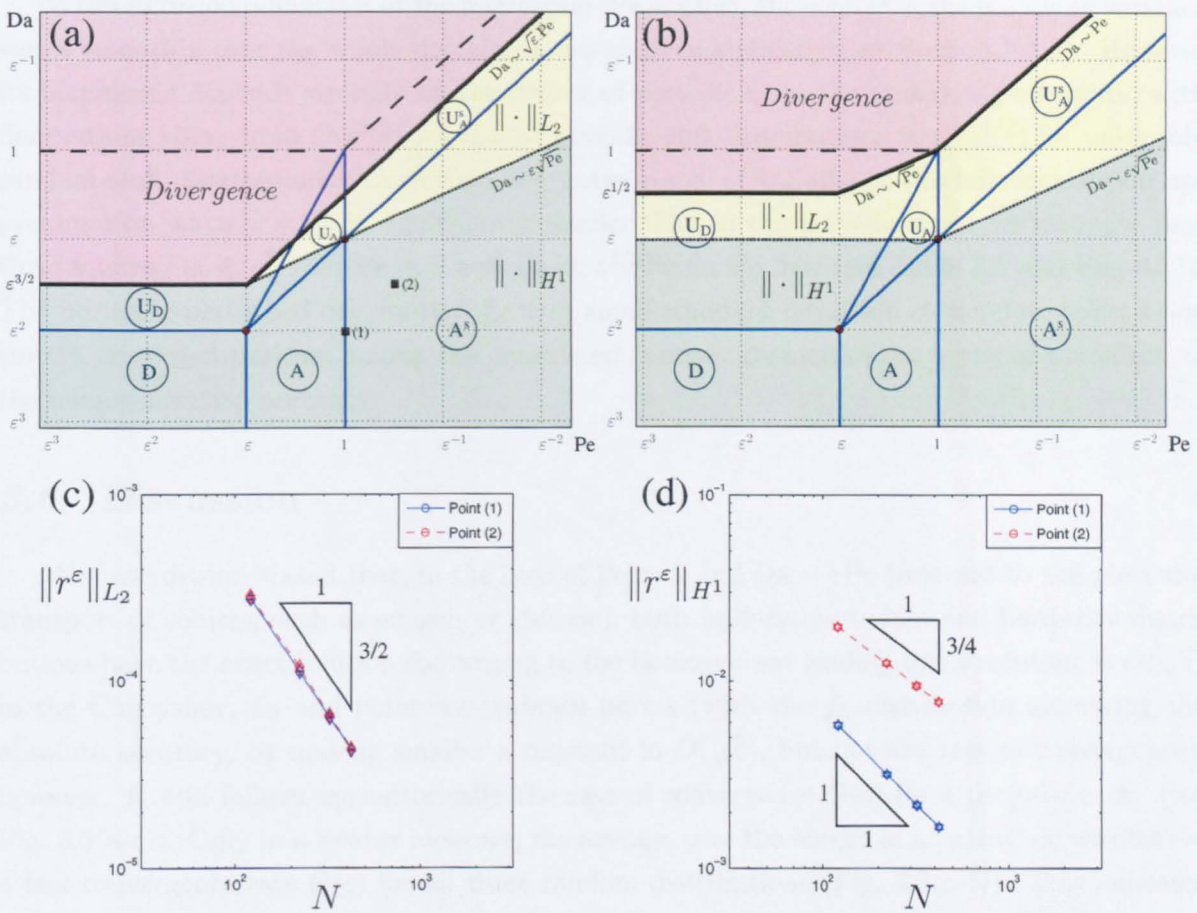

Figure 3.13. Types of convergence in (Pe, Da)-space for stochastic homogenization of solute transport with (a) uniformly random distributed sinks, and (b) normally-perturbed sinks (for $\sigma_0 = O(1)$). The region of "strong" convergence in the Sobolev (H^1) norm is shaded in green, the region of "weak" convergence in the mean-squared norm (L_2)-norm is shaded in yellow, and the region of global divergence (in L_2-norm) is shaded in red (plotted for $\varepsilon = 0.05$). The black dashed lines in (a,b) indicate the lower border of the divergence region in the case of a periodic array (see Fig. 2.2a). The convergence rates for the points (1) $\mathrm{Pe} = 1$, $\mathrm{Da} = \varepsilon^2$ (solid line) and (2) $\mathrm{Pe} = \varepsilon^{-1/2}$, $\mathrm{Da} = \varepsilon^{3/2}$ (dashed line) from the parameter space (a) are illustrated in panels (c,d) (ensemble average over 1000 samples for each N); triangles give a theoretical slope, in accord with Tables 3.1 and 3.2.

is the greatest for small Péclet number $\mathrm{Pe} \ll 1$, while the presence of strong advection seems to alleviate the damaging effect of fluctuations due to an irregular microstructure. Interestingly, in the case a uniformly random distribution (Fig. 3.13a) for $\mathrm{Pe} \ll O(\varepsilon)$, the magnitude of the fluctuations is such that the region of strong convergence (green; in $\|\cdot\|_{H^1}$) and the region of divergence (red) of the homogenization residue collapse to eliminate the transitional weak convergence region (yellow; in $\|\cdot\|_{L_2}$).

When diffusion dominates at the microscale ($\mathrm{Pe} = O(\varepsilon)$, $\mathrm{Da} = O(\varepsilon^2)$), the pointwise variance varies smoothly over the whole domain, as we show analytically (see Section 3.4.2). However its magnitude depends strongly on the degree of periodicity in the underlying structure, with fluctuations rising from $O(\varepsilon^{3/2})$ for almost periodic sink distributions to $O(\varepsilon^{1/2})$ for uniformly random sink distributions. Correspondingly, the range of validity of the homogenization approximation when $f = f_u$ is significantly smaller than in the periodic case: we estimate that this requires $\mathrm{Da} \ll \varepsilon^{3/2}$ for $\mathrm{Pe} \ll \varepsilon$ and $\mathrm{Da} \ll \varepsilon^{1/2}\mathrm{Pe}$ for $\mathrm{Pe} \gg \varepsilon$ (see Table 3.1 and Fig. 3.13). The normally-perturbed distribution f_n with small standard deviation σ therefore takes a distinctly privileged position among the considered random geometries, in terms of the effect on the homogenization accuracy.

3.6 Discussion

We have demonstrated that, in the case of $\mathrm{Pe} \gg 1$ and $\mathrm{Da} = \varepsilon\mathrm{Pe}$ (relevant to the placental transport of solutes, such as oxygen or glucose), both uniformly-random and hard-core distributions have the exact solution converging to the homogenized leading-order solution as $O(\sqrt{\varepsilon})$ in the Chebyshev, L_2 and pointwise-variance norms (with the f_h distribution increasing the absolute accuracy, by making smaller a constant in $O(\sqrt{\varepsilon})$, but not the rate of convergence); however, f_n still follows asymptotically the rate of convergence $O(\varepsilon)$ for a periodic array (see Fig. 3.5(a-c)). Only in a weaker measure, the average over the length of an array, do we observe a fast convergence rate $O(\varepsilon)$ for all three random distributions (Fig. 3.5(d-f)). This indicates the robustness of the homogenization technique for periodic arrays and guarantees higher accuracy for a dense sorbing medium with underlying regularity than for an intrinsically random microstructure.

Even though the Matérn hard-core process (with $d = 0.65\varepsilon$; Fig. 3.2b) appears closer to the regular array than the normal perturbations (with $\sigma = 10\varepsilon$; Fig. 3.2c) for $N = 49$, the solution on a hard-core-distributed array converges slower to $C^{(0)}$ than on a normally-perturbed array for sufficiently large N (small ε). This apparent difference in the convergence properties is explained by the lower degree of long-range correlations between unit cells for the normal perturbations (*cf.* panels (e) and (f) in Fig. 3.10), since each sink in f_n, for small σ, is expected to be displaced symmetrically and independently about its position in a regular array. However, the homogenization error for a normally-perturbed array quickly ceases to exhibit its unique properties as sink fluctuations increase, becoming essentially indistinguishable from the residue for a uniformly-random array when $\sigma \gtrsim 0.3$, i.e. for fluctuations over a third of the whole domain (see Fig. 3.10h).

We also remark on the clustering phenomenon occurring in a uniformly-random distribution

(or in normal perturbations for large σ) (as can be seen in Fig. 3.2a) that significantly contributes to the deviation of the exact solution from a homogenized one. The presence of clusters can be treated asymptotically either by considering an array of sinks of varying strength (e.g. alternating q and $2q$) with larger inter-sink distance, or by introducing a third lengthscale for inter-cluster spacing ε_1, intermediate between the regular microscale ε and the global scale 1 ($\varepsilon \ll \varepsilon_1 \ll 1$), and then performing reiterated homogenization [34].

Our analysis of the fluctuations of the homogenization residue in this chapter extends the upper bounds for applicability of homogenization from the periodic arrays (Fig. 2.2a) to the random sink distributions (Fig. 3.13(a,b)). Although the homogenized leading-order concentration profile is asymptotically applicable to a wide range of stationary random sink distributions, we observe a pronounced shrinkage of the convergence region in the (Pe, Da)-parameter space (Fig. 3.13), especially for small Péclet number. This suggests that corrections to the leading-order approximation cannot be neglected even when the exact solution is sufficiently "smooth".

We can compare our analytical and numerical predictions with existing theoretical results for random homogenization of the problems similar to (3.2.1) that take into account the spatial autocorrelation properties of coefficients of corresponding governing equations. Bourgeat and Piatnitski [47] show in their Lemma 4.2 that the homogenization error of a one-dimensional diffusion-reaction equation (without advective transport) is $\mathbb{E}[\max_X |r^\varepsilon(X)|^2]^{1/2} \leq O(\sqrt{\varepsilon})$ when the diffusion coefficient is a stationary random process with "short-term memory" ($\alpha > 1$ for the corresponding autocorrelation function (3.2.2)), and $\mathbb{E}[\max_X |r^\varepsilon|^2]^{1/2} \leq O(\varepsilon^{\alpha/2})$ for a "long-term memory" coefficient ($0 < \alpha < 1$). Bal and Jing [22] generalise these results for a linear transport-attenuation-scattering equation in two and three dimensions and show that when the equation coefficients are bounded functions of a Poisson point process (with short-term memory, $\alpha > 1$), the following estimate holds: $\mathbb{E}[\|r^\varepsilon\|_{L_2}^2]^{1/2} \leq O(\sqrt{\varepsilon})$. Since the source term in (3.2.1), defined by a sink distribution, is a short-term-memory stationary process (see Figs 3.3 and 3.4), one might expect similar upper bound on the residue r^ε being applicable. We indeed observe that the homogenization error for all three stochastic sink distributions (f_u, f_h and f_n) are bounded by $O(\sqrt{\varepsilon})$ for $\mathrm{Pe} \gtrsim 1$, $\mathrm{Da} = O(\varepsilon \mathrm{Pe})$ (Fig. 3.5(a-c)). This upper bound is exact for a uniformly-random or hard-core distributions; however, it considerably overestimates the error in the case of a normally-perturbed sink distribution (which can be as low as $O(\varepsilon)$ for this parameter regime), highlighting the importance of direct distribution-specific error estimation.

To sum up, the magnitude of the difference between the homogenization approximation and the exact solution depends on how one chooses to measure it. In a weak (L_2) norm, the residue with a periodic sink distribution is typically $O(\varepsilon)$ (for example for $\mathrm{Pe} = O(1)$, $\mathrm{Da} = O(\varepsilon)$), falling to $O(\varepsilon^2)$ at sufficiently low Pe and Da. However when sinks have a uniformly random distribution, the residue (in the appropriate norm) rises to $O(\varepsilon^{1/2})$ in both cases ((3.4.27), Figure 3.10(a,b)). The magnitude of the residue falls for distributions with a greater degree of periodicity ((3.4.18), Figure 3.10(g,h)) but grows with increasing sink strength. Significantly, even when sink distributions are correlated only over short distances, the residues appear to be correlated over distances comparable with the domain size when advection dominates at the macroscale (Figure 3.10(d,e,f)). This is also the case when diffusion dominates at the microscale, as revealed by estimates of the transverse covariance (Figs 3.6(c)–3.8(c)). One can estimate ε

crudely to be between 0.001 and 0.01 (taking the overall size of the placentone ~ 1 cm and the size of an individual villous branch $\sim 10 - 100$ μm [33]), suggesting errors in homogenization approximations due to stochasticity of up to 10% that fluctuate across distances comparable to an individual placental lobule.

We will further analyse the impact of the findings of this chapter by identifying which, if any, of the three random distributions (f_u, f_h, f_n) describes the villous pattern of the normal human placenta. However, since the histological images are two-dimensional (see Fig 1.1b), we first need to extend some of the results to the case of two spatial dimensions.

IV Homogenization of Flow and Transport in Two Dimensions and Non-linear Effects

4.1 Introduction

Many physiological systems involve phenomena at different spatial scales. One of the examples is the human placenta, whose tortuous villous structure provides an interface of the feto-maternal exchange with enormous surface area per unit volume (of the order of 10 m^2 for the whole mature placenta) [33] (see Figs 1.1 and 1.3 of Chapter 1). In addition to the geometrical complexity, we need to take into account the microscopic nonlinear effects of solute carriers, such as haemoglobin, on transport at the macroscale.

In order to understand the impact of these effects, while preserving the essential information about the structure and physico-chemical processes at the microscale, we again adopt a homogenization technique to generalise the models studied in Chapter 2.

The aim of this Chapter is to derive the effective description of advective-diffusive solute transport in a flow orthogonal to an array of sorbing cylinders with nonlinear dissociation kinetics, mimicking solute transport in the intervillous space (Fig. 4.1).

Apart from placental transport, potential applications of these models include gas exchange

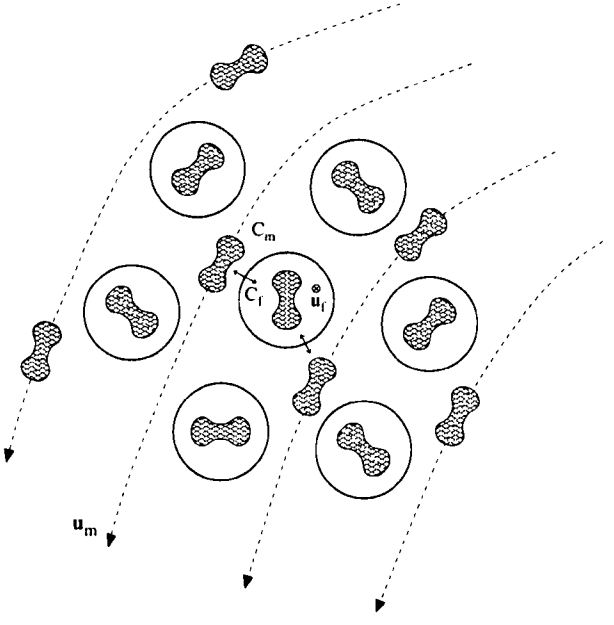

Figure 4.1. A schematic diagram of flow in the intervillous space, facilitated by the solute carriers ($\mathbf{u}_m$, $\mathbf{u}_f$ and C_m, C_f denotes the maternal/fetal fluid velocities and concentrations respectively).

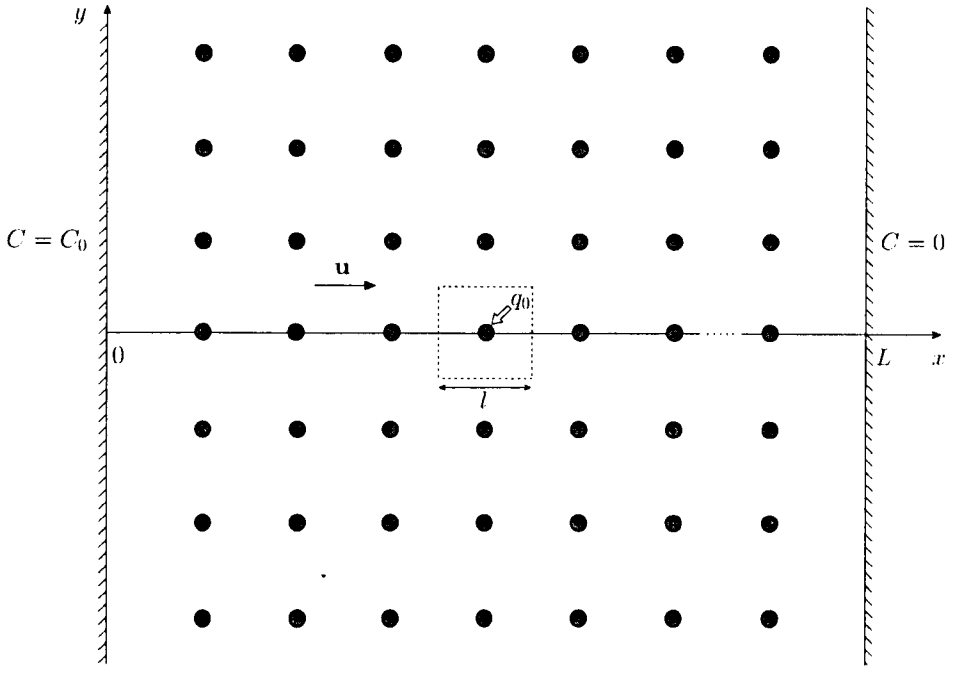

Figure 4.2. The model geometry.

in a capillary network [271], solute transport in certain bioreactors [1], dialysis machines [118] and other artificial organs [145]. The role of erythrocytes as oxygen carriers can be shared in full or in part by artificial blood substitutes [141].

4.2 Advection-diffusion in an array of point sinks

We start by considering a model for a square-periodic array of point sinks (see Fig. 4.2), extending the problem (2.2.1) studied in Chapter 2 to two dimensions.

Although Hasimoto and others [112, 229] have shown that the local flow past cylinders of vanishing radius retains the spatial dependence due to logarithmic singularities, we assume a uniform flow past the array, which will be justified later in Section 4.3.4, at leading order, for averaged solute transport in an array of cylinders, taking the limit of their radii tending to zero.

4.2.1 Problem statement

Let steady advection-diffusion in a two-dimensional array ($L \times L$) of N^2 point sinks be subjected to a horizontal inlet flow of given velocity u_0 and solute concentration C_0:

$$u_0 \frac{\partial C^*}{\partial x^*} = D\left(\frac{\partial^2 C^*}{\partial x^{*2}} + \frac{\partial^2 C^*}{\partial y^{*2}}\right) - q_0 l \sum_{i,j=1}^{N} \delta(x^* - x_i^*)\,\delta(y^* - y_j^*), \tag{4.2.1a}$$

$$0 < x^* < L,\ 0 < y^* < L,$$

$$C^*|_{x^*=0} = C_0, \tag{4.2.1b}$$

$$C^*|_{x^*=L} = 0 \quad \text{or} \quad C^*|_{x^*=x_0^*} = \left.\frac{\partial C^*}{\partial x^*}\right|_{x^*=x_0^*} = 0, \quad \text{for} \quad 0 < x_0^* \le L, \tag{4.2.1c}$$

$$C^*|_{y^*=0} = C^*|_{y^*=L}, \quad \left.\frac{\partial C^*}{\partial y^*}\right|_{y^*=0} = \left.\frac{\partial C^*}{\partial y^*}\right|_{y^*=L}, \quad \text{(periodicity)} \tag{4.2.1d}$$

where D is the molecular diffusion coefficient, q_0 is the solute uptake rate (flux density per unit cell, in $[\,\mathrm{mol}/(\mathrm{m}^2 \cdot \mathrm{s})\,]$), l is the inter-sink distance, $x_i^* = il$, $y_j^* = jl$ $(i,j = 1,\ldots,N)$ are positions of the sinks in a square array (see Fig. 4.2), and $x_0^* = x_0^*(y^*)$ defines an internal free boundary for a sufficiently strong uptake.

In dimensionless variables $C^* = C_0\,C$, $x^* = l\,x$, $y^* = l\,y$, (4.2.1) takes the form

$$\mathrm{Pe}\,\frac{\partial C}{\partial x} = \frac{\partial^2 C}{\partial x^2} + \frac{\partial^2 C}{\partial y^2} - \mathrm{Da}\sum_{i,j=1}^{N}\delta(x-x_i)\,\delta(y-y_j), \quad 0 < x < \varepsilon^{-1},\ 0 < y < \varepsilon^{-1} \tag{4.2.2a}$$

$$C|_{x=0} = 1, \tag{4.2.2b}$$

$$C|_{x=\varepsilon^{-1}} = 0 \quad \text{or} \quad C|_{x=x_0} = \left.\frac{\partial C}{\partial x}\right|_{x=x_0} = 0\,, \quad \text{for} \quad 0 < x_0 \le \varepsilon^{-1}, \tag{4.2.2c}$$

$$C|_{y=0} = C|_{y=\varepsilon^{-1}}, \quad \left.\frac{\partial C}{\partial y}\right|_{y=0} = \left.\frac{\partial C}{\partial y}\right|_{y=\varepsilon^{-1}}, \tag{4.2.2d}$$

where $\varepsilon = l/L$, $\mathrm{Pe} = u_0\,l/D$ is a local Péclet number and $\mathrm{Da} = q_0\,l/(D\,C_0)$ is a local Damköhler number.

4.2.2 Small microscopic Péclet number transport regime

Let $\mathrm{Pe} = O(\varepsilon) = \varepsilon\,p$, $\mathrm{Da} = O(\varepsilon^2) = \varepsilon^2\,q$ $(p,q = O(1))$, representing the global advective-diffusive-uptake flux balance, analogous to (2.2.6) of Chapter 2.

Analogous to the one-dimensional case, we look for an approximate solution to (4.2.2) in the form of two-scale asymptotic power series

$$C(x,y) = \tilde{C}(x,y,X,Y) = C^{(0)}(x,y,X,Y) + \varepsilon\,C^{(1)}(x,y,X,Y) + \varepsilon^2\,C^{(2)}(x,y,X,Y) + \ldots\,, \tag{4.2.3}$$

with slowly varying global coordinates $X = \varepsilon x$, $Y = \varepsilon y$.

Substituting (4.2.3) into (4.2.2) and collecting the terms at powers of ε, we get at $O(1)$:

$$C^{(0)}_{xx} + C^{(0)}_{yy} = 0\,, \quad -1/2 < x,y < 1/2,\ 0 < X,Y < 1\,, \tag{4.2.4a}$$

$$C^{(0)}|_{X=0} = 1\,, \quad C^{(0)}|_{X=1} = 0 \ \text{ or } \ C^{(0)}|_{X=X_0} = C^{(0)}_X|_{X=X_0} = 0\,; \tag{4.2.4b}$$

$$C^{(0)}|_{Y=0} = C^{(0)}|_{Y=1}, \quad C^{(0)}_Y|_{Y=0} = C^{(0)}_Y|_{Y=1}\,, \tag{4.2.4c}$$

which implies independence of the leading-order solution on the local (microscopic) coordinates:

$$C^{(0)} = C^{(0)}(X,Y)\,. \tag{4.2.5}$$

Collecting the terms at $O(\varepsilon)$ and taking into account (4.2.5), we have

$$C^{(1)}_{xx} + C^{(1)}_{yy} = 0\,, \quad -1/2 < x,y < 1/2,\ 0 < X,Y < 1\,, \tag{4.2.6a}$$

$$C^{(1)}|_{X=0} = C^{(1)}|_{X=1} = 0\,, \tag{4.2.6b}$$

$$C^{(1)}|_{Y=0} = C^{(1)}|_{Y=1}, \quad C^{(1)}_y|_{Y=0} = C^{(1)}_y|_{Y=1}\,, \tag{4.2.6c}$$

leading to

$$C^{(1)} \equiv 0\,. \tag{4.2.7}$$

Collecting the terms at $O(\varepsilon^2)$, accounting for (4.2.5) and (4.2.7), we get

$$C^{(0)}_{XX} + C^{(0)}_{YY} - p\,C^{(0)}_X = q \sum_{i,j=1}^{N} \delta(x - x_i)\,\delta(y - y_j) - (C^{(2)}_{xx} + C^{(2)}_{yy})\,, \tag{4.2.8a}$$

$$C^{(2)}|_{X=0} = C^{(2)}|_{X=1} = 0\,, \tag{4.2.8b}$$

$$C^{(2)}|_{Y=0} = C^{(2)}|_{Y=1}, \quad C^{(2)}_y|_{Y=0} = C^{(2)}_y|_{Y=1}\,. \tag{4.2.8c}$$

Integrating (4.2.8) over the unit cell ($x_i - \frac{1}{2} \le x \le x_i + \frac{1}{2}$, $y_j - \frac{1}{2} \le y \le y_j + \frac{1}{2}$), we obtain

$$C^{(0)}_{XX} + C^{(0)}_{YY} - p\,C^{(0)}_X = q - \int_{y_j-1/2}^{y_j+1/2} \underbrace{\left(C^{(2)}_x|_{x=\frac{1}{2}} - C^{(2)}_x|_{x=-\frac{1}{2}}\right)}_{=0} \mathrm{d}y - \int_{x_i-1/2}^{x_i+1/2} \underbrace{\left(C^{(2)}_y|_{y=\frac{1}{2}} - C^{(2)}_y|_{y=-\frac{1}{2}}\right)}_{=0} \mathrm{d}x\,, \tag{4.2.9}$$

which, due to the periodicity assumption for $C^{(2)}$, reduces to

$$C^{(0)}_{XX} + C^{(0)}_{YY} - p\,C^{(0)}_X = q\,. \tag{4.2.10}$$

Equation (4.2.10), together with the Y-periodic boundary conditions (4.2.4c), implies that[1]

$$C^{(0)} = C^{(0)}(X)\,, \tag{4.2.11}$$

and the averaged leading-order concentration field therefore obeys

$$C^{(0)}_{XX} - p\,C^{(0)}_X = q\,, \tag{4.2.12a}$$

$$C^{(0)}|_{X=0} = 1\,, \quad C^{(0)}|_{X=1} = 0 \quad \text{or} \quad C^{(0)}|_{X=X_0} = C^{(0)}_X|_{X=X_0} = 0\,, \tag{4.2.12b}$$

that is identical to the leading-order problem (2.3.8) for advection-diffusion in a one-dimensional array of sinks. The corresponding distinct asymptotic forms of the solution to (4.2.12) are plotted in Fig. 2.2(b).

We now consider cell problems to find the first non-vanishing correction to the leading order solution.

Substituting (4.2.10) in (4.2.8), we can write the problem for a single unit cell:

$$C^{(2)}_{xx} + C^{(2)}_{yy} = q\,\delta(x)\,\delta(y) - q\,, \tag{4.2.13a}$$

$$C^{(2)} \text{ is } x,y\text{-periodic in a unit cell}, \tag{4.2.13b}$$

$$C^{(2)}|_{X=0} = C^{(2)}|_{X=1} = 0\,, \tag{4.2.13c}$$

$$C^{(2)}|_{Y=0} = C^{(2)}|_{Y=1}, \quad C^{(2)}_y|_{Y=0} = C^{(2)}_y|_{Y=1}\,, \tag{4.2.13d}$$

where we translated the local coordinates to the centre of the unit cell by $x' = x - x_i$, $y' = y - y_j$ (primes over the variables are dropped).

[1] A (Y-periodic and bounded) solution to (4.2.10) can be sought in the form $C^{(0)} = g_1(X) + g_2(X,Y)$, where g_1 satisfies (4.2.12) and g_2 is a trivial (constant) solution to the corresponding homogeneous problem.

Since $G_\infty = \frac{1}{2\pi} \ln \sqrt{x^2+y^2}$ is the 2D fundamental solution of $\nabla^2 G_\infty = \delta(x)\delta(y)$ in $\mathbb{R}^2$, the corresponding cell solution, satisfying the no-flux symmetry boundary conditions is $G(x,y) = \sum_{i,j=-\infty}^{\infty} G_\infty(x-i, y-j)$, in accord with an infinite system of images for the sink in the middle of a unit cell ($x = y = 0$).

Therefore the solution to (4.2.13) is

$$C^{(2)}(x,y) \approx -\frac{q}{2}\left(\sum_{i,j=-m}^{m} -\tfrac{1}{\pi} \ln\sqrt{(x-i)^2+(y-j)^2} + \tfrac{1}{2}(x^2+y^2)\right) + \tilde{C}^{(2)}, \quad -\tfrac{1}{2} \le x, y \le \tfrac{1}{2}, \tag{4.2.14}$$

where $m \gg 1$ is the number of the images for the fundamental solution (Neumann Green's function), and $\tilde{C}^{(2)}$ is a constant dependent on m and the global boundary conditions. Correction (4.2.14) generalises one-dimensional diffusion-dominated solute transport (2.3.12) $C^{(2)}(x) = -\frac{q}{2}\left(-|x| + x^2 + \frac{1}{6}\right) + \langle C^{(2)} \rangle$ to the case of two dimensions.

Numerical simulation of the original problem (4.2.2) is performed using a Finite Element-based solver of `COMSOL Multiphysics`. The problem, in the framework of the Finite Element Method, is approximated using a discretised weak formulation, multiplying equations and boundary conditions by an appropriate piecewise-polynomial test function C_{test} and integrating over the entire domain or its boundary respectively (a second-order basis function, giving a piecewise-quadratic test function, is used in simulations). Each point sink therefore reduces to a prescribed value $\int \delta(x-x_i)\delta(y-y_j) C_{\text{test}}\, dx\, dy = C_{\text{test}}(x_i, y_j)$ over the corresponding finite element of the mesh. The mesh convergence is tested by successive refinements and by comparing against the analytical solution.

The analytical solution (4.2.14) is compared to simulations performed for a square array of 19×19 sinks, using ca. 300,000 finite elements (the absolute inaccuracy is less than 10^{-3} in the Chebyshev $\|\cdot\|_{\max}$ norm and less than 10^{-5} in the L_2-norm), as shown in Figure 4.3 for $\tilde{C}^{(2)} = -139.081$, $m = 10$, and demonstrates a good agreement. Although the average of the partial sum in (4.2.14) grows with m, it can be renormalised by subtracting an appropriate constant $\tilde{C}^{(2)}$, and the accuracy rapidly saturates with increasing m. For example, for $m = 0$ ($\text{Pe} = \varepsilon$, $\text{Da} = \varepsilon\text{Pe}$, $\varepsilon = 0.05$), the absolute inaccuracy between the numerical and analytical correction $C^{(2)}$ is about 0.01, while for $m = 5$ the difference is less than 0.001. Figure 4.3(b,d) also shows how the average of the residue $r^\varepsilon = C - C^{(0)}$ depends on the vertical position y_0 within the unit cell, due to the uniform global boundary conditions at $X = 0; 1$.

We observe that the microscopic correction $C^{(2)}$ becomes $O(\varepsilon^{-1})$ when $q = \text{Da}/\varepsilon^2 = O(\varepsilon^{-1})$ ($\text{Da} = O(\varepsilon)$), suggesting another asymptotic regime at $\text{Pe} = O(1)$, $\text{Da} = O(1)$, analogous to Section 2.3.

4.2.3 Regime of moderate microscopic Péclet number

Let $\text{Pe} = O(1)$, $\text{Da} = O(\varepsilon) = \varepsilon\, q_1$ ($q_1 = O(1)$).

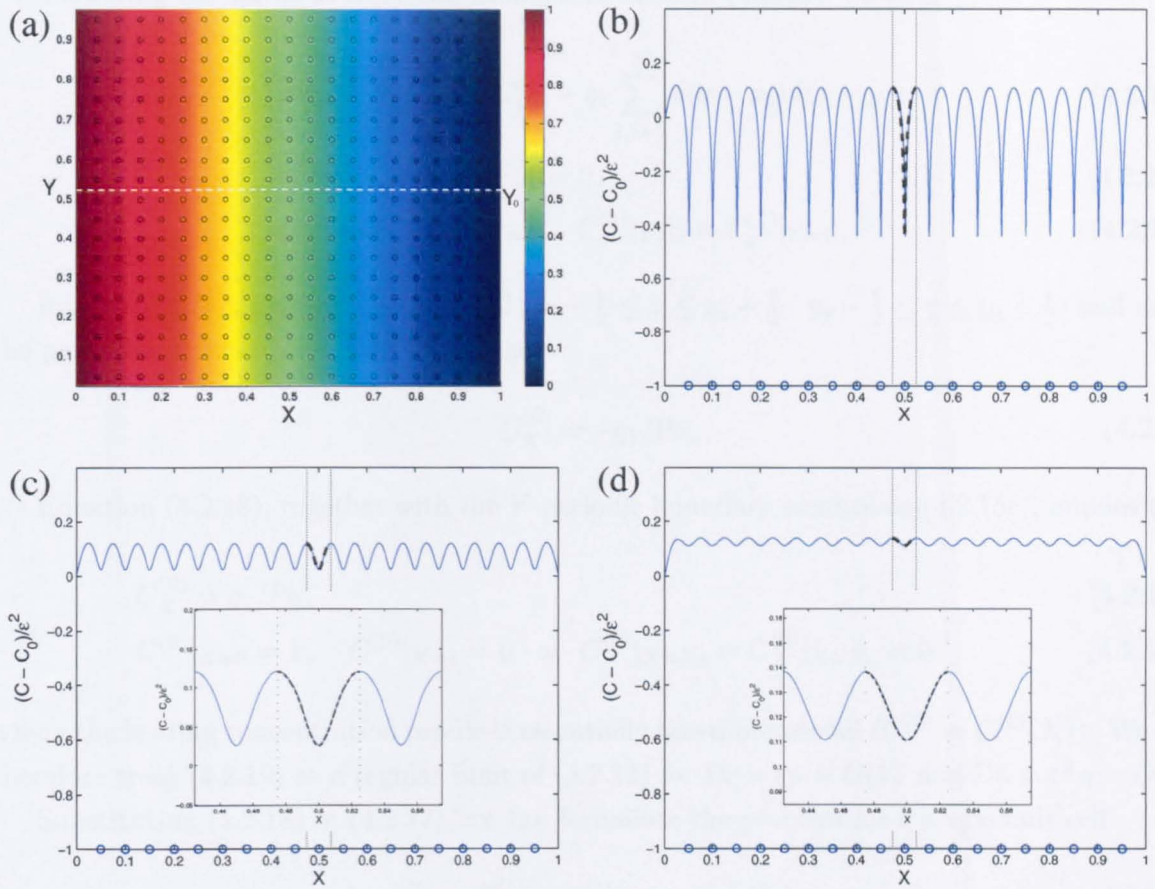

Figure 4.3. Comparison of analytical and numerical solutions to (4.2.2) (a) Numerical solution C (colours) for $\mathrm{Pe} = \varepsilon$, $\mathrm{Da} = \varepsilon\mathrm{Pe}$ in a square array of $N \times N$ point sinks ($N = 19$, $\varepsilon = 0.05$); black circles indicate the sinks' position. (b-d) Correction $C^{(2)} = C - (1 - X)$ scaled by ε^{-2} plotted in a cross-section at $y_0 = 0.01$ (b), $y_0 = 0.2$ (c), $y_0 = 0.5$ (d) in local coordinates ($Y_0 = 0.5 + \varepsilon\, y_0$, indicated by a dashed line in (a)); numerical solution is shown in solid blue and analytical solution (4.2.14) is given in dashed black; the boundaries of a single unit cell are indicated by dotted lines.

Substituting (4.2.3) into (4.2.2) and collecting the terms at powers of ε, we get at $O(1)$:

$$\mathrm{Pe}\, C^{(0)}_x = C^{(0)}_{xx} + C^{(0)}_{yy}\,, \qquad -1/2 < x, y < 1/2,\ 0 < X, Y < 1\,, \tag{4.2.15a}$$

$$C^{(0)}|_{X=0} = 1\,, \quad C^{(0)}|_{X=1} = 0 \ \text{ or } \ C^{(0)}|_{X=X_0} = C^{(0)}_X|_{X=X_0} = 0\,; \tag{4.2.15b}$$

$$C^{(0)}|_{Y=0} = C^{(0)}|_{Y=1}, \quad C^{(0)}_y|_{Y=0} = C^{(0)}_y|_{Y=1}\,, \tag{4.2.15c}$$

which implies independence of the leading-order solution on the local (microscopic) coordinates:

$$C^{(0)} = C^{(0)}(X, Y)\,. \tag{4.2.16}$$

Collecting the terms at $O(\varepsilon)$ and taking into account (4.2.16), we have

$$\mathrm{Pe}\, C_X^{(0)} = C_{xx}^{(1)} + C_{yy}^{(1)} - q_1 \sum_{i,j=1}^{N} \delta(x - x_i)\, \delta(y - y_j)\,, \tag{4.2.17a}$$

$$C^{(1)}|_{X=0} = C^{(1)}|_{X=1} = 0\,, \tag{4.2.17b}$$

$$C^{(1)}|_{Y=0} = C^{(1)}|_{Y=1}, \quad C_y^{(1)}|_{Y=0} = C_y^{(1)}|_{Y=1}\,, \tag{4.2.17c}$$

Integrating (4.2.17) over the unit cell $(x_i - \frac{1}{2} \le x \le x_i + \frac{1}{2},\ y_j - \frac{1}{2} \le y \le y_j + \frac{1}{2})$ and using the periodicity assumption for $C^{(1)}$, we get

$$C_X^{(0)} = -q_1/\mathrm{Pe}\,, \tag{4.2.18}$$

Equation (4.2.18), together with the Y-periodic boundary conditions (4.2.15c), implies that

$$C_X^{(0)} = q_1/\mathrm{Pe}\,, \tag{4.2.19a}$$

$$C^{(0)}|_{X=0} = 1\,, \quad C^{(0)}|_{X=1} = 0 \ \text{ or } \ C^{(0)}|_{X=X_0} = C_X^{(0)}|_{X=X_0} = 0\,, \tag{4.2.19b}$$

where the leading concentration profile is essentially one-dimensional ($C^{(0)} = C^{(0)}(X)$). We can therefore treat (4.2.19) as a regular limit of (4.2.12) for $\mathrm{Pe} = \varepsilon p = O(1)$ and $\mathrm{Da} = \varepsilon^2 q = O(\varepsilon)$.

Substituting (4.2.18) in (4.2.17), we can formulate the problem for a single unit cell

$$-\mathrm{Pe}\, C_x^{(1)} + C_{xx}^{(1)} + C_{yy}^{(1)} = q_1\, \delta(x)\, \delta(y) - q_1\,, \tag{4.2.20a}$$

$$C^{(1)} \text{ is } x,y\text{-periodic in a unit cell,} \tag{4.2.20b}$$

$$C^{(1)}|_{X=0} = C^{(1)}|_{X=1} = 0\,, \tag{4.2.20c}$$

$$C^{(1)}|_{Y=0} = C^{(1)}|_{Y=1}, \quad C_y^{(1)}|_{Y=0} = C_y^{(1)}|_{Y=1}\,, \tag{4.2.20d}$$

where we translated the local coordinates to the centre of the unit cell by $x' = x - x_i$, $y' = y - y_j$ (primes over the variables are dropped).

Following [247], we look for a fundamental solution G of 2D advection-diffusion differential operator

$$-\mathrm{Pe}\frac{\partial G}{\partial x} + \nabla^2 G = \delta(x)\delta(y)\,, \quad (x,y) \in \mathbb{R}^2 \tag{4.2.21}$$

in the form $G(x,y) = \mathrm{e}^{\frac{\mathrm{Pe}}{2}x}\, g(x,y)$, which (according to the property $\mathrm{e}^{-\mathrm{Pe}\,x}\delta(x) = \delta(x)$) transforms (4.2.21) into a fundamental problem for the Helmholtz-type operator:

$$\nabla^2 g - \tfrac{\mathrm{Pe}^2}{4}\, g = \delta(x)\delta(y)\,, \quad (x,y) \in \mathbb{R}^2\,, \tag{4.2.22}$$

which has a solution $g = -\frac{1}{2\pi} K_0\big(\frac{\mathrm{Pe}}{2}\sqrt{x^2+y^2}\big)$.

Therefore, the fundamental solution to the advection-diffusion operator (4.2.21) in $\mathbb{R}^2$ is

$$G_\infty = -\tfrac{1}{2\pi}\, \mathrm{e}^{\frac{\mathrm{Pe}}{2}x}\, K_0\Big(\tfrac{\mathrm{Pe}}{2}\sqrt{x^2+y^2}\Big)\,, \quad (x^2+y^2 > 0) \tag{4.2.23}$$

We again construct the fundamental solution that preserves no-flux symmetry condition

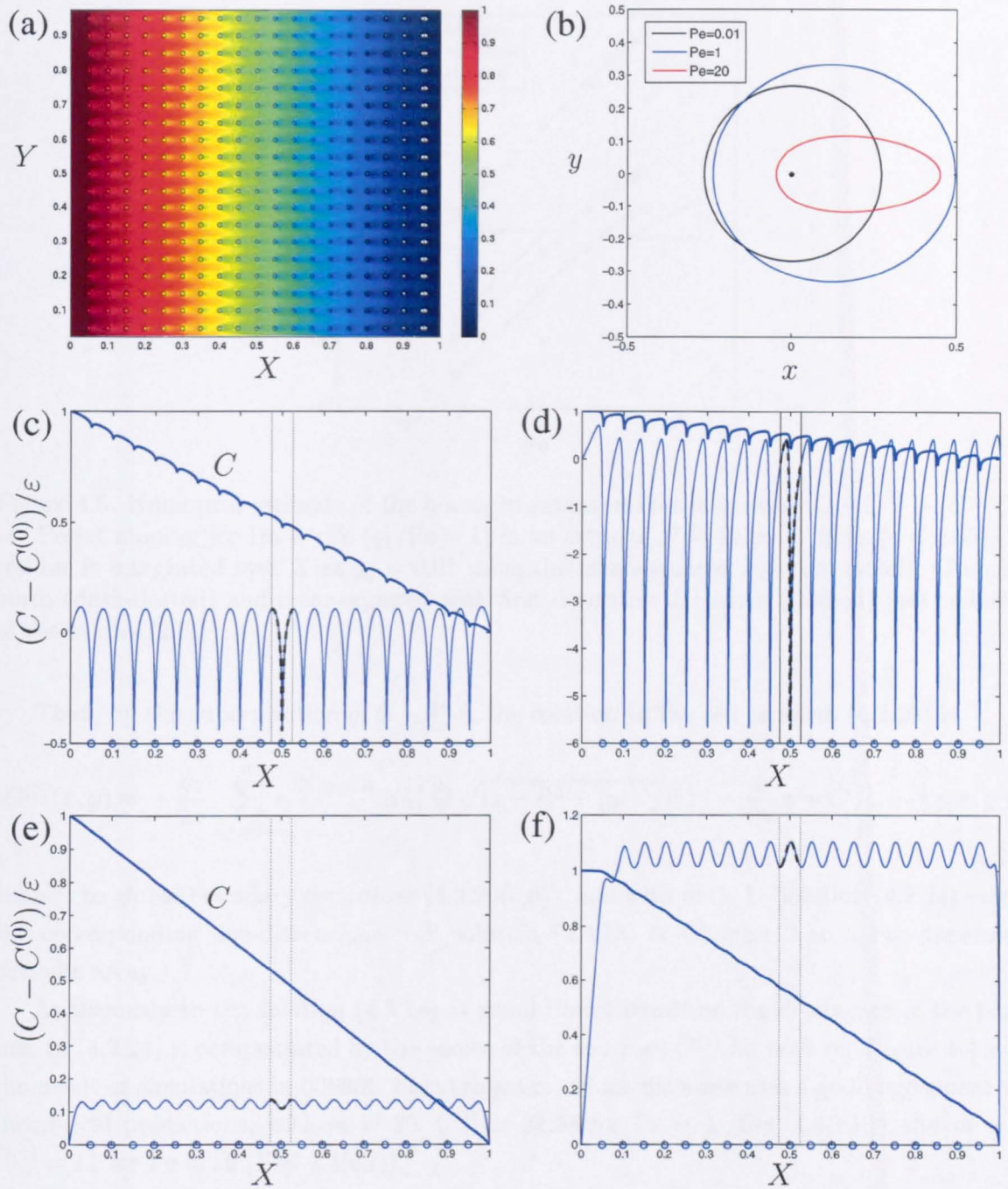

Figure 4.4. (a) Numerical solution C (colours) to (4.2.2) for Pe = 15, Da = εPe in a square-periodic array of 19×19 point sinks ($\varepsilon = 0.05$); black circles indicate the sinks' position. Note a concentration wake created about each sink. (b) Contours of the fundamental solution (4.2.23) taken at the level of $0.75 \max |G_\infty|$ for Pe = 0.01, 1, 20, showing the formation of a wake at high Pe. (c,d) Numerical solution C and correction $C^{(1)} = C - (1 - X)$ scaled by ε^{-1} ($\varepsilon = 0.05$) close to the centre of the unit cell ($y_0 = 0.01$) for Pe = 1 (c) and Pe = 15 (d); (e,f) Numerical solution and correction at the boundary of the unit cell ($y_0 = 0.5$) for Pe = 1 (e) and Pe = 15 (f); analytical solution (4.2.24) is shown in dashed black within a unit cell (vertical dotted lines).

at the boundary of the unit cell by adding an infinite system of images at $(x, y) = (i, j)$, $i, j = 0, \pm 1, \pm 2, \ldots$, to obtain $G(x, y) = \sum_{i,j=-\infty}^{\infty} G_\infty(x - i, y - j)$, $x, y \in [-\frac{1}{2}, \frac{1}{2}]$.

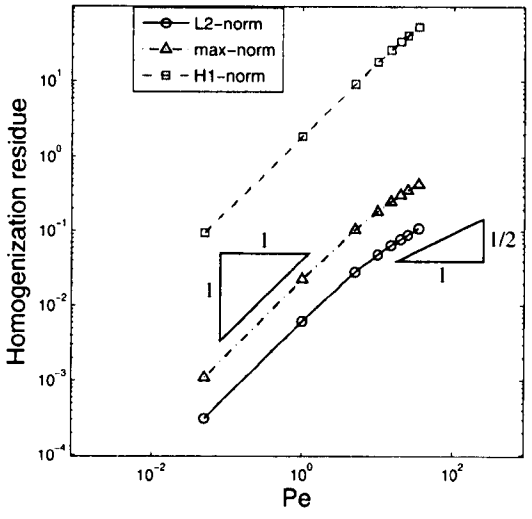

Figure 4.5. Numerical estimate of the homogenization residue magnitude $C - C^{(0)} - \langle C - C^{(0)} \rangle$ *vs.* Péclet number for $\mathrm{Da} = \varepsilon \mathrm{Pe}$ ($q_1/\mathrm{Pe} = 1$) in an array of $N = 19$ point sinks ($\varepsilon = 0.05$). The residue is integrated over X at $y_0 = 0.01$ using the mean-squared L_2-norm (solid), Chebyshev norm (dash-dotted) and mean-squared with first derivative H^1-norm (dashed) (see definitions of the norms (2.6.1)).

Then, by the superposition $q_1\, G - \frac{q_1}{\mathrm{Pe}}\, x$, the solution to the cell problem (4.2.20) is

$$C^{(1)}(x,y) \approx -\frac{q_1}{2\pi} \sum_{i,j=-m}^{m} \mathrm{e}^{\frac{\mathrm{Pe}}{2}(x-i)}\, K_0\Big(\tfrac{\mathrm{Pe}}{2}\sqrt{(x-i)^2+(y-j)^2}\Big) - \frac{q_1}{\mathrm{Pe}}\, x + \tilde{C}^{(1)}, \quad -\tfrac{1}{2} \le x, y \le \tfrac{1}{2}, \tag{4.2.24}$$

subject to global boundary conditions (4.2.20(c,d)), and with $m \gg 1$. Solution (4.2.24) extends the corresponding one-dimensional cell solution (2.4.13) of Chapter 2 to a two-dimensional periodic array.

Analogously to the solution (4.2.14) at small Péclet numbers, the divergence of the partial sum in (4.2.24) is compensated by the choice of the constant $\tilde{C}^{(1)}$ for each m. Figure 4.4 shows the result of simulations in `COMSOL Multiphysics`, which demonstrates a good agreement with theoretical predictions, with $m = 30$, $\tilde{C}^{(1)} \simeq 31.58$ for $\mathrm{Pe} = 1$ (Fig. 4.4(c,d)) and $m = 10$, $\tilde{C}^{(1)} = 11$ for $\mathrm{Pe} = 15$ (Fig. 4.4(e,f)).

Taking the limit of large Péclet number $\mathrm{Pe} \gg 1$ in (4.2.24), we obtain

$$C^{(1)}(x,y) \approx -\frac{q_1}{\sqrt{\mathrm{Pe}}} \sum_{i,j=-m}^{m} \frac{\exp\Big(\frac{\mathrm{Pe}}{2}\Big[(x-i) - \sqrt{(x-i)^2+(y-j)^2}\Big]\Big)}{\sqrt{4\pi}\,\big[(x-i)^2+(y-j)^2\big]^{1/4}} - \frac{q_1}{\mathrm{Pe}}\, x + \tilde{C}^{(1)}, \tag{4.2.25}$$

for $-\frac{1}{2} \le x, y \le \frac{1}{2}$, where we have used the asymptotic form of a modified Bessel function of the second kind [150]: $K_0(z) \approx \sqrt{\frac{\pi}{2}}\, \mathrm{e}^{-z}/\sqrt{z}$ for $z \gg 1$.

Based on (4.2.25), we expect $C^{(1)}$ to be $O(q_1/\sqrt{\mathrm{Pe}})$ at large Pe, away from the sink ($x^2 + y^2 > 0$). Computations of the magnitude of the homogenization residue (like shown by a blue solid line in Fig. 4.4(c,d)) about its mean value for $q_1/\mathrm{Pe} \equiv \mathrm{Da}/(\varepsilon \mathrm{Pe}) = 1$ agree with the asymptotics (approaching $\sqrt{\mathrm{Pe}}$ for large Pe, as presented in Fig. 4.5). The asymptotic behaviour

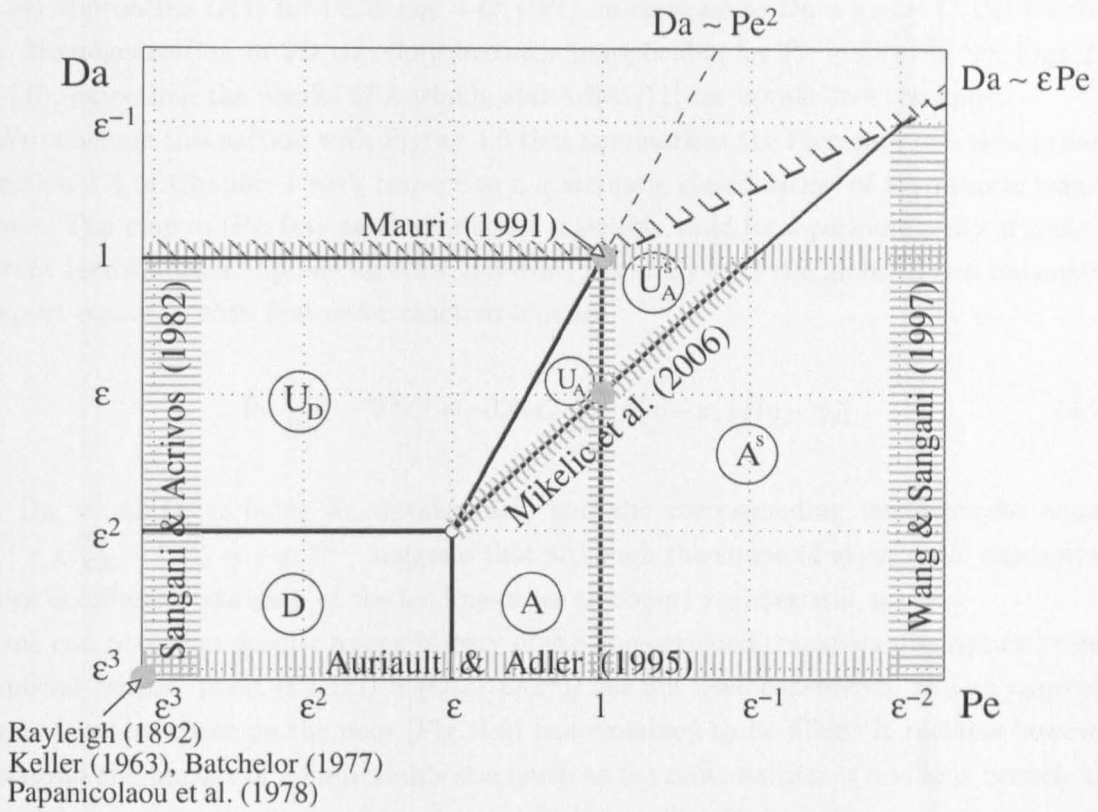

Figure 4.6. A schematic representation of previous results in effective description of advection-diffusion-reaction in two dimensions. The range of (Pe, Da) values considered by different authors is shown as a grey shade in the parameter space, with grey dots being the principal scaling chosen. The upper bound of homogenization applicability in 2D for $\mathrm{Pe} > 1$ (thick dashed) is conjectured based on (4.2.25) and Fig. 4.5. Shaded areas at the edges indicate the limits of $\mathrm{Pe} \to 0$ (left), $\mathrm{Pe} \to \infty$ (right), and $\mathrm{Da} \to 0$ (bottom). See Section 1.4 of Chapter 1 for details.

of the residue thus differs from a one-dimensional case (see, e.g. (2.4.16)), where the magnitude of $r^\varepsilon = C - C^{(0)}$ remains constant for $q_1/\mathrm{Pe} = 1$, $\mathrm{Pe} \gg 1$. Figure 4.5 also indicates that a significant non-smoothness of the concentration distribution at large Péclet number makes the residue r^ε greater than $O(1)$ in the Sobolev H^1-norm, implying only weak convergence (e.g. in L_2-norm) in this region, similarly to the one-dimensional case (see Fig. 2.2(a)).

4.2.4 Transport in a 2D array of point sinks: Summary

In this section we have generalised the effective description of advective-diffusive-uptake solute transport in a one-dimensional periodic array (developed in Chapter 2) to the two-dimensional case.

The concentration at leading-order (4.2.12) is shown to be identical in both cases. Therefore, all the transport regimes of Fig. 2.2 remain valid.

The 1D and 2D cases however differ in the properties of the correction to the leading-order solution $C^{(0)}$. At small local Péclet number ($\mathrm{Pe} \ll 1$) the homogenization residue $r^\varepsilon = C - C^{(0)} \approx \varepsilon^2 C^{(2)}$ (4.2.14) becomes $O(1)$ for $\mathrm{Da} = \varepsilon^2 q = O(1)$, as in the one-dimensional case; however, our results suggest that at large Péclet number ($\mathrm{Pe} \gg 1$), the residue $r^\varepsilon \approx \varepsilon C^{(1)}$

(4.2.24) approaches $O(1)$ for $\mathrm{Da} \equiv \varepsilon\, q_1 = O(\sqrt{\mathrm{Pe}})$, in contrast to $\mathrm{Da} \equiv \varepsilon\, q_1 = O(\mathrm{Pe})$ for the 1D case. Homogenization in 2D therefore becomes inapplicable for $\mathrm{Pe} \gtrsim O(\varepsilon^{-2})$ (*cf.* Figs 2.2(a) and 4.6), extending the results of Auriault and Adler [11] for uptake-free transport.

We conclude this section with Figure 4.6 that summarises the literature overview presented in Section 1.4 of Chapter 1 with respect to a systematic classification of asymptotic transport regimes. The map in (Pe, Da)-parameter space is strictly valid for a periodic array of sinks with constant (zeroth-order) uptake kinetics; however, the analysis of the global fluxes balance for a transport equation with first-order reaction kinetics

$$\mathrm{Pe}\,\frac{\partial C}{\partial x} - \nabla^2 C = -\mathrm{Da}\, C \sum_{i,j=1}^{N} \delta(x - x_i)\,\delta(y - y_j), \tag{4.2.26}$$

with $\mathrm{Da} = \alpha l/D$, α being an uptake rate, and the corresponding leading-order equation $p C^{(0)}_X - C^{(0)}_{XX} - C^{(0)}_{YY} = -q\, C^{(0)}$, suggests that although the shape of asymptotic concentration profiles is different, the map of the leading-order transport regimes still applies.

One can note that despite a long history of the homogenized transport description research, the special "triple" point $(\mathrm{Pe}, \mathrm{Da}) = (O(\varepsilon), O(\varepsilon^2))$ has not been considered, and an appreciable amount of white space on the map (Fig. 4.6) has remained to be filled. It remains however to understand the impact of a finite sink's size (such as the cross-section of a villous brunch in the human placenta) on the flow and transport, which we will address in the next Section.

4.3 Advection-diffusion in an array of sorbing cylinders

This section extends two-dimensional homogenized solute transport to the case of sinks of a finite size, modelled as cylinders.

4.3.1 Model assumptions and problem statement

We assume the liquid to be an incompressible and Newtonian fluid; solute uptake at the interface is considered to be by passive diffusion only; we also approximate the shape of the interface by a circle (see Fig. 4.1).

In addition, we assume that there is a representative periodic domain (*unit cell*) Ω composed of the liquid-phase subdomain Ω_m, simulating the maternal space, and (not necessarily simply-connected) villous solid region $\Omega \backslash \Omega_m$, with an interface Γ where uptake takes place (see Fig. 4.7).

We consider a two-dimensional array of size $L \times L$, composed of N^2 unit cells of size $l \times l$ ($N = (L/l) - 1$). The steady flow of incompressible liquid in a unit cell Ω is given by the Stokes equations

$$\nabla \cdot \mathbf{u}^* = 0\,, \quad \nabla P^* = \mu \nabla^2 \mathbf{u}^*\,, \tag{4.3.1}$$

where μ is the viscosity of the maternal blood, subject to a no-slip boundary condition on Γ ($\mathbf{u}^*|_\Gamma = 0$). We set the global conditions to be a uniform speed u_0 at the inlet ($\mathbf{u}^*|_{x^*=0} = u_0\, \mathbf{e}_x$), free flow (zero normal total stress) at the outlet ($-\mathbf{e}_x P^* + \mu\, \mathbf{e}_x \cdot [\nabla \mathbf{u}^* + (\nabla \mathbf{u}^*)^{\mathrm{T}}]|_{x^*=L} = 0$) and a periodic global boundary condition in the transverse to flow direction ($\mathbf{u}^*|_{y^*=0} = \mathbf{u}^*|_{y^*=L}$) (see Fig. 4.2).

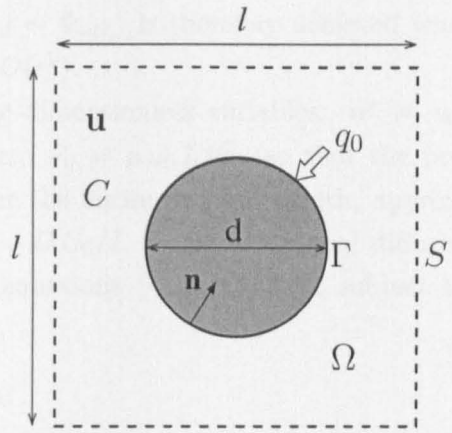

Figure 4.7. A two-dimensional unit cell Ω of size $l \times l$, containing a solid cylinder of perimeter $\mathcal{P} = \pi d$. Local solute concentration and flow velocity fields are C and $\mathbf{u}$ respectively (the stars over the dimensional variables are omitted). The flux density q_0 is prescribed at the interface Γ, with $\mathbf{n}$ being the unit normal to Γ pointing out of the liquid-phase (maternal) subdomain Ω_m. All field quantities are periodic on the outer cell boundary S.

We describe steady solute transport by the advection-diffusion equation for the dissolved concentration C^*

$$(\mathbf{u}^* \cdot \nabla)\, C^* = -\nabla \cdot \mathbf{F}^*, \quad \mathbf{F}^* = -D\, \nabla C^*, \tag{4.3.2}$$

were $\mathbf{F}^*$ is the diffusive flux density. Equation (4.3.2) is subject to the boundary condition $\mathbf{n} \cdot \mathbf{F}^*|_\Gamma = q_0$, where q_0 is a given flux density ($[q_0] = \text{mol}/(\text{m}^2 \cdot \text{s})$) across the interface Γ, $\mathbf{n}$ is the normal vector to Γ (pointing outwards Ω). Note that the uptake of the solute in the placenta is shared between the chemical reactions in the villous tissue and the advective transport with the fetal circulation along the capillaries, the latter can be represented by a cross-section averaged balance between the advection and diffusive mass-transport. Therefore, in the case of a constant concentration gradient along the fetal capillary, the contribution from the fetal circulation can be considered as uptake with zeroth-order kinetics, giving flux density (averaged over capillary length) $\langle \mathbf{n} \cdot \mathbf{F}^* \rangle|_\Gamma \approx const$. This assumption is not uniformly valid, and for solute transport at high Péclet number in fetal villous capillaries, a linear first-order uptake could be more appropriate. Although in this chapter we limit our analysis to the case $q_0 = const$, we address the effect of a variety of uptake kinetics in Chapter 6.

The transport equation (4.3.2), subject to boundary conditions, describes the competition between advection, diffusion and uptake. We take the inlet concentration to be C_0 at $x^* = 0$, set the outlet concentration to zero at $x^* = L$ (so that the global concentration drop $\Delta C = C_0$), and apply periodic boundary conditions at $y^* = 0,\, L$. Integrating (4.3.2), we get the reference global fluxes across the macroscopic domain:

$$\Phi_{\text{adv}} \sim u_0\, C_0\, L, \quad \Phi_{\text{dif}} \sim D\, C_0, \quad \Phi_{\text{upt}} \sim N^2\, q_0\, l \sim q_0\, L^2/l\,. \tag{4.3.3}$$

Let us define $\text{Pe} = u_0\, l/D$ as the local (microscopic) Péclet number, $\text{Da} = q_0\, l/(D\, C_0)$ as the local Damköhler number, and $\varepsilon = l/L$ as the scale-separation parameter, the three parameters that entirely define the nature of solute transport at the microscale. The balance between

all three fluxes ($\Phi_{\text{adv}} \sim \Phi_{\text{dif}} \sim \Phi_{\text{upt}}$) is therefore achieved when $\varepsilon^{-1}\text{Pe} \sim 1 \sim \varepsilon^{-2}\text{Da}$, giving $\text{Pe} = O(\varepsilon)$, $\text{Da} = O(\varepsilon\text{Pe}) = O(\varepsilon^2)$.

We choose the following dimensionless variables: $\mathbf{u}^* = u_0\,\mathbf{u}$, $P^* = P_0\,P$, $C^* = C_0\,C$, $\mathbf{F}^* = F_0\,\mathbf{F}$, $\mathbf{x}^* = l\,\mathbf{x}$, where $P_0 = \mu\,u_0\,L/l^2$ (so that the pressure gradient P_0/L, equal to the global pressure drop per the entire domain length, approximately balances local viscous dissipation $\mu u_0/l^2$) and $F_0 = D\,C_0/L$ (using the global diffusive flux density as a reference), and rewrite the system of equations (4.3.1)–(4.3.2), subject to boundary conditions, in the non-dimensional form:

$$\begin{aligned}
&\nabla\cdot\mathbf{u} = 0\,, \quad \nabla P = \varepsilon\,\nabla^2\mathbf{u}\,,\\
&\mathbf{u}|_\Gamma = 0\,, \qquad\qquad P,\ \mathbf{u} \text{ are periodic on } S\,, \qquad\qquad \text{(flow problem)}\\
&\mathbf{u}|_{X=0} = \mathbf{e}_x\,, \quad \mathbf{e}_x\cdot\left(-P\,\mathbf{I} + \varepsilon\,[\nabla\mathbf{u} + (\nabla\mathbf{u})^{\mathrm{T}}]\right)|_{X=1} = 0\,,
\end{aligned} \tag{4.3.4}$$

$$\begin{aligned}
&\text{Pe}\,(\mathbf{u}\cdot\nabla)\,C = -\varepsilon\,\nabla\cdot\mathbf{F}\,, \quad \varepsilon\,\mathbf{F} = -\nabla C\,,\\
&\varepsilon\,\mathbf{n}\cdot\mathbf{F}|_\Gamma = \text{Da}\,, \qquad C,\ \mathbf{F} \text{ are periodic on } S\,, \qquad\qquad \text{(transport problem)}\\
&C|_{X=0} = 1\,, \quad C|_{X=1} = 0 \text{ or } C|_{X=X_0} = \mathbf{n}\cdot\mathbf{F}|_{X=X_0} = 0 \text{ for } 0 < X_0 \le 1\,,
\end{aligned} \tag{4.3.5}$$

subject to Y-periodicity of the fields on $Y = 0$ and $Y = 1$, with $(\mathbf{I})_{ij} \equiv \delta_{ij}$ being a unit tensor and $(\nabla\mathbf{u})_{ij} \equiv \frac{\partial u_i}{\partial x_j}$ being an outer (dyadic) product.

We can estimate ε based on the typical volume fraction ϕ of normal villous tissue in a fully developed normal human placenta, being about 0.5 [172]. If we consider a square unit cell of side l, we have $\phi = \pi d^2/4l^2$, and hence $l = d\sqrt{\pi/4\phi} \sim 100$ μm for the terminal villus diameter $d \sim 100$ μm [33, 126]. Taking the reference macroscale size (of a placentone) to be $L \sim 1$ cm [98], we obtain the estimate $\varepsilon = l/L \sim 10^{-2}$, in agreement with our estimate for a one-dimensional array in Sec. 2.8 of Chapter 2.

4.3.2 Small microscopic Péclet number transport regime

Based on the balance of global fluxes (4.3.3), we take $\text{Pe} = O(\varepsilon) = \varepsilon\,p$, $\text{Da} = O(\varepsilon^2) = \varepsilon^2\,q$, with $p, q = O(1)$ (analogous to Section 4.2.2).

Since the scale-separation parameter ε is small, following [11, 177, 228], we consider the two-scale spatial dependences of the problem variables

$$P = \tilde{P}(\mathbf{x},\mathbf{X})\,, \quad \mathbf{u} = \tilde{\mathbf{u}}(\mathbf{x},\mathbf{X})\,, \quad C = \tilde{C}(\mathbf{x},\mathbf{X})\,, \quad \mathbf{F} = \tilde{\mathbf{F}}(\mathbf{x},\mathbf{X})\,, \tag{4.3.6}$$

where $\mathbf{X} = \varepsilon\mathbf{x}$, and hence $\nabla = \nabla_x + \varepsilon\nabla_X$. Here $\mathbf{x}$ represents the local "micro-coordinates" of the unit cell Ω (at the scale of individual villi), and $\mathbf{X}$ is the slowly changing global coordinates of the macroscopic problem (at the scale of the entire placentone).

Using (4.3.6) we can rewrite the system (4.3.4),(4.3.5) as

$$\nabla_x\cdot\tilde{\mathbf{u}} + \varepsilon\,\nabla_X\cdot\tilde{\mathbf{u}} = 0\,, \tag{4.3.7a}$$

$$\nabla_x\tilde{P} + \varepsilon\,\nabla_X\tilde{P} = \varepsilon\left[\nabla_x^2\tilde{\mathbf{u}} + 2\,\varepsilon\,(\nabla_x\cdot\nabla_X)\tilde{\mathbf{u}} + \varepsilon^2\,\nabla_X^2\tilde{\mathbf{u}}\right], \tag{4.3.7b}$$

$$\tilde{\mathbf{u}}|_\Gamma = 0\,, \qquad \tilde{P},\ \tilde{\mathbf{u}} \text{ are periodic on } S\,, \tag{4.3.7c}$$

$$\tilde{\mathbf{u}}|_{X=0} = \mathbf{e}_x\,, \quad \mathbf{e}_x\cdot\left(-\tilde{P}\,\mathbf{I} + \varepsilon\left[\nabla_x\tilde{\mathbf{u}} + \varepsilon\,\nabla_X\tilde{\mathbf{u}} + (\nabla_x\tilde{\mathbf{u}} + \varepsilon\,\nabla_X\tilde{\mathbf{u}})^{\mathrm{T}}\right]\right)\Big|_{X=1} = 0\,, \tag{4.3.7d}$$

$$\varepsilon p \left[\nabla_x \cdot (\tilde{C}\tilde{\mathbf{u}}) + \varepsilon \nabla_X \cdot (\tilde{C}\tilde{\mathbf{u}})\right] = -\varepsilon \left[\nabla_x \cdot \tilde{\mathbf{F}} + \varepsilon \nabla_X \cdot \tilde{\mathbf{F}}\right], \tag{4.3.8a}$$

$$\varepsilon \tilde{\mathbf{F}} = -\nabla_x \tilde{C} - \varepsilon \nabla_X \tilde{C}, \tag{4.3.8b}$$

$$\varepsilon \mathbf{n} \cdot \tilde{\mathbf{F}}|_\Gamma = \varepsilon^2 q, \qquad \tilde{C}, \tilde{\mathbf{F}} \text{ are periodic on } S, \tag{4.3.8c}$$

$$\tilde{C}|_{X=0} = 1, \quad \tilde{C}_{X=1} = 0 \text{ or } \tilde{C}|_{X=X_0} = \mathbf{n} \cdot \tilde{\mathbf{F}}|_{X=X_0} = 0 \text{ for } 0 < X_0 \leq 1. \tag{4.3.8d}$$

where we have used the incompressibility condition (4.3.4a) and identity $\nabla \cdot (C\mathbf{u}) = (\mathbf{u} \cdot \nabla)C + C(\nabla \cdot \mathbf{u})$ to transform the advective term in (4.3.5a) into conservative form.

We look for an approximate solution of (4.3.7),(4.3.8) in the form of power series in ε

$$\begin{aligned}
\tilde{P} &= P^{(0)} + \varepsilon P^{(1)} + \varepsilon^2 P^{(2)} + \dots, \\
\tilde{\mathbf{u}} &= \mathbf{u}^{(0)} + \varepsilon \mathbf{u}^{(1)} + \varepsilon^2 \mathbf{u}^{(2)} + \dots, \\
\tilde{C} &= C^{(0)} + \varepsilon C^{(1)} + \varepsilon^2 C^{(2)} + \dots, \\
\tilde{\mathbf{F}} &= \mathbf{F}^{(0)} + \varepsilon \mathbf{F}^{(1)} + \varepsilon^2 \mathbf{F}^{(2)} + \dots.
\end{aligned} \tag{4.3.9}$$

Substituting (4.3.9) in (4.3.7),(4.3.8) and collecting the terms in powers of ε, we find at $O(\varepsilon^0)$:

$$\nabla_x \cdot \mathbf{u}^{(0)} = 0, \quad \nabla_x P^{(0)} = 0, \tag{4.3.10}$$

$$\nabla_x C^{(0)} = 0, \tag{4.3.11}$$

subject to the local boundary condition $\mathbf{u}^{(0)}|_\Gamma = 0$ and the corresponding global boundary conditions: $\mathbf{u}^{(0)}|_{X=0} = \mathbf{e}_x$, $P^{(0)}|_{X=1} = 0$, $C^{(0)}|_{X=0} = 1$, $C^{(0)}|_{X=1} = 0$.

Equations (4.3.10b),(4.3.11) imply that the pressure and concentration fields at leading-order are independent of the local coordinates $\mathbf{x}$:

$$P^{(0)} = P^{(0)}(\mathbf{X}), \quad C^{(0)} = C^{(0)}(\mathbf{X}). \tag{4.3.12}$$

Collecting the terms in (4.3.7),(4.3.8) at $O(\varepsilon^1)$, we have the following equations:

$$\nabla_x \cdot \mathbf{u}^{(1)} + \nabla_X \cdot \mathbf{u}^{(0)} = 0, \quad \nabla_x P^{(1)} + \nabla_X P^{(0)} = \nabla_x^2 \mathbf{u}^{(0)}, \tag{4.3.13}$$

$$p \nabla_x \cdot \left(C^{(0)} \mathbf{u}^{(0)}\right) = -\nabla_x \cdot \mathbf{F}^{(0)}, \tag{4.3.14}$$

$$\mathbf{F}^{(0)} = -\nabla_x C^{(1)} - \nabla_X C^{(0)}, \tag{4.3.15}$$

and local boundary conditions: $\mathbf{u}^{(1)}|_\Gamma = 0$, $\mathbf{n} \cdot \mathbf{F}^{(0)}|_\Gamma = 0$, and global boundary conditions: $\mathbf{u}^{(1)}|_{X=0} = C^{(1)}|_{X=0;1} = 0$, $\mathbf{e}_x \cdot (-P^{(1)}\mathbf{I} + [\nabla_x \mathbf{u}^{(0)} + (\nabla_x \mathbf{u}^{(0)})^{\mathrm{T}}])|_{X=1} = 0$, and $\mathbf{u}^{(1)}$, $C^{(1)}$ are Y-periodic with period 1.

Using (4.3.10a) and (4.3.11), we reduce (4.3.14) to

$$\nabla_x \cdot \mathbf{F}^{(0)} = 0. \tag{4.3.16}$$

Collecting the terms in (4.3.7) and (4.3.8) at $O(\varepsilon^2)$, we get

$$\nabla_x \cdot \mathbf{u}^{(2)} + \nabla_X \cdot \mathbf{u}^{(1)} = 0\,, \quad \nabla_x P^{(2)} + \nabla_X P^{(1)} = \nabla_x^2 \mathbf{u}^{(1)} + 2\,(\nabla_x \cdot \nabla_X)\,\mathbf{u}^{(0)}\,, \tag{4.3.17}$$

$$p\left[\nabla_x \cdot \left(C^{(1)}\,\mathbf{u}^{(0)} + C^{(0)}\,\mathbf{u}^{(1)}\right) + \nabla_X \cdot \left(C^{(0)}\,\mathbf{u}^{(0)}\right)\right] = -\nabla_x \cdot \mathbf{F}^{(1)} - \nabla_X \cdot \mathbf{F}^{(0)}\,, \tag{4.3.18}$$

$$\mathbf{F}^{(1)} = -\nabla_x\, C^{(2)} - \nabla_X\, C^{(1)}\,, \tag{4.3.19}$$

and local boundary conditions: $\mathbf{u}^{(2)}|_\Gamma = 0$, $\mathbf{n} \cdot \mathbf{F}^{(1)}|_\Gamma = q$.

Averaging (4.3.13a) and (4.3.18) over the fluid-phase (maternal) sub-domain of the unit cell (of volume $|\Omega_m|$, with the boundary $\partial\Omega_m$ consisting of the fluid-solid interface Γ and the outer boundary of the unit cell S ($\partial\Omega_m = S \cup \Gamma$); see Fig. 4.7) and using the no-slip boundary condition $\mathbf{u}^{(0)} = \mathbf{u}^{(1)} = 0$ on Γ, we have

$$\frac{1}{|\Omega_m|} \int_S \mathbf{u}^{(1)} \cdot \mathbf{n}\, \mathrm{d}S_x + \nabla_X \cdot \langle \mathbf{u}^{(0)} \rangle_m = 0\,, \tag{4.3.20}$$

$$\begin{aligned} p\left[\frac{1}{|\Omega_m|} \int_S C^{(1)}\,\mathbf{u}^{(0)} \cdot \mathbf{n}\, \mathrm{d}S_x + \frac{1}{|\Omega_m|} \int_S C^{(0)}\,\mathbf{u}^{(1)} \cdot \mathbf{n}\, \mathrm{d}S_x + \nabla_X \cdot \left(C^{(0)} \langle \mathbf{u}^{(0)} \rangle_m\right)\right] = \\ = -\frac{1}{|\Omega_m|} \int_S \mathbf{F}^{(1)} \cdot \mathbf{n}\, \mathrm{d}S_x - \frac{1}{|\Omega_m|} \int_\Gamma \mathbf{F}^{(1)} \cdot \mathbf{n}\, \mathrm{d}S_x - \nabla_X \cdot \langle \mathbf{F}^{(0)} \rangle_m\,, \end{aligned} \tag{4.3.21}$$

where $\langle \mathbf{f} \rangle_m \equiv \frac{1}{|\Omega_m|} \int_{\Omega_m} \mathbf{f}\, \mathrm{d}V_x$, denotes an averaged "macroscopic" variable. Since the volume of the whole unit cell $|\Omega| = 1$, the volume fraction of the fluid in the unit cell (porosity) $\phi_m \equiv |\Omega_m|$, $0 < \phi_m < 1$, which is constant (as we neglect the deformations of the medium) and relates to the solid-phase volume fraction ϕ as $\phi_m = 1 - \phi$. The average of the leading-order concentration is $\langle C^{(0)} \rangle_m \equiv C^{(0)}$, in accord with (4.3.12).

We further take into account periodic boundary conditions for the flow and concentration fields (namely, for $C^{(1)}\,\mathbf{u}^{(0)} \cdot \mathbf{n}$, $C^{(0)}\,\mathbf{u}^{(1)} \cdot \mathbf{n}$ and $\mathbf{F}^{(1)} \cdot \mathbf{n}$)) on S to set the corresponding boundary integrals to zero. Equations (4.3.20)–(4.3.21) then reduce to

$$\nabla_X \cdot \langle \mathbf{u}^{(0)} \rangle_m = 0\,, \tag{4.3.22}$$

$$p\,\nabla_X \cdot \left(C^{(0)} \langle \mathbf{u}^{(0)} \rangle_m\right) = -\nabla_X \cdot \langle \mathbf{F}^{(0)} \rangle_m - \frac{1}{|\Omega_m|} \int_\Gamma \mathbf{F}^{(1)} \cdot \mathbf{n}\, \mathrm{d}S_x\,. \tag{4.3.23}$$

The integral in (4.3.23) represents the "interfacial" flux between the maternal and fetal circulations [275]. We estimate this integral using the boundary condition $\mathbf{n} \cdot \mathbf{F}^{(1)}|_\Gamma = q$, and we also apply the incompressibility condition (4.3.22) to simplify the advective term:

$$p\left(\langle \mathbf{u}^{(0)} \rangle_m \cdot \nabla_X\right) C^{(0)} = -\nabla_X \cdot \langle \mathbf{F}^{(0)} \rangle_m - \frac{\mathcal{P}}{\phi_m}\, q\,, \tag{4.3.24}$$

where $\mathcal{P}$ is the perimeter of the interface Γ (with dimensional perimeter $\mathcal{P}^* = l\mathcal{P}$), at which uptake takes place (see Fig. 4.7).

To complete the macro-scale description, we need to find a relation between the pressure $P^{(0)}$ and the averaged velocity field $\langle \mathbf{u}^{(0)} \rangle_m$, and between the concentration $C^{(0)}$ and the averaged concentration flux $\langle \mathbf{F}^{(0)} \rangle_m$. It is the examination of the micro-scale equations (4.3.10)–(4.3.16) that allows us to find these dependences.

Closure problems

It follows from (4.3.10a) and (4.3.13b), complemented by our assumption of $\mathbf{x}$-periodicity of the flow and pressure fields, that we can relate $\mathbf{u}^{(0)}$, $P^{(0)}$ and $P^{(1)}$ by the micro-scale flow problem

$$\begin{aligned} &\nabla_x \cdot \mathbf{u}^{(0)} = 0\,, \quad \nabla_x P^{(1)} - \nabla_x^2 \mathbf{u}^{(0)} = -\nabla_X P^{(0)}(\mathbf{X})\,, \quad \text{in } \Omega \\ &\mathbf{u}^{(0)}|_\Gamma = 0\,, \qquad \mathbf{u}^{(0)},\ P^{(1)} \text{ are periodic on } S\,. \end{aligned} \tag{4.3.25}$$

Since the source $\nabla_X P^{(0)}$ does not depend on $\mathbf{x}$, the solution to the linear problem (4.3.25) is proportional to $\nabla_X P^{(0)}$.

Analogously to the flow problem, (4.3.15) and (4.3.16) give the micro-scale transport for $\mathbf{F}^{(0)}$ and $C^{(1)}$:

$$\begin{aligned} &\nabla_x \cdot \mathbf{F}^{(0)} = 0\,, \quad \nabla_x C^{(1)} + \mathbf{F}^{(0)} = -\nabla_X C^{(0)}(\mathbf{X})\,, \quad \text{in } \Omega \\ &\mathbf{n} \cdot \mathbf{F}^{(0)}|_\Gamma = 0, \qquad \mathbf{F}^{(0)},\ C^{(1)} \text{ are periodic on } S\,. \end{aligned} \tag{4.3.26}$$

Again, since the problem (4.3.26) is linear and $\nabla_X C^{(0)}$ is constant in the unit cell, the solution to (4.3.26) is proportional to $\nabla_X C^{(0)}$.

Therefore, without loss of generality, we look for solution to (4.3.25)–(4.3.26) in the following form [177, 228]:

$$\mathbf{u}^{(0)} = -\mathsf{K} \cdot \nabla_X P^{(0)}\,, \quad P^{(1)} = -\mathbf{m} \cdot \nabla_X P^{(0)} + P_0^{(1)}\,, \tag{4.3.27}$$

$$\mathbf{F}^{(0)} = -\mathsf{A} \cdot \nabla_X C^{(0)}\,, \quad C^{(1)} = -\mathbf{b} \cdot \nabla_X C^{(0)} + C_0^{(1)}\,, \tag{4.3.28}$$

where $\mathsf{K} = \mathsf{K}(\mathbf{x}, \mathbf{X})$ and $\mathsf{A} = \mathsf{A}(\mathbf{x}, \mathbf{X})$ are permeability and diffusivity tensors; $\mathbf{m} = \mathbf{m}(\mathbf{x}, \mathbf{X})$, $\mathbf{b} = \mathbf{b}(\mathbf{x}, \mathbf{X})$ are vectors, and $P_0^{(1)} = P_0^{(1)}(\mathbf{X})$, $C_0^{(1)} = C_0^{(1)}(\mathbf{X})$ are scalars.

We substitute (4.3.27), (4.3.28) into (4.3.25)–(4.3.26) to find the coefficients:

$$\begin{aligned} &\nabla_x \cdot \mathsf{K} = 0\,, \quad \nabla_x \mathbf{m} = \nabla_x^2 \mathsf{K} + \mathsf{I}\,, \quad \text{in } \Omega \\ &\mathsf{K}|_\Gamma = 0\,, \qquad \mathbf{m},\ \mathsf{K} \text{ are periodic on } S\,, \end{aligned} \tag{4.3.29}$$

$$\begin{aligned} &\nabla_x \cdot \mathsf{A} = 0\,, \quad \mathsf{A} = -\nabla_x \mathbf{b} + \mathsf{I}\,, \quad \text{in } \Omega \\ &\mathsf{A} \cdot \mathbf{n}|_\Gamma = 0\,, \quad \mathbf{b},\ \mathsf{A} \text{ are periodic on } S\,, \end{aligned} \tag{4.3.30}$$

where $\mathsf{I} \equiv \delta_{ij}$ is the Kronecker-delta unit tensor, $\mathbf{n} \equiv n_i$ is the unit normal vector to Γ. The tensor inner product and the vector outer product for a tensor T and vectors $\mathbf{u}, \mathbf{v}$ are denoted as $\mathsf{T} \cdot \mathbf{u} = T_{ij}\, u_i$ and $\mathbf{u}\,\mathbf{v} = u_i\, v_j$ respectively; and the summation convention over the repeating index is used.

The linear elliptic problems (4.3.29) and (4.3.30) constitute the closure to the averaged macro-scale flow and transport equations (4.3.22) and (4.3.24), subject to boundary conditions,

through relations (4.3.27)–(4.3.28).

Effective macroscale flow and transport problems: small Pe regime.

We perform the averaging of (4.3.27a) over the volume of Ω_m to find a relation between the pressure gradient and the averaged local fluid velocity:

$$\langle \mathbf{u}^{(0)} \rangle_m = -\langle \mathsf{K} \rangle_m \cdot \nabla_X P^{(0)} . \tag{4.3.31}$$

Averaging (4.3.15) over the unit cell and using (4.3.28b), we obtain the closure relation between the concentration flux and the averaged concentration gradient of solute in Ω_m:

$$\langle \mathbf{F}^{(0)} \rangle_m = -\left(\mathbf{I} - \langle \nabla_x \mathbf{b} \rangle_m\right) \cdot \nabla_X C^{(0)} . \tag{4.3.32}$$

Therefore, (4.3.32) transforms the transport equation (4.3.24) to

$$p \left(\langle \mathbf{u}^{(0)} \rangle_m \cdot \nabla_X \right) C^{(0)} = \nabla_X \cdot \left(\left(\mathbf{I} - \langle \nabla_x \mathbf{b} \rangle_m\right) \cdot \nabla_X C^{(0)} \right) - \frac{\mathcal{P}}{\phi_m} q , \tag{4.3.33}$$

Following [276], we define *superficial average* over the whole unit cell as $\langle \mathbf{f} \rangle \equiv \phi_m \langle \mathbf{f} \rangle_m \equiv |\Omega|^{-1} \int_{\Omega_m} \mathbf{f} \, \mathrm{d}V_x$ for $\mathbf{f} = \mathbf{u}^{(0)}, \mathbf{F}^{(0)}, \mathsf{K}, \mathbf{b}$, and $\langle f \rangle \equiv f \equiv |\Omega|^{-1} \int_{\Omega} f \, \mathrm{d}V_x$ for $f = P^{(0)}, C^{(0)}$. Dropping the superscripts over the variables and the subscript X in ∇_X, we obtain, from (4.3.22), (4.3.31) and (4.3.33), the effective flow and transport description at leading order

$$\nabla \cdot \langle \mathbf{u} \rangle = 0 , \quad \langle \mathbf{u} \rangle = -\langle \mathsf{K} \rangle \cdot \nabla \langle P \rangle , \tag{4.3.34a}$$

$$\langle \mathbf{u} \rangle |_{X=0} = \mathbf{e}_x , \ \langle P \rangle |_{X=1} = 0 , \quad \langle \mathbf{u} \rangle \text{ is } Y\text{-periodic} , \tag{4.3.34b}$$

$$p \, \langle \mathbf{u} \rangle \cdot \nabla \langle C \rangle = \nabla \cdot \left(\mathsf{D}_{\mathrm{eff}} \cdot \nabla \langle C \rangle \right) - \mathcal{P} q , \tag{4.3.35a}$$

$$\langle C \rangle |_{X=0} = 1 , \ \langle C \rangle |_{X=1} = 0 , \quad \langle C \rangle \text{ is } Y\text{-periodic} , \tag{4.3.35b}$$

where $\mathsf{D}_{\mathrm{eff}}$ is the *effective diffusivity* tensor

$$(\mathsf{D}_{\mathrm{eff}})_{ij} = (1 - \phi) \, \delta_{ij} - \langle \nabla_x \mathbf{b} \rangle_{ij} = (1 - \phi) \, \delta_{ij} - \int_{\Gamma} n_i \, b_j \, \mathrm{d}S_x , \tag{4.3.36}$$

simplified by applying a generalised Gauss's Theorem $\int_{\Omega_m} \nabla_x \mathbf{b} \, \mathrm{d}V_x = \int_{\partial\Omega_m} \mathbf{b}\,\mathbf{n} \, \mathrm{d}S_x$ and using the $\mathbf{x}$-periodicity of $\mathbf{b}$ on S ($\partial\Omega_m = S \cup \Gamma$). Here ϕ is the villous volume fraction per unit cell volume ($\phi \equiv 1 - \phi_m$) and n_i is a component of the unit normal to Γ. The superficial average of permeability tensor K and the effective diffusivity tensor $\mathsf{D}_{\mathrm{eff}}$ are to be found from solutions to the closure cell problems (4.3.29) and (4.3.30).

Note that since u_0 is the reference scale for $\mathbf{u}$, $P_0 = \mu u_0 L / l^2$ for P and $1/L$ for ∇, (4.3.34a) implies that the dimensional permeability K^* equals $l^2 \, \mathsf{K}$, l being the size of a unit cell. Analogously, (4.3.35a) gives the dimensional form of effective diffusivity as $\mathsf{D}^*_{\mathrm{eff}} = D \, \mathsf{D}_{\mathrm{eff}}$, where D is the molecular diffusivity of a solute.

Equations (4.3.34a) represent the Darcy flow at the macroscale, which are together with equation (4.3.35a), subject to boundary conditions in the macroscopic domain, provide a complete macro-scale description of solute flow and transport in the case $\mathrm{Pe} = O(\varepsilon)$, $\mathrm{Da} = O(\varepsilon^2)$. In Sections 4.3.5 and 4.3.6 below, we estimate the effective permeability and diffusivity for a simple geometry as a computational benchmark for processing the experimentally acquired villous shapes of the human placenta in Chapter 5.

Before moving to a direct numerical simulation for the small Péclet number ($\mathrm{Pe} = O(\varepsilon)$), we observe that the transport cell problem (4.3.30) does not contain parameters (p, q) and depends only on the shape and size of the (materno-fetal) interface Γ, so that the effective diffusivity tensor $\mathsf{D}_{\mathrm{eff}} \lesssim O(1)$, as will be shown below. Thus, in the limit of large Pe and Da ($p \sim q \gg 1$), the average transport equation (4.3.35a) becomes of an advective-uptake type. Similarly to the case of a two-dimensional array of point sinks (see Sec. 4.2.2), this suggests a new transport regime at $\mathrm{Pe} = O(1)$, $\mathrm{Da} \sim \varepsilon \mathrm{Pe} = O(\varepsilon)$ (in accord with the global flux-balance relation (4.3.3)).

4.3.3 The transport regime for moderate local Péclet number.

We therefore consider the case $\mathrm{Pe} = O(1)$, $\mathrm{Da} = O(\varepsilon) = \varepsilon\, q_1$ ($q_1 = O(1)$). Using (4.3.6), analogously to Section 4.3.2, we rewrite (4.3.5) as

$$\mathrm{Pe}\left[\nabla_x \cdot (\tilde{C}\,\tilde{\mathbf{u}}) + \varepsilon\, \nabla_X \cdot (\tilde{C}\,\tilde{\mathbf{u}})\right] = -\varepsilon\left[\nabla_x \cdot \tilde{\mathbf{F}} + \varepsilon\, \nabla_X \cdot \tilde{\mathbf{F}}\right], \tag{4.3.37a}$$

$$\varepsilon\, \tilde{\mathbf{F}} = -\nabla_x \tilde{C} - \varepsilon\, \nabla_X \tilde{C}, \tag{4.3.37b}$$

$$\varepsilon\, \mathbf{n} \cdot \tilde{\mathbf{F}}|_\Gamma = \varepsilon\, q_1, \qquad \tilde{C},\ \tilde{\mathbf{F}} \text{ are periodic on } S, \tag{4.3.37c}$$

$$\tilde{C}|_{X=0} = 1, \quad \tilde{C}_{X=1} = 0 \text{ or } \tilde{C}|_{X=X_0} = \mathbf{n} \cdot \tilde{\mathbf{F}}|_{X=X_0} = 0 \text{ for } 0 < X_0 \leq 1. \tag{4.3.37d}$$

Substituting (4.3.9) in (4.3.37) and collecting the terms at powers of ε, we find at $O(\varepsilon^0)$:

$$\mathrm{Pe}\, \nabla_x \cdot \left(C^{(0)}\, \mathbf{u}^{(0)}\right) = 0, \tag{4.3.38}$$

$$\nabla_x\, C^{(0)} = 0, \tag{4.3.39}$$

subject to the boundary conditions $\mathbf{u}^{(0)}|_\Gamma = 0$, $C^{(0)}|_{X=0} = 1$, $C^{(0)}_{X=1} = 0$ (assuming, for brevity, $C^{(0)} > 0$ for $0 < X < 1$).

Equation (4.3.38) is identically satisfied, taking into account (4.3.10a) and (4.3.39), and (4.3.39) again implies a slowly varying leading-order concentration field $C^{(0)} = C^{(0)}(\mathbf{X})$.

Collecting the terms in (4.3.37) at $O(\varepsilon^1)$, we have

$$\mathrm{Pe}\left[\nabla_x \cdot \left(C^{(1)}\, \mathbf{u}^{(0)} + C^{(0)}\, \mathbf{u}^{(1)}\right) + \nabla_X \cdot \left(C^{(0)}\, \mathbf{u}^{(0)}\right)\right] = -\nabla_x \cdot \mathbf{F}^{(0)}, \tag{4.3.40}$$

$$\mathbf{F}^{(0)} = -\nabla_x\, C^{(1)} - \nabla_X\, C^{(0)}, \tag{4.3.41}$$

with local boundary conditions: $\mathbf{u}^{(1)}|_\Gamma = 0$, $\mathbf{n} \cdot \mathbf{F}^{(0)}|_\Gamma = q_1$.

Using (4.3.13a) and (4.3.39), we rewrite (4.3.40) as follows:

$$\mathrm{Pe}\left[\nabla_x \cdot (C^{(1)}\,\mathbf{u}^{(0)}) + \mathbf{u}^{(0)} \cdot \nabla_X C^{(0)}\right] = -\nabla_x \cdot \mathbf{F}^{(0)} \tag{4.3.42a}$$

$$\mathbf{n} \cdot \mathbf{F}^{(0)}|_\Gamma = q_1\,, \quad \mathbf{u}^{(0)}|_\Gamma = 0\,, \quad \mathbf{u}^{(0)},\, \mathbf{F}^{(0)},\, C^{(1)} \text{ are periodic on } S\,. \tag{4.3.42b}$$

Averaging (4.3.42a) over the fluid-phase sub-domain of the unit cell Ω_m and using periodicity to eliminate surface integrals over S ($\partial\Omega_m = S \cup \Gamma$; see Fig. 4.7), we get

$$\mathrm{Pe}\left[\frac{1}{\phi_m}\int_\Gamma \left(C^{(1)}\,\mathbf{u}^{(0)}\right)\cdot \mathbf{n}\,\mathrm{d}S_x + \langle \mathbf{u}^{(0)}\rangle_m \cdot \nabla_X C^{(0)}\right] = -\frac{1}{\phi_m}\int_\Gamma \mathbf{F}^{(0)}\cdot\mathbf{n}\,\mathrm{d}S_x\,. \tag{4.3.43}$$

We apply the local no-slip and flux boundary conditions (4.3.42b), so that (4.3.43) reduces to

$$\mathrm{Pe}\,\langle \mathbf{u}^{(0)}\rangle_m \cdot \nabla_X C^{(0)} = -\frac{\mathcal{P}}{\phi_m}\,q_1\,, \tag{4.3.44}$$

or, using the superficial average $\langle \mathbf{u}^{(0)}\rangle \equiv \phi_m \langle \mathbf{u}^{(0)}\rangle_m$, $C^{(0)} \equiv \langle C^{(0)}\rangle$, and dropping the superscript $^{(0)}$ over the variables and the subscript $_X$ in ∇_X, we obtain the effective macroscopic transport problem at moderate Péclet number, subject to the global boundary conditions

$$\begin{aligned} \mathrm{Pe}\,\langle \mathbf{u}\rangle \cdot \nabla\langle C\rangle &= -\mathcal{P}\,q_1\,, \\ \langle C\rangle|_{X=0} = 1, \quad &\langle C\rangle \text{ is } Y\text{-periodic}\,, \end{aligned} \tag{4.3.45}$$

which is a regular limit of (4.3.35) for large $p = O(\varepsilon^{-1})$ ($p = \mathrm{Pe}/\varepsilon$, $q = q_1/\varepsilon$).

Although (4.3.45) for $\langle C\rangle \equiv C^{(0)}$ is already in a closed form, we estimate the first correction $C^{(1)}$ to understand the role of advective transport at the micro-scale.

Transport cell problem: moderate Pe regime

Equations (4.3.41), (4.3.42a) constitute the following transport problem in a unit cell that relate $C^{(1)}$ and $\mathbf{F}^{(0)}$ with $C^{(0)}$:

$$\mathrm{Pe}\left[\nabla_x \cdot (C^{(1)}\,\mathbf{u}^{(0)}) + \mathbf{u}^{(0)} \cdot \nabla_X C^{(0)}\right] = -\nabla_x \cdot \mathbf{F}^{(0)}\,, \quad \mathbf{n}\cdot\mathbf{F}^{(0)}|_\Gamma = q_1\,, \tag{4.3.46a}$$

$$\mathbf{F}^{(0)} = -\nabla_x C^{(1)} - \nabla_X C^{(0)}\,, \tag{4.3.46b}$$

subject to the local boundary conditions (4.3.42b). Substituting (4.3.46b) into (4.3.46a) and using $\nabla_x \cdot \mathbf{u}^{(0)} = 0$ from (4.3.10a), we have

$$\nabla_x^2 C^{(1)} - \mathrm{Pe}\,\mathbf{u}^{(0)} \cdot \nabla_x C^{(1)} = \mathrm{Pe}\,\mathbf{u}^{(0)} \cdot \nabla_X C^{(0)}\,, \tag{4.3.47a}$$

$$\mathbf{n} \cdot \nabla_x C^{(1)}\Big|_\Gamma = -\mathbf{n}\cdot\nabla_X C^{(0)}\Big|_\Gamma - q_1\,, \tag{4.3.47b}$$

$$\mathbf{u}^{(0)}|_\Gamma = 0\,, \quad \mathbf{u}^{(0)},\, C^{(1)} \text{ are periodic on } S\,. \tag{4.3.47c}$$

Since the linear transport problem (4.3.47) has source terms proportional to q_1 and $\mathrm{Pe}\,\nabla_X C^{(0)}$,

which are independent of $\mathbf{x}$, we look for a general solution in the form

$$C^{(1)} = a_1(\mathbf{x})\, q_1 - \mathrm{Pe}\, \mathbf{b_1}(\mathbf{x}) \cdot \nabla_X C^{(0)} + C_0^{(1)}, \tag{4.3.48}$$

where $C_0^{(1)}$ is a scalar independent of $\mathbf{x}$, and $a_1 = a_1(\mathbf{x})$, $\mathbf{b_1} = \mathbf{b_1}(\mathbf{x})$ are some coefficients that satisfy the following cell problems:

$$\begin{aligned} &\nabla_x^2 a_1 - \mathrm{Pe}\, \mathbf{u}^{(0)} \cdot \nabla_x a_1 = 0, \\ &\mathbf{n} \cdot \nabla_x a_1 = -1 \ \text{ on } \Gamma, \\ &\mathbf{u}^{(0)}|_\Gamma = 0, \quad \mathbf{u}^{(0)},\, a_1 \text{ are periodic on } S, \quad \langle a_1 \rangle = const; \end{aligned} \tag{4.3.49}$$

$$\begin{aligned} &\nabla_x^2 \mathbf{b_1} - \mathrm{Pe}\, \mathbf{u}^{(0)} \cdot \nabla_x \mathbf{b_1} = -\mathbf{u}^{(0)}, \\ &\mathbf{n} \cdot \nabla_x \mathbf{b_1} = \mathrm{Pe}^{-1}\, \mathbf{n} \ \text{ on } \Gamma, \\ &\mathbf{u}^{(0)}|_\Gamma = 0, \quad \mathbf{u}^{(0)},\, \mathbf{b_1} \text{ are periodic on } S, \quad \langle \mathbf{b_1} \rangle = const. \end{aligned} \tag{4.3.50}$$

We observe that (4.3.49)–(4.3.50) generalise the corresponding unit cell problems (2.4.9)–(2.4.10) in 1D, derived in Chapter 2. When $\mathrm{Pe} \ll 1$, (4.3.50) approaches (4.3.30) for $\mathbf{b} = \mathrm{Pe}\, \mathbf{b_1}$ and for $q = q_1/\varepsilon = O(1)$, and we have, from (4.3.48) $C^{(1)} = -\mathbf{b}(\mathbf{x}) \cdot \nabla_X C^{(0)} + C_0^{(1)} + O(\varepsilon)$, as expected.

4.3.4 Limiting case of small villous volume fraction

Setting the limit of small villous volume fraction $\phi \ll 1$ or, equivalently, the surface area $|\Gamma| \to 0$, we find from (4.3.36) that $\mathsf{D}_{\mathrm{eff}} \to \mathbf{I}$, and from (4.3.29) that $\langle \mathsf{K} \rangle \to k\mathbf{I}$, $k = \frac{1}{4\pi}(-0.738 - 0.5\ln(\phi) + O(\phi))$ [112]. Relation (4.3.27a) therefore implies that for small but finite volume fraction, $\langle \mathbf{u}^{(0)} \rangle = -k(\phi)\nabla_X P^{(0)}(\mathbf{X})$ is independent of local coordinates $\mathbf{x}$, and the global boundary conditions (4.3.34b) then give $\langle \mathbf{u}^{(0)} \rangle \equiv \mathbf{e}_x$. Finally, assuming that the net concentration flux across Γ remain finite as $|\Gamma| \sim \mathcal{P} \to 0$, we have $\mathcal{P} q \to q^*$. Problem for the effective transport (4.3.35) therefore transforms to the corresponding problem (4.2.12) that has been derived in Section 4.2 for an array of point sinks (with $q \equiv q^*$). Having justified solute transport in an array of point sinks at leading order, we note that the velocity field $\mathbf{u}^{(0)}$ does not, in general, become uniform in the limit of small volume fraction. The unit cell problem (4.3.47) for the next-to-leading-order correction to the concentration field at high Péclet number thus differs from the case of a point array of sinks, as will be shown below.

The closure cell problem (4.3.30) for transport coefficients A, $\mathbf{b}$, at small Pe number, can be rewritten in polar coordinates (r, θ) for a unit cell with the circular interface $\Gamma = \{r = a\}$ ($a \equiv d/2$), normal $\mathbf{n} = (-1, 0)$ to Γ, pointing outwards of the domain (see Fig.4.7), and the outer product

$$\nabla \mathbf{b} \equiv \begin{pmatrix} \frac{\partial b_1}{\partial r} & \frac{\partial b_2}{\partial r} \\ \frac{1}{r}\left(\frac{\partial b_1}{\partial \theta} - b_2\right) & \frac{1}{r}\left(\frac{\partial b_2}{\partial \theta} + b_1\right) \end{pmatrix},$$

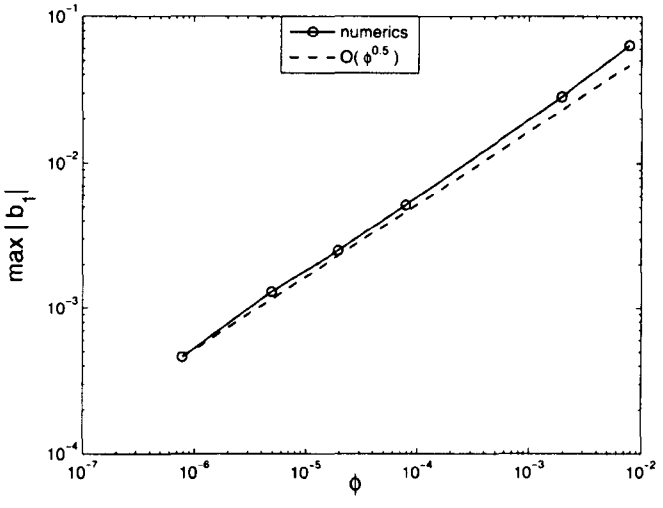

Figure 4.8. Maximal absolute value of the horizontal component b_1 of a solution to the cell transport problem (4.3.30) *vs.* the area fraction ϕ of the cylinder: numerical simulations (solid) and the asymptotic estimate (dashed).

giving

$$\frac{1}{r}\frac{\partial}{\partial r}\left(r\frac{\partial b_i}{\partial r}\right)+\frac{1}{r^2}\frac{\partial^2 b_i}{\partial \theta^2}=0\,,\quad r>a,\,0\le\theta<2\pi\,,\quad i=1,2\,, \tag{4.3.51a}$$

$$\left.\frac{\partial b_1}{\partial r}\right|_{r=a}=1\,,\quad \left.\frac{\partial b_2}{\partial r}\right|_{r=a}=0\,, \tag{4.3.51b}$$

$$b_{1,2}\text{ are periodic on }S\,, \tag{4.3.51c}$$

where b_1 and b_2 are the radial and azimuthal components of the vector $\mathbf{b}=(b_1,b_2)$. The boundary conditions and the symmetry of the problem (4.3.51) imply $b_1=b_1(r)$, $b_2=const$, reducing the problem to

$$\begin{aligned}&\nabla_r^2 b_1=\frac{\mathcal{P}}{2\pi r}\,\delta(r-a)\quad\text{in }\Omega\,,\\ &b_1\text{ is periodic on }S\,.\end{aligned} \tag{4.3.52}$$

The solution to the linear elliptic problem (4.3.52) is proportional to the perimeter $\mathcal{P}\equiv 2\pi a\sim\sqrt{\phi}$ at small area fractions $\phi\equiv\pi a^2\ll 1$ (see Fig. 4.8). Therefore as $\mathcal{P}$ tends to 0, we get $\mathbf{b}\equiv const$, and thus, from (4.3.28), $C^{(1)}=C^{(1)}(\mathbf{X})$, *i.e.* $C^{(1)}$ is constant in each unit cell. In order to satisfy the global boundary conditions $C^{(1)}|_{X=0}=0$, $C^{(1)}|_{X=1}=0$ or $C^{(1)}|_{X=X_0}=C_X^{(1)}|_{X=X_0}=0$, we must demand $C^{(1)}\equiv 0$. In other words, the first correction to the leading-order concentration profile at small Péclet number vanishes for small villous volume fraction $\phi\sim\mathcal{P}^2\to 0$, giving the homogenization error $O(\varepsilon^2)$.

Analogously, the cell problem (4.3.47) at moderate Péclet number, in the limit $|\Gamma|\sim\mathcal{P}\to 0$,

takes the form

$$\nabla_x^2 C^{(1)} - \mathrm{Pe}\,\frac{\partial C^{(1)}}{\partial x} - \mathrm{Pe}\,\tilde{\mathbf{u}}^{(0)} \cdot \nabla_x C^{(1)} = -\mathcal{P}\,q_1 + \mathcal{P}\,q_1\,\delta(x)\delta(y) + \mathrm{Pe}\,\tilde{\mathbf{u}}^{(0)} \cdot \nabla_X C^{(0)}\,, \quad (4.3.53a)$$

$$\tilde{\mathbf{u}}^{(0)} \equiv \mathbf{u}^{(0)} - \langle \mathbf{u}^{(0)} \rangle\,, \quad (4.3.53b)$$

$$\tilde{\mathbf{u}}^{(0)},\ C^{(1)} \text{ are periodic on } S\,, \quad (4.3.53c)$$

where we have used $\langle \mathbf{u}^{(0)} \rangle \equiv \mathbf{e}_x$ and (4.3.45a), and neglected the $O(\mathcal{P})$ term on the right-hand-side of (4.3.53a), assuming that $\mathcal{P}\,q_1$ remains finite. We accordingly find that the limiting form (4.3.53) for $C^{(1)}$, in the case of moderate Pe and small ϕ, differs from the corresponding cell problem (4.2.20) obtained for a periodic array of point sinks (where q_1 is substituted with $q_1^* \equiv \mathcal{P}\,q_1$) by the terms containing a perturbation $\tilde{\mathbf{u}}^{(0)}(\mathbf{x})$ of the unit-cell averaged leading-order flow field $\langle \mathbf{u}^{(0)} \rangle$ (indicating that the important features of flow do not disappear in the limit of solute transport past an array of "needles"; see also [112, 229]).

4.3.5 Numerical solution to the closure cell problem: effective permeability

We now verify the homogenization results by solving the flow cell problem (4.3.29) and comparing the effective permeability with existing theoretical approximations. We note that (4.3.29) can be equivalently rewritten as two Stokes flow problems, driven by unit pressure gradients in the horizontal and vertical directions respectively

$$\begin{aligned} &\nabla \cdot \hat{\mathbf{u}}_1 = 0\,, \quad \nabla \hat{P}_1 = \nabla^2 \hat{\mathbf{u}}_1 + \mathbf{f}_1\,, \quad f_1 \equiv (1,\,0)^{\mathrm{T}} \quad \text{in } \Omega\,, \\ &\hat{\mathbf{u}}_1|_\Gamma = 0\,, \qquad \hat{P}_1,\ \hat{\mathbf{u}}_1 \text{ are periodic on } S\,, \end{aligned} \quad (4.3.54)$$

$$\begin{aligned} &\nabla \cdot \hat{\mathbf{u}}_2 = 0\,, \quad \nabla \hat{P}_2 = \nabla^2 \hat{\mathbf{u}}_2 + \mathbf{f}_2\,, \quad f_2 \equiv (0,\,1)^{\mathrm{T}} \quad \text{in } \Omega\,, \\ &\hat{\mathbf{u}}_2|_\Gamma = 0\,, \qquad \hat{P}_2,\ \hat{\mathbf{u}}_2 \text{ are periodic on } S\,, \end{aligned} \quad (4.3.55)$$

where $\hat{\mathbf{u}}_1 \equiv (\mathsf{K}_{11}, \mathsf{K}_{12})$, $\hat{\mathbf{u}}_2 \equiv (\mathsf{K}_{21}, \mathsf{K}_{22})$, $\mathbf{m} \equiv (\hat{P}_1, \hat{P}_2)$, and we dropped the subscript in ∇_x.

The two flow problems (4.3.54)–(4.3.55) with no-slip condition on Γ and periodic boundary conditions on S (see Fig. 4.7) are solved by a stationary linear finite-element solver of `COMSOL Multiphysics`, where an absolute error for 9478 elements is less than 10^{-6}. An example of obtained field quantities K and q_1 for $d/l = 0.5$ ($\phi \approx 0.2$) is shown in Figure 4.9. The corresponding effective permeability, averaged over the unit cell Ω, is

$$\langle \mathsf{K} \rangle \approx \begin{pmatrix} 0.02 & 0 \\ 0 & 0.02 \end{pmatrix}\,, \quad (4.3.56)$$

which is isotropic, as expected from the symmetry of the problem.

We compare the numerical solution for varying area fraction ϕ of the cylinder with the empirical Kozeny–Carman formula (derived for a porous medium treated as a set of parallel

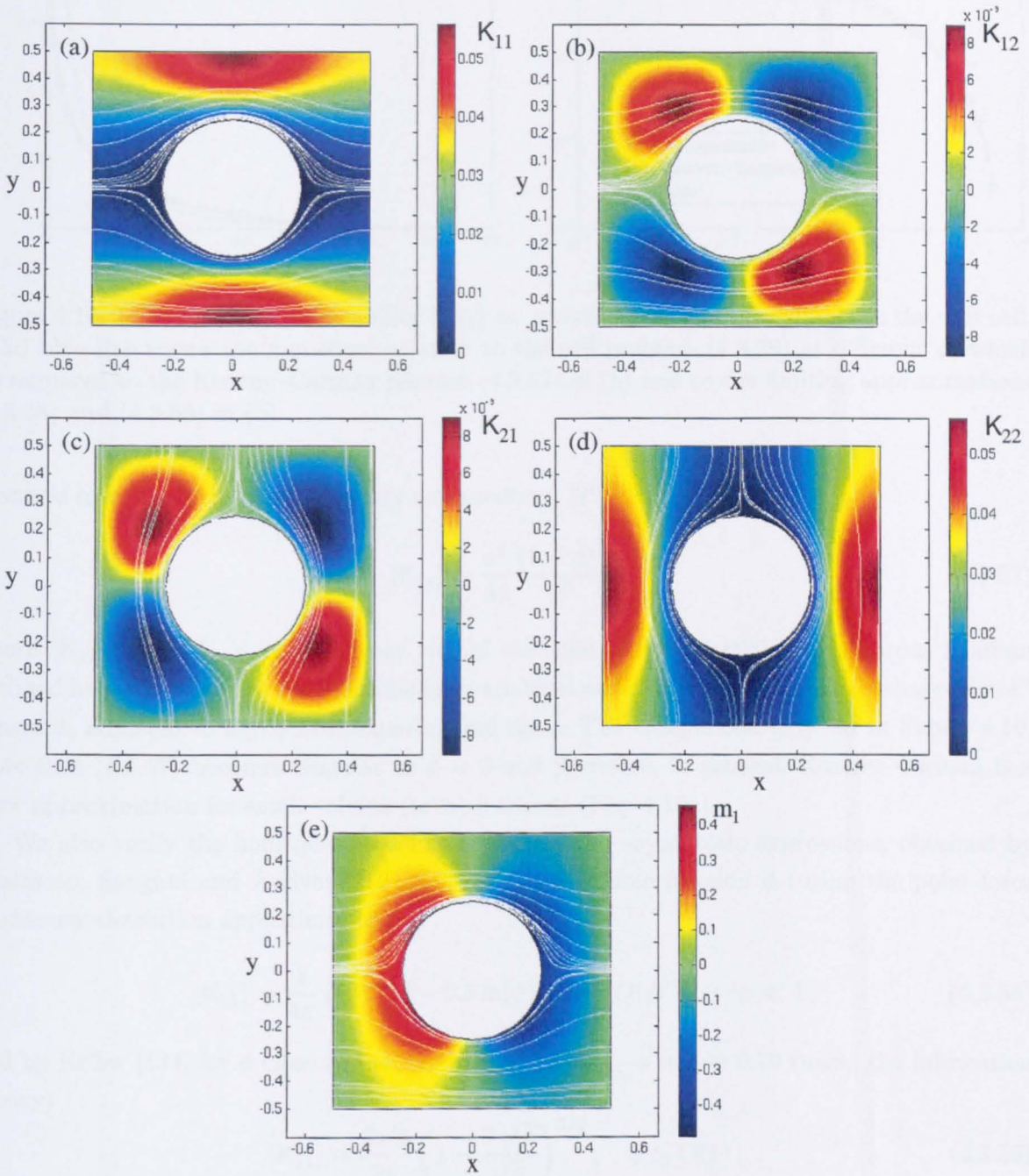

Figure 4.9. Numerical solution to the closure flow problem (4.3.54)–(4.3.55) in a unit cell for $\phi = \pi d^2/(4l^2) \approx 0.2$ $(d/l = 0.5)$. (a-d) components of the symmetric permeability tensor K, corresponding to the velocity fields (colours) and streamlines (solid white); (e) the first component of the vector $\mathbf{m}$, corresponding to the pressure field (colours).

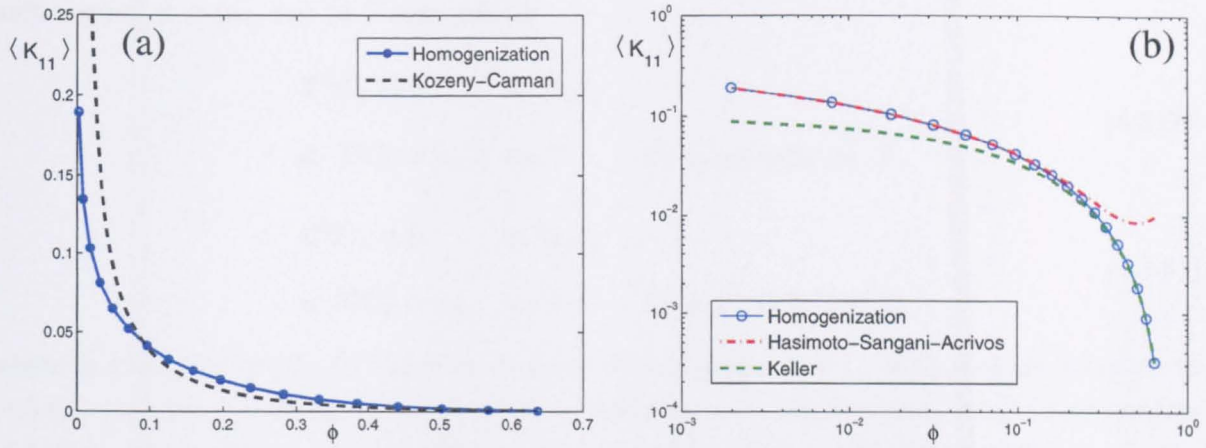

Figure 4.10. (a,b) Effective permeability $\langle \mathsf{K}_{11} \rangle$ *vs.* area fraction ϕ of the cylinder in the unit cell. Solid blue line shows the numerical solution to the cell problem (4.3.29) at different ϕ, which is compared to the Kozeny–Carman relation (4.3.57) in (a) and to the limiting approximations (4.3.58) and (4.3.59) in (b).

channels of equal length and arbitrary cross-section) [29]

$$\langle \mathsf{K}_{11} \rangle = \frac{a^2}{4c} \frac{(1-\phi)^3}{\phi^2}, \tag{4.3.57}$$

where $\langle \mathsf{K}_{11} \rangle \equiv \langle \mathsf{K}_{22} \rangle$, a is an average size of the solid phase "particle" of a porous medium (defined here as $a = \sqrt{\phi/\pi}$, in dimensionless variables) and $c = 15$ is an empirical "shape-factor" constant, adjusted to agree with experimental data. The comparison is given in Figure 4.10. Note that (4.3.57) becomes singular at $\phi = 0$ and therefore, in general, Kozeny–Carman is a poor approximation for small volume (area) fractions (Fig. 4.10a).

We also verify the homogenized solution against the asymptotic expressions, obtained by Hasimoto, Sangani and Acrivos [112, 229] for small volume fraction ϕ (using the point-force fundamental-solution approximation)

$$\langle \mathsf{K}_{11} \rangle = \frac{1}{4\pi} \left(-0.738 - 0.5 \ln(\phi) + \phi + O(\phi^2) \right), \quad \phi \ll 1, \tag{4.3.58}$$

and by Keller [134] for ϕ close to the maximal value $\phi_{\max} = \pi/4 \approx 0.79$ (using the lubrication theory)

$$\langle \mathsf{K}_{11} \rangle \approx \frac{2\sqrt{2}}{9\pi} \left(1 - \frac{2\sqrt{\phi}}{\sqrt{\pi}} \right)^{5/2}, \quad \phi \lesssim O(1), \tag{4.3.59}$$

which demonstrate a good agreement (Fig. 4.10b).

4.3.6 Numerical solution to the closure cell problem: effective diffusivity

Analogously to Section 4.3.5, we solve the transport closure problem (4.3.30) and compare the effective diffusivity with existing theoretical approximations. We observe that (4.3.30) can be equivalently rewritten as two diffusion problems in a periodic cell, with a concentration flux at the inner boundary Γ proportional to the horizontal and vertical components of the outward

unit normal $\mathbf{n} = (n_1, n_2)$ to Γ respectively

$$\begin{aligned} &\nabla^2 \hat{C}_1 = 0 \qquad \text{in } \Omega_m\,, \\ &\mathbf{n}\cdot\nabla \hat{C}_1 = n_1 \quad \text{on } \Gamma\,, \qquad \hat{C}_1 \text{ is periodic on } S\,, \end{aligned} \tag{4.3.60}$$

$$\begin{aligned} &\nabla^2 \hat{C}_2 = 0 \qquad \text{in } \Omega_m\,, \\ &\mathbf{n}\cdot\nabla \hat{C}_2 = n_2 \quad \text{on } \Gamma\,, \qquad \hat{C}_2 \text{ is periodic on } S\,, \end{aligned} \tag{4.3.61}$$

where $\mathbf{b} \equiv (b_1, b_2) \equiv (\hat{C}_1, \hat{C}_2)$ and we dropped the subscript in ∇_x. Note that the solution to (4.3.60)–(4.3.61) is defined up to an arbitrary additive constant; however, it is the derivatives of $\mathbf{b}$ that determine the effective diffusivity D_{eff} (4.3.36), which is therefore unique.

Figure 4.11(a-c) shows a sample solution to the flow problems (4.3.60)–(4.3.61), obtained by an adaptive stationary finite-element solver of `COMSOL Multiphysics` for 36411 elements with an absolute error less than 10^{-9}, $d/l = 0.5$ ($\phi \approx 0.2$). The corresponding effective diffusivity (4.3.36), averaged over the unit cell Ω, is

$$\mathsf{D}_{\text{eff}} = (1-\phi)\,\mathbf{I} - \int_\Gamma \mathbf{n}\,\mathbf{b}\,\mathrm{d}S_x \approx \begin{pmatrix} 0.67 & 0 \\ 0 & 0.67 \end{pmatrix}, \tag{4.3.62}$$

which is diagonal, as expected.

We compare the homogenized solution for varying area fraction ϕ of the cylinder with the asymptotic expressions obtained by Fricke [100, 101] for small volume fraction ϕ (estimating the contribution of adjacent ellipsoidal "inclusions" via the superposition principle; this formula generalises the pioneering homogenization result by Maxwell (1.4.1), discussed in Chapter 1)

$$(\mathsf{D}_{\text{eff}})_{11} \approx \frac{\gamma(1-\phi)}{\gamma+\phi} \quad \phi \ll 1\,, \quad \gamma = \begin{cases} 1, & \text{cylindrical inclusions}\,, \\ 2, & \text{spherical inclusions}\,, \end{cases} \tag{4.3.63}$$

and by Keller [133] for ϕ close to the maximal value $\phi_{\max} = \pi/4 \approx 0.79$ (exploiting small aspect-ratio of the narrow gaps between the cylinders in a cubic array and using harmonic function theory)

$$(\mathsf{D}_{\text{eff}})_{11} \approx \frac{1}{\pi}\left(1 - \frac{4\phi}{\pi}\right)^{1/2}, \quad \phi \lesssim O(1)\,. \tag{4.3.64}$$

Figure 4.11(d) demonstrates a good agreement between the analytical and homogenized solutions, especially in the regions of $\phi \lesssim 0.4$ and $\phi \gtrsim 0.75$.

4.3.7 Flow and transport in an array of cylinders: Summary

In this Section, we have obtained effective flow (4.3.34) and transport (4.3.35) descriptions at leading order, with corresponding closure unit cell problems (4.3.29) and (4.3.30). We have demonstrated that the effective macroscopic transport equation (4.3.35a)

$$p\,\langle \mathbf{u}\rangle \cdot \nabla\langle C\rangle = \nabla\cdot(\mathsf{D}_{\text{eff}}\cdot\nabla\langle C\rangle) - \mathcal{P}\,q\,, \tag{4.3.65}$$

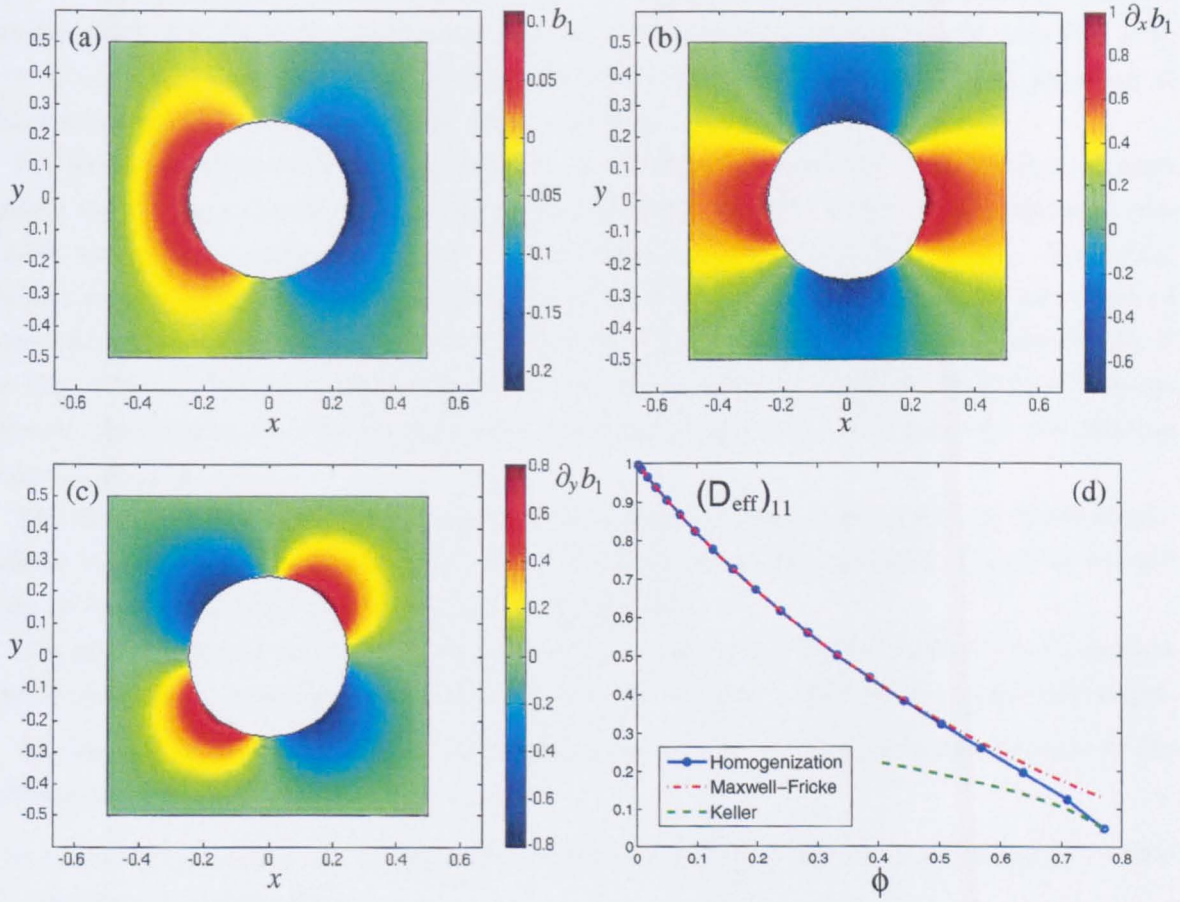

Figure 4.11. (a-c) Numerical solution to the closure flow problem (4.3.60) in a unit cell for $\phi \approx 0.2$ ($d/l = 0.5$): the first component of the auxiliary vector $\mathbf{b}$, corresponding to the concentration field is shown in (a; colours), and the corresponding derivatives $\partial_x b_1$, $\partial_y b_1$ are plotted in (b,c) respectively. (The solution b_2 to the conjugated problem (4.3.61) is the $\pi/2$-rotated anti-clockwise relative to b_1 due to the symmetry of the geometry). (d) Effective diffusivity $(\mathsf{D}_{\text{eff}})_{11}$ *vs.* area fraction ϕ of the cylinder in the unit cell. Solid blue line shows the numerical solution to the cell problem (4.3.60) for different ϕ, which is compared to the limiting approximations (4.3.63) (dash-dotted line) and (4.3.64) (dashed line).

$\mathsf{D}_{\text{eff}} \lesssim O(1)$ being determined from (4.3.30), is valid for both small and moderate Péclet numbers ($\text{Pe} = O(\varepsilon) - O(1)$), so that it becomes independent of the cell problem for $\text{Pe} \sim \varepsilon^{-1}\,\text{Da} \gg O(\varepsilon)$ ($p \sim q \gg 1$):

$$\langle \mathbf{u} \rangle \cdot \nabla \langle C \rangle = -\mathcal{P}\,\frac{\text{Da}}{\varepsilon\,\text{Pe}}\,. \tag{4.3.66}$$

We have shown that the transport problems at leading order (4.3.65), (4.3.66) agree with respective problems for an array of point sinks in the limit of infinitesimal villous volume fraction $\phi \sim \mathcal{P}^2$. And for example, when $\text{Pe} = O(\varepsilon)$ ($p \sim q = O(1)$), the limiting form (4.3.52) indicates that for small but finite ϕ, the homogenization residue is proportional to $\sqrt{\phi}$ (see Fig. 4.8): $r^\varepsilon \equiv C - C^{(0)} \sim \max\{O(\varepsilon\sqrt{\phi}),\, O(\varepsilon^2)\}$, whereby causing a slight drop in the accuracy of homogenization on a periodic array of finite sink-size.

We have also obtained the dependence of the effective permeability on the villous volume fraction by solving numerically the closure flow problem (4.3.29), which is approximated reasonably well by the empirical Kozeny–Carman formula for $\phi \gtrsim 0.4$ (Fig. 4.10a). Numerical solution to the transport closure problem (4.3.30) (Fig. (4.11d) shows that the net effect of "non-conducting inclusions" represented by the solid-phase (villous) subdomain bounded by Γ (see Fig. 4.7) is in hindering free molecular diffusion, thereby reducing the effective diffusivity. However, the drop in the effective diffusivity with increasing ϕ is not as rapid as for the effective conductivity (Fig. 4.10a).

The developed computational framework is straightforward to generalise to anatomically realistic non-circular two-dimensional shapes of the materno-fetal interface Γ, which we will study in the next chapter with the aid of image analysis.

It is also noteworthy that if the flux density ($q = q(\mathbf{x})$, $\mathbf{x} \in \Gamma$) is non-uniform on Γ, the sink term $\mathcal{P}\,q$ in (4.3.65) must be replaced with $\int_\Gamma q(\mathbf{x})\,\mathrm{d}S_x$; the rest of the results remain unchanged.

We neglect, in the framework of the present model, the following features relevant to the placental transport:

- elastic deformations of the interface Γ (villous surface) or its deviation from the central position in a unit cell;
- nonlinear uptake kinetics for certain solutes, such as glucose, at the interface Γ, due to the presence of active transporters;
- solute carriers, such as haemoglobin, contributing to the advective transport of oxygen and carbon dioxide.

It is the role of the latter that we address in the following section.

4.4 Non-linear effects of solute carriers

We consider a steady motion of liquid with suspended particles, e.g. red blood cells containing haemoglobin, capable of carrying solute molecules in the maternal subdomain Ω_m with inner boundary Γ (see Fig. 4.7). We assume that the interface Γ is permeable to the freely dissolved molecules but not to the solute-carrying particles. We also neglect diffusivity of the solute-carrying particles compared to the diffusivity of the free solute molecules.

4.4.1 Problem statement

Let $C^*_{\rm tot}$ be the total local concentration of the solute in the fluid, C^* be the local concentration of the freely dissolved solute, and $C^*_{\rm bound}$ be the concentration of the solute bounded to the solute-carriers. Then the advected concentration can be represented, following [153], as

$$C^*_{\rm tot}(\mathbf{x}) = C^* + C^*_{\rm bound}, \quad C^*_{\rm bound} = C^*_{\rm max}\, f(C^*)\,, \tag{4.4.1}$$

where $C^*_{\rm max}$ is the maximal local concentration of solute bounded to the fully saturated carriers and $f(C^*)$ is a nonlinear sigmoid function (association/dissociation curve) describing the equilibrium between the dissolved and bounded states of the solute, which is given, for example, by Hill's law (in dimensionless variables, $C = C^*/C_0$):

$$f(C) = \frac{C^n}{k^n + C^n}\,, \tag{4.4.2}$$

where n is a dissociation factor (about 2.65 for oxygen [76]) and k is the half-saturation constant, which are identified by fitting to experimental data (see Fig. 4.12(a) for oxygen kinetics of maternal and fetal blood, and Fig. 4.12(b) for haemoglobin- and perfluorocarbon-based blood substitutes). The implicit assumption of the quasi-steady balance between free- and oxygen-bound haemoglobin has been justified theoretically in many cases [76, 271] (with the error up to about 10%, particularly in the regions of very low oxygen concentration), and the typical time for oxygen unloading of haemoglobin from 80% to 30% of saturation is about 0.04 s [76].

Observing that the advective term $(\mathbf{u}\cdot\nabla)\,C$ in (4.3.5a) (in a dimensionless form) becomes $(\mathbf{u}\cdot\nabla)\,C_{\rm total} = [1 + \frac{C^*_{\rm max}}{C_0}\, f'(C)](\mathbf{u}\cdot\nabla)\,C$, the transport problem (4.3.5) then is modifies to

$$\begin{aligned}
&{\rm Pe}\,[1 + \alpha_0\, f'(C)]\,(\mathbf{u}\cdot\nabla)\,C = -\varepsilon\,\nabla\cdot\mathbf{F}\,, \quad \varepsilon\,\mathbf{F} = -\nabla C\,,\\
&\varepsilon\,\mathbf{n}\cdot\mathbf{F}|_\Gamma = {\rm Da}\,, \qquad\qquad C,\,\mathbf{F} \text{ are periodic on } S\,,\\
&C|_{X=0} = 1\,, \quad C|_{X=1} = 0 \text{ or } C|_{X=X_0} = \mathbf{n}\cdot\mathbf{F}|_{X=X_0} = 0 \text{ for } 0 < X_0 \le 1\,,
\end{aligned} \tag{4.4.3}$$

subject to Y-periodicity of C. Here $\alpha_0 = C^*_{\rm max}/C_0$ is the dimensionless solute-carrier capacity, and C_0 is the inlet concentration.

Observing from (4.4.2) that $\langle f'(C)\rangle = O(1)$ and integrating (4.4.3a) over Ω, similarly to Section 4.3, we get the reference global fluxes across the macroscopic domain:

$$\Phi_{\rm adv} \sim \alpha_0\, u_0\, C_0\, L, \quad \Phi_{\rm dif} \sim D\, C_0, \quad \Phi_{\rm upt} \sim N^2\, q_0\, l \sim \varepsilon^{-1}\, q_0\, L\,. \tag{4.4.4}$$

Therefore, the flux-balance $\Phi_{\rm adv} \sim \Phi_{\rm dif} \sim \Phi_{\rm upt}$ ($\varepsilon^{-1}\,\alpha_0\,{\rm Pe} \sim 1 \sim \varepsilon^{-2}\,{\rm Da}$) gives the first organising centre $({\rm Pe}, {\rm Da}) = (\varepsilon/\alpha_0,\, \varepsilon^2)$.

Using $\alpha_0 \approx 60 - 70$ for oxygen [153, 179] and taking $\varepsilon \sim 10^{-2}$ (as has been estimated earlier in Sec. 4.3), we have $\alpha_0 = O(\varepsilon^{-1})$.

As has been estimated in Section 2.8, a likely range of Péclet number for intervillous transport of oxygen in the human placenta is ${\rm Pe} \sim 10 - 10^2$. However, analogously to Section 4.3, we need to start by considering an asymptotic expansion around the main organising centre $({\rm Pe}, {\rm Da}) = (\varepsilon^2,\, \varepsilon^2)$, which provides the leading-order description valid for a wide range of Pe

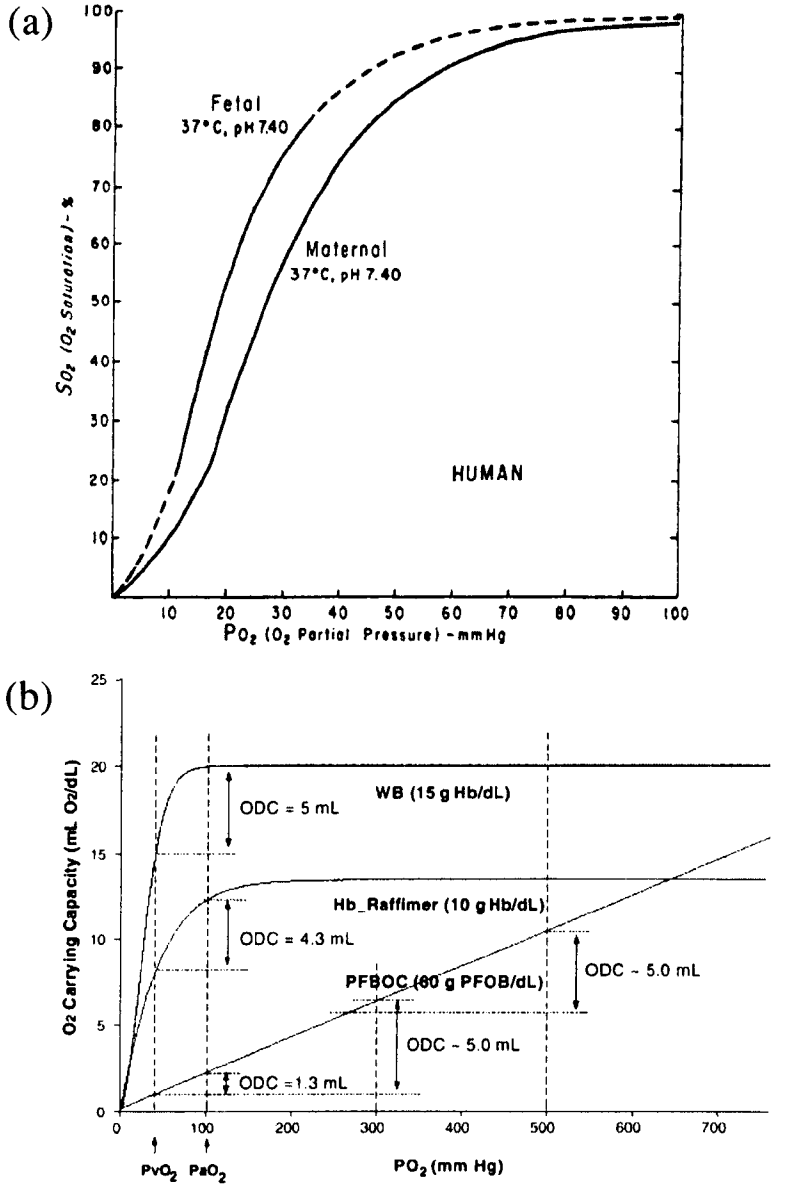

Figure 4.12. (a) Oxygen-haemoglobin dissociation curves for human fetal and maternal blood. Abscissa shows partial pressure of oxygen (P_{O_2}); ordinate expresses the percentage saturation of haemoglobin with oxygen (S_{O_2}) (reproduced from [179]). (b) Oxygen carrying capacity versus oxygen partial pressure for normal whole blood (WB), haemoglobin-based blood substitute (Hb_Raffimer) and perfluorocarbon-based blood substitute (PFBOC). The physiological range of partial pressures in the veins and arteries are marked by PvO_2 and PaO_2 respectively. Note a Hill-type dissociation law (4.4.2) for the first two curves and the linear relation for PFBOC. Reproduced from [141].

number values, as will be shown below. In doing so, we also broaden the scope of potential applications of the solute-carrier-facilitated transport model to other media, such as dialysis machines [265] and bioreactors [1], which may be characterised by a smaller value of Péclet number.

4.4.2 Small microscopic Péclet number transport regime

Based on the above flux-balance estimates (4.4.4), we consider the following scaling: $\alpha_0 = O(\varepsilon^{-1}) = \varepsilon^{-1}\,\alpha$, $\mathrm{Pe} = O(\varepsilon^2) = \varepsilon^2\,p_a$, $\mathrm{Da} = O(\varepsilon^2) = \varepsilon^2\,q$, $\alpha, p_a, q = O(1)$.

Using the two-scale dependence (4.3.6), we rewrite (4.4.3) as

$$\varepsilon^2\,p_a\left[1+\varepsilon^{-1}\,\alpha\,f'(\tilde{C})\right]\left[\nabla_x\cdot(\tilde{C}\tilde{\mathbf{u}})+\varepsilon\,\nabla_X\cdot(\tilde{C}\tilde{\mathbf{u}})\right] = -\varepsilon\left[\nabla_x\cdot\tilde{\mathbf{F}}+\varepsilon\,\nabla_X\cdot\tilde{\mathbf{F}}\right], \tag{4.4.5a}$$

$$\varepsilon\,\tilde{\mathbf{F}} = -\nabla_x\tilde{C}-\varepsilon\,\nabla_X\tilde{C}\,, \tag{4.4.5b}$$

$$\varepsilon\,\mathbf{n}\cdot\tilde{\mathbf{F}}|_\Gamma = \varepsilon^2\,q\,, \qquad \tilde{C},\,\tilde{\mathbf{F}} \text{ are periodic on } S\,, \tag{4.4.5c}$$

$$\tilde{C}|_{X=0} = 1\,, \quad \tilde{C}_{X=1} = 0\,, \quad \tilde{C} \text{ is } Y\text{-periodic.} \tag{4.4.5d}$$

again using the incompressibility condition (4.3.4a) to transform the advective term in (4.4.3a) into conservative form.

Substituting two-scale asymptotic series (4.3.9) in (4.4.5), we again find at the order ε^0, $\nabla_x C^{(0)} = 0$ and hence

$$C^{(0)} = C^{(0)}(\mathbf{X})\,, \tag{4.4.6}$$

satisfying the global boundary conditions $C^{(0)}|_{X=0} = 1$, $C^{(0)}_{X=1} = 0$, $C^{(0)}$ is Y-periodic.

Noting the asymptotic Taylor expansion for the derivative of the dissociation curve $f'(\tilde{C})$

$$\begin{aligned}&\tilde{C} = C^{(0)}+\varepsilon\,C^{(1)}+\varepsilon^2\,C^{(2)}+O(\varepsilon^3)\,,\\ &f'(\tilde{C}) = f'(C^{(0)})+\varepsilon\,f''(C^{(0)})\,C^{(1)}+\varepsilon^2\left[f''(C^{(0)})\,C^{(2)}+\frac{1}{2}f'''(C^{(0)})\left(C^{(1)}\right)^2\right]+O(\varepsilon^3)\,,\end{aligned} \tag{4.4.7}$$

and collecting the terms in (4.4.5) at $O(\varepsilon^1)$, we have

$$p_a\,\alpha\,f'(C^{(0)})\,\nabla_x\cdot\left(C^{(0)}\,\mathbf{u}^{(0)}\right) = -\nabla_x\cdot\mathbf{F}^{(0)}\,, \tag{4.4.8}$$

$$\mathbf{F}^{(0)} = -\nabla_x C^{(1)}-\nabla_X C^{(0)}\,, \tag{4.4.9}$$

where, using (4.3.10), relation (4.4.8) reduces to

$$\nabla_x\cdot\mathbf{F}^{(0)} = 0\,. \tag{4.4.10}$$

Collecting the terms in (4.4.5) at $O(\varepsilon^2)$, we get

$$\begin{aligned}&p_a\,\alpha\,f'(C^{(0)})\left[\nabla_x\cdot\left(C^{(1)}\,\mathbf{u}^{(0)}+C^{(0)}\,\mathbf{u}^{(1)}\right)+\nabla_X\cdot\left(C^{(0)}\,\mathbf{u}^{(0)}\right)\right]+\\ &+p_a\left[1+\alpha\,f''(C^{(0)})\,C^{(1)}\right]\nabla_x\cdot\left(C^{(0)}\,\mathbf{u}^{(0)}\right) = -\nabla_x\cdot\mathbf{F}^{(1)}-\nabla_X\cdot\mathbf{F}^{(0)}\,,\end{aligned} \tag{4.4.11}$$

$$\mathbf{F}^{(1)} = -\nabla_x C^{(2)}-\nabla_X C^{(1)}\,, \tag{4.4.12}$$

and local boundary conditions: $\mathbf{u}^{(0)}|_\Gamma = 0$, $\mathbf{n} \cdot \mathbf{F}^{(1)}|_\Gamma = q$.

Incompressibility (4.3.10a), (4.3.13a) and slowly varying leading-order concentration (4.4.6), reduce (4.4.11) to

$$p_a \, \alpha \, f'(C^{(0)}) \left[\nabla_x \cdot \left(C^{(1)} \, \mathbf{u}^{(0)} \right) + \mathbf{u}^{(0)} \, \nabla_X \cdot C^{(0)} \right] = -\nabla_x \cdot \mathbf{F}^{(1)} - \nabla_X \cdot \mathbf{F}^{(0)} , \tag{4.4.13}$$

Averaging (4.4.13) over the maternal sub-domain Ω_m, using the no-slip condition $\mathbf{u}^{(0)}|_\Gamma = 0$, periodic boundary conditions for the flow and concentration fields and a given interfacial flux $\mathbf{n} \cdot \mathbf{F}^{(1)}|_\Gamma = q$, we have

$$p_a \, \alpha \, f'(C^{(0)}) \left(\langle \mathbf{u}^{(0)} \rangle_m \cdot \nabla_X \right) C^{(0)} = -\nabla_X \cdot \langle \mathbf{F}^{(0)} \rangle_m - \frac{\mathcal{P}}{\phi_m} q , \tag{4.4.14}$$

which generalises the leading-order averaged linear transport (4.3.24), by taking into account the advective nonlinearity.

We observe that the cell closure problem, constituted by (4.4.10) and (4.4.12) is identical to the cell problem in the linear case (4.3.15) and (4.3.16), studied in Section 4.3.2. The resulting closure relation (4.3.32) between the local averaged concentration flux $\langle \mathbf{F}^{(0)} \rangle_m$ and global concentration field $C^{(0)}$ allows us to complete the effective transport description.

Effective nonlinear transport: small Pe regime.

The closure relation (4.3.32) between the averaged local and global concentration gradients in Ω_m transforms the transport equation (4.4.14) to

$$p_a \, \alpha \, f'(C^{(0)}) \left(\langle \mathbf{u}^{(0)} \rangle_m \cdot \nabla_X \right) C^{(0)} = \nabla_X \cdot \left((\mathbf{I} - \langle \nabla_x \mathbf{b} \rangle_m) \cdot \nabla_X C^{(0)} \right) - \tfrac{\mathcal{P}}{\phi_m} q , \tag{4.4.15}$$

Using the superficial average $\langle \mathbf{u}^{(0)} \rangle \equiv \phi_m \langle \mathbf{u}^{(0)} \rangle_m$ and $\langle C^{(0)} \rangle \equiv C^{(0)}$, dropping the superscripts over the variables and the subscript X in ∇_X, we obtain, from (4.4.15), the effective description of transport in presence of solute-carriers for $\mathrm{Pe} = O(\varepsilon)$

$$\begin{aligned} & p_a \, \alpha \, f'(\langle C \rangle) \, \langle \mathbf{u} \rangle \cdot \nabla \langle C \rangle = \nabla \cdot (\mathsf{D}_{\mathrm{eff}} \cdot \nabla \langle C \rangle) - \mathcal{P} \, q , \\ & \langle C \rangle|_{X=0} = 1, \; \langle C \rangle|_{X=1} = 0, \quad \langle C \rangle \text{ is } Y\text{-periodic} , \end{aligned} \tag{4.4.16}$$

where $p_a \equiv \mathrm{Pe}/\varepsilon^2$, $q \equiv \mathrm{Da}/\varepsilon^2$, and $\mathsf{D}_{\mathrm{eff}}$ is the effective diffusivity tensor (4.3.36), which is found from a solution to the cell closure problem (4.3.30).

To account for advective effects at the microscale for $\alpha_0 \, \mathrm{Pe} \gtrsim 1$, analogously to Section 4.3.3, we repeat the homogenization procedure around the next organising centre (balancing global advective and uptake fluxes $\Phi_{\mathrm{adv}} \sim \Phi_{\mathrm{upt}}$ in (4.4.4)): $(\mathrm{Pe}, \mathrm{Da}) = (O(1/\alpha_0), O(\varepsilon))$ for $\alpha_0 = O(\varepsilon^{-1})$.

4.4.3 Moderate microscopic Péclet number transport regime

Setting $\alpha_0 = O(\varepsilon^{-1}) = \varepsilon^{-1} \, \alpha$, $\mathrm{Pe} = O(\varepsilon) = \varepsilon \, p$, $\mathrm{Da} = O(\varepsilon) = \varepsilon \, q_1$, $(\alpha, p, q_1 = O(1))$ and using (4.3.6), we write (4.4.3) as

$$\varepsilon p \left[1 + \varepsilon^{-1} \alpha f'(\tilde{C})\right] \left[\nabla_x \cdot (\tilde{C}\tilde{\mathbf{u}}) + \varepsilon \nabla_X \cdot (\tilde{C}\tilde{\mathbf{u}})\right] = -\varepsilon \left[\nabla_x \cdot \tilde{\mathbf{F}} + \varepsilon \nabla_X \cdot \tilde{\mathbf{F}}\right], \tag{4.4.17a}$$

$$\varepsilon \tilde{\mathbf{F}} = -\nabla_x \tilde{C} - \varepsilon \nabla_X \tilde{C}, \tag{4.4.17b}$$

$$\varepsilon \mathbf{n} \cdot \tilde{\mathbf{F}}|_\Gamma = \varepsilon q_1, \qquad \tilde{C}, \tilde{\mathbf{F}} \text{ are periodic on } S, \tag{4.4.17c}$$

$$\tilde{C}|_{X=0} = 1, \quad \tilde{C}_{X=1} = 0, \quad \tilde{C} \text{ is } Y\text{-periodic.} \tag{4.4.17d}$$

Substituting two-scale asymptotic series (4.3.9) in (4.4.17), and expanding the derivative f' according to (4.4.7), we find at $O(\varepsilon^0)$

$$p \alpha f'(C^{(0)}) \nabla_x \cdot \left(C^{(0)} \mathbf{u}^{(0)}\right) = 0, \tag{4.4.18}$$

$$\nabla_x C^{(0)} = 0, \tag{4.4.19}$$

which again reduces to $C^{(0)} = C^{(0)}(X)$, subject to the global boundary conditions (4.4.17d).

Collecting the terms in (4.4.17) at $O(\varepsilon^1)$, we have

$$\begin{aligned} &p \alpha f'(C^{(0)}) \left[\nabla_x \cdot \left(C^{(1)} \mathbf{u}^{(0)} + C^{(0)} \mathbf{u}^{(1)}\right) + \nabla_X \cdot \left(C^{(0)} \mathbf{u}^{(0)}\right)\right] + \\ &+ p \left[1 + \alpha f''(C^{(0)}) C^{(1)}\right] \nabla_x \cdot \left(C^{(0)} \mathbf{u}^{(0)}\right) = -\nabla_x \cdot \mathbf{F}^{(0)}, \end{aligned} \tag{4.4.20}$$

and

$$\mathbf{F}^{(0)} = -\nabla_x C^{(1)} - \nabla_X C^{(0)}, \tag{4.4.21}$$

where (4.4.20), similarly to (4.4.11), simplifies to

$$p \alpha f'(C^{(0)}) \left[\nabla_x \cdot \left(C^{(1)} \mathbf{u}^{(0)}\right) + \mathbf{u}^{(0)} \nabla_X \cdot C^{(0)}\right] = -\nabla_x \cdot \mathbf{F}^{(0)}, \tag{4.4.22}$$

subject to $\mathbf{n} \cdot \mathbf{F}^{(0)}|_\Gamma = q_1$.

Averaging (4.4.22) over the fluid-phase subdomain Ω_m of the unit cell, applying the no-slip condition $\mathbf{u}^{(0)}|_\Gamma = 0$, periodic boundary conditions for $\mathbf{u}^{(0)}$, $\mathbf{F}^{(0)}$ and $C^{(1)}$ on S (see Fig. 4.7), and a given interfacial diffusive flux $\mathbf{n} \cdot \mathbf{F}^{(0)}|_\Gamma = q_1$, we get

$$p \alpha f'(C^{(0)}) \left(\langle \mathbf{u}^{(0)} \rangle_m \cdot \nabla_X\right) C^{(0)} = -\frac{\mathcal{P}}{\phi_m} q_1, \tag{4.4.23}$$

which generalises the leading-order averaged linear transport at moderate Péclet number (4.3.44), by taking into account the advective nonlinearity, and it is also a regular limit of (4.4.14) for $p_a \sim q \gg 1$.

Although the leading-order concentration field $C^{(0)}(X)$ again decouples from the microscopic cell problem given by (4.4.21)–(4.4.22) at large Pe, we analyse the governing equations for $C^{(1)}$ in the following subsection to understand the role of nonlinear advection at the micro-scale.

Nonlinear transport cell-problem: moderate Pe regime

Equations (4.4.21)–(4.4.22), subject to boundary conditions and (4.3.10a), constitute the following unit cell problem:

$$\begin{aligned} & p\,\alpha\, f'(C^{(0)})\big]\left[\mathbf{u}^{(0)}\cdot\nabla_x C^{(1)}+\mathbf{u}^{(0)}\cdot\nabla_X C^{(0)}\right]=-\nabla_x\cdot\mathbf{F}^{(0)}\,, \\ & \mathbf{F}^{(0)}=-\nabla_x C^{(1)}-\nabla_X C^{(0)}\,, \\ & \mathbf{n}\cdot\mathbf{F}^{(0)}|_\Gamma=q_1\,,\quad C^{(1)},\ \mathbf{F}^{(0)}\ \text{are periodic on } S\,, \end{aligned} \tag{4.4.24}$$

or

$$\begin{aligned} & -\frac{1}{p\,\alpha\, f'(C^{(0)})}\,\nabla_x^2 C^{(1)}+\mathbf{u}^{(0)}\cdot\nabla_x C^{(1)}=-\mathbf{u}^{(0)}\cdot\nabla_X C^{(0)}\,, \\ & \mathbf{n}\cdot\nabla_x C^{(1)}\Big|_\Gamma=-\mathbf{n}\cdot\nabla_X C^{(0)}-q_1\,,\quad C^{(1)}\ \text{is periodic on } S\,, \end{aligned} \tag{4.4.25}$$

generalising the linear problem (4.3.47).

We see that although the unit cell problem (4.4.25) depends not only on the global concentration gradient but also on the slowly varying leading-order concentration itself, it remains a linear elliptical problem, albeit with inhomogeneous coefficients. Therefore, from the structure of source terms in (4.4.24a), similarly to (4.3.48), we look for a general solution in the form

$$C^{(1)}=a_1(\mathbf{x},C^{(0)})\,q_1-\mathbf{b_1}(\mathbf{x},C^{(0)})\cdot\nabla_X C^{(0)}+C_0^{(1)}\,, \tag{4.4.26}$$

where $C_0^{(1)}$ is a scalar independent of $\mathbf{x}$, and $a_1=a_1(\mathbf{x},C^{(0)})$, $\mathbf{b_1}=\mathbf{b_1}(\mathbf{x},C^{(0)})$ are some coefficients that satisfy the following cell problems:

$$\begin{aligned} & \nabla_x^2 a_1-p\,\alpha\, f'(C^{(0)})\,\mathbf{u}^{(0)}\cdot\nabla_x a_1=0\,, \\ & \mathbf{n}\cdot\nabla_x a_1=-1\ \text{ on }\Gamma\,, \\ & a_1\ \text{is periodic on } S,\quad \langle a_1\rangle=const\,, \end{aligned} \tag{4.4.27}$$

$$\begin{aligned} & \nabla_x^2\mathbf{b_1}-p\,\alpha\, f'(C^{(0)})\,\mathbf{u}^{(0)}\cdot\nabla_x\mathbf{b_1}=-p\,\alpha\, f'(C^{(0)})\,\mathbf{u}^{(0)}\,, \\ & \mathbf{n}\cdot\nabla_x\mathbf{b_1}=\mathbf{n}\ \text{ on }\Gamma\,, \\ & \mathbf{b_1}\ \text{is periodic on } S,\quad \langle\mathbf{b_1}\rangle=const\,. \end{aligned} \tag{4.4.28}$$

Here $\mathbf{u}^{(0)}$ is given by the corresponding microscopic Stokes flow (4.3.25). Setting $f'(C^{(0)})$ to 1 and $p\alpha\equiv \mathrm{Pe}\,\alpha_0$ to Pe in (4.4.27)–(4.4.28), we obtain the linear advection-diffusion-uptake of Section 4.3.3. In general, however, microscopic transport depends on a slowly varying leading-order concentration field. There is potential therefore to modulate the balance between advection and diffusion across the whole domain and within each unit cell, depending on the local value of $C^{(0)}$.

To expose more clearly the effect of nonlinear advection, we consider the limiting case of a uniform flow and one-dimensional transport in array of point sinks (which becomes exact at leading-order for a vanishingly small villous volume fraction $\phi=|\Omega_m|/|\Omega|$).

4.4.4 The role of non-linear advection in oxygen transport: one-dimensional point-sink-array example

Oxygen transport (4.4.3) in a one-dimensional periodic array of N point sinks is described by

$$\begin{aligned} &\mathrm{Pe}\,[1+\alpha_0 f'(C)]\,\frac{\mathrm{d}C}{\mathrm{d}x} = \frac{\mathrm{d}^2C}{\mathrm{d}x^2} - \mathrm{Da}\sum_{n=1}^{N}\delta(x-n)\,, \quad 0<x<\varepsilon^{-1} \\ &C|_{X=0}=1\,, \quad C|_{X=1}=0 \text{ or } C|_{X=X_0}=C_X|_{X=X_0}=0 \text{ for } 0<X_0\le 1\,, \end{aligned} \tag{4.4.29}$$

We first illustrate the dynamics of (4.4.29) by solving the problem numerically, using a non-linear adaptive solver of `COMSOL Multiphysics`. Results are shown in Figure 4.13(b). One can define the effective microscopic Péclet number $\mathrm{Pe}_{\mathrm{eff}} \equiv \mathrm{Pe}\,(1+\alpha_0 f'(C))$, which is a slowly varying function of the concentration field. Since the derivative of the dissociation curve (Fig. 4.13a) rises rapidly as the dissolved in blood oxygen concentration falls, this can lead to a significant increase in the effective Péclet number. Figure 4.13(b) indeed shows that there is a switch from an uptake-dominated (for $X \lesssim 0.7$) to an advection-dominated (for $X \gtrsim 0.7$) macroscopic transport regime (solid line), coinciding with a peak in $\mathrm{Pe}_{\mathrm{eff}}$ (dash-dotted line). This is further demonstrated by comparing with a linear solution (Fig. 4.13(c)) for two piecewise-constant values of $f'(C)$ averaged over the segments $(0, C_{\mathrm{th}})$ and $(C_{\mathrm{th}}, 1)$, where the threshold concentration to switch between the two levels is set to $C_{\mathrm{th}} = 0.7$. Since the Damköhler number is fixed to $\mathrm{Da} = 2\varepsilon^2$, we find the effective Péclet number moving in the (Pe Da)-parameter space from $\mathrm{U_D}$-asymptotic transport regime at the inlet to A-regime near the outlet (see Fig. 2.2(a) of Chapter 2).

We now explore the problem (4.4.29) within the homogenization framework. Similarly to the limiting case of Sec. 4.3.4, using $p_a\,\alpha \equiv \varepsilon^{-1}\,\mathrm{Pe}\,\alpha_0$, $q \equiv \varepsilon^{-2}\,\mathrm{Da}$ and assuming $\mathcal{P}\,q = const$ as $\mathcal{P} \sim \sqrt{\phi} \to 0$, the effective leading-order transport (4.4.14a) reduces to

$$\varepsilon^{-1}\,\mathrm{Pe}\,\alpha_0\,f'(C^{(0)})\,C_X^{(0)} = C_{XX}^{(0)} - \varepsilon^{-2}\,\mathrm{Da}\,, \tag{4.4.30}$$

for small Péclet number, and to

$$\mathrm{Pe}\,\alpha_0\,f'(C^{(0)})\,C_X^{(0)} = -\varepsilon^{-1}\,\mathrm{Da}\,, \tag{4.4.31}$$

for moderate Péclet number, subject to global boundary conditions $C^{(0)}|_{X=0}=1$, $C^{(0)}|_{X=1}=0$, or $C|_{X=X_0} = C_X|_{X=X_0} = 0$, for some $(0 < X_0 \le 1)$. We also remark on a diffusive boundary layer of thickness $O((\mathrm{Pe}\,\alpha_0)^{-1})$ developed at the downstream end, which is not captured by the leading-order problem (4.4.31) for large Pe, so that only a boundary condition at the inlet can be used.

Using Hill's law (4.4.2) to approximate oxygen-haemoglobin dissociation kinetics, and rewriting (4.4.31) as

$$\frac{\mathrm{d}f(C^{(0)})}{\mathrm{d}X} = -\frac{\mathrm{Da}}{\varepsilon\,\mathrm{Pe}\,\alpha_0}\,, \quad f(C) = \frac{C^n}{k^n + C^n}, \quad C^{(0)}|_{X=0} = 1, \tag{4.4.32}$$

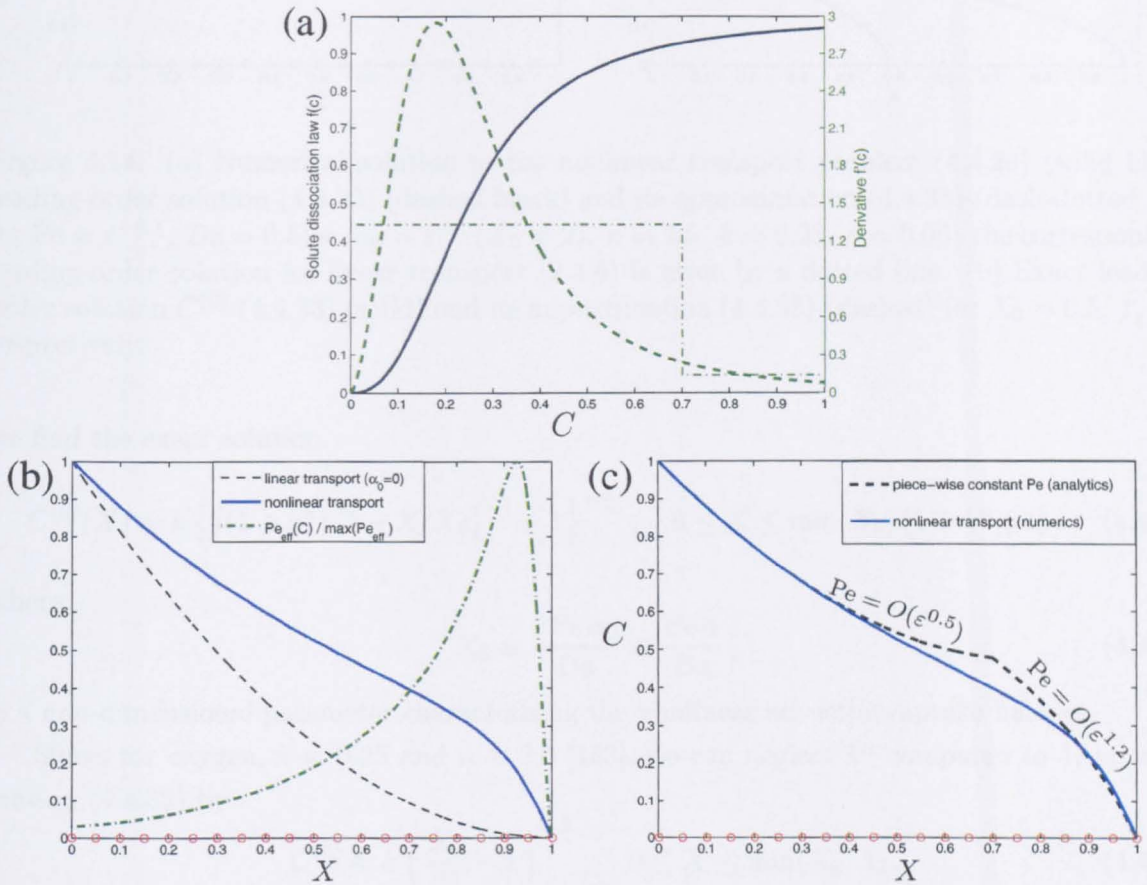

Figure 4.13. (a) Hill-type dissociation curve (4.4.2) for $f(C)$ (solid), its derivative (dashed) and a piecewise-constant approximation of $f'(C)$ (dash-dotted). (b) Numerical solution to (4.4.29) (solid) and the corresponding effective Péclet number $\mathrm{Pe}_{\mathrm{eff}} = \mathrm{Pe}\,(1 + \alpha_0\, f'(C))$ (dash-dotted) on a periodic array for $\mathrm{Pe} = \varepsilon^2$, $\mathrm{Da} = 2\varepsilon^2$, $\alpha_0 = 70$, $n = 2.5$, $k = 0.25$, $\varepsilon = 0.05$. The corresponding linear solution (for $\alpha_0 = 0$) is shown by the dashed line. (c) The nonlinear solution (solid) with continuously varying effective Péclet number and its linear approximation with piecewise-constant Pe (dashed) (chosen as shown by the dashed-dotted line in panel (a)).

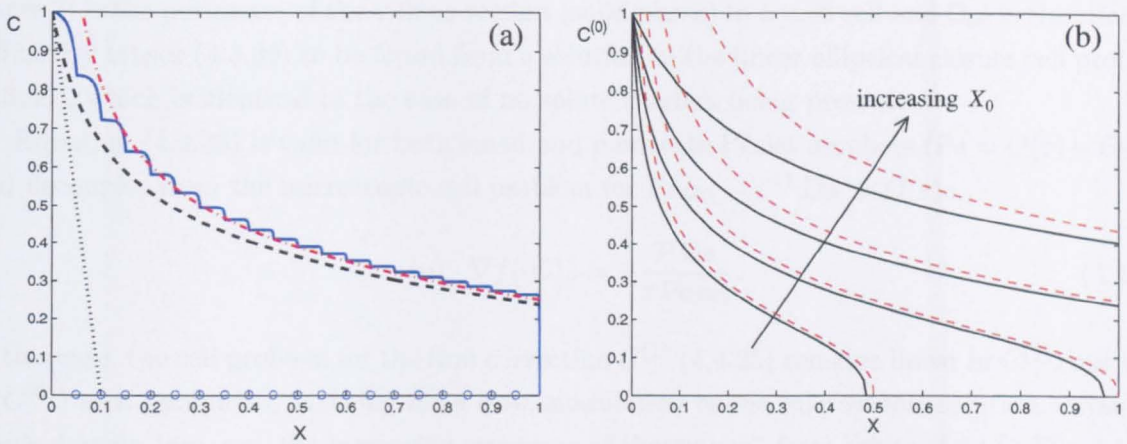

Figure 4.14. (a) Numerical solution to the nonlinear transport problem (4.4.29) (solid blue), leading-order solution (4.4.33) (dashed black) and its approximation (4.4.35) (dash-dotted red) for $\mathrm{Pe} = \varepsilon^{-0.1}$, $\mathrm{Da} = 0.5\mathrm{Pe}$, $\alpha_0 = \varepsilon^{-1}$ ($X_0 = 2$), $n = 2.5$, $k = 0.25$, $\varepsilon = 0.05$; the corresponding leading-order solution for linear transport (2.4.6) is given by a dotted line. (b) Exact leading-order solution $C^{(0)}$ (4.4.33) (solid) and its approximation (4.4.35) (dashed) for $X_0 = 0.5$, 1, 2, 5 respectively.

we find the exact solution

$$C^{(0)}(X) = k\left\{\left[(1+k^n)^{-1} - X/X_0\right]^{-1} - 1\right\}^{-\frac{1}{n}}, \quad 0 \le X \le \min(X_0/(1+k^n),\, 1)\,, \tag{4.4.33}$$

where

$$X_0 \equiv \frac{\varepsilon\,\mathrm{Pe}\,\alpha_0}{\mathrm{Da}} \equiv \frac{\mathrm{Pe}\,\alpha}{\mathrm{Da}}\,, \tag{4.4.34}$$

is a non-dimensional parameter characterising the nonlinear advection-uptake balance.

Since, for oxygen, $k \approx 0.25$ and $n \approx 2.5$ [153], we can neglect k^n compared to 1, approximating (4.4.33) by

$$C^{(0)} \approx k\left(\frac{X_0}{X} - 1\right)^{-\frac{1}{n}}, \quad 0 \le X \le \min(X_0,\, 1)\,, \tag{4.4.35}$$

which matches the exact solution reasonably well (Fig. 4.14). This is to be compared with the corresponding leading-order solution (2.4.6) $C^{(0)} = 1 - \frac{\mathrm{Da}}{\varepsilon\,\mathrm{Pe}}\,X$ to the linear transport problem (2.4.5). We note that when the nonlinearly-advected solute concentration extends to the entire domain ($X_0 = 1$), the concentration in the case of linear (solute-carrier-free) transport drops to zero at a characteristic distance $\varepsilon\mathrm{Pe}/\mathrm{Da} \equiv X_0/\alpha_0 \ll 1$ (see the dotted line in Fig. 4.14a).

4.4.5 Flow and transport in the presence of solute carriers: Summary

In this section, we have obtained the effective transport description for a solute, such as oxygen, in the presence of solute carriers, such as red blood cells, in a periodic media in one and two dimensions. We have found that the averaged macroscopic nonlinear transport equation (4.4.16a) is given by

$$\varepsilon^{-1}\,\mathrm{Pe}\,\alpha_0\,f'(\langle C\rangle)\,\langle \mathbf{u}\rangle \cdot \nabla\langle C\rangle = \nabla\cdot(\mathsf{D}_{\mathrm{eff}}\cdot\nabla\langle C\rangle) - \varepsilon^{-2}\,\mathcal{P}\,\mathrm{Da}\,, \tag{4.4.36}$$

where $\mathcal{P}$ is the perimeter of the villous section (solid phase) in a unit cell and D_{eff} is the effective diffusivity tensor (4.3.36) to be found from a solution to the linear elliptical closure cell problem (4.3.30), which is identical to the case of no solute carriers being present.

Equation (4.4.36) is valid for both small and moderate Péclet numbers ($\mathrm{Pe} = O(\varepsilon) - O(1)$), and decouples from the microscopic cell problem for $\mathrm{Pe}\,\alpha_0 \sim \varepsilon^{-1}\,\mathrm{Da} \gg O(\varepsilon)$:

$$\langle \mathbf{u} \rangle \cdot \nabla f(\langle C \rangle) = -\frac{\mathcal{P}\,\mathrm{Da}}{\varepsilon\,\mathrm{Pe}\,\alpha_0}\,. \tag{4.4.37}$$

In this case, the cell problem for the first correction $C^{(1)}$ (4.4.25) remains linear in $C^{(1)}$, but with $f'(C^{(0)})$ as a parameter, allowing for a slow modulation of the microscopic solution across the whole domain (see, e.g. the increasing steepness of the "stairs" from left to right in Fig. 4.14a). Since the ratio of solute carrier-capacity to blood plasma-capacity α_0 is typically very large [153, 179], we can approximate the effective Péclet number by $\mathrm{Pe}_{\text{eff}} \approx \mathrm{Pe}\,\alpha_0\,f'(C^{(0)})$, which thus becomes a slowly varying function of the macroscopic concentration field. This can lead to a switch from a diffusion- or uptake-dominated to an advection-dominated macroscopic transport regime within the same domain at constant Pe, as has been shown in Figure 4.13(b,c).

Furthermore, in the limit of small villous volume fraction, the solution to (4.4.37) can be approximated by (4.4.35)

$$C^{(0)} \approx k\left(\frac{X_0}{X} - 1\right)^{-\frac{1}{n}}, \quad X_0 \equiv \frac{\varepsilon\,\mathrm{Pe}\,\alpha_0}{\mathrm{Da}}, \qquad 0 \le X \le \min(X_0,\, 1)\,, \tag{4.4.38}$$

which incorporates in a compact form all transport and dissociation-kinetic parameters and exhibits a markedly different behaviour compared to a linear concentration drop for solute-carrier-free transport (Fig. 4.14a). The primary characteristics of the transport in a suspension of solute carriers is an enhanced advection in the regions of low dissolved solute concentration (by releasing the solute from the bounded form into the blood plasma). This makes the solute distributed more uniformly across the entire domain and allows for homogenization at higher Da than for linear transport. For example, the 1D homogenization limit becomes $\mathrm{Da} \ll \max\{1,\, \alpha_0\,\mathrm{Pe}\}$.

4.5 Discussion

To sum up, we have studied the effective macroscopic solute transport models and their corrections, extending the results of Chapter 2 to two spatial dimensions and accounting for nonlinear effects.

In particular, we have generalised the map of asymptotic transport regimes in $(\mathrm{Pe}, \mathrm{Da})$-parameter space for the case of a 2D periodic array of point sinks (Fig. 4.6). We have developed a computational framework for estimating the effective diffusivity and permeability for sinks of a finite size, exploring the role of villous volume fraction. The transport regime and the accuracy of the effective (averaged) solute transport description therefore in general depend on the villous volume fraction ϕ, Péclet and Damköhler numbers, as well as on the statistical properties of the micro-geometry (characterised for a regular media by the scale-separation parameter ε; see also Sec. 3.6 of Chapter 3).

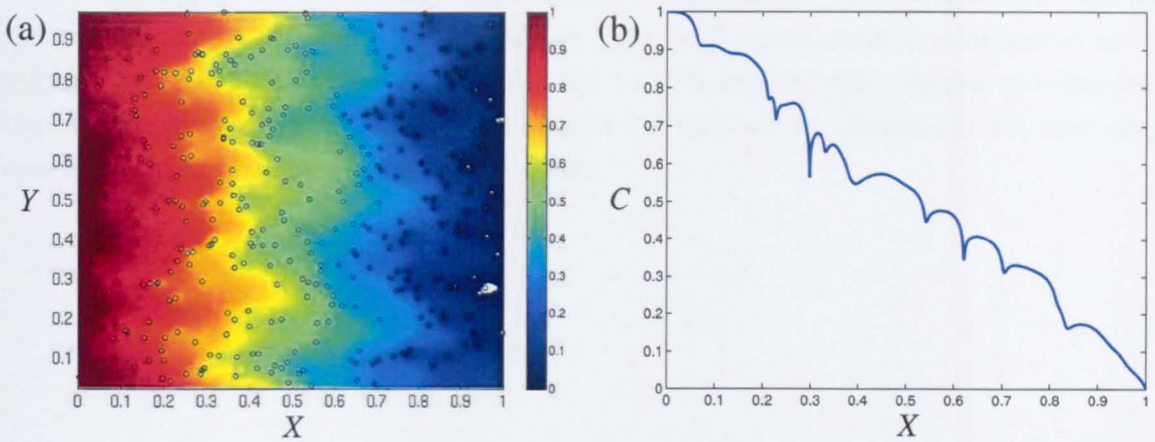

Figure 4.15. (a) Numerical solution C (colours) to (4.2.2) for a single realisation of a normally-perturbed square-periodic array of 19×19 point sinks ($\varepsilon = 0.05$), with $\mathrm{Pe} = 4$, $\mathrm{Da} = \varepsilon\mathrm{Pe}$, and the standard deviation $\sigma = \varepsilon$; black circles indicate the sinks' position. (b) The corresponding concentration profile C along the horizontal cross-section through the middle of the array ($Y = 0.5$).

Further studies could focus on understanding the statistical properties of the homogenization residue for transport in random arrays in two dimensions. For example, if one considers a normally-perturbed square-periodic array on a torus (with periodic boundary conditions), as shown in Figure 4.15(a), stochasticity breaks the transverse symmetry of the solute distribution (*cf.* Fig. 4.4a). However, cross-sections of the concentration field (Fig. 4.15b) can be studied and compared against corresponding one-dimensional results of Chapter 3.

Finally, we have investigated the role of solute carriers and developed further Lardner's analysis [153] of oxygen exchange to understand the effect of placental microstructure on non-linear advective transport. The homogenized effective equations are similar to the results of Salathe *et al.* [224, 226] obtained by volume averaging in vascular networks; however, the homogenization results of this chapter offer more details on the interaction between the macro- and macro-scales. We have shown, for example, that the transport regime in (Pe, Da)-parameter space becomes dynamic, sensing the leading-order concentration and "homogenising" the solute distribution across the oxygen-poor parts of the domain (see Fig. 4.13c). Indeed, as has been discussed in Section 2.8 of Chapter 2, a likely range of Péclet and Damköhler numbers for intervillous transport of oxygen is $\mathrm{Pe} \sim 10 - 10^2$, $\mathrm{Da} \sim 1 - 10$. Taking $\varepsilon \sim 10^{-2}$, we have $\mathrm{Da}/(\varepsilon\mathrm{Pe}) \gtrsim 1$. Therefore, without a contribution of the solute carriers, the distribution of solute could be highly non-uniform, with the solute concentration falling sharply close to the inlet (as illustrated in Fig. 4.14(a) for $\mathrm{Da}/(\varepsilon\mathrm{Pe}) = 10$). Apart from placental transport, potential applications of this model include gas exchange in a capillary network [225, 271], solute transport in certain bioreactors [1], dialysis machines [265] and other artificial organs [145, 213]. The role of haemoglobin-containing erythrocytes as oxygen-carriers can be shared in full or in part by other biological metalloproteins, such as haemocyanin [102], and by artificial blood substitutes, such as Polyheme or Perftoran [141].

We now apply the developed computational framework for the effective flow and transport parameters at leading order (4.3.34)–(4.3.35), with corresponding microscopic unit cell problems (4.3.29)–(4.3.30) (see also Figs 4.9 and 4.11), to anatomically realistic two-dimensional shapes of the materno-fetal interface Γ in a unit cell that will be obtained in the next chapter from histological images of the human placenta.

Placental Shape Analysis and Effective Parameter Estimation

5.1 Introduction

This chapter describes imaging techniques and statistical tools to analyse placental geometry. The purpose of the "homogenized" description outlined in Chapters 2–4 is to inform a macroscopic model with the properties of the microstructure, gathered from experimental data. In the human placenta this amounts to characterising the geometry of villous tissue.

Stereology (or "quantitative microscopy") is a quantitative statistical description of three-dimensional heterogeneous material composition from its two-dimensional microscopic sections, utilising systematic random sampling [16, 171]. Placental stereology has provided estimates of bulk quantities (e.g. total villous volumes, surface areas and lengths) and local measures such as star volumes (the mean volume of all parts of a space which are visible when viewed in all directions from a given point within it) [206]. For a spatially homogeneous isotropic media, all the following empirical estimates are asymptotically unbiased [16]:

$$\phi_{\text{volume}} = \phi_{\text{area}} = \phi_{\text{linear}} = \text{Test points ratio}, \tag{5.1.1}$$

where $\phi_{\text{volume}} \equiv \phi$, ϕ_{area}, ϕ_{linear} are the volumetric, area and linear fraction (or density) of a given phase in heterogeneous media, and Test points ratio $\equiv N(\mathbf{x} \in \text{phase})/N_{\text{total}}$ is a proportion of N_{total} random test points falling onto this phase. Although stereology provides unbiased and computationally efficient estimates, it should be pointed out that "if the material is not spatially homogeneous and isotropic, classical stereological methods do not apply" [16]. Therefore, owing to the complexity of placental anatomy, further measures, particularly of averaged bulk properties and statistical variability at different spatial scales, are necessary in order to develop comprehensive models of placental transport.

We use fluorescent immunohistochemistry and ionic toluidine blue staining to visualise histological sections of normal placentas. Using histological images, we illustrate how methods of spatial statistics [82] can be applied to characterise some of the important underlying length-scales in villous trees. We further compute microscopic flow and transport in a sample unit cell to extract the effective permeability and diffusivity of the medium. The images from the digital microscopy are post-processed and analysed with open-source software packages `ImageJ` and `R` as described below.

5.2 Methods

The experimental data of this chapter is based on placentas from pregnancies monitored at the Queen's Medical Centre in Nottingham. Local ethics committee approval and written

patient consent were obtained (for more details, see [156]). All tissue sections were cut from a single maternal lobule taken from the periphery of a normal full-term human placenta (delivered by elective cesarian section). The placental lobule was frozen in liquid nitrogen-cooled isopentane (at ca. -160 °C), stored in a -80 °C freezer and defrosted to about -20 °C before cutting into 8 μm-thick sections, according to a systematic random sampling protocol shown in Figure 5.1. Note that a single placental lobule, delineated by the grooves of the placental septa, can contain several chorionic trees (see Figs 1.1, 1.2) and therefore is not necessarily identical to a single placentone; however, the smaller peripheral lobules tend to match the corresponding placentones [33] (see Fig. 5.2).

5.2.1 Specific and non-specific staining for digital microscopy

Digital microscopy of tissue samples requires them to be biochemically stained in order to get acceptable contrast and reduce the amount of background noise and artifacts.

One of the most common non-specific staining used to highlight all tissue structures is the tolonium chloride (Toluidine Blue) dye that reacts with the most common anionic (negatively charged) groups (e.g. COO^-, SO_4^{2-}) of DNA, polysaccharides, and other molecules in cells. The cell nuclei are stained in blue while the extracellular matrix is stained in purple [81, 218]. The benefit of this method is in giving uniformly high-contrast contours of the chorionic villi as well as medium-to-large feto-placental vasculature. The images can be taken at any resolution allowed by a conventional bright-field objective ($\times 1.5$ to $\times 100$, using the available microscopes `Nikon LaboPhot-2` and `Zeiss Axioplan`, in conjunction with the digital cameras `Nikon DS-Fi1` 1.2 Mpx and `QImaging MicroPublisher` 5 Mpx respectively). The shortcomings of the non-specific staining are the inability to distinguish between vascularised and non-vascularised villi, especially of the terminal villi and immature villous sprouts [33], and the higher level of artifacts in the intervillous space as compared to the specific staining.

The specific staining in histochemistry is primarily due to the use of antibodies raised as a result of the immunologic response to a biological structure (antigen) of interest in laboratory animals. In the indirect method, the primary antibody of, say mouse, binds specifically with a high affinity to, e.g. human cytokeratin-7 found in the epithelial and trophoblast cells. The secondary antibody is raised in the rabbit against mouse antibodies and is subsequently conjugated with a detectable label (radioactive isotope, chemically active enzyme or fluorescent dye). The secondary antibody therefore reacts specifically with the layer of the primary (mouse) antibodies and amplifies the overall staining [198] (see Fig. 5.3). We used the protocols developed by Leach *et al.* [157], where two different sets of primary and secondary antibodies are employed for double-immunostaining (Fig. 5.4a). The limitations of the fluorescent immunostaining are the spatially varying staining brightness, due to a non-uniform distribution of antibodies over the section, and the need for a higher optical magnification ($\times 6.3$ and more) in order to obtain appropriate resolution and contrast of the microscopic images. Figure 5.4 shows the acquired images for specific (a) and non-specific (b) staining of samples from the normal human placenta.

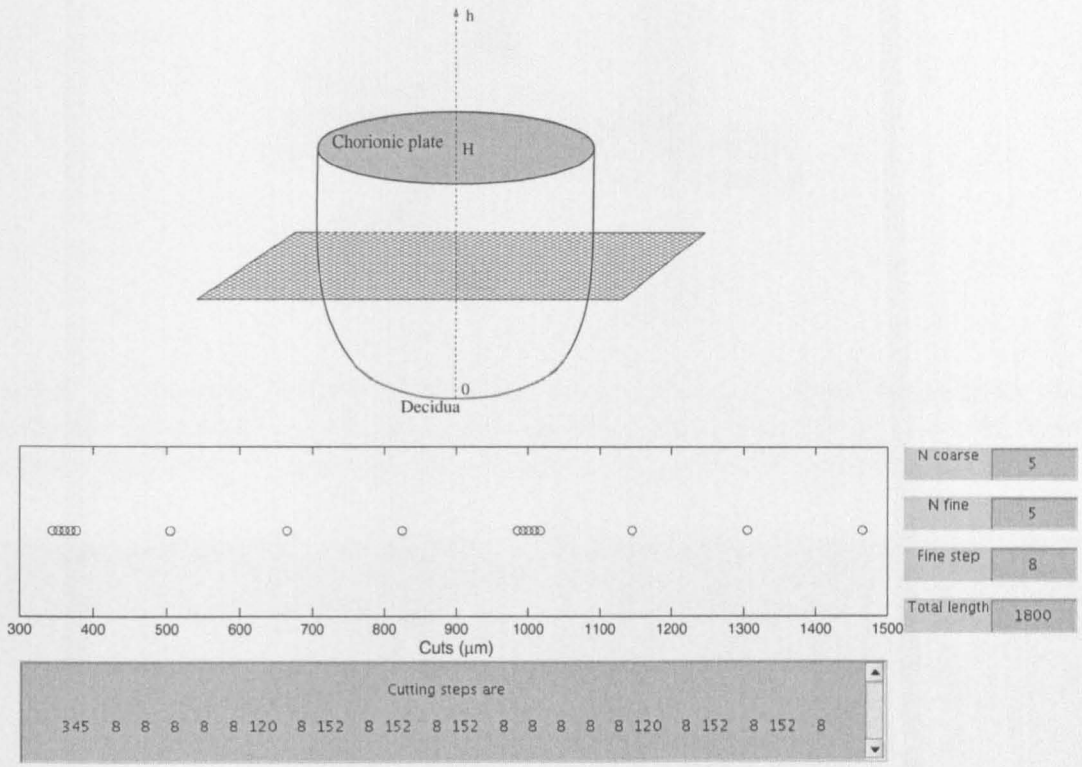

Figure 5.1. Approximate positions of 16 horizontal sections (of 8 μm thickness each) of a single peripheral maternal lobule of the normal human placenta used in the protocol for cutting with a cryostat. The initial and intermediate cutting positions were randomised. All dimensional values are given in μm.

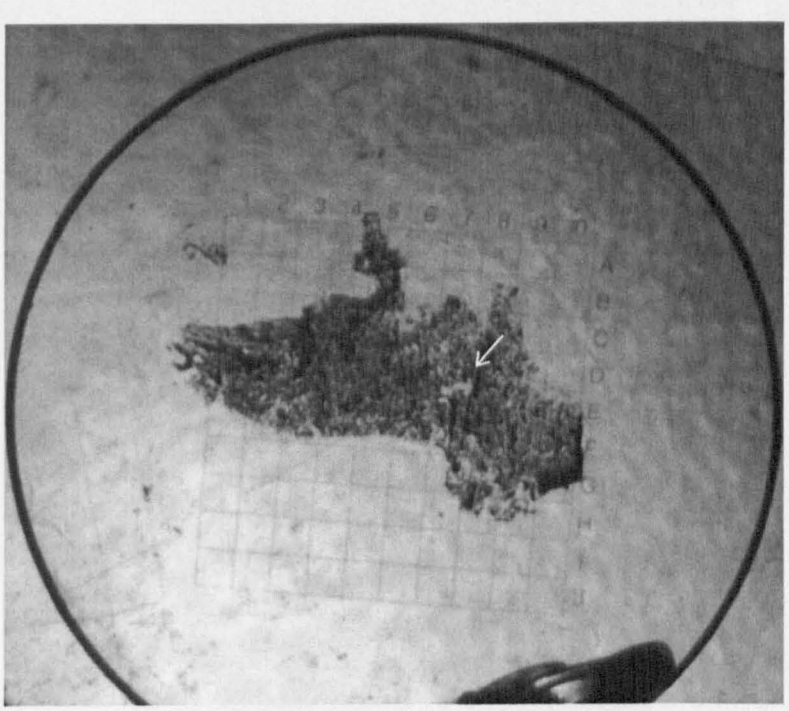

Figure 5.2. A macroscopic survey of the toluidine blue-stained cross-section No. 11 of a normal peripheral placental lobule (see protocol in Fig. 5.1) with a superimposed reference millimetre grid. Note a loose central area (arrow), resembling the central cavity of a placentone (*cf.* Fig. 1.2).

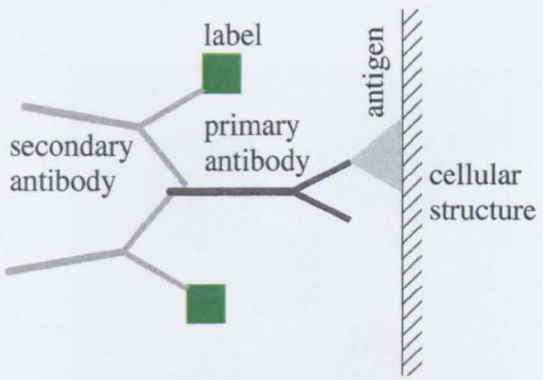

Figure 5.3. A schematic of the indirect immunostaining method, where the primary antibody is specific for the antigen (a part of the cellular structure of tested tissue), and the secondary antibody, labelled with a fluorescent dye, is specific for the primary antibody.

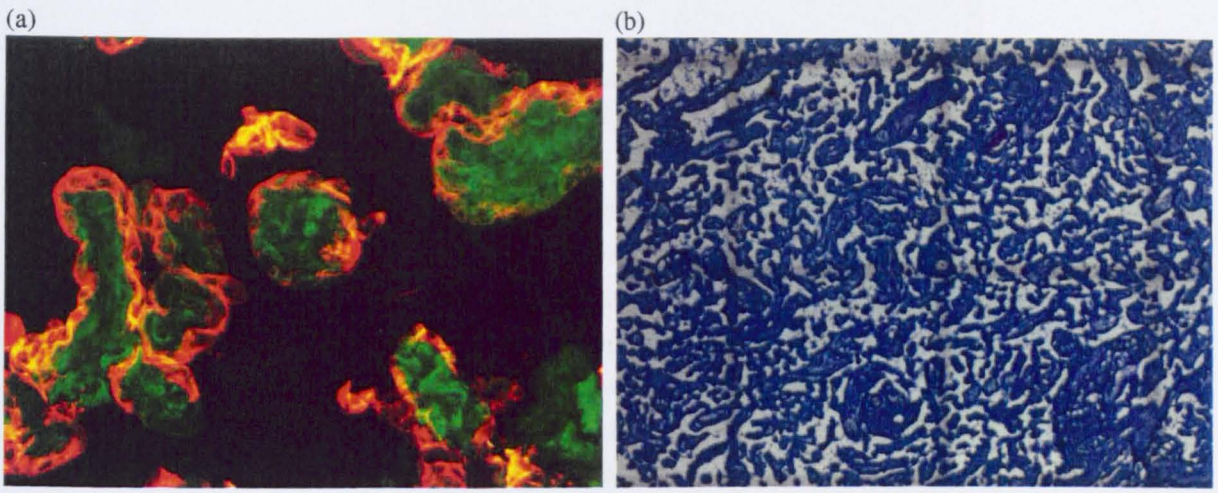

Figure 5.4. Sample images of the normal human placental chorionic villi: (a) fluorescent immunostaining specific for V-Cadherin of endothelial junctions in vessels (green) and for Cytokeratin-7 of trophoblast cells (orange)[1] (optical magnification ×20); (b) non-specific Toluidine Blue staining of most cellular structures (nucleic-acids, carbohydrates, etc.) in cross-section No. 11 at optical magnification ×2.5, revealing the chorionic villi and the medium-to-large blood vessels within them. (the reference grid with 1 mm spacing is shown as a grey shadow).

5.2.2 Morphology image processing and spatial statistics

In order to extract the statistical properties of the villous geometry from the histological sections we use the methods of statistical shape analysis [83] and spatial point processes [82].

The open-source software `ImageJ` is used for a semi-automated morphological analysis (computing area fractions, identifying villous contours, calculating their perimeters and centres of mass) [189]. The command menu sequence is as follows: (i) Image → Adjust → Threshold → Black & White (converts a greyscale/colour bitmap to a black & white 8-bit bitmap); (ii*) Image → Color → Edit LUT → Invert (sets black particles on white background); (iii) Analyze → Set Scale (relates the "distance in pixels" to a known dimensional length, e.g. by using the reference millimetre grid over-imposed on the slide during microscopy as shown in Fig. 5.4b); (iv*) Process → Noise → Despeckle (deletes sharp-contrast noise of a few pixels in diameter –

[1]Tissue sample obtained from the central placental lobule by Ruta Deshpande.

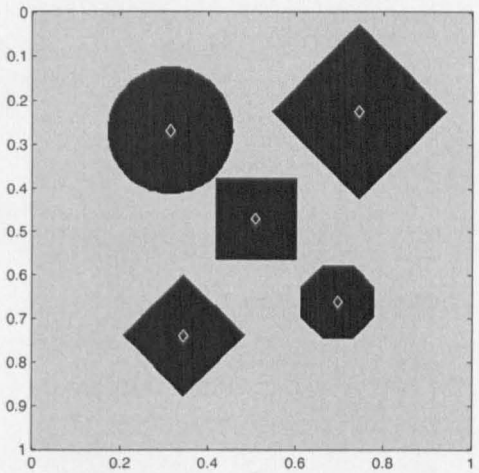

Figure 5.5. A test image with randomised positions and sizes of geometrical objects used to verify the accuracy of `ImageJ` morphology analysis.

the operation (iv) can be repeated several times); (v*) Process → Binary → Watershed (breaks continuous villous contours into independent particles in the thinnest junctions); (vi) Analyze → Set Measurements → Center of Mass, Perimeter, Area; (vii) Analyze → Analyze Particles → Show: Outlines, Display Results, Summarize (performs morphology analysis). The operations marked with * are optional when calculating only villous area fractions but they are required for more specific information on villous "particles".

We employ the statistical package `R` to analyse the pattern of the villous centres of mass extracted by `ImageJ`. The K-function is used to estimate the cross-correlation of intervillous distances and to test the pattern for regularity or clustering as compared to the "complete spatial randomness" represented by a Poisson point process [82], which will be explained in more detail below.

5.3 Estimation of the unit-cell-size with respect to the villous area fraction

The accuracy of the "Analyze Particles" algorithm of `ImageJ` has been tested using an image with known total area fraction ($\phi \simeq 0.24$) and particle centres of mass coordinates, generated with `Matlab` (Fig. 5.5). The output of the `ImageJ` algorithm differs from the exact values by less than 1%.

The question to be addressed is how the area fraction depends on the window size used for its calculation. When the window size is less than the spatial dimension of terminal villi ($\sim$ 100 μm), we expect substantial oscillations of the villous area fraction between zero and one, depending on whether the window falls in the villous tissue or in the intervillous space. As we increase the window size, the sensitivity of the window's position on the area fraction reduces, and at large enough macroscopic spatial scales we can treat the homogeneous porous medium as a continuous medium of constant (or at least slowly varying) area fraction. The

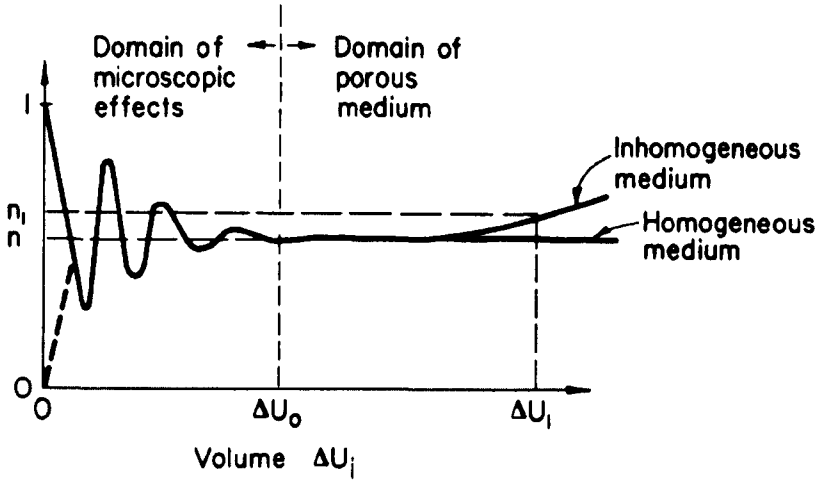

Figure 5.6. Volumetric fraction of i^{th} phase in a porous medium *vs.* volume of consideration ΔU_i. The minimal volume ΔU_0 that significantly reduces microscopic noise effects is a representative elementary volume (REV) of the porous medium (reproduced from [29]).

smallest size of the window that ensures negligible variation of area fraction due to fluctuations of the microstructure is called a *representative elementary area* (REA) (being a two-dimensional analogue of representative elementary volume (REV), shown in Fig. 5.6). The REA defines a *meso-scale* of 2D porous medium, being intermediate between the micro-scale of an individual villus and the macro-scale of the whole placentone. It is the meso-scale of REA (or REV) at which Darcy's law of flow in a porous medium (1.4.15) operates most accurately.

Keeping the REA concept in mind, we study the variability of the villous area fraction with size of the selection window in `ImageJ`. We process the right-hand-side of cross-section No. 11 (obtained according to the protocol; see Fig. 5.1) taken at optical magnification $\times 2.5$. Following the procedures described in Sec. 5.2.2, we compute void area fractions $(1 - \phi)$ of the inverted black-and-white image at different sizes of the selection window (see Fig. 5.7)[2].

Figure 5.7 shows how the villous area fraction ϕ depends on the size W of the window used to compute it. When W is comparable to the diameter of terminal villi (below 100 μm), we see vigorous oscillations of ϕ, depending whether the window falls in villous tissue or intervillous space. As W increases, variations in ϕ fall and are significantly reduced for $W \gtrsim 1$ mm. Above this threshold, we can reasonably treat the intervillous space in this sample as a continuous medium of uniform (or at least slowly varying) area fraction, as was assumed in [74, 86] for example. $W_0 = 1$ mm can be used as a reference size for the unit cell in the homogenization method (see Sec. 4.3 of Chapter 4).

[2]One should note that the reference millimetre grid could affect the thresholding procedure, described in Sec. 5.2.2, by sharpening some boundaries; however, the effect of the grid is believed not to affect the results due to the low contrast and large grid-spacing compared to the contrast and lengthscales of the villous tissue.

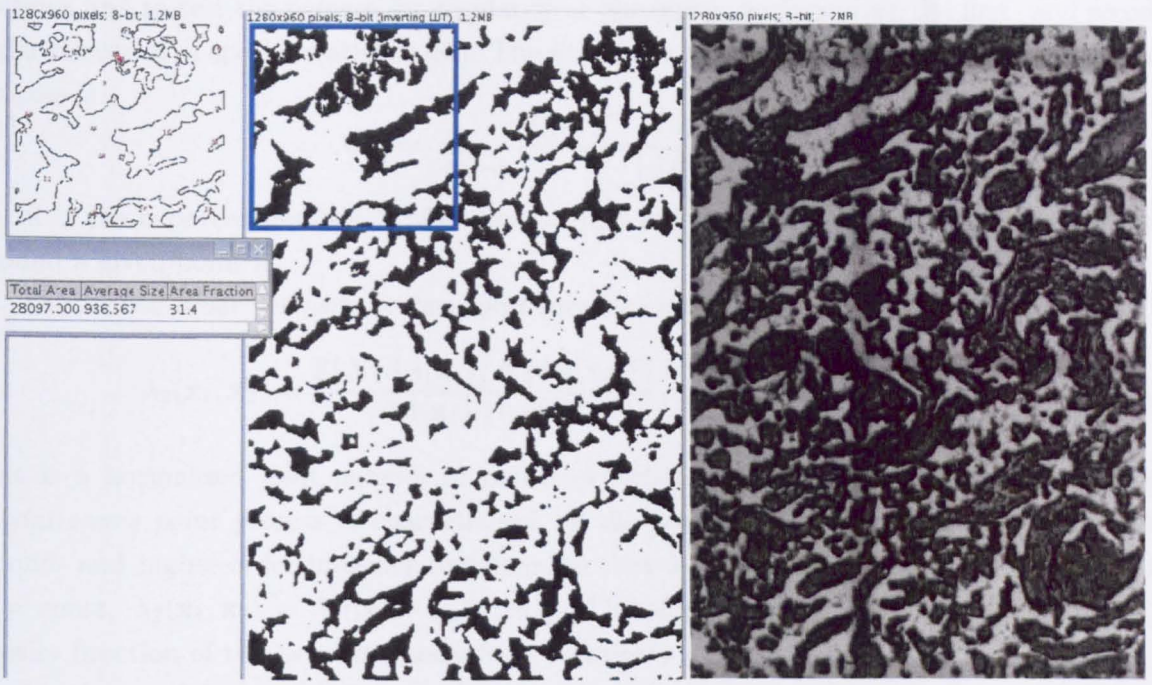

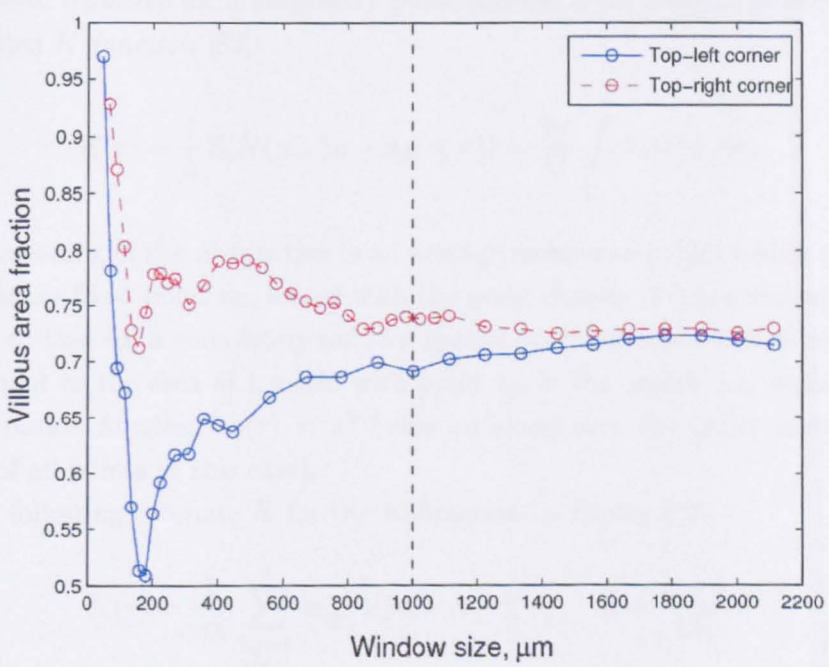

Figure 5.7. Determination of a villous meso-scale with respect to the area fraction. Top: computation procedure for the window size $W = 300$ px ≈ 670 μm (solid blue), taken from the left-top corner; Bottom: villous area fraction dependence on the window size for windows taken from the top-left (solid blue) and top-right (dashed red) corners of the sample shown in Fig. 5.4b.

5.4 Spatial villous pattern of the normal human placenta

In order to quantify the distribution of the villous "particles" in the histological cross-sections and to test the pattern for regularity or clustering, we introduce the first- and second-order measures of spatial statistics [82]. The *first-order intensity* or "density" of a spatial point process is

$$\lambda(\mathbf{x}) = \lim_{|\mathrm{d}A|\to 0} \frac{\mathbb{E}[N\{\mathbf{x}' : \mathbf{x}' \in \mathrm{d}A(\mathbf{x})\}]}{|\mathrm{d}A|}, \tag{5.4.1}$$

i.e. it is the expected number N of points per unit area, where $\mathrm{d}A(\mathbf{x})$ is an infinitesimal area around a given point $\mathbf{x}$.

The *second-order intensity* or *two-point correlation function* is defined as

$$\lambda_2(\mathbf{x}_1, \mathbf{x}_2) = \frac{\mathbb{E}[\,N\{\mathrm{d}A(\mathbf{x}_1)\}\,N\{\mathrm{d}A(\mathbf{x}_2)\}\,]}{|\,\mathrm{d}A(\mathbf{x}_1)|\,|\,\mathrm{d}A(\mathbf{x}_2)|}, \quad |\,\mathrm{d}A(\mathbf{x}_1)|, |\,\mathrm{d}A(\mathbf{x}_2)| \to 0\,, \tag{5.4.2}$$

that is a normalised joint number of points expected around two given points $\mathbf{x}_1$ and $\mathbf{x}_2$. A *stationary point process* is characterised by the spatial translational invariance of first-, second- and higher-order intensity functions, so that $\lambda_2(\mathbf{x}_1 + \mathbf{a}, \mathbf{x}_2 + \mathbf{a}) = \lambda_2(\mathbf{x}_1, \mathbf{x}_2))$, giving $\lambda = \text{const}$, $\lambda_2(\mathbf{x}_1, \mathbf{x}_2) = \lambda_2(|\mathbf{x}_1 - \mathbf{x}_2|)$ [261]. Therefore (5.4.2) is related to the probability density function of two-point distances for a stationary point process [82].

Another useful quantity for a stationary point process is an integral measure of two-point correlation, called *K-function* [82]:

$$K(r) = \frac{1}{\lambda}\,\mathbb{E}[N\{\mathbf{x} : |\mathbf{x} - \mathbf{x}_0| \le r\}] = \frac{2\pi}{\lambda^2} \int_0^r \lambda_2(r)\, r\, \mathrm{d}r\,. \tag{5.4.3}$$

The empirical meaning of the K-function is an average number of points within a given distance r from an arbitrary fixed point $\mathbf{x}_0$, scaled with the point density λ (expected number of points per unit area), so that for a completely random spatial point process (Poisson process) we have this number equal to the area of a circle with point $\mathbf{x}_0$ in the centre, i.e. equal to πr^2 (with two-point correlation function $\lambda_2(r) = \lambda^2$ being constant over the entire domain due to the independence of all points in this case).

We use the following estimate $\hat{K}$ for the K-function by Ripley [82]:

$$\hat{K}(r) = \frac{1}{n\hat{\lambda}} \sum_{\substack{i,j=1 \\ (i\neq j)}}^{n} w_{ij}^{-1}\, \mathrm{I}(|\mathbf{x}_i - \mathbf{x}_j| \le r)\,, \quad \hat{\lambda} = \frac{n-1}{|A|}\,, \tag{5.4.4}$$

where n is the total number of points in a given rectangular domain of area $|A|$, I is an indicator function that is equal to 1 if $\mathbf{x}_i$, $\mathbf{x}_j$ lie within a distance r, and is equal to 0 otherwise; w_{ij} is Ripley's trigonometric weighting function to correct for the edge effects [82].

To estimate the variance of $\hat{K}$ for a completely random (uniformly Poisson) distribution, we employ the formula by Lotwick and Silverman

$$\mathbb{E}[\hat{K}_{\text{Poisson}}] = \pi r^2 ,$$
$$\mathbb{V}ar[\hat{K}_{\text{Poisson}}] = \frac{|A|^2}{n(n-1)} \left(2b(r) - a_1(r) + (n-2)a_2(r) \right) , \tag{5.4.5}$$

where a_1, a_2 and b are Lotwick and Silverman's polynomials [161]: $a_1(r) = |A|^{-2}(0.21Pr^3 + 1.3r^4)$, $a_2(r) = |A|^{-3}(0.24Pr^5 + 2.62r^6)$ and $b(r) = \pi r^2|A|^{-1}(1 - \pi r^2|A|^{-1}) + |A|^{-2}(1.0716Pr^3 + 2.2375r^4)$, P being the perimeter of the domain. The estimate (5.4.5b) is exact for r not exceeding 1/4 of the smallest side of a rectangular domain [161]. We estimate $\hat{K}$ in (5.4.4) and (5.4.5) using the `Kest` function of the `Spatstat` package for `R` [17].

Before analysing the villous pattern, we illustrate the K-function by considering some standard point distributions shown in Figures 5.8–5.9. The uniformly random distribution (Fig. 5.8(a,b)) has the K-function indistinguishable (within a theoretical 95%-confidence interval, shown by dashed lines), from a Poisson process, as expected, while the K-function for a more regular hard-core distribution (Fig. 5.8(c,d) generated by a sequence of points drawn from a uniform distribution, not closer than distance d apart) falls below the lower bound of the theoretical confidence interval at small distances, with no points at $r < d$. On the other hand, for a Neyman-Scott cluster process (Fig. 5.8(e,f)), the K-function demonstrates higher average number of points than for a Poisson process. The Neyman-Scott cluster process is generated by a two-level algorithm [253]: first, "parent" points, defining the centres of clusters, are drawn from a Poisson process of a given intensity (mean number of points per unit area); next, the "daughter" points (e.g. representing the actual villous branches) are generated within each cluster of a fixed radius according to a hard-core distribution (mimicking the finite size of the villous cross-sections). Note that at larger distances both hard-core and Neyman-Scott distributions can become indistinguishable from a uniformly random; this however strongly depends on the parameter values of the distributions.

In addition we consider, following [257], a distribution with underlying regularity, such as a normally-perturbed square periodic array (with a given standard deviation σ and periodic boundary conditions). The K-function corresponding to the normally-perturbed distribution (Fig. 5.9(a,b) exhibits clear oscillations near the theoretical curve for a Poisson process at moderate σ, approaches the uniformly random case for large σ (Fig. 5.8b) and develops clear steps in the limit of $\sigma = 0$ (Fig. 5.9(c,d)). Finally, we highlight the limitations of the K-function inference approach by drawing a "cell" point process of Baddeley and Silverman [18], which has the same first- and second-order intensities, and thus K-function, as a homogeneous Poisson process (Fig. 5.9f), while qualitatively exhibiting a more regular pattern with occasional dense clusters than one expects from a completely random distribution (*cf.* Figs 5.8(a) and 5.9(e)). The Baddeley-Silverman cell-process is generated by subdividing the domain into a regular lattice of rectangular cells, where each cell contains 10 uniformly randomly distributed points with probability 1/90, 1 point with probability 8/9, or no points with probability 1/10 [18].

We now proceed with the analysis of actual histological data of a normal mature placenta. The centres of mass of villous "particles" from a cross-section sample were extracted with `ImageJ` according to the protocol described in Sec. 5.2.2. We estimate the K-function (5.4.4) and the sample variance of a Poisson distribution (5.4.5), representing "complete spatial variance", using

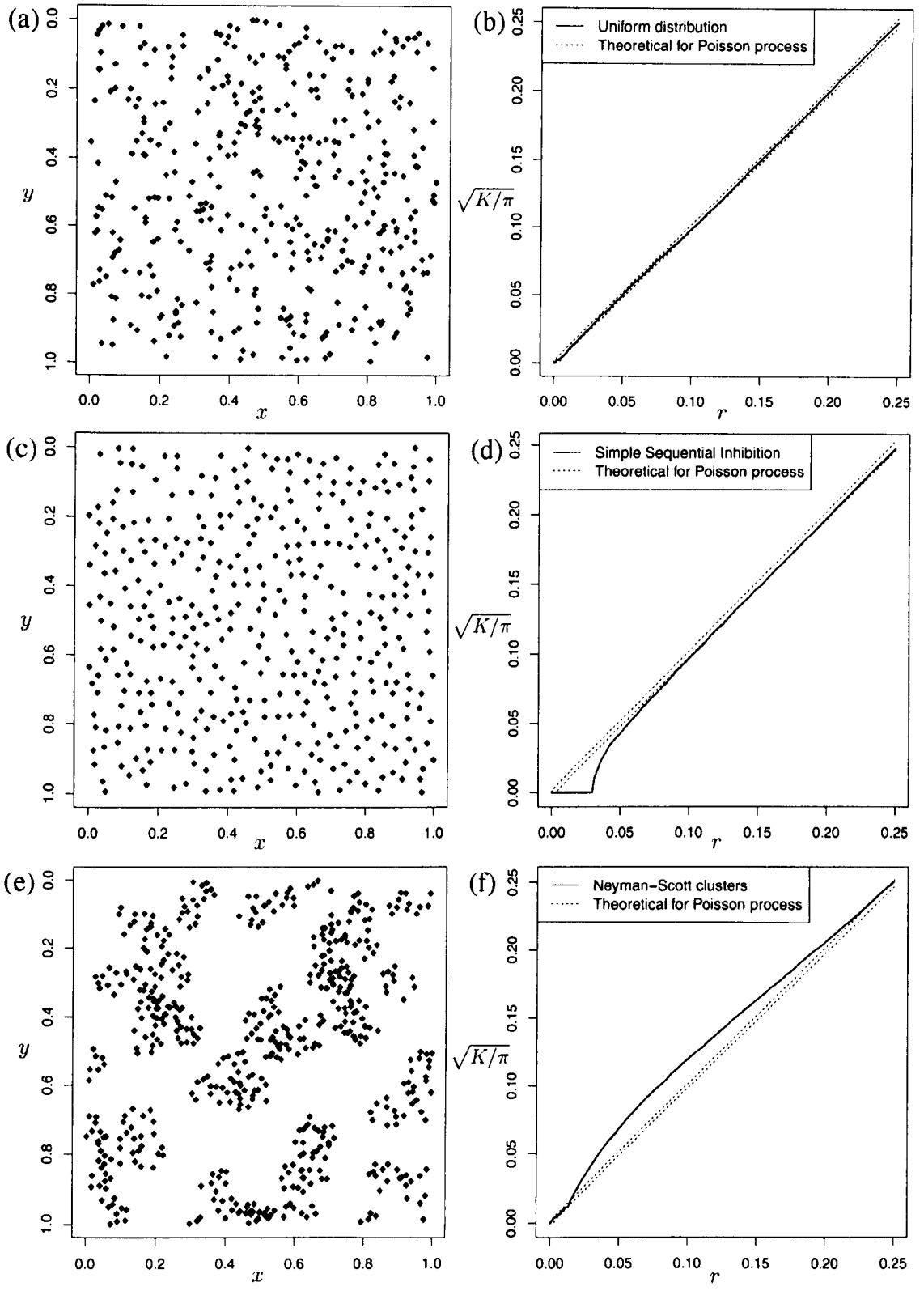

Figure 5.8. Examples of standard point patterns (left) and corresponding computed K-functions (right). (a) Uniformly-random distribution of $N = 400$ points, and (b) the corresponding linear $\sqrt{K}$-function (solid), with a 95%-confidence theoretical interval $\left(\mathbb{E}[\hat{K}] \pm 2\sqrt{\mathbb{V}\mathrm{ar}[\hat{K}]}\right)^{1/2}$ (dashed) given by (5.4.5) for a completely random (Poisson) point distribution; (c,d) Hard-core (simple sequential inhibition) point process with $N = 400$ points and minimal-distance parameter $d = 0.6\varepsilon$ ($\varepsilon = 1/\sqrt{N} = 0.05$); (e,f) Neyman-Scott cluster process for parent cluster-centre intensity $\lambda = 50$, cluster radius $R = 0.054$, number of daughter points $N = 10$ and daughter hard-core parameter $d = 0.4\varepsilon$ ($\varepsilon = 2R/\sqrt{N} \approx 0.03$).

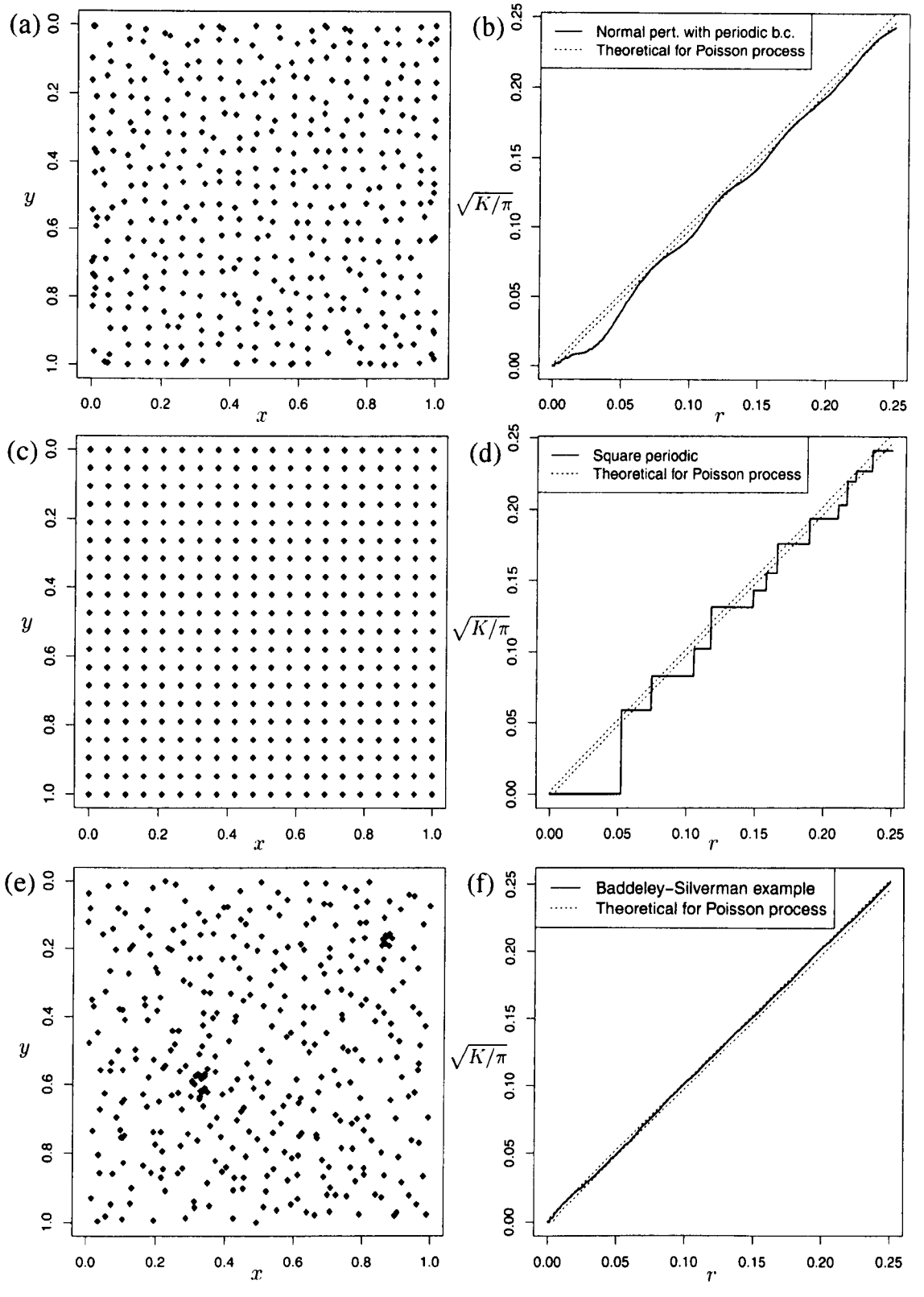

Figure 5.9. Figure 5.8 contd. (a,b) Normally-perturbed square periodic array 20×20 ($\sigma = 0.15\varepsilon$, $\varepsilon = 0.05$); (c,d) square periodic array 20×20, used as an unperturbed configuration for (a); (e,f) Baddeley-Silverman's cautionary example of a non-Poisson process (for the domain divided into 20×20 equal cells), giving "false-positive" conclusion of a complete spatial randomness, as indicated by the K-function (f).

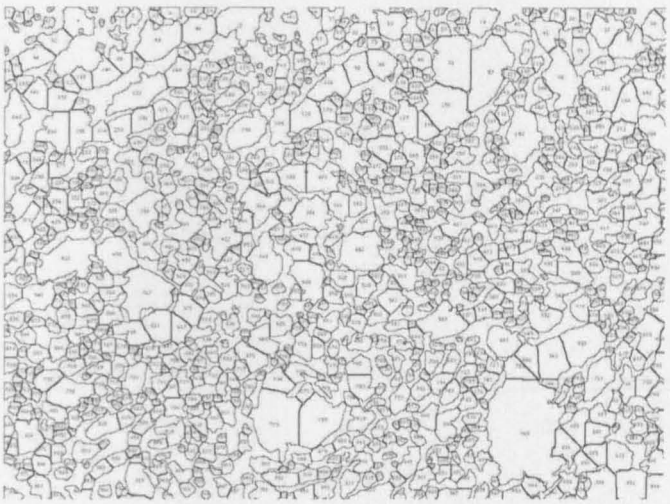

Figure 5.10. Villous 'particles' contours produced by the morphology analysis of `ImageJ` from section No. 11 (Fig. 5.4b). Each particle is marked with an ordinal number.

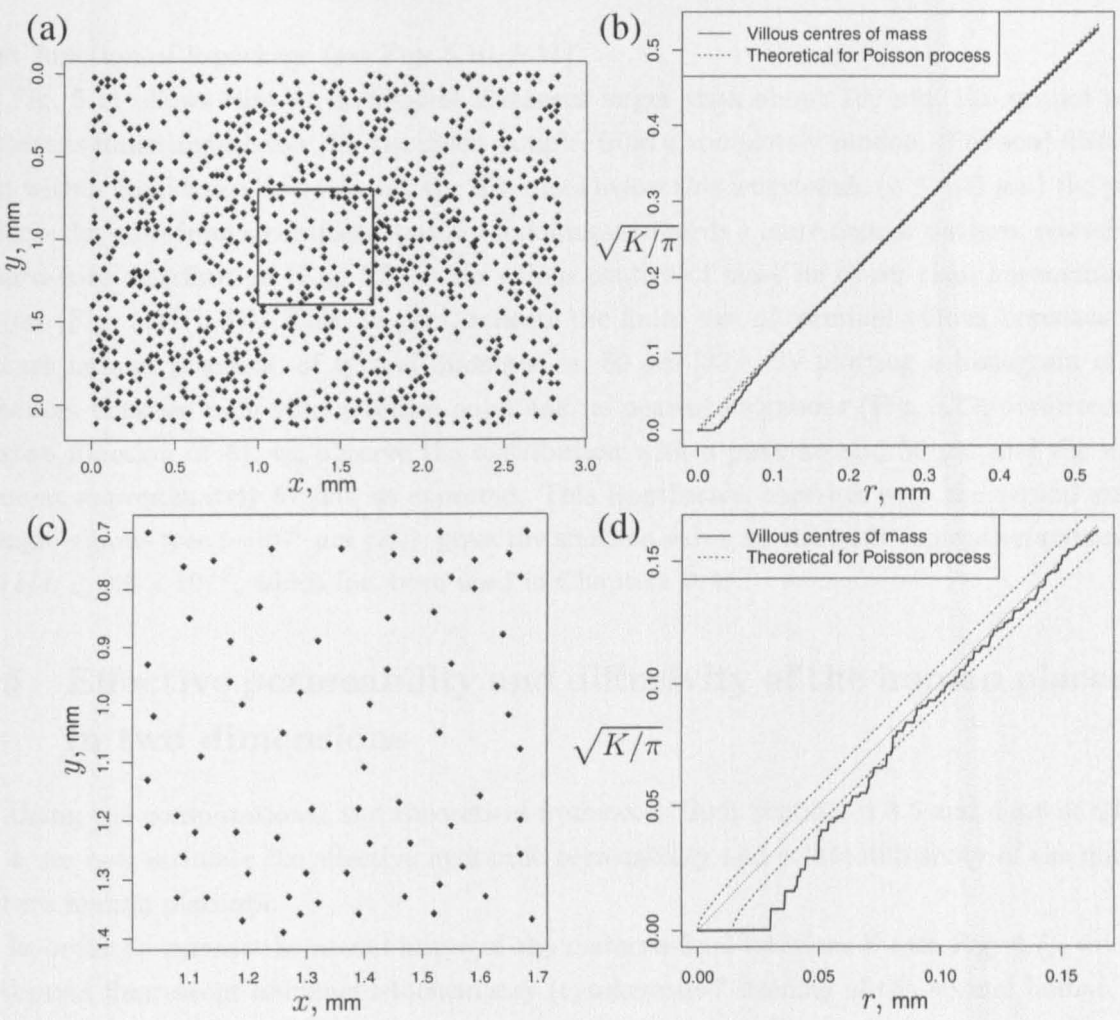

Figure 5.11. The spatial point process generated by the centres of mass of villous cross-sections and the square root of corresponding K-function (solid lines) in the whole domain (a,b) and in the central subdomain 0.7×0.7 mm (c,d), shown as a solid square in (a). Theoretical 95%-confidence interval (mean ± 2 std. err.; dashed lines) and the mean (dotted line) of the $\sqrt{K}$-function for a Poisson point process are computed using (5.4.5).

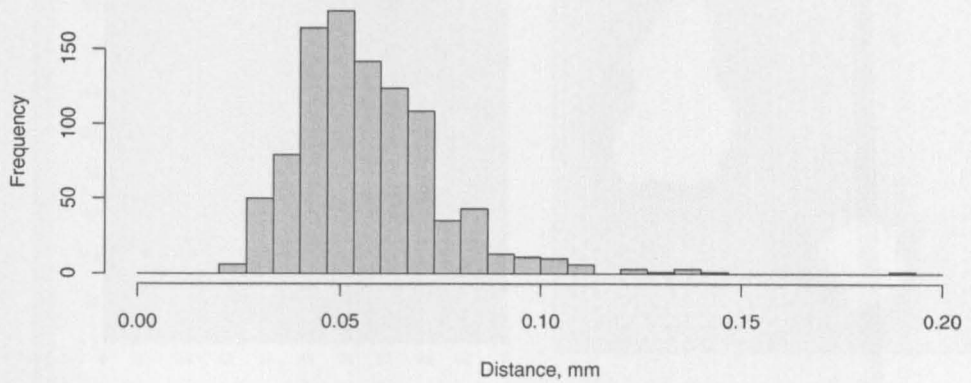

Figure 5.12. A histogram of the nearest-neighbour distances for the villous point pattern shown in Fig. 5.11(a).

`Kest` function of `R`-package (see Figs 5.10, 5.11).

Fig. 5.11 shows that at inter-point distances larger than about 100 μm, the spatial point pattern is indistinguishable, for the given sample, from a completely random (Poisson) distribution within confidence intervals. At the distances below this lengthscale ($r \lesssim 100$ μm) the point process deviates from a complete spatial randomness towards a more regular pattern, resembling a hard-core distribution (Fig. 5.8d). No villous centres of mass lie closer than approximately 30 μm (Fig. 5.11(b,d)). This, in part, reflects the finite size of terminal villous branches of a mature human placenta, of typical diameter ca. 50 μm [33]. By plotting a histogram of the distances between each villous centre-point and its nearest neighbour (Fig. 5.12; performed by `nndist` function of `R`), we observe the distribution with a peak around 50 μm and the mean value at approximately 57 μm, as expected. This lengthscale, together with the typical size of a single villous tree ($\sim 10^4$ μm [98]), gives the smallest value for the scale-separation parameter $\varepsilon \equiv l/L \gtrsim 0.6 \times 10^{-2}$, which has been used in Chapters 2–4.

5.5 Effective permeability and diffusivity of the human placenta in two dimensions

Using the computational and theoretical framework from Sections 4.3.5 and 4.3.6 of Chapter 4, we now estimate the effective hydraulic permeability and solute diffusivity of the normal mature human placenta.

In order to extract the actual shape of the materno-fetal interface Γ (see Fig. 4.7), we first performed fluorescent immunohistochemistry (cytokeratin-7 staining of the normal human placenta at term; see methods in Sec. 5.2.1) and digital microscopy (at $\times 20$ optical magnification) of terminal villi, followed by semi-automated harmonic interpolation for 24 equiangular points on the villous surface (estimating the centre of mass with trapezium quadrature and using `MATLAB` fast Fourier interpolation routine `interpft`), as shown in Figure 5.13(a). Finally, we compute solutions to the cell problems (4.3.54)–(4.3.55) and (4.3.60)–(4.3.61) for the obtained

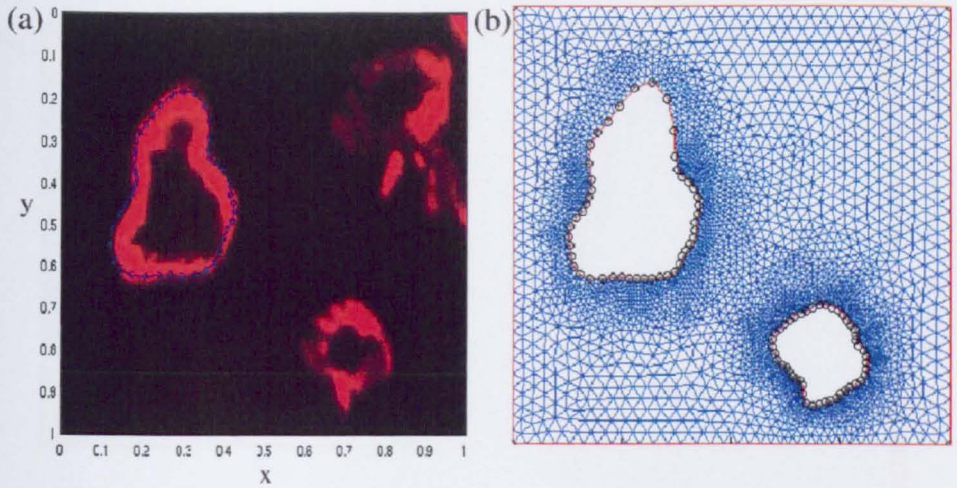

Figure 5.13. (a) Harmonic equiangular shape fitting of villous cross-sections (obtained from a normal placenta stained with trophoblast-specific cytokeratin-7; optical magnification $\times 20$)[3]; (b) Final geometry and mesh generated for a unit cell used to compute the permeability tensor.

geometry (Fig. 5.13b), using `COMSOL Multiphysics` steady adaptive finite-element solver with second-order Lagrange elements. The resulting fields are shown in Figures 5.14 and 5.15.

The corresponding effective permeability tensor (calculated as described in Sec. 4.3.5 and averaged over the unit cell Ω) for this particular example is

$$\langle \mathsf{K} \rangle \approx \begin{pmatrix} 0.0140 & -0.0004 \\ -0.0004 & 0.0153 \end{pmatrix} . \tag{5.5.1}$$

Because the permeability is a positive-definite matrix [85], it is diagonalisable with positive eigenvalues. Thus, from (5.5.1), we have eigenvalues $\lambda_1 \approx 0.0139$, $\lambda_2 \approx 0.0153$ and eigenvectors $\mathbf{v_1} \approx (1.00, 0.25)$, $\mathbf{v_2} \approx (-0.25, 1.00)$. The degree of anisotropy in the permeability in the considered unit cell is therefore

$$\text{Advective anisotropy} = \frac{|\lambda_1 - \lambda_2|}{\max\{\lambda_1, \lambda_2\}} \approx 0.096 , \tag{5.5.2}$$

and the angle between the coordinate axes ($\mathbf{e_x} = (1, 0)$ and $\mathbf{e_y} = (0, 1)$) and the principal axes of the unit cell (see Fig. 5.16) is

$$\arctan\left(\frac{\mathbf{v_1} \cdot \mathbf{e_y}}{\mathbf{v_1} \cdot \mathbf{e_x}}\right) \approx 14^\circ .$$

Analogously, the effective diffusivity tensor (defined by (4.3.36) and computed as described in Sec. 4.3.6) is

$$\mathsf{D}_{\text{eff}} = (1 - \phi)\,\mathbf{I} - \int_\Gamma \mathbf{n}\,\mathbf{b}\, \mathrm{d}S_x \approx \begin{pmatrix} 0.1605 & -0.0063 \\ -0.0063 & 0.0815 \end{pmatrix} , \tag{5.5.3}$$

[3]The samples were kindly provided by Dr Ruta Deshpande.

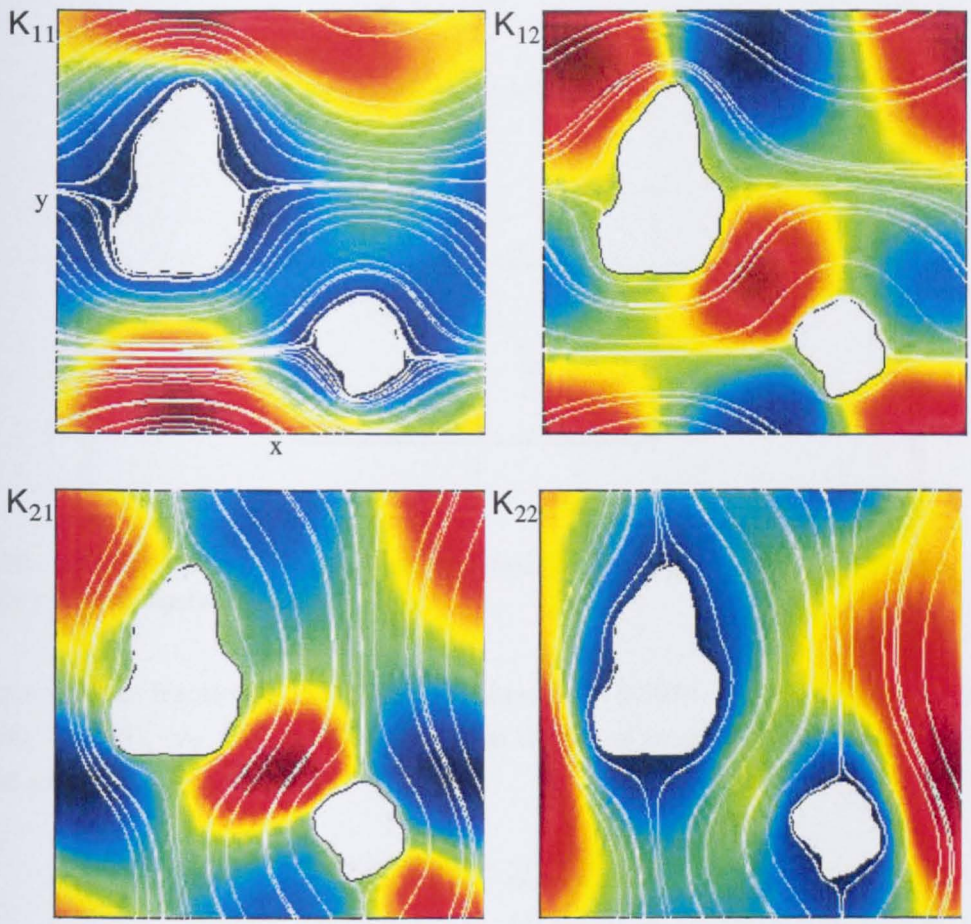

Figure 5.14. Components of permeability tensor K (colours, where dark-red corresponds to the field maxima and dark-blue to the minima) and streamlines (solid white lines) for a periodic unit cell, with geometry of Fig. 5.13.

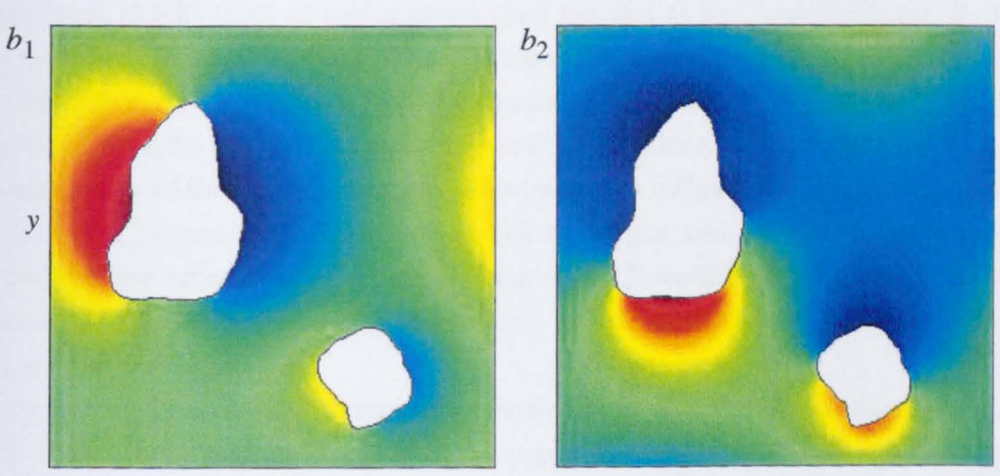

Figure 5.15. Components of the auxiliary vector **b** (colours, where dark-red corresponds to the field maxima and dark-blue to the minima), used to compute the effective diffusivity tensor (4.3.36) for a periodic unit cell, with geometry of Fig. 5.13.

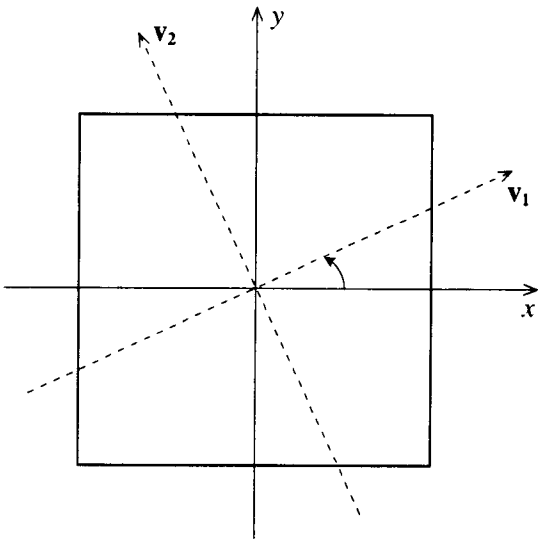

Figure 5.16. Principal axis of the unit cell (dashed), defined by the eigenvectors $(\mathbf{v_1}, \mathbf{v_2})$ of the permeability and diffusivity tensors.

with villous volume fraction $\phi \approx 0.13$, eigenvalues $\lambda_1 \approx 0.1610$, $\lambda_2 \approx 0.0810$ and eigenvectors $\mathbf{v_1} \approx (1.00, -0.079)$, $\mathbf{v_2} \approx (-0.079, 1.00)$. The degree of anisotropy in the diffusivity in the considered unit cell is therefore

$$\text{Diffusive anisotropy} = \frac{|\lambda_1 - \lambda_2|}{\max\{\lambda_1, \lambda_2\}} \approx 0.50\,, \tag{5.5.4}$$

and the angle between the coordinate axes ($\mathbf{e_x} = (1,0)$ and $\mathbf{e_y} = (0,1)$) and the principal axes of the unit cell (see Fig. 5.16) is

$$\arctan\left(\frac{\mathbf{v_1} \cdot \mathbf{e_y}}{\mathbf{v_1} \cdot \mathbf{e_x}}\right) \approx -4.5^\circ\,.$$

We see from (5.5.2) that, at scales larger than the size of the considered unit cell, we can treat the medium permeability (and hence the advective solute transport) as close to isotropic, since λ_1 differs from λ_2 in less than 10%. Interestingly, for the same geometry, (5.5.4) indicates that effective diffusivity in the horizontal and vertical directions differ in about 50%, suggesting stronger anisotropy of the intervillous space with respect to diffusive transport. The latter result however may not be significant for solutes (such as oxygen and glucose) transported at high Péclet numbers (see estimates in Sec. 2.8 of Chapter 2). Nevertheless, more data are needed to justify these findings for larger averaging windows, as well as to test the variability of placental structure within the population.

To estimate the dimensional permeability coefficient k^* ($\mathsf{K}^* \approx k^* \mathsf{I}$), we recall (see the end of Sec. 4.3.2) that the dimensional form of the permeability tensor $\mathsf{K}^* = l^2\,\mathsf{K}$ can be measured in m^2, with $l \sim 100\ \mu\text{m} \sim 10^{-4}$ m being a reference lengthscale of the unit cell used in averaging (Fig. 5.13a). Therefore, from estimate (5.5.1), we have $k \sim 10^{-2}$ ($\mathsf{K} \approx k\,\mathsf{I}$), resulting in the placental permeability $k^* \approx l^2\,k \sim 10^{-10}$ m^2, which is in agreement with the estimates based on *ex vivo* perfusion experiments and empirical permeability–volume fraction relations [92].

5.6 Discussion

Heterogeneous and disordered biological media such as the human placenta require careful consideration of the statistical properties of the underlying micro-geometry when simulating transport processes, in particular, for the solutes such as oxygen or glucose which appear to operate in the advection/uptake-dominated regime (see Sec. 2.8 of Ch. 2).

In this chapter, we have illustrated how sampling villous area fraction (Fig. 5.7) and estimation of the K-function (Fig. 5.11) reveal important intrinsic lengthscales in the distribution of villous branches. For the sample considered, our data show no evidence against uniformly random distribution patterns of villous trees over sufficiently large distances and no evidence of underlying periodicity that would give rise to clear steps in the K-function [257]. The K-function instead resembles a hard-core distribution at shorter lengthscales (Fig. 5.11(b,d)), consistent with the requirement that branches cannot overlap.

Apart from the K-function-aided inference of the regularity/randomness of underlying placental microstructure, we have used the semi-automated identification of villous branch outlines and computation of their area fraction ϕ as a function of window size (Fig. 5.7). Area fraction oscillations can be employed as a measure of medium heterogeneity at different scales [29] and has been used to identify the reference size for a representative unit cell. We observe that ϕ becomes insensitive to the local fluctuations in microstructure at the scales ($\sim$ 1 mm) larger than the distances at which the villous centres appear uniformly randomly distributed ($\gtrsim$ 0.1 mm), which can be in part attributed to the intricate non-circular shapes not captured by the K-function. Further development of semi-automated image analysis, e.g. in watershedding segmentation algorithms [189], should allow bulk processing of histological data and reduce systematic errors. Future studies can be used to fit parameters of suitable spatial models to histological data and to assess how these features of tissue architecture may vary during development, in disease and between individuals.

Finally, we have estimated the effective hydraulic permeability (Fig. 5.14) and solute diffusivity (Fig. 5.15) of tissue from a normal mature human placenta, using a unit cell with the feto-maternal interface geometry extracted from histological data of a single sample. The averaged permeability and diffusivity tensors ((5.5.1) and (5.5.3)) have been calculated by simulating microscopic flow and transport in the unit cell. We have assessed the anisotropy of the unit cell and have found that while the medium (intervillous space) is close to isotropic for the flow (anisotropy of less than 10%), it is relatively anisotropic for diffusion (anisotropy of about 50%). The latter however may not impact noticeably solute transport at high Péclet number (e.g. for oxygen or glucose). Nevertheless, these estimates must be replicated for multiple samples to get statistically significant results. The obtained permeability tensor (5.5.1) agrees, to the nearest order of magnitude, with the indirect estimates of placental flow resistance available in the literature, and therefore justifies the applicability of Darcy's law to the human placenta.

Having justified the Darcy flow (Sec. 5.5) and advection-dominated transport (Sec. 4.3) in the uniform and isotropic intervillous space, as a leading-order approximation, we integrate our results in the next chapter by considering a simple yet physiologically interesting model of flow and transport in a single placental functional unit, a placentone.

VI A Mathematical Model of Blood Flow and Nutrient Transport in the Human Placentone

6.1 Introduction

Here, we develop and study a mathematical model to characterise some of the primary physiological features of maternal blood flow and solute transport in a placental circulatory functional unit, a placentone (see Fig. 1.2), indicated in Chapter 1.

As has been briefly discussed in Section 1.2 of Chapter 1, the number and position of the supplying spiral arteries and draining decidual veins are still uncertain [33]. There are three main hypotheses for the distribution of venous openings: random; concentrated near placental margins; and concentrated in the periphery of placentones and near the placental septa [49]. The last hypothesis is the closest to current views [33]. Another important determinant of the successful pregnancy outcome is the degree of dilatation of the spiral arteries through a remodelling process (see Sec. 1.2). The functional impact of both structural placental properties will be analysed in the present Chapter by means of a mathematical model.

We also highlight the necessity to take into account simultaneously spatial uteroplacental blood flow distribution and solute uptake kinetics, which was overlooked in most of the previous models (see Sec. 1.3 of Ch. 1).

To address these combined effects, based on the results of Chapters 4 and 5, we formulate a simple theoretical model for maternal blood flow and solute transport in a mature human placentone. Our aim is to examine the influence of the maternal blood flow rates as well as decidual vessels' position and calibre on the solute patterns and the effectiveness of nutrient uptake into the villous tree in a single mature placentone. We use the model to perform an optimisation analysis in terms of key geometric and physical parameters.

6.2 The mathematical model

6.2.1 Model assumptions

We model the villous tree in a placentone as an undeformable porous medium of uniform and isotropic permeability k (in Sec. 5.3 we have shown that the intervillous space is approximately homogeneous at the scale of the order of 1 mm, which is much less than the size of a single placentone, and in Sec. 5.5 the permeability tensor is estimated to be close to isotropic). The intervillous space is perfused by an incompressible Newtonian liquid of viscosity μ, representing maternal blood. The placentone is assumed to be enclosed in an impermeable hemisphere (S_2), at the circular base of which (S_1) are a central source (a spiral artery), supplying blood with

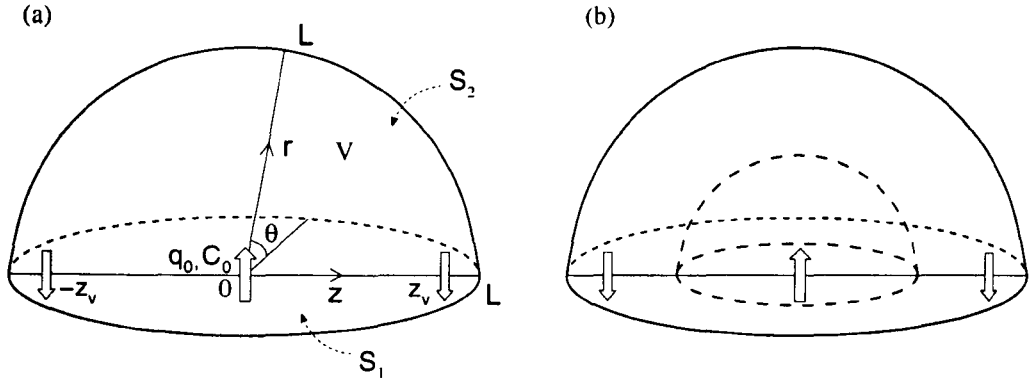

Figure 6.1. A schematic placental circulatory unit confined between the plane S_1 and hemispherical surface S_2 of radius L. Maternal blood enters from a source (artery) at $z = 0$ and exits through sinks (veins) at $z = \pm z_v$, as indicated by arrows: (a) homogeneous intervillous space; (b) including a central cavity. In the cylindrical coordinate system, z measures distance along the axis in S_1 on which the spiral artery and decidual veins lie; r measures distance perpendicular to this axis. The flow is assumed axisymmetric, i.e. independent of the azimuthal angle θ measured in a plane perpendicular to the z-axis from the plane S_1.

steady flow rate q, and two identical sinks (decidual veins), aligned along a diameter of the basal plate (see Fig. 6.1). The radius L of the hemisphere characterises the size of the fetal villous tree; the sinks are placed symmetrically with respect to the source on S_1 a distance $\pm z_v$ from it, where $0 < z_v < L$. This three-dimensional geometry mimics the shape of the placentone (see Fig. 1.2). The placentone border is assumed impermeable, due to the presence of septa and adjacent placentones. We consider steady flow that is axisymmetric about the line through the source and sinks (Fig. 6.1a), ignoring pulsatile variations in flow from the spiral artery. Uterine contractions are also neglected due to the shorter timescales required for the perfusion of a placentone (< 1 min) compared to the period of relaxation (≈ 5 min) [207]. We also consider the situation in which the porous medium contains a central cavity above the spiral artery (Fig. 6.1b).

The advantage of assuming such a simple geometry for a placentone is that the transport problem can be solved analytically to obtain flow and pressure fields in an explicit form (see expressions (6.3.3) and (6.3.4) below). We can then investigate how nutrient distribution is affected by typical flow and consumption rates as well as by geometrical parameters.

The model assumes that the flow of maternal blood in the intervillous space is described by Darcy's law [27, 29] (see equations (4.3.34a), with permeability shown to be approximately isotropic in Sec. 5.5 of Ch. 5). The steady distribution of a passive solute is described by the advective-reactive transport equation (analogous to (4.3.66) obtained at leading order for large Péclet number in Sec. 4.3.7; see also Table 6.1), according to which the solute is convected along streamlines and "absorbed" by the solid phase of the porous medium.

Typical quantitative data for a normal placenta at term are presented in Table 6.1.

6.2.2 Model limitations

The predictions of the model should be interpreted with some caution, being more qualitative than quantitative. The limitations of the model are rooted in its assumptions, which can serve

Parameter	Value	Reference
Placental diameter	15 – 22 cm	[33, 186]
Placental thickness	2 – 3 cm	[186]
Thickness of decidua	0.6 – 0.7 cm	[186]
Number of maternal lobules	10 – 40	[33, 186]
Number of villous trees per lobule	1 – 3	[33]
Total villous surface area	11.0 – 13.3 m^2	[33]
Diameter of terminal villi (d)	$\simeq 50$ μm	[33]
Feto-maternal barrier thickness	$\simeq 5$ μm	[33]
Diffusivity in blood plasma (D) for oxygen	$\simeq 10^{-3}$ cm^2/min	[24]
glucose	$\simeq 10^{-4}$ cm^2/min	[217]
Arterial concentration (C_0) of dissolved oxygen	$\simeq 0.1$ mM	[122]
glucose	$\simeq 4$ mM	[203]
Saturation factor for oxygen (k_0)	$\simeq 0.25$	[132]
Radius of the decidual vessels (a)	$\simeq 1$ mm	[87]
Number of basal arterial openings at term	$\simeq 100$	[33, 49]
Number of decidual vein outlets	50 – 200	[33]
Total flow rate of incoming blood	500 – 700 ml/min	[186, 203]
Blood density (ρ)	10^3 kg/m^3	[61]
Blood viscosity (μ)	4×10^{-3} Pa · s	[61]
Placental hydraulic permeability (k)	$\sim 10^{-10}$ m^2 †	[92]
Flow rate per a single spiral artery (q_0)	5 ml/min	
Average diameter of a maternal lobule	$\simeq 2 - 4$ cm ‡	
Reference radius of a placentone (L_0)	2 cm	
Characteristic pressure drop in placentone (P_0)	1 mmHg	
Reference blood pressure in placentone (P_{ref})	5 mmHg	
Reference solute consumption rate (α_0)	1 min^{-1}	
Reynolds number (Re $= \rho q_0 / \mu L_0$)	~ 1	
Péclet number (Pe $= q_0 / L_0 D$)	$\sim 10^3 - 10^4$	

Table 6.1. Literature-based and calculated parameters for a normal full-term human placenta used in the model (all data for haemodynamics and metabolic exchange refer to the materno-placental/systemic circulation).

only as a first approximation to placentone anatomy and physiology.

For example, the human placentone's shape is not a perfect hemisphere; the central position of the spiral artery and only two draining veins per placentone symmetric about the centre are oversimplifications; the placentone is not completely isolated, and there is likely to be an interaction between adjacent placentones, especially in the central part of the human placenta; and the compliance, anisotropy and heterogeneity of the villous tissue are neglected.

†Estimated in Sec. 5.5 of Chapter 5.

‡Measurements by Flavia Sciota and ILC on a normal placenta delivered by elective cesarian section at the Queen's Medical Centre.

The model does not account explicitly for the fetal placental circulation and neglects the inertia and pulsatility of entering maternal blood, as well as uterine contractions. Newtonian rheology is assumed for maternal blood flow in the intervillous space, ignoring the complexities involved in modelling the flow of a concentrated suspension of deformable cells in a porous medium.

Finally, the contribution of diffusion due to molecular motion and dispersion inside the intervillous space is not considered in the framework of the present model (which is shown to be a reasonable approximation at leading order for high Péclet number; see Sec. 4.3.7). The representative nutrient transported across the placentone is assumed to have homogeneous solubility, and oxygen carriers, glucose transporters and other facilitated or active transport factors are not explicitly accounted for (the role of oxygen carriers as slow modulators of the effective Péclet number is discussed in Sec. 4.4.5). We focus therefore on uptake into placental villous tissue, for example of glucose (Hill-type uptake), and the exchange of passive inert substances (first-order uptake) at low concentration of solute in the fetal circulation relative to its concentration in the intervillous space [25], neglecting possible reversibility of materno-fetal solute exchange.

However, the advantage of assuming such a simple structure and physiology of a placentone is that it allows for a mathematically transparent analysis of its function. This will, we hope, bring some insight to the development of more advanced models for placental circulation and metabolic exchange.

6.2.3 Problem statement

When the volume flux q of maternal blood into the placentone is prescribed, the problem is characterised by two dimensionless parameters: the uptake parameter (also known as the Damköhler number) $\mathrm{Da} = \alpha L^3/q$, which expresses the local nutrient consumption rate in fetal terminal villi relative to the rate of convective mass transfer by maternal blood; and the geometrical ratio $h = z_v/L$ (where $0 < h < 1$), which reflects the position of the basal vessels relative to the placentone boundary.

The *absolute net uptake rate* of a solute from the maternal blood N_a is defined as the difference between the concentration flux at the source qC_0 and the concentration flux at the sinks. The *relative net uptake rate* (measured relative to the available flux of solute) is defined as $N_r = N_a/qC_0$ (the computational details will be given in Sec. 6.3 below). These integral measures enable us to investigate the influence of model parameters Da and h on the net uptake efficiency of the placentone.

If, instead of q, the difference in blood pressure ΔP between the supplying spiral artery and draining decidual veins is prescribed, we must evaluate q in terms of the permeability k of the porous medium, which depends on the volume fraction ϕ of space occupied by villous branches. Variation of the geometric parameters h and ϕ in the model enables us to explore how the placentone's structure influences its function in terms of solute uptake.

We use cylindrical coordinates (z, r, θ) with a local maternal blood velocity $\mathbf{u}(r, z) = (u_z(r, z),\ u_r(r, z),\ 0)$ to describe the axisymmetric flow, where z is the axis of symmetry (on which the source and sinks lie), r is the radial distance normal to the axis and θ is the azimuthal angle

(so that the placentone occupies $|z| \leq L$, $0 \leq r \leq L$, $0 \leq \theta \leq \pi$, $r^2 + z^2 \leq L^2$, see Fig. 6.1a).

Neglecting fluid inertia due to the low Reynolds number (see Table 6.1) and averaging mass and momentum conservation laws over lengthscales large compared to the scale of villous microstructure, but small compared to the placentone radius L, we can describe the steady flow of maternal blood by Darcy's law at leading order (see (4.3.34a))

$$\nabla \cdot \mathbf{u} = 0\,, \tag{6.2.1}$$

$$\mathbf{u} = -\frac{k}{\mu}\nabla P\,, \tag{6.2.2}$$

where $\mathbf{u}$ and P are the velocity and pressure of blood in the intervillous space; k is the permeability coefficient (inverse flow resistance), and μ is blood viscosity, which are both assumed constant. Because the Darcy flow (6.2.2) is by definition irrotational ($\nabla \times \mathbf{u} = 0$), we introduce a Stokes stream function and velocity potential with appropriate boundary conditions and apply the method of images to obtain the exact solution to the flow problem. In doing so we find analytical expressions for the pressure and velocity fields in closed form.

Analogously to problem (4.3.45) obtained in Section (4.3.3) for solute transport past a periodic array at moderate-to-large local Péclet number, we describe steady advection-dominated transport of a passive solute in a homogeneous isotropic porous medium, at leading order, by

$$\begin{aligned} (\mathbf{u}\cdot\nabla)\,C &= -\alpha\, C_0\, f(C/C_0)\,, \\ C|_{r,z=0} &= C_0\,, \end{aligned} \tag{6.2.3}$$

where C is the concentration of a solute (gas or nutrient) in the maternal blood, C_0 is the solute concentration at the source (the spiral artery entering the placentone), α is a solute consumption rate averaged over the pore length scale (characterising uptake by the villous tissue), and f is a dimensionless function of $C_* \equiv C/C_0$ defining the uptake kinetics. According to (6.2.3), the solute is convected along streamlines (due to relatively large Péclet number, see Table 6.1).

We consider three types of reaction kinetics for uptake of a solute, dissolved gas or nutrient into the villous tree: first- and second-order passive uptake (with rate function $f(C_*) = C_*$, $f(C_*) = C_*^2$), and Hill-type kinetics ($f(C_*) = C_*^2/(k_0^2 + C_*^2)$, where k_0 is a dimensionless saturation factor). These types of uptake kinetics may be appropriate in the case of passive or facilitated transport of certain metabolites such as glucose, for which advective transport dominates over molecular diffusion (see Table 6.1); we do not seek to account for the more complex reaction kinetics of oxygen, carbon dioxide or amino-acids in maternal and fetal blood [122, 238].

Equations (6.2.1)–(6.2.2) are solved subject to boundary conditions $\lim_{r\to 0} r\,u_r = \frac{q}{\pi}\big(\delta(z) - \frac{1}{2}\,[\delta(z - z_v) + \delta(z + z_v)]\big)$ on $S_1 = \{r^2 + z^2 \leq L^2,\ \theta = 0,\ \theta = \pi\}$ and $\mathbf{u}\cdot\mathbf{n} = 0$ on $S_2 = \{r^2 + z^2 = L^2,\ 0 \leq \theta \leq \pi\}$; here the Dirac δ-function is used to approximate the flow rate distribution of a singular source and sinks, q is the flow rate at the source (which is split equally between the sinks), and $\mathbf{n}$ is the outward unit normal vector to the hemispherical surface S_2 (see Fig. 6.1b). We explain how the finite sizes of the source and sink vessels influence the flow solution below.

Equations (6.2.1)–(6.2.3) complemented by boundary conditions constitute the complete system describing steady blood flow and transport processes in the intervillous space.

The incompressibility condition (6.2.1) is identically satisfied if we introduce the Stokes stream function $\psi(r,z)$ in a cylindrical coordinate system, defined as $u_r = -\frac{1}{r}\frac{\partial \psi}{\partial z}$, $u_z = \frac{1}{r}\frac{\partial \psi}{\partial r}$, where u_r and u_z are radial and axial velocity components. Equation (6.2.2) implies that the flow field is irrotational, so we can introduce a velocity potential $\Phi = -\frac{k}{\mu}P$, such that $\mathbf{u} = \nabla\Phi$. Thus, from (6.2.1)–(6.2.2) we obtain

$$\nabla^2\psi - \frac{2}{r}\frac{\partial \psi}{\partial r} = 0\,, \quad \nabla^2 P = 0\,. \tag{6.2.4}$$

Since a single source emits in the half-space a flux q, the boundary condition for the Stokes stream function on S_1, describing a system of one source and two sinks with zero net flux, is $\lim_{r\to 0} r\,u_r = -\left.\frac{\partial \psi}{\partial z}\right|_{r=0} = \frac{q}{\pi}\left(\delta(z) - \frac{1}{2}\left[\,\delta(z-z_v) + \delta(z+z_v)\,\right]\right)$. In order to satisfy $\mathbf{u}\cdot\mathbf{n} = 0$ on S_2, we take $\psi =$ constant and $\mathbf{n}\cdot\nabla P = 0$ on S_2. Without loss of generality, we set $\psi = 0$ on S_2.

We rewrite (6.2.3) and (6.2.4), subject to boundary conditions, in dimensionless form. We choose the following non-dimensional variables: $r = L\,r'$, $z = L\,z'$, $\mathbf{u} = U\,\mathbf{u}'$ and $\psi = q\,\psi'$, $P = P_{\rm ref} + P_0\,P'$, $C = C_0\,C'$, where $U = q/L^2$ is typical flow velocity scale of maternal blood, $P_0 = \mu q/kL$ is a pressure scale characteristic of the viscous pressure drop across a porous medium, and $P_{\rm ref}$ is a reference pressure intermediate between the arterial and venous pressures (see Table 6.1). Then the dimensionless problem for blood flow and solute transport in the hemispherical domain reads:

$$\begin{aligned}
&\nabla^2\psi' - \frac{2}{r'}\frac{\partial \psi'}{\partial r'} = 0\,, \quad \nabla^2 P' = 0\,, \quad \frac{1}{r'}\left(\frac{\partial \psi'}{\partial r'}\frac{\partial C'}{\partial z'} - \frac{\partial \psi'}{\partial z'}\frac{\partial C'}{\partial r'}\right) = -\mathrm{Da}\,f(C') \qquad \text{in } V',\\
&\left.\begin{aligned}
&-\left.\frac{\partial \psi'}{\partial z'}\right|_{r'=0} = \frac{1}{\pi}\left(\delta(z') - \frac{1}{2}\left[\,\delta(z'-h) + \delta(z'+h)\,\right]\right),\\
&-\lim_{r'\to 0} r'\frac{\partial P'}{\partial r'} = \frac{1}{\pi}\left(\delta(z') - \frac{1}{2}\left[\,\delta(z'-h) + \delta(z'+h)\,\right]\right),
\end{aligned}\right\} \quad \text{on } S_1'\\
&\psi' = 0, \quad \frac{\partial P'}{\partial n} = 0 \qquad \text{on } S_2',\\
&C'|_{r'=z'=0} = 1\,.
\end{aligned} \tag{6.2.5}$$

where $V' = \{|z'| < 1,\ 0 < r' < 1,\ 0 < \theta < \pi,\ r'^2 + z'^2 \le 1\}$, $S_1' = \partial V' \cap \{\theta = 0\,, \theta = \pi\}$, $S_2' = \partial V' \cap \{r'^2 + z'^2 = 1\}$. The Damköhler number is denoted by $\mathrm{Da} = \alpha L^3/q$, and the dimensionless source-sink distance is $h = z_v/L$. In the subsequent analysis, the primes over dimensionless variables are dropped.

6.3 Methods

6.3.1 The method of images for Darcy's flow in a hemispherical domain

The fundamental solutions (Green's functions) to the stream function and pressure equations with a singular uniform source at $z = 1$ on the axis of symmetry in an unbounded domain ($z \in \mathbb{R}$,

$r > 0,\ 0 \le \theta < 2\pi$) are as follows [182]:

$$G_\psi = -\frac{1}{4\pi}\frac{z-1}{\sqrt{(z-1)^2+r^2}}, \quad G_P = \frac{1}{4\pi}\frac{1}{\sqrt{(z-1)^2+r^2}}. \tag{6.3.1}$$

The flow and pressure solutions of problem (6.2.5) in the unbounded half-space ($|z| > 0$, $r > 0,\ 0 < \theta < \pi$) are given by superposition of the fundamental solutions (6.3.1) as

$$\begin{aligned}
\psi_\infty(r,z) &= -\frac{1}{2\pi}\left(\frac{z}{\sqrt{z^2+r^2}} - \frac{1}{2}\left[\frac{z-h}{\sqrt{(z-h)^2+r^2}} + \frac{z+h}{\sqrt{(z+h)^2+r^2}}\right]\right), \\
P_\infty(r,z) &= \frac{1}{2\pi}\left(\frac{1}{\sqrt{z^2+r^2}} - \frac{1}{2}\left[\frac{1}{\sqrt{(z-h)^2+r^2}} + \frac{1}{\sqrt{(z+h)^2+r^2}}\right]\right).
\end{aligned} \tag{6.3.2}$$

Thus along the z-axis, ψ_∞ takes the values $0, +\frac{1}{2\pi}, -\frac{1}{2\pi}, 0$ as z increases from -1 to $+1$.

The method of images allows us to satisfy the boundary conditions on S_2 by adding a correction to the flow and pressure fields (6.3.2). In order to do so, we apply Butler's and Weiss's Sphere theorems, which generalise Milne-Thomson's Circle theorem for three-dimensional axisymmetric fluid motions [182]:

Theorem 6.1 (Butler [58]):
Let there be axisymmetrical irrotational flow of incompressible inviscid fluid with no rigid boundaries, characterised by the stream function $\psi_0(R,\theta)$ in spherical coordinate system (R,θ,φ), all of those singularities are at a distance greater than a from the origin, and let $\psi_0 = O(R^2)$ at the origin. If the rigid sphere $R = a$ be introduced into the flow, the stream function becomes

$$\psi(R,\theta) = \psi_0(R,\theta) - \frac{R}{a}\psi_0\left(\frac{a^2}{R},\theta\right).$$

Theorem 6.2 (Weiss [267]):
Let there be irrotational flow of incompressible inviscid fluid with no rigid boundaries, characterised by the velocity potential $\Phi_0(R,\theta,\varphi)$, all of those singularities are at a distance greater than a from the origin. If the rigid sphere $R = a$ be introduced into the flow, the velocity potential becomes

$$\Phi(R,\theta,\varphi) = \Phi_0(R,\theta,\varphi) + \frac{1}{a}\int_0^{a^2/R} R'\,\frac{\partial\,\Phi_0(R',\theta,\varphi)}{\partial\,R'}\,\mathrm{d}R'.$$

Let the unperturbed flow and pressure fields be given by $\psi_\infty(r,z)$, $P_\infty(r,z)$ from (6.3.2). Then, according to Theorem 6.1, the stream function satisfying $\psi = 0$ on S_2 is

$$\psi(r,z) = \psi_\infty(r,z) + \frac{\sqrt{K}}{2\pi}\left(\frac{z}{\sqrt{r^2+z^2}} - \frac{1}{2}\left[\frac{z-Kh}{\sqrt{r^2+(z-Kh)^2}} + \frac{z+Kh}{\sqrt{r^2+(z+Kh)^2}}\right]\right), \tag{6.3.3}$$

where $K = r^2 + z^2$, $r, z \in V$. The image system consists of two point sinks at inverse points with respect to the sphere ($(r,z) = (0, \pm 1/h)$ for $(0, \pm h)$) and two line sinks, stretched from

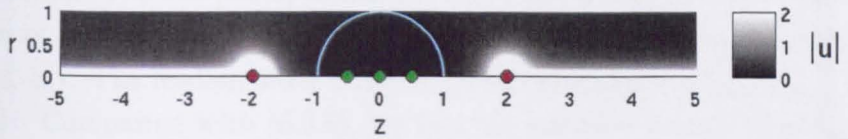

Figure 6.2. Illustration to the image system: absolute fluid velocity distribution near the axis of symmetry $r = 0$ (plotted in dimensionless variables). Position of original source and sinks is shown by green dots, the inverse points are depicted in red ($h = 0.5$, the radius of the hemisphere (solid blue) is equal to 1).

the inverse points to infinity ($r = 0$, $|z| \geq 1/h$) (as shown in Fig. 6.2).

By setting $K = 1$ in (6.3.3) we can readily see that $\psi = 0$ on S_2 as required. One can also check, by direct calculation using (6.3.3), that the normal component of fluid velocity at the boundary vanishes: $(\mathbf{u} \cdot \mathbf{n}) = \frac{z}{r}\frac{\partial \psi}{\partial r} - \frac{\partial \psi}{\partial z} = 0$ on S_2.

Application of Theorem 6.2 gives the pressure perturbation in the presence of a hemisphere:

$$P(r,z) = P_\infty(r,z) + \frac{1}{2\pi}\left(\ln r - \frac{1}{2}\left[\frac{z_v^*}{\sqrt{(z-z_v^*)^2+r^2}} + \ln\left(\frac{\sqrt{z^2+r^2}-z}{\sqrt{(z-z_v^*)^2+r^2}-(z-z_v^*)}\right)\right.\right.$$
$$\left.\left. + \frac{z_v^*}{\sqrt{(z+z_v^*)^2+r^2}} + \ln\left(\frac{\sqrt{z^2+r^2}+z}{\sqrt{(z+z_v^*)^2+r^2}+(z+z_v^*)}\right)\right]\right), \tag{6.3.4}$$

where $z_v^* = 1/h$ and $r, z \in V$.

In doing so we obtain exact solutions (6.3.3), (6.3.4) to the flow and pressure distributions of boundary-value problem (6.2.5).

We can also find a relation between the (dimensional) source-sink pressure drop $\Delta P = P|_{r=a,z=0} - P|_{r=a,z=z_v}$ (evaluated in the vicinity of the vessel's junctions on the basal plate) and the flow rate q, based on (6.3.2) for an unbounded domain (in dimensional variables):

$$q = \frac{2\pi k}{\mu}\Delta P\left[\frac{3}{2a} - \frac{2}{\sqrt{a^2+z_v^2}} + \frac{1}{2\sqrt{a^2+4z_v^2}}\right]^{-1} = \frac{4\pi k a}{3\mu}\Delta P\left(1+O\left(\frac{a}{z_v}\right)\right). \tag{6.3.5}$$

Here $a \ll z_v$ is the width of a small neighbourhood of a source or sink, of scale comparable with the maternal vessels' radius. We are here exploiting the singular pressure distributions in (6.3.2) near $z = 0, \pm h$, and are matching the arterial pressure P_a to $P_\mathrm{ref} + \mu q/(2\pi k a)$ and venous pressure P_v to $P_\mathrm{ref} - \mu q/(4\pi k a)$. Thus we define $P_\mathrm{ref} = (P_\mathrm{a} + 2P_\mathrm{v})/3$ $\left(\Delta P = P_\mathrm{a} - P_\mathrm{v} = 3\mu q/(4\pi k a)\right.$, agreeing with (6.3.5) to the leading order; in dimensional variables, for, e.g. $P_a = 9$ mmHg, $P_v = 3$ mmHg, we have $P_\mathrm{ref} = 5$ mmHg and $\left.\Delta P = 6 \text{ mmHg}\right)$. The relation (6.3.5) also gives a good approximation in the case of the bounded hemispherical domain: one can show, via expansion in a power series in a, that for $L = 10a$, $z_v = 0.9L$, the relative difference between expression (6.3.5) and relation based on the precise formula (6.3.4) is of the order of 10 %. Therefore, the intervillous maternal blood pressure in Figs 6.3(c,d) is defined within levels set by the respective radii a of the basal vessels and the fluxes they carry, determining the overall pressure drop ΔP across the placentone.

One can generalise relation (6.3.5) to the case of the spiral artery (source) and decidual veins (sinks) of different radii a_s and a_v respectively, providing that they are sufficiently small and far apart (a_s, $a_v \ll z_v$). The leading order terms in (6.3.2) give $\Delta P = P|_{r=a_s,z=0} - P|_{r=a_v,z=z_v} \approx \frac{\mu q}{2\pi k}\left(\frac{1}{a_s} + \frac{1}{2\,a_v}\right)$. Comparing with (6.3.5), we find the effective vessel's lengthscale a to be a weighted harmonic mean of the source and sinks' lengthscales:

$$a = \frac{3}{2}\left(\frac{1}{a_s} + \frac{1}{2\,a_v}\right)^{-1}. \tag{6.3.6}$$

A direct corollary of (6.3.6) is the dominant influence of the vessels of smaller calibre on the placentone's overall conductance. Indeed, $a \sim 3a_v$ for $a_s \gg a_v$; $a \sim 3a_s/2$ for $a_s \ll a_v$, and $a = a_s$ for $a_s = a_v$.

Another important characteristic of the placentone is the volume fraction of villous tissue ϕ. A qualitative analysis can be performed using the Kozeny–Carman formula [29] for permeability $k = (1-\phi)^3/(c\,\sigma_s^2)$ (with specific surface area of porous medium $\sigma_s = \frac{\text{(wetted solid area)}}{\text{(unit cell volume)}} = 6\phi/d$ and the "shape-factor" constant $c = 5$), giving

$$k = \frac{d^2}{180}\,\frac{(1-\phi)^3}{\phi^2}, \tag{6.3.7}$$

where d is an average diameter of villi in the intraplacentone space. Expression (6.3.7) is most precise for a medium formed by a periodic array of solid spheres of constant diameter d [29].

Using (6.3.5) and (6.3.7), we can express the flow rate at the source q in terms of volume fraction, for a constant pressure drop $\Delta P = P|_{r=a,z=0} - P|_{r=a,z=z_v}$ in dimensional variables (evaluated a distance $a = 0.8$ mm from the vessels, where a is comparable to the radius of each vessel; see Table 6.1), as follows:

$$q(\phi) \simeq \frac{\pi a\, d^2 \Delta P}{135\mu}\,\frac{(1-\phi)^3}{\phi^2}. \tag{6.3.8}$$

6.3.2 Numerical scheme to compute the solute distribution and net uptake rate

The concentration distribution of solute $C(r,z)$ is computed by numerical integration of the velocity field along streamlines, which are the trajectories of fluid "particles" in the intervillous space. The absolute and relative net uptake rates are estimated as a weighted sum of uptakes per unit time over individual streamlines.

The steady advective transport of a solute (6.2.3) is described in dimensionless form by

$$(\mathbf{u}\cdot\nabla)\,C = -\mathrm{Da}\,f(C), \quad C|_{r,z=0} = 1, \tag{6.3.9}$$

where $f(C)$ is a rational function of C defining the type of passive uptake kinetics.

The concentration distribution of solute is computed by integration of the velocity field along streamlines. We use a Lagrangian formulation to rewrite equation (6.3.9) as

$$\frac{\mathrm{d}C}{\mathrm{d}t} = -\mathrm{Da}\,f(C), \quad C(0) = 1, \tag{6.3.10}$$

where $C = C(t)$, $\mathbf{x} = (r(t), z(t))$ belongs to a particular streamline, defined as $\mathrm{d}\mathbf{x}/\mathrm{d}t = \mathbf{u}$, and $t = 0$ at the source ($r = z = 0$). Here t represents time evolution following a material particle along a streamline.

For the considered three types of uptake kinetics, by direct integration of (6.3.10), we find the explicit time dependencies to be as follows:

$$\text{1st-order}: \quad f(C) = C, \quad C(t) = e^{-\mathrm{Da}\,t},$$

$$\text{2nd-order}: \quad f(C) = C^2, \quad C(t) = \frac{1}{1 + \mathrm{Da}\,t},$$

$$\text{Hill-type}: \quad f(C) = \frac{C^2}{k_0^2 + C^2}, \quad C(t) = -\frac{\mathrm{Da}\,t + k_0^2 - 1}{2} + \sqrt{\frac{(\mathrm{Da}\,t + k_0^2 - 1)^2}{4} + k_0^2}\,.$$

The relative net uptake rate of a solute is

$$N_r = 1 - \int_{S_{\mathrm{sink}}} C\,\mathbf{u}\cdot\mathbf{n}\,\mathrm{d}S, \tag{6.3.11}$$

where S_{sink} is a surface in a small vicinity of the sink and $\mathbf{n}$ is the outward unit normal vector to this surface. The dimensional absolute net uptake rate is $N_a = q\,C_0\,N_r$.

The absolute and relative net uptake rates (6.3.11) are estimated as a weighted sum of uptakes per unit time over individual streamlines using a trapezium quadrature. The time t elapsed since a fluid particle has travelled along a streamline is calculated numerically from $t = \int \frac{\mathrm{d}s}{|\mathbf{u}|}$, where s is a distance along the streamline:

$$t \approx \sum_{i=1}^{n_i} \sqrt{\frac{(\Delta r_i)^2 + (\Delta z_i)^2}{u_r^2(r_i, z_i) + u_z^2(r_i, z_i)}},$$

where $\Delta r_i = r_{i+1} - r_i$, $\Delta z_i = z_{i+1} - z_i$, n_i is the number of points at discretisation of a streamline, velocities u_r and u_z are computed in accord with the definition of the stream function and by use of the exact formula (6.3.3).

The relative computational inaccuracy is of order $1/N$, where N is the number of points of a uniform mesh taken at discretisation in both the z and r directions. Typically 200 streamlines and $N = 800$ uniform grid points are used in the calculations. Linear interpolation between streamlines is used to get a continuous concentration field.

6.4 Results

6.4.1 Flow and pressure distributions

Fig. 6.3 shows flow and pressure fields (described by formula (6.3.3)) in a hemispherical placentone with two different relative decidual artery-vein distances. Streamlines (blue, in Fig. 6.3(a,b)) display paths followed by maternal blood from the central spiral artery outwards to the two decidual veins. Because of the axial symmetry of flow (Fig. 6.1), the streamlines do not depend on the azimuthal angle θ. The orthogonal green isobars show how the pressure falls from

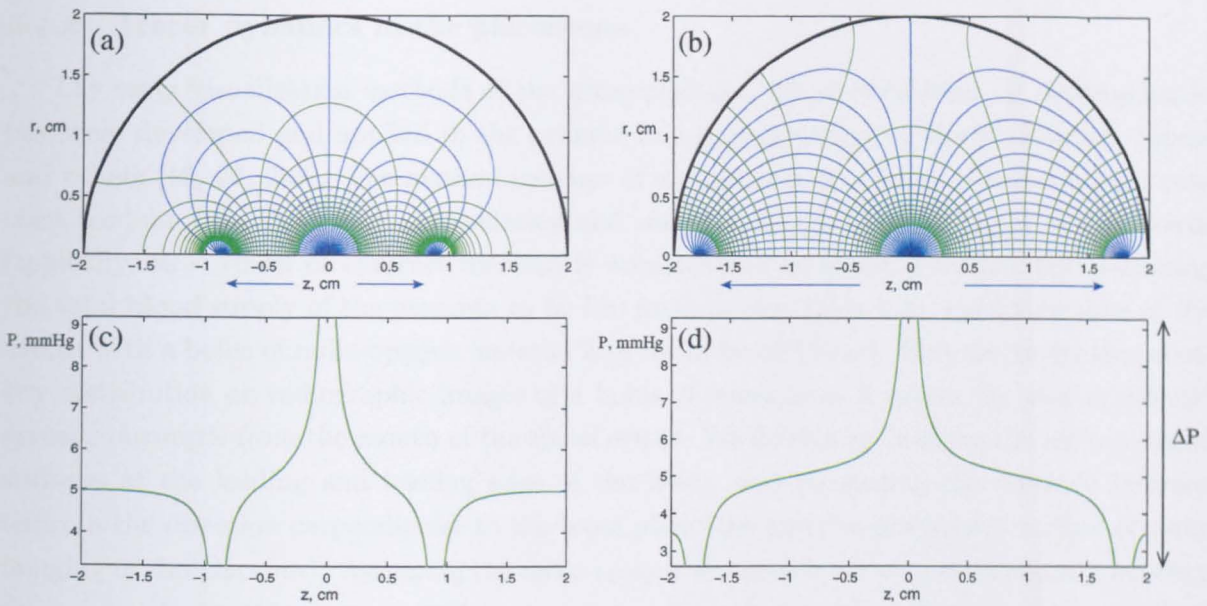

Figure 6.3. (a,b) predicted streamlines (blue) and constant pressure lines (green) for steady flow in a homogeneous placentone plotted in a cross-section perpendicular to the z-axis holding the basal vessels, where r is a distance from the axis of symmetry. Arrows indicate the direction of flow. (c,d) Intervillous blood pressure along the z-axis ($r \simeq 0.01\,\text{cm}$, $P_{\text{ref}} = 5\,\text{mmHg}$, $q_0 = 5\,\text{ml/min}$). The decidual veins are located either near the centre ((a,c), $h = 0.45$) or near the periphery ((b,d), $h = 0.9$) of the placentone.

a high value near the flow source to a low value near each sink; the isobars meet the impermeable placentone boundaries orthogonally. The pressure distribution along the z-axis (Fig. 6.3(c,d)) shows how the pressure rises (falls) very rapidly near the artery (veins), determining the overall pressure drop ΔP across the placenta. The intervillous pressure on the hemispherical boundary, far from these vessels, with a value intermediate between the arterial and venous pressures, is set to $P_{\text{ref}} = 5$ mmHg (see (6.3.5) for more details); the pressure drop ΔP across the placentone shown in Fig. 6.3(c,d) for the reference values of Table 6.1 is moderate, exhibiting low resistance to the maternal flow in the intervillous space [185]. The magnitudes of the pressures at the exit of the spiral artery and inlets of the decidual veins are primarily determined in the model by the width of the vessels and the volume fluxes passing through them.

When the distance between the source and sinks is small compared to the width of the placentone ($h = z_v/L = 0.45$, Fig. 6.3(a,c)), the flow pattern is localised due to the short-circuit of blood from the basal arteries to the nearby veins, unlike the flow that penetrates deeper into the dense intervillous space when the veins are situated near the periphery of the placentone (Fig. 6.3(b,d)). While flow patterns depend strongly on h, the overall conductivity of the placentone (the ratio of flow rate q to the overall pressure drop ΔP) is relatively insensitive to either the source-sink distance z_v or the placentone radius L, being instead approximately proportional to the ratio $k\,a/\mu$, where a is a length comparable to the width of the exit of the spiral artery and the entrance of each decidual vein, or whichever is the smaller (see equations (6.3.5) and (6.3.6)).

6.4.2 Tracer dynamics in the placentone

The early visualisation methods of the utero-placental blood circulation by radioangiography were developed and applied to the primate and human uterus by Borell, Ramsey, Freese and others [46, 96, 207]. The method consists of an injection of a bolus of radio-opaque contrast medium into the systemic circulation and subsequent serial x-ray imaging of the uterus (typically, 60 – 70 ml of contrast medium is administered in about 5 sec [46, 96]; assuming the total blood supply of the placenta to be 500 ml/min (see Table 6.1), the filling time of the uterus with a bolus of radio-opaque material is of the order of 10 sec). Here we model the intensity distribution on radiographic images of a bolus of material as it enters the placentone and spreads outwards from the mouth of the spiral artery. We do this by tracking the axisymmetric surfaces at the leading and trailing edge of the bolus, and computing the distance between them in the direction perpendicular to the basal plate (the anterior-posterior direction of x-ray imaging of the placenta). Assuming the radio-opaque material is distributed uniformly between the two surfaces, this distance will be proportional to the relative intensity of the resulting radioangiographic image.

Fig. 6.4(a) shows the leading and trailing fronts of tracer (dots) and the distance between them (thin solid) in a section perpendicular to the basal plate at a fixed moment of time following the introduction of a passive tracer into the spiral artery; the time-dependence of cross-sectional area occupied by a tracer bolus is plotted in Fig. 6.4(d). The growth rate of the bolus area slows down as it approaches the veins at the periphery of the placentone.

Ring-like structures, colloquially (but inappropriately, given the absence of rotation of fluid particles) known as "smoke rings" [33, 96], appear on x-ray images of the primate and human uterus shortly after injection as shown in Fig. 6.4(e) by Freese [96]. We visualise the tracer distribution as explained above using two tracer fronts separated by a 10 sec time interval, projected to the basal plate (z, x), where $x = r\cos\theta$, in Fig. 6.4(b,c) ($h = 0.99$). The non-uniform intensity distribution arises because the thickness of the radially expanding bolus shell is maximal near its margins (Fig. 6.4a). The bright ring remains approximately circular until it gets close to the decidual veins (Fig. 6.4c).

6.4.3 Representative solute distributions

Representative solute concentration distributions for first-order uptake kinetics at varying values of the non-dimensional uptake parameter $\mathrm{Da} = \alpha L^3/q$ and varying artery-vein distances $h = z_v/L$ are depicted in Fig. 6.5. Fig. 6.5(a,b) shows the effect of changing the artery-vein distance, and Fig. 6.5(c,d) shows the effect of varying the local solute consumption rate α relative to the inlet volume flux q. The consequence of reducing the source-sink distance is similar to increasing the uptake parameter Da; in both Fig. 6.5(a) and Fig. 6.5(d) the nutrient pattern is localised in the lower half of the domain, providing poor nutrient supply to the rest of placentone. Comparing Figures 6.5(b) and 6.5(c), we see that the solute concentration near the veins is increased (in Fig. 6.5c) by reducing Da, i.e. by reducing the local consumption rate α, the size of the placentone L or by increasing the inlet flow rate q, effects which reduce the overall relative net uptake rate N_r.

The influence of changing independently the artery-vein distance h, solute consumption

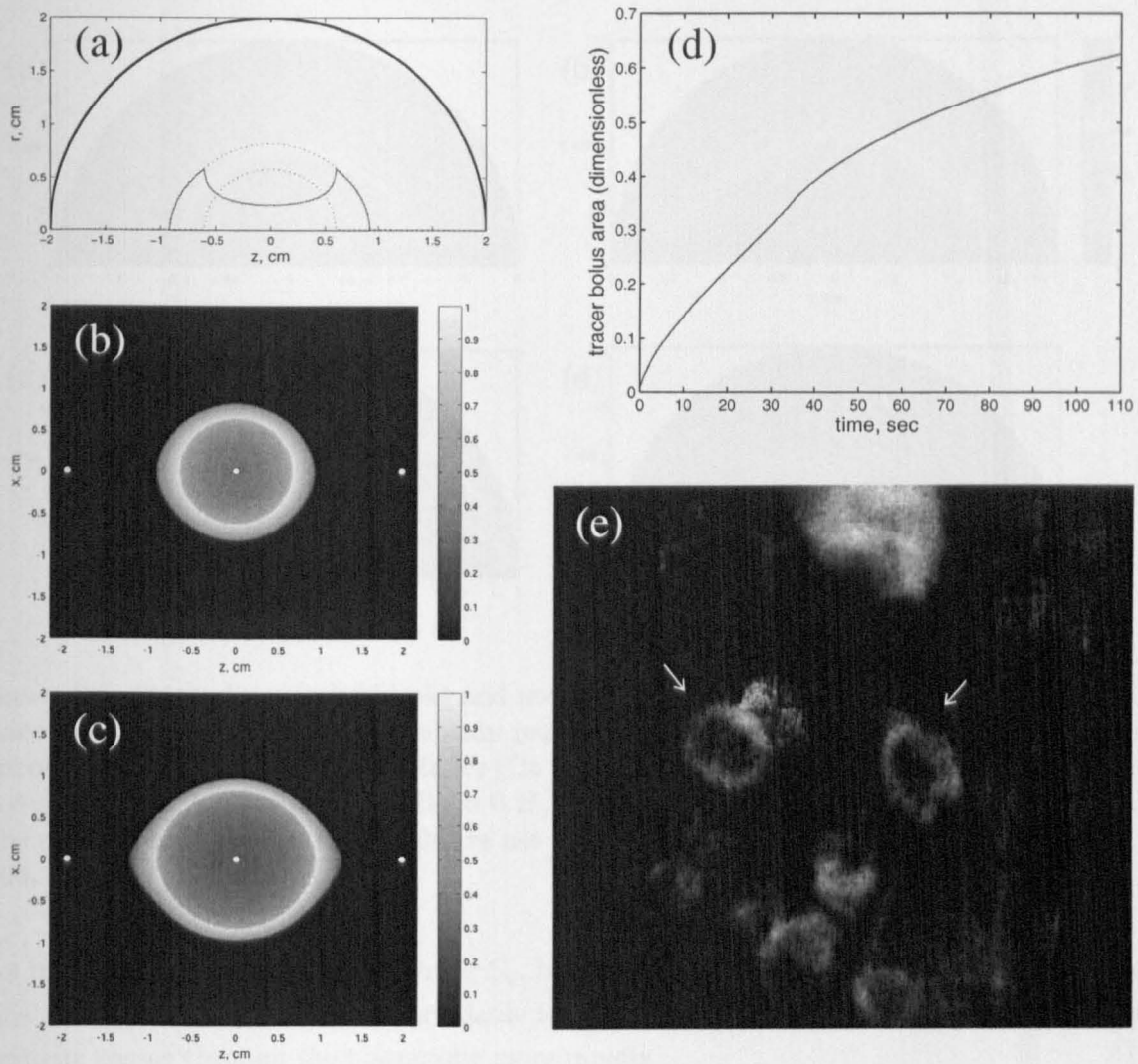

Figure 6.4. Tracer dynamics in the placentone: (a) leading and trailing tracer fronts (dots) and the shell thickness profile (thin solid, representing x-ray intensity) 15 sec following the appearance of the tracer from the spiral artery (shown in a sagittal section through the placentone, with the outer boundary indicated by a thick solid line; the decidual veins lie at $z \simeq \pm 2$ cm); (b,c) computed intensity of the tracer (greyscale) in the orthogonal projection on the basal plate 15 sec (b) and 25 sec (c) after the introduction of tracer to the model (white dots indicate the location of the spiral artery and decidual veins); (d) dependence of cross-sectional area of tracer bolus on time; (e) serial radioangiographic film of monkey uterus 18.5 sec following injection of Renografin (arrows indicate ring-like structures), reproduced from [96].

rate α, inlet blood flow rate q and the size of the placentone L on the relative net uptake rate N_r under different types of uptake kinetics is shown in Fig. 6.6. Results are presented relative to reference values of the parameters L_0, α_0, q_0 given in Table 6.1. N_r reaches its maximum when h approaches 1 (Fig. 6.6a), saturating at large consumption rate α or large placentone radius L (Fig. 6.6(b,d)).

The dependence of net uptake rate on inlet flow rate is more subtle: measured relative to a fixed inlet solute flux $q_0 C_0$, the absolute net uptake rate $N_a/q_0 C_0$ increases with q, as more material is delivered to the placentone per unit time by the increased flux; measured relative to

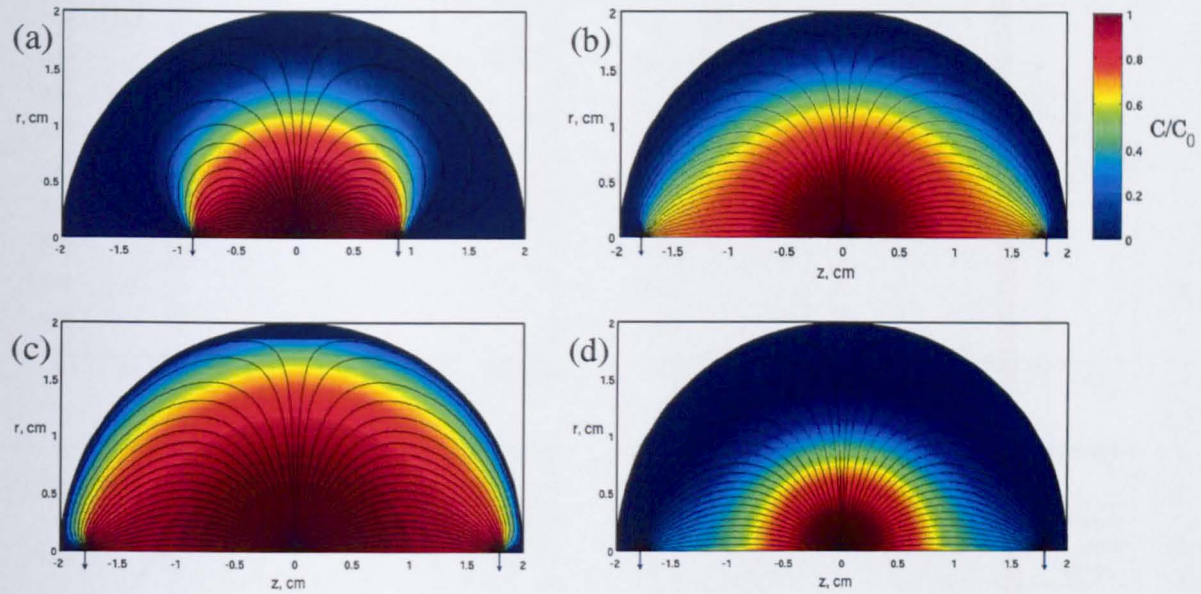

Figure 6.5. Streamlines (solid black) and normalised concentration field (C/C_0, colours) in the placentone for different values of uptake parameter and relative position of the decidual veins (arrows): (a) small source-sink distance (Da = 1, $h = 0.45$); (b) veins near the periphery (Da = 1, $h = 0.9$); (c) low uptake rate (Da = 0.25, $h = 0.9$); (d) high uptake rate (Da = 4, $h = 0.9$). The corresponding values of the relative net uptake rate N_r are (a) 0.43, (b) 0.68, (c) 0.33, (d) 0.94.

the increasing flux of available solute $q\,C_0$, however, the relative net uptake rate $N_r = N_a/q\,C_0$ falls with q, as there is less time available for absorption to take place at higher flow rates as nutrient passes through the placentone more rapidly.

Figures 6.5(c) and 6.6(c) indicate that, when the veins are located near the periphery of the placentone, there is saturation of the whole placentone with solute at high flow rates q for fixed solute consumption rate α and placentone size L (i.e. at Da < 1, Fig. 6.5c). This can be explained by the fact that at high blood flow speeds the concentration distribution in the hemisphere is nearly equal to the initial solute concentration in the spiral artery, making the solute consumption rate α a limiting factor for solute extraction.

Plotting both the relative net uptake rate N_r and averaged over the whole domain solute concentration $\langle C \rangle$ (relative to the inlet concentration C_0) as a function of Da in Figure 6.7, we observe that there is a trade-off between the high uptake rates and a uniform solute distribution in a placentone. Thus, although an increase either in α or in the maternal blood flow rate q gives a higher absolute net uptake rate N_a/q_0C_0, it is essential to keep their ratio (characterised by the Damköhler number) below about 1, in order to provide a more homogeneous spatial solute distribution (*cf.* Fig. 6.5(c,d)).

6.4.4 Influence of volume fraction of villous tissue on net uptake rate

An important characteristic of the placentone is the volume fraction of villous tissue ϕ (the ratio of the volume occupied by villi to the total volume of the placentone).

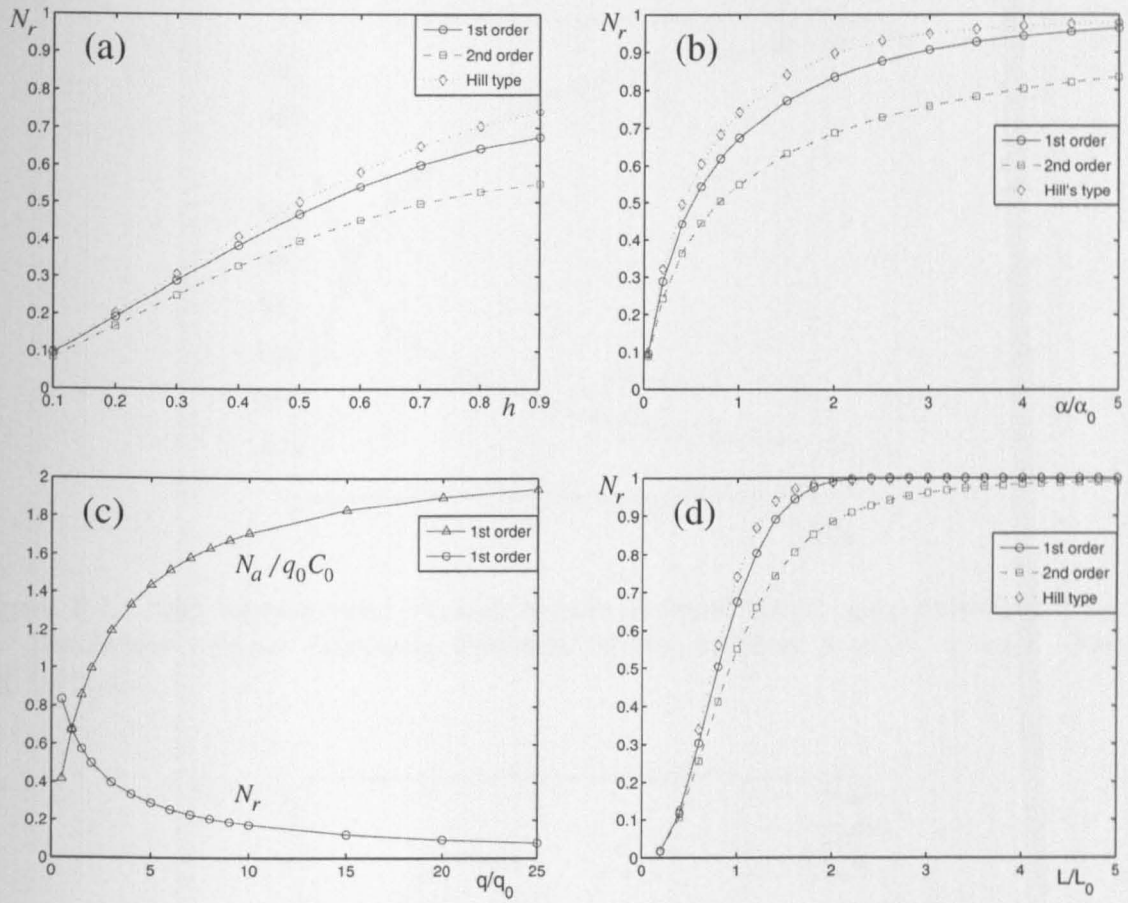

Figure 6.6. Effect of basal vessels' position and solute consumption rate on a net uptake rate for different types of uptake kinetics. Dependence of the net uptake rate N_r on: (a) decidual artery-vein distance $h = z_v/L$ (Da = 1); (b) solute consumption rate α relative to the reference consumption rate α_0 at fixed inlet flux of maternal blood ($h = 0.9$, $q = q_0$); (c): inlet blood flow rate q relative to the reference flow rate q_0 ($h = 0.9$, $\alpha = \alpha_0$); (d): size of the placentone L relative to the reference placentone radius L_0 ($h = 0.9$, $\alpha = \alpha_0$, $q = q_0$). See Table 6.1 for parameter values.

Making simple assumptions about the geometric structure of the villous branches, the flow resistance of the villous tissue can be expressed in terms of ϕ. Changes in the volume flux q through the placentone by varying ϕ under fixed pressure drop ΔP (relative to a reference value q_0) can be estimated as $q \approx 2q_0\,(1-\phi)^3/\phi^2$ (see Sec. 6.3, equation (6.3.8)). If we assume that the solute consumption rate per unit volume α is proportional to the surface area of villous tissue (and assuming the shape of numerous terminal villi, which dominate in the mature human placenta [70, 126], to be close to spherical), then $\alpha \approx 1.6\,\alpha_0\,\phi^{2/3}$, where the coefficients of proportionality are chosen in such a way that $\alpha = \alpha_0$, $q = q_0$ at $\phi = 0.5$ (see Table 6.1).

Therefore, we can investigate how the absolute net uptake rate N_a/q_0C_0, scaled to a reference inlet concentration flux, depends on the villous volume fraction. Fig. 6.8 demonstrates the existence of an optimal volume fraction for all considered types of passive uptake, although what is optimal for one transported species may be sub-optimal for another having different reaction kinetics. However, the difference between the three model uptake rate functions is

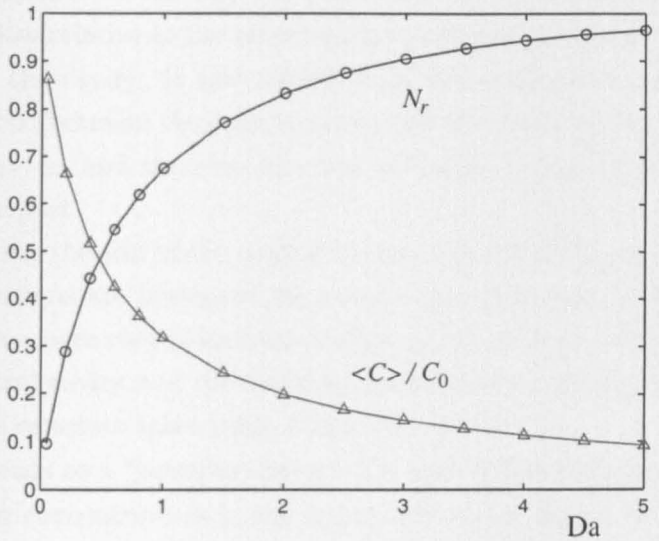

Figure 6.7. Net uptake rate N_r and volume-averaged solute concentration $\langle C \rangle / C_0$ *vs.* the Damköhler number (assuming first-order uptake kinetics; $h = 0.9$, $q = q_0$). See also Fig. 6.5(c,d).

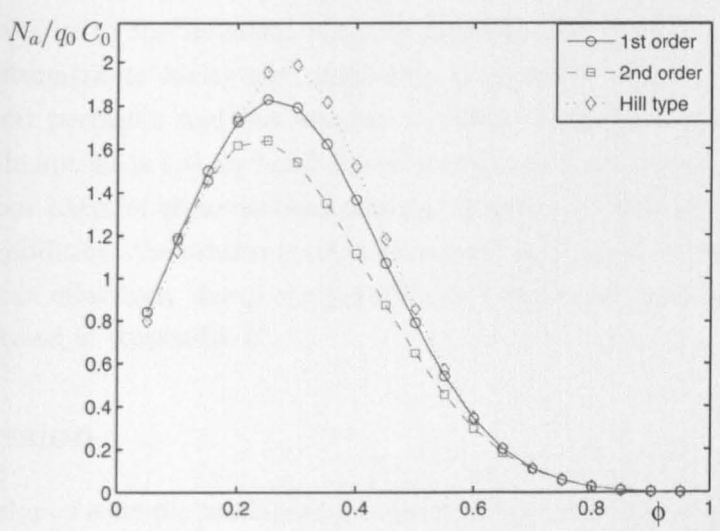

Figure 6.8. Absolute net uptake rate N_a relative to the reference concentration flux of solute $q_0 C_0$ *vs.* volume fraction ϕ for different types of uptake kinetics ($h = 0.9$, $k_0 = 0.25$).

modest, as anticipated from the plots of relative net uptake rates in Fig. 6.6.

6.4.5 Influence of the central cavity on solute concentration distribution

In order to investigate the role of the central cavity of the placentone in the framework of our simple mathematical model, we employ the following additional assumptions: first, the solute consumption rate in the central cavity is negligible compared to the rest of placentone tissue ($\alpha = 0$); second, the border of the central cavity is delineated by a constant pressure line of the flow in a homogeneous hemisphere (one of the isobars shown in green in Fig. 6.3b). The

latter condition corresponds to the case when the flow velocity of maternal blood in the dense intervillous space is slow relative to the blood motion in the central cavity, allowing the pressure to equilibrate within the cavity. It also follows from this assumption that blood is driven by the same pressure drop (between the central cavity and the decidual veins) toward the top and the side of the placentone, and therefore the flow velocities in the top region are smaller than velocities in the lower part.

The effect of varying the size of the central cavity is shown in Fig. 6.9(a,b), where flow and concentration distributions are presented for a small and large cavity. We define the effective cavity radius R as the square root of its cross-sectional area A ($R = \sqrt{2A/\pi}$); the pressure drop ΔP between the central cavity and the decidual veins is held constant in the two simulations. We assume no uptake of solute takes place within the cavity.

The large cavity leads to a "boundary-layer"–like solute distribution pattern in the intervillous space with higher concentrations in the upper half of the domain (Fig. 6.9b) compared to the case of homogeneous uptake in the placentone (Fig. 6.5b), while the relative net uptake rate N_r decreases with increasing cavity size at constant pressure drop (Fig. 6.9c). As in Fig. 6.6(c), the smaller volume of villous tissue provides less flow resistance, so that q increases with R; at the same time, the smaller volume has less capacity to absorb nutrient. Both effects cause N_r to fall with R. However, computations show that the dependence of the absolute net uptake rate N_a (relative to the reference concentration flux $q_0 C_0$) on the cavity radius exhibits a peak for an intermediate cavity size, indicating an optimal relation between the resistance to maternal blood perfusion and the amount of villous tissue participating in solute uptake (Fig. 6.9c). While uptake is low for large R, the cavity may play an important role in shielding villous tissue from harmful shear stresses associated with maternal blood emerging from the spiral artery. In addition, the central cavity surrounded by a dense viscoelastic porous medium (villous tissue) can effectively damp the pulsatile flow emerging from the spiral artery, as we have briefly analysed in Appendix C.

6.5 Discussion

We have developed a simple mathematical model to describe steady maternal flow and solute transport in the human placentone. The placenta is characterised by high degrees of geometric complexity and substantial variability between individuals. We have sought to incorporate only the most significant geometric and haemodynamical features in our model, treating the placentone as a hemispherical structure (Fig. 6.1). This enabled us to derive an analytical expression for the three-dimensional internal flow field (6.3.3), (6.3.4) (see Sec. 6.3 for details), from which simple estimates of nutrient uptake were obtained. Bearing all these limitations in mind, we can now assess the model's predictions.

First, in the absence of a cavity, the localised source and sinks that drive flow through the villous tree (Figs 6.3 and 6.5) show large flow speeds (about 2 cm/s at a distance of order 1 mm from the spiral artery for parameter values from Table 6.1, shown by crowding of streamlines, which is broadly consistent with estimates of Burton *et al.* [57]) and large pressure gradients in the immediate neighbourhood of the decidual artery and veins. This implies that shear

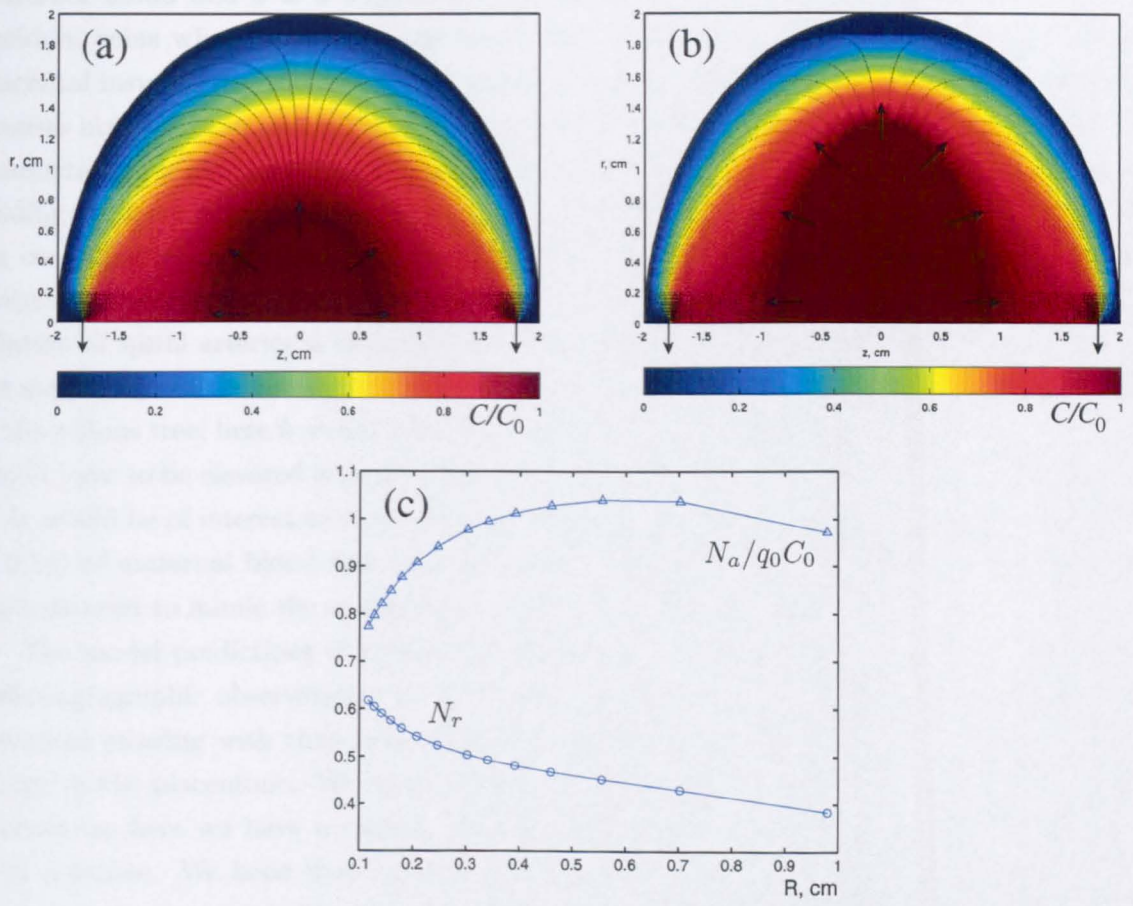

Figure 6.9. Top: flow streamlines (solid) and concentration distribution (colours) in a hemisphere in the presence of the central cavity (assuming first-order uptake kinetics, $h = 0.9$): (a) a small cavity of effective radius $R \simeq 0.6$ cm with Da $\simeq 0.43$ outside the cavity and relative net uptake rate $N_r \simeq 0.45$; (b) a large cavity of effective radius $R \simeq 1$ cm with Da $\simeq 0.39$ and $N_r \simeq 0.37$; Bottom: (c) dependence of net uptake rates N_r, N_a on the cavity size R (with $h = 0.9$).

stresses on villous tissue will be largest in these locations. These flow patterns provide a strong argument for the remodelling of the tree to form a cavity above the arterial opening (Fig. 6.9), and possibly above the veins also, to protect tissues from high stresses [249] and to increase the overall conductance of the placentone. Our model also shows that, in a homogeneous placentone, the flow and solute concentration are more evenly distributed when the decidual veins are located peripherally (Fig. 6.6a), supporting the hypothesis [49, 98] that decidual veins are primarily located at the periphery of the placentone. It may be possible to generalise these findings to explain potential benefits arising from elevated openings of decidual veins on the placental septa [33, 117].

Our model indicates that the calibre of the spiral artery and decidual veins may be a dominant determinant of the overall conductance of the placentone. In particular, Equation (6.3.5) shows that the ratio of the maternal blood flow rate q through the placentone to the driving pressure difference ΔP between the spiral artery and decidual veins is $4\pi ka/3\mu$, where k is the effective hydraulic conductivity of the villous tissue, μ is the effective viscosity of

maternal blood and a is a lengthscale representative of the calibre of the spiral artery and decidual veins where they meet the basal plate of placenta. This may have implications for placental insufficiency such as in pre-eclampsia, where inadequate trophoblast invasion of spiral arteries may result in reduced lumenal diameter [57] and hence significantly reduced placentone conductance to maternal blood flow. In case of an early onset of failed trophoblast invasion leading to lower arterial calibre a over normal values, there may be sufficient time available for compensatory remodelling of the villous tree (increasing the placentone conductivity k) to maintain physiologically normal values of q at constant pressure drop ΔP. However, if the dilation of spiral arteries is impaired in the late stage of pregnancy, or an acute constriction of the supplying vessels takes place, there may not be sufficient time for compensatory remodelling of the villous tree; here k would remain constant, and maternal systemic arterial blood pressure would have to be elevated in order to maintain the same flow rate level q at the reduced value of a. It would be of interest to verify experimentally the linear dependence (predicted in Equation (6.3.5)) of maternal blood flow rate through an isolated fetal cotyledon on the calibre of the cannula used to mimic the spiral artery in an *ex vivo* perfusion model.

The model predictions of tracer distribution in a placentone (Fig. 6.4) are in accord with radioangiographic observations *in vivo* in primates and humans. The formation of a ring-like structure growing with time is demonstrated even without explicitly accounting for a central cavity in the placentone. We need to stress that the term "smoke ring" is misleading in this context, as here we have a radially outward maternal flow without any localised rotation of fluid particles. We hope that rapid development of new techniques in ultrasound imaging [2, 148], complementing traditional radioangiography and used in conjunction with mathematical modelling, may offer new tools for monitoring placental function with a lower risk to mother and fetus.

For a given geometry, the ratio of nutrient uptake rate to volume flux, expressed by the dimensionless Damköhler number $\mathrm{Da} = \alpha L^3/q$, determines the homogeneity of uptake: if Da is sufficiently large, for example, uptake is confined to the immediate neighbourhood of the spiral artery (Fig. 6.5d). Evidently materials with differing uptake rates and kinetics (and therefore different Da) will be absorbed in different regions of the placentone. The relative net uptake rate N_r can be interpreted as a relative difference between solute concentrations in the spiral artery and decidual vein, scaled with arterial concentration at constant blood flow rate in the spiral artery. A range of values for oxygen partial pressure suggests that N_r for oxygen varies between 0.3 and 0.7 [153], which is close to the predicted range in Fig. 6.6(a). One possible explanation of a modest relative net uptake rate is that it helps to keep solute more homogeneously distributed in the placentone, as in Fig. 6.5(c). While the dependence of the relative net uptake rate N_r on the consumption rate α (Fig. 6.6b) follows the predictions of the placental oxygen exchange in Lardner's compartmental model (see [153, Fig.2]), we predict that the oxygen pattern would be highly localised at the very large values of the "nondimensional diffusion coefficient" (the analogue of the uptake parameter $\mathrm{Da} \sim 10 - 10^2$), with much of the placental tissue being kept in a hypoxic state.

The placentone exhibits a trade-off between flow resistance and uptake capacity. A higher density of villous material offers a larger surface area for uptake, but also higher flow resistance

and hence lower perfusion (for a given pressure drop between artery and veins). Likewise with a low density of villous tissue, nutrients could flow rapidly through the placentone, too quickly for substantial uptake to take place. We used our model to demonstrate the existence of an optimal volume fraction of $\phi \approx 0.3$ that maximises the absolute net uptake rate of our representative solute (see Fig. 6.8). In relating uptake rates and likely fluxes to volume fractions, we used standard expressions from the porous medium literature (e.g. the Kozeny–Carman formula), which is derived assuming the porous medium is a uniform distribution of spheres. As a result of these and our other modelling assumptions, the resulting prediction of optimal volume fraction falls below values measured in previous studies (for example, estimates of the villous volume fraction, based on stereological data of Mayhew [172] for normal, high altitude and diabetic placentas, vary between approximately 0.3 and 0.6 with a tendency towards low values in the high-altitude group, used as a model for pre-eclampsia; there was no significant difference in the volume of intervillous space and villous volume between the control and diabetic groups [172]). Numerous additional factors will influence the optimal value of ϕ, which we did not explore explicitly here.

While considering flow and solute transport in the placentone, we ignored the inertia and pulsatility of a jet of maternal blood issuing from a spiral artery, as well as deformability of the villous tissue. These factors will be attenuated both by mixing in the cavity above the artery and by viscous effects in the intervillous space: while the Reynolds number based on placentone diameter is of order unity (Table 6.1), the Reynolds number based on intervillous pore diameter is substantially smaller, and so inertial effects can safely be neglected everywhere except possibly in the immediate neighbourhood of the spiral artery [57]. The impact of the blood flow pulsatility and villous deformability is partially addressed in Appendix C. We show how the Darcy flow in the dense intervillous space, coupled with incompressible pulsatile flow in the cavity and a viscoelastic constitutive law for the villous tissue, give a flow-driven dissipative oscillator model for the cavity radius (see Equation (C.2.10)). Parameter estimation (Fig. C.4) indicates that the system is heavily damped and the static description of the central cavity appears to be a reasonably good approximation. Thus, the central cavity, apart from optimising the overall intervillous flow resistance and solute uptake, may also act as a damper that transforms a pulsatile flow from the spiral artery to a steady flow in the intervillous space, where most of the solute exchange takes place.

VII Conclusions and Further Directions

7.1 Summary of the results

Flow and transport in the human placenta is a fundamentally multiscale process, integrating the solute exchange at the scale of individual terminal villi ($\lesssim 0.01$ cm) with the flow distribution around a single villous tree (~ 1 cm) and in the whole organ ($\gtrsim 10$ cm). The aim of this thesis is to examine the interplay between some of these scales and to develop a theoretical and computational framework for systematic modelling of the placental transport function in health and disease.

Building on the works of Auriault, Mei, Mikelić and many others [11, 177, 180], we have studied the theoretical implication of flow past a periodic microscopic array of sinks, representing the villous branches, in Chapter 2. We classify distinct asymptotic transport regimes, each characterised by the dominance of advective, diffusive or uptake effects, at the macroscale, and provide a comprehensive estimate of the accuracy of the homogenized description summarised as a map in (Pe, Da)-parameter space (Fig. 2.2a). In addition, we identify the most physiologically relevant placental transport regime in the (Pe, Da)-space, which is characterised by an approximate balance of advective and uptake factors at high Péclet number. In this region, the convergence of the exact solution to a homogenized solution is weak (applying in the L_2 but not the H^1 norm), because corrections have large spatial gradients on lengthscales below the inter-sink distance. Such fine-scale features, not captured by leading-order homogenization, are likely to be of importance in models that resolve the detailed arrangement of fetal vessels within villous branches.

Although the homogenized leading-order concentration profile for a periodic array is applicable to a wide range of ergodic stationary random sink distributions, the next-to-leading-order correction can exhibit very different behaviour, depending on statistical properties of the array. This becomes particularly important for a moderate scale separation (characterised by a scale-separation parameter ε), as is common in many applications, including the human placenta. We address the impact of micro-structure stochasticity on the macroscopic solute transport in Chapter 3, where we have used our simplified model to illustrate some generic features of homogenization approximations for disordered media. While assessing the accuracy of the homogenized solution $C^{(0)}(X)$ in random arrays, one must compare it not only to an expected value of the exact solution C but also to the fluctuations of C about the mean. Our results for three illustrative stationary random sink distributions (uniformly random, hard-core and normally-perturbed) agree with the upper bounds for the homogenization residue $C - C^{(0)}$ developed by Bal, Bourgeat, Piatnitski and others [22, 47], e.g. in the mean-squared norm: $\mathbb{E}[\,\|C - C^{(0)}\|_{L_2}^2\,]^{1/2} \leq O(\sqrt{\varepsilon})$. However, the underlying regularity of the normally-perturbed sink distribution, at sufficiently small standard deviation, secures a much higher homogenization accuracy (see Fig. 3.13(a,b)), particularly for small Pe. Furthermore, we find that for virtually

all considered sink statistics - with sinks almost uncorrelated to each over - the homogenization residue correlates strongly at the lengthscales of the whole domain. Therefore, we expect the boundary conditions such as concentrations and concentration fluxes in the maternal decidual vessels to determine the distribution not only of averaged leading-order concentration but also of concentration fluctuations in the intervillous space.

In order to test experimentally the transport properties of the human placenta, we have extended the homogenization results to two dimensions in Chapter 4. We demonstrate that the map of transport regimes in the (Pe, Da)-space remains largely unchanged relative to the one-dimensional case (Fig. 2.2a) and highlight that the volume fraction ϕ of a sink in a unit cell emerges as another parameter influencing the accuracy of the homogenized description. We have further generalised the linear transport model to take into account the carriers of a solute, such as red blood cells carrying oxygen. Homogenization of the solute-carrier-facilitated transport introduces an effective Péclet number that depends on the slowly varying leading-order concentration $C^{(0)}$, so that an asymptotic transport regime can be changed within the domain of fixed Pe and Da (Fig. 4.13). At large Pe and Da numbers (typical for oxygen transport in the human placenta), nonlinear advection due to solute-carriers leads to a more uniform solute distribution than for a linear carrier-free transport (Fig. 4.14a), suggesting a "homogenizing" effect of red blood cells on placental oxygen transport. Finally, following [177, 228], we have derived and verified a homogenized description of flow and transport with effective diffusivity and permeability tensors dependent on the microscopic shapes.

In Chapter 5 we have characterised the pattern of villous centres of mass, comparing it to the random point sink distributions of Chapter 3. The second-order statistical properties, quantified by the K-function, give no evidence against the considered sample exhibiting a uniformly random distribution of villous centres at the lengthscales larger than about 0.1 mm and a hard-core distribution at the distances below this scale (Fig. 5.11); in addition, estimates of the villous area fraction indicate that the microscopic noise is significantly reduced at the averaging scales larger than 1 mm (Fig. 5.7). For the mean inter-point distance of about 50 μm and a reference placentone size of the order of 1 cm, we have $\varepsilon \approx 0.005$. The results of Chapter 3 for uniform or hard-core sink distributions then give the relative magnitude of homogenization residue fluctuations of up to 10%, compared to the residue magnitude below 1% for a slightly normally-perturbed or strictly periodic array. We have also evaluated effective permeability and diffusivity for a placental sample, by solving the corresponding unit cell problems of Chapter 4. The effective permeability estimate has modest anisotropy, suggesting a homogeneous isotropic porous medium is a reasonable leading-order approximation of the intervillous space.

Having established the homogenized description of flow and transport and its potential accuracy, in Chapter 6 we have formulated and analysed a leading-order mathematical model of intervillous flow and solute transport in a simplified geometry of a single placentone. The model supports the hypothesis that basal veins are located on the periphery of the placentone in order to optimise distribution of nutrients and predicts the existence of an optimal volume fraction of villous tissue and an optimal size of the central cavity. We have also used the model to explain the ring-like structures ("smoke rings") observed in experimental radioangiographic studies of tracer dynamics in the primate and human placentas. Besides the villous volume fraction, the

calibre of the spiral arteries and decidual veins is shown to be a dominant determinant of the overall flow resistance of a placentone, clarifying the physical basis of the arterial remodelling during the pregnancy. The central cavity is also shown to act as a damper of the pulsatile flow from a spiral artery. The central cavity of the placentone is thus likely to play multiple functions that include shielding the villous tissue from high blood pressure and shear stress, and the regulation of the overall resistance to placentone perfusion.

To sum up, modelling flow and transport in the human placenta requires coupling of physical and chemical processes across multiple scales in a complex micro-geometry. A direct predictive simulation of these processes for the entire organ is not only prohibitively computationally expensive, but is very hard to achieve from a methodological standpoint, because the entire villous microstructure (with the total interface surface area of about 10 m^2 packed into the volume of just $\sim 10^{-3}$ m^3, nearly the size of a Frisbee; see Table 6.1) and the corresponding heterogeneous boundary conditions for flow and concentration cannot be measured simultaneously. Moreover, such level of detail is not of primarily clinical interest, where net trans-placental transport and averaged placentone-wide flow and concentration fields are of more significance for monitoring fetal well-being. Homogenization approaches provide a powerful tool in multiscale modelling and are likely to figure prominently in future integrative models of the human placenta (and for other tissues with fine-grained periodic or random microstructure such as the liver [45] or the lung [245]). This study shows the merits of stepping beyond the leading-order approximation in order to resolve fine-scale structures at the microscale and, perhaps more importantly, to assess carefully the magnitude and nature of cumulative (and parameter-dependent) errors that arise from stochastic variation. These errors must be interpreted using the language of non-smooth functions and distributions (where large deterministic local gradients and random fluctuations both contribute to the error of a homogenized description). Such steps will be particularly important when building complex models that integrate numerous competing processes, in order to avoid errors arising at each level of approximation from accumulating and disrupting the overall predictive capacity of the model.

7.2 Future development

Future models of the human placenta will need to address the implications of assuming an idealised geometry and our numerous other approximations (see Sec. 6.2.2). For instance, while the rheology of blood in narrow capillaries has been well characterised experimentally [199], little is known at present about the rheology of maternal blood moving through tortuous intervillous spaces. We have also considered only very simple models of advective nutrient transport and uptake, ignoring transport in the fetal microcirculation and assuming only simple uptake kinetics that may be mediated by nonlinear active transport mechanisms in the syncytiotrophoblast [238].

Further potential developments span the following areas: (i) theoretical homogenization of solute transport; (ii) automated microscopic image analysis and macroscopic parameter estimation of the human placenta; (iii) effective placental flow and transport modelling informed by the microstructure. We briefly outline some open questions of these areas below.

A priority for a theoretical homogenized description of solute transport is to compile the maps of "transport regimes" and "homogenization accuracy" in the (Pe, Da)-space (similar to Figs 2.2(a) and 3.13(a,b) in the one-dimensional case) for different solutes and to investigate further the structural stability (with respect to uptake kinetics, statistics of the micro-geometry and other factors) of distinct asymptotic regions. In particular, one can consider the homogenization errors and macro-correlations for different types of uptake kinetics and the global boundary conditions; extend the statistical analysis of homogenization residue to random micro-geometries in two-dimensions (e.g. a normally-perturbed on torus *vs.* a uniformly random sink distributions); account for the sink's volume fraction ϕ, understanding the impact of interacting concentration wakes on the statistical properties of homogenization residue at high Péclet number and extending the parameter space to three dimensions (Pe, Da, ϕ); calculate higher-order corrections to the averaged flow problem, include the advanced rheology for fluid (see, e.g. [44, 199, 239]) and allow for small elastic deformations in the sink's position and shape (coupling the transport with the Biot-type flow [54]).

Image analysis of morphological, flow and transport parameters of the human placenta could be extended to compare K-functions of normal/diabetic/pre-eclamptic placentas (using the protocols developed in Chapter 5, with further development of semi-automated image analysis that would allow bulk processing of histological data and reduce systematic errors); to create a representative unit cell of the normal placenta and of each pathological group and extract the cell-averaged permeability and diffusivity tensors; to fit parameters of suitable spatial models to histological data and to assess how these features of tissue architecture may vary during development; to account explicitly for the micro-architecture of the villous tree, giving improved estimates of hydraulic permeability, diffusivity and uptake as a function of volume fraction, based on variability of placental samples from different regions of the same placenta as well as between individuals. These can then be used to assess with more confidence the relation between the structure and function of a placenta in health and disease.

Advances in effective placental flow and transport obviously lie beyond the uniform Darcy flow and have to be coupled with the fetal circulation, studied in recent works [104, 115, 188, 277]. Some further potential investigations, at the maternal side, are as follows: analyse flow about the opening of a spiral artery immersed in a pool of the central cavity, coupled with the flow in a porous (and deformable) intervillous space outside the cavity; take account of a possible modulation of the intervillous space volume due to the smooth-muscle contractions of the myometrium in the uterine wall as well as of longitudinally arranged myofibroblasts in the anchoring stem villi [33, p. 86]; develop a framework for patient-specific modelling of placental perfusion and uptake rates for the model parameters estimated from Doppler ultrasound, MRI or micro-CT scans, analogously to the histological sections.

It is hoped that the integrated approach undertaken in this thesis not only has led to a better understanding of solute transport in the intervillous space of the human placenta and fundamental properties of homogenization in disordered media, but will also open a door to modelling-based diagnostics and treatment of placental disorders.

Mechanisms of Placentone Development

This appendix provides a supplementary overview and analysis of biochemical and mechanical regulatory factors contributing to the placentone genesis, discussed in Section 1.2 of Chapter 1.

A.1 Early placentation stage

What determines the temporal development of the architecture of a single placentone? It is known that the formation of distinct fetal villous trees is complete by the end of the second trimester [33]; therefore, many mechanisms can contribute to the creation of placentone's spatial heterogeneity.

After implanting into the outer layer (endometrium) of the wall of the uterus, the future embryo, a *blastocyst*[1], develops an interconnected network of cavities (lacunae) in its outer trophoblast layer, which are the proxies of the future villous trees.

The trabeculae of syncytial trophoblast[2], which separate the lacunar spaces, are at first arranged in a random pattern; however, with further growth of the blastocyst they become radially orientated [252]. Moreover, at the initial stage of lacunar formation the human placenta has labyrinthine features [252], suggesting the existence of a switch to the villous-type placental architecture. These phenomena may indicate the guiding influence of the decidual vasculature on villous development.

A typical spiral artery supplies approximately $4 - 9$ mm^2 of the endometrial surface [87]. Therefore, a characteristic distance between the centres of adjacent areas of supply is about $2 - 3$ mm, which is much more than 0.2 mm, the initial diameter of the invading blastocyst [49]. This ensures sufficient spatial separation between the spiral arteries that are later invaded by the extravillous trophoblast.

There is increasing recent interest in the process of trophoblast invasion in the decidua in humans and the remodelling of the spiral arteries [67–69, 144, 154, 163, 164, 195, 197, 210]. Starting from the works of Pijnenborg *et al.* [194], attention has focused mainly on the dynamics of extravillous trophoblasts from the second half of the first trimester and covers the period of the 6th to 22nd weeks of gestation [144, 163]. Blastocyst delivery and the initial stage of implantation in the uterine wall are less investigated [8, 64, 65, 193], although a number of theoretical models have been proposed [60, 278]. The intermediate step of trophoblast behaviour, connecting the beginning of implantation with the formation of tertiary villi, is less well studied, partially because very little human data is available at this stage [214]. Observations in animal models, mainly in *Macaca mulatta*, show that trophoblast invasion and migration towards spi-

[1](from Greek "germinative vesicle"): an early stage of mammalian embryo development, consisting of the inner cell mass and a thin trophoblast layer [251].

[2](from Latin "small beam"): boundaries of a meshwork created in the fused multinucleated trophoblast cell mass [251].

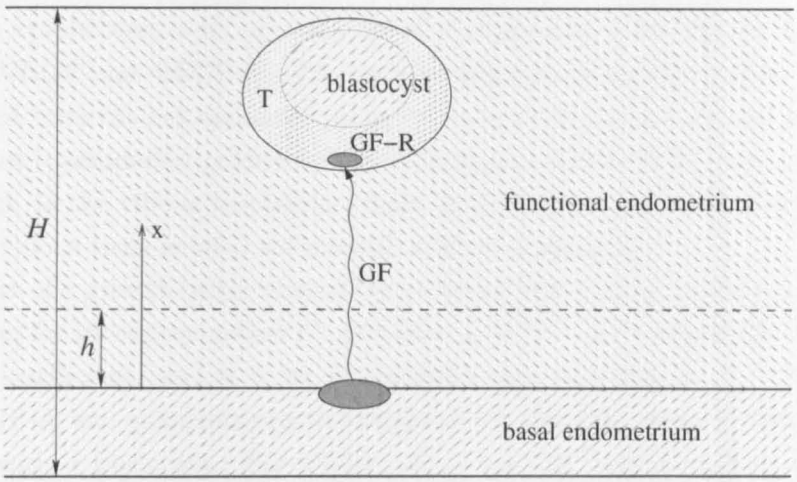

Figure A.1. A scheme of growth factor (GF) diffusion through the endometrium towards a growth factor receptor (GF-R) in the trophoblast layer (T) of the invading blastocyst. The overall thickness of the endometrium $H = 9 - 12$ mm [93, 233] is greater than the diffusive penetration distance of GF $h \lesssim 1$ mm along the axis x perpendicular to the uterine wall (see Table A.1).

ral arteries begins as early as 10 days post conception [84, 144]. During this time the lacunar system is formed, providing a frame for the future villous structure. These first 20 days seem to be vitally important for successful placentation.

Recent advances in the biochemistry of the vascular endothelial growth factors[3] family (VEGF-A – VEGF-E) and placental growth factor (PlGF) [5, 72, 80, 154, 231, 243] brought evidence that VEGF-receptors (Flt-1 and others) are present in trophoblasts. Analysis of the influence of angiogenic growth factors on trophoblast proliferation, motility, and invasion in the decidua showed that a VEGF-A gradient can direct the migration of trophoblast cells *in vitro* both from the first trimester and full-term placentas [155]; the extent of the physiological significance of the observed effect, however, is still unclear [10, 154]. This suggests that a similar paracrine mechanism[4] may allow cross-talk between a decidual source of VEGF (or another growth factor) and trophoblast-cells *in situ*, and may lead to directed invasion (Fig. A.1). It is also reported that knocking out Flt-1 production by the trophoblast does not affect placentation in the mouse [123], but one can speculate that in this case there is no need for spatial co-organisation of spiral arteries and the fetal circulation, since the mouse placenta has a semi-closed maternal circulation [4] and is a poor model for trophoblast invasion in humans [66].

In vitro three-dimensional spheroidal cultures formed from first-trimester cytotrophoblast cells demonstrate more intensive invasion in collagen gel than those from the third trimester, and outgrowths are strongly accelerated by the addition of epidermal (EGF) and angiogenic growth factors [149]. Nonetheless, further evidence of trophoblast chemotaxis[5] factors is certainly required.

[3]Natural substances produced to promote growth and development by directing cell maturation and differentiation. For example, angiogenic growth factors (e.g. VEGF) stimulate the formation of new blood vessels, and epidermal growth factor (EGF) upregulates the development of cells covering free surfaces, such as skin [251].

[4](from Greek "closely separated"): related to the effects restricted to the local environment [251].

[5](from Greek "chemically ordered"): movement of cells or organisms in response to chemical compounds, whereby the cells are attracted or repelled [251].

Because the trophoblast cells are capable of synthesising both growth factors and their receptors (e.g. VEGF and VEGF-R) [72], another scenario is possible: since extravillous trophoblasts derived from the cell columns[6] scatter very early in pregnancy and are localised near the spiral arteries (presumably guided by the EPH/ephrin-family [209]), they too can begin to send signals back to the villous trophoblast cells in the form of growth factors, so stimulating proliferation of villous trees around the arterial orifices (openings).

The transport of a growth factor towards the trophoblasts can be described by the diffusion-reaction equation for its concentration C: $\partial C/\partial t = D\,\nabla^2 C - \alpha\, C$, where the D is the growth-factor diffusion coefficient, and α is its degradation rate (see Fig. A.1). The diffusion and reaction of VEGF-A was quantitatively investigated *in vitro* [73], using a rectangular diffusion chamber filled with a fibrin gel. For VEGF, $D = 7 \times 10^{-7}$ cm^2/s and $\alpha \sim 10^{-4}$ s^{-1} [73]. Therefore, in steady state, one can estimate the characteristic penetration depth h over which the VEGF concentration falls approximately 3-fold as $h_{\mathrm{VEGF}} \simeq \sqrt{D/\alpha} \sim 1$ mm.

We can likewise estimate the effective distance of penetration for a variety of growth factors. To estimate α, we assume a typical half-life of 1 hour in each case, so that $\alpha = \ln(2)/t_{1/2} \simeq 1.9 \times 10^{-4}$ s^{-1}. To estimate D, we use the empirical formula $D = a\,M^{-b}$ cm^2/s with parameters a, b fitted to cover a range of solute molecular weights M [127, 254]. Estimates of penetration depth are summarised in Table A.1. Epidermal growth factor (EGF) has the highest diffusivity among other growth factors present in the placenta due to its low molecular weight, and therefore the greatest estimated penetration distance.

While pure protein solutes are usually characterised by short life-times, their compounds with polysaccharides, heparin or stable mutant homologies can increase their life-time as much as 10-fold [281]. The penetration depth will then be increased around 3-fold. On the other hand, there are growth-factor-binding sites in the extracellular matrix (e.g. heparin) that can significantly decrease the diffusivity of signalling molecules [105]. The two combined effects may not lead to large changes in penetration distance, however. Finally, one also should take account of the integrin and matrix metalloproteinase (MMP) interactions with the decidual extracellular matrix, which can modulate its conductance for signalling molecules [8].

The effective penetration distances estimated in Table A.1 are much less than the thickness of the endometrium (Fig. A.1), reported to be of about 9–12 mm [93, 233]. Therefore, it is unlikely that growth-factor-mediated trophoblast proliferation and migration can be established at the very beginning of implantation. However, with the rapid advance of a ball-shaped blastocyst, with initial diameter of about 0.2 mm [49, 149], across the depth of the uterine wall, the required distance may be achieved and the uterine-artery-derived growth factor can start to attract the trophoblast cells. This mechanism may launch the spiral-artery-specific spatial development of a future villous tree, giving a full term placentone.

[6]Cell columns are the massive trophoblastic connections, attaching the anchoring villi to the basal plate or to the placental septa (see Fig. 1.1a), and providing a source of extravillous trophoblasts invading the decidual vessels [33].

Growth factor	Molecular weight (kDa)	Diffusion coefficient (cm^2/s)	Effective distance (mm)
HGF	83 [196]	2.8×10^{-9}	0.04
Ang-1	75 [42]	3.7×10^{-9}	0.04
PIGF	50 [138]	1.2×10^{-8}	0.08
$VEGF_{189}$	40 [196]	2.4×10^{-8}	0.1
$TGF\beta$	25 [196]	0.89×10^{-7}	0.2
$VEGF_{164}$	23 [196]	0.95×10^{-7}	0.2
$VEGF_{121}$	17 [42]	1.2×10^{-7}	0.2
FGF-1, FGF-2	15 [196]	1.3×10^{-7}	0.3
IGF-2	7.5 [196]	2.2×10^{-7}	0.3
EGF	6 [196]	2.6×10^{-7}	0.4

Table A.1. Estimated diffusive properties of the most common placental growth factors: hepatocyte growth factor (HGF), angiopoietin (Ang), placental growth factor (PIGF), vascular endothelial growth factor (VEGF), transforming growth factor (TGF), fibroblast growth factor (FGF), insulin-like growth factor (IGF) and epidermal growth factor (EGF). *Diffusivity* D is estimated by the empirical formula $D = a\,M^{-b}$ cm^2/s with $a = 1.778 \times 10^{-4}$ $cm^2\,Da^b/s$, $b = 0.75$ (obtained by Swabb, Wei and Gullino [254] for solute molecular weights M in the range $3.2 \times 10^{-4} - 69$ kDa in biological tissues at 37 °C *in vitro*), and $a = 10^6$ $cm^2\,Da^b/s$, $b = 2.96$ (fitted by Jain *et al.* [127] for dextran molecular weights M in the range 19.4 – 150 kDa in rabbit granulation tissue *in vivo*). The Swabb *et al.* formula is used for $M \leq 25$ kDa and the Jain *et al.* formula for $M > 25$ kDa. These dependences differ from the Stokes–Einstein relation for the free diffusion of a homogeneous spherical particle in Newtonian medium ($b = 1/3$) due to the hindering effects of biological tissue. The effective diffusive distance is estimated as $h \simeq \sqrt{D/\alpha}$, where $\alpha \simeq 1.9 \times 10^{-4}$ s^{-1}.

A.2 Role of haemodynamical forces and oxygen tension

At the beginning of placentation the villi demonstrate homogeneous development around the chorionic sac[7], but soon disproportionate growth of villi opposite to the implantation pole occurs, and by the end of the first trimester the smooth chorion (devoid of villous trees) is formed [33, 186]. The effect of oxygen tension in this non-uniform growth has been recognised by Burton *et al.* [55, 56], where the decidual arteries and arterioles less plugged with trophoblast in the region opposite to the implantation pole were shown to provide a highly oxidative environment and thereby to suppress villous development.

The chorionic villi are exposed to viscous shear stresses and blood pressure as well as to maternal oxygen tension from the end of the first trimester, when the maternal blood supply is gradually increased [56, 195]. The spatial heterogeneity of antioxidant enzymes' activity in a mature fetal cotyledon matches the centre-to-periphery pattern of maternal blood flow [117].

The origin of the central cavity (see Fig. 1.2) in the placentone is reflected by static structural differences, with less differentiated villi in the central portion and more terminal branches in the periphery, [33, 237]; the dynamical effect of force exerted on non-anchored villi from flowing blood from the supplying spiral artery has also been suggested as a mechanism for cavity

[7](from Latin "bag"): an outer membrane around embryo [33].

formation [215]. The latter reason is less likely to dominate, since the pressure in the ostium of a spiral artery is of the order of 10 mmHg at term [108], which is about 5 mmHg higher than the pressure in the amniotic fluid in macaque Rhesus [184]. Nevertheless, the possible effect of viscous shear stress on villous development might be significant.

The remodelling of the spiral arteries that establishes normal circulation in the intervillous space is not complete until about the 20th week of gestation [129, 195] and, according to the *in vivo* ultrasound observations of Jauniaux *et al.* in pre-eclamptic and IUGR placentas, altered intervillous blood flow opposite the non-remodelled arterial openings of small calibre is correlated with the formation of villous-free "placental lakes" [128, 129]. Therefore, haemodynamic forces are likely to play an important role in the shaping of the placentone between the 12th and 20th weeks.

We shall remark that the remodelling of the spiral arteries (resulting in their dilatation and destruction of the vascular smooth-muscle layer) likely involves not only the trophoblast invasion but also the nitric oxide-induced dilatation due to an elevated shear stress, once the intervillous circulation is established [250]. Moreover, the shear-stress regulatory mechanism is known to have an instability leading to a collapse of daughter branches of a smaller calibre [204]. In the light of the absence of innervation in the spiral arteries and the diminished total neural regulation of vascular tone in uterus [140], it is the shear stress that might contribute to reducing the total number of arterial openings in favour of a few large functional ones.

Proliferation and differentiation of the villi and feto-placental angiogenesis are thought to be dependent on the oxygen level [5, 131] and, possibly, on shear stress via mechanosensitivity of trophoblast cells [195, 249]. These effects could provide the basis for an early switch from branching to non-branching villous development in the central portion of the fetal cotyledon; this region is associated with a spiral artery and experiences higher oxygen concentration and flow velocities than the peripheral part.

Another important aspect to be clarified is whether the anchoring villi are initially uniformly distributed over the placental bed and then start to lose and form their attachments, as suggested in [216], under the influence of haemodynamical factors, or whether the formation of the fetal cotyledons around the arterial openings is pre-programmed at the beginning of implantation.

A.3 Pathological implications of failed placentone formation

Although earlier studies addressed the topography of human uteroplacental vasculature [108, 216], a few recent reviews describing simultaneously the growth of both the maternal and fetal placental circulatory systems [125, 139] do not represent the spatial organisation of feto-maternal circulation from the developmental point of view.

It is usually suggested that a failure in fetal placental angiogenesis or remodelling of maternal spiral arteries are two main factors of placental insufficiency. Nevertheless, if one accepts the placentone structure of the primate and human placenta, a failure in forming the optimal spatial arrangement between maternal and fetal circulatory systems (as described in Section 1.2 of Chapter 1; Fig. 1.2) provides a third potential source of placental pathology.

Therefore, the development of chorionic villi should not be considered in isolation from

the decidual vessels and *vice versa* because the haemodynamics of the haemochorial placenta, characterised by the presence of openly circulating maternal blood in a close contact with chorionic villous trees, is strongly affected by the spatial organisation of the feto-maternal functional units, placentones.

The available data tends to support the concept that a villous tree develops around a specific supplying decidual artery, optimising its spatial arrangement for effective metabolic exchange. The mechanism underlying the genesis of the placentone may be provided by the decidual arterial cell or endovascular-trophoblast-derived VEGF and other growth factors, which are sensed by villous trophoblast cells via corresponding receptors. Haemodynamical forces may then contribute further to villous development. We pose a preliminary hypothesis that the process is likely to be separated into two stages: an initial finding of spiral arteries by villous trophoblast assisted by the gradient of growth factor concentration during the early villous state; and later artery-specific development of the villous tree, directed also by fluid shear stress and oxygen partial pressure distributions in the intervillous space.

This idealised two-stepped structural evolution of placental circulatory units may be too simplistic to reflect all details, but it highlights a general tendency to ordered rather than chaotic organisation of the intervillous blood supply observed in full term placentas, confirming the description of Freese [98]: "There is a nicely designed system of maternal blood flow in the intervillous space".

B Additional Results for Asymptotic Transport Regimes

This appendix contains additional asymptotic analysis for the transport regimes in a one-dimensional array of sinks, developed in Chapters 2 and 3.

B.1 Limiting case of diffusive transport (Pe = 0)

Setting $p = \mathrm{Pe}/\varepsilon = 0$ in (2.3.9), we obtain a regular limit

$$C^{(0)} = \tfrac{q}{2} X^2 - (1 + \tfrac{q}{2}) X + 1, \quad q \leq 2. \tag{B.1.1}$$

In case of no sinks are present ($q = 0$), a linear diffusive profile is restored for the concentration, since $C^{(0)} = 1 - X$ and $C^{(1)} = C^{(2)} = \ldots = 0$. A cell problem for the second correction $C^{(2)}$ is identical to (2.3.11) due to its independence on p. Analogously, one can show that the third and successive corrections are all equal to zero.

The solution to (2.2.2) is therefore $C(x) = C^{(0)}(X) + \varepsilon^2 C^{(2)}(x, X)$, where $C^{(0)}$ is given by (B.1.1), $C^{(2)}$ is given by (2.3.12) and $X = \varepsilon x$. Substituting the solution to the governing equation $C_{xx} = 0$, we find that $(C^{(0)} + \varepsilon^2 C^{(2)})_{xx} = \varepsilon^2 + \varepsilon^2(-1 + \varepsilon^2 \langle C^{(2)} \rangle_{XX}) = 0$, and hence $\langle C^{(2)} \rangle_{XX} = 0$. An average $\langle C^{(2)} \rangle$ of the second correction over the unit cell is therefore a linear function of the slowly changing variable X, with the arbitrary constants determined by the boundary conditions. In this problem, the Dirichlet conditions $C^{(2)}|_{x=0,X=0} = C^{(2)}|_{x=0,X=1} = 0$ require $\langle C^{(2)} \rangle$ to be a constant, which is equal to $\langle C^{(2)} \rangle = \frac{q}{12}$ as identified in Section 2.3 of Chapter 2.

B.2 Array of sinks of a finite size: the role of volume fraction (case Pe = $O(\varepsilon)$)

To test the role of the finite size of villous branches, we now account for an array with each sink of a size ϕ (in dimensionless variables) that occupies a portion of a unit cell ($0 \leq \phi < 1$), as shown in Fig. B.1.

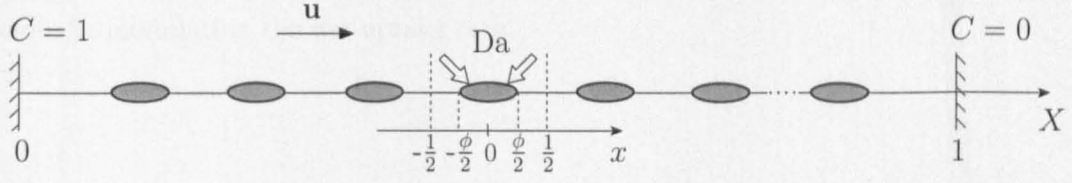

Figure B.1. A periodic array of finite-size sinks.

Assuming free uniform flow over each sink and a fixed drop of uptake flux between its upstream and downstream end, in addition to all the assumptions of Section 2.2, we rewrite (2.2.3) as follows:

$$\mathrm{Pe}\frac{\mathrm{d}C}{\mathrm{d}x} = \frac{\mathrm{d}^2C}{\mathrm{d}x^2}, \quad 0 < x < \varepsilon^{-1}, \tag{B.2.1a}$$

$$C|_{x=0} = 1, \tag{B.2.1b}$$

$$C|_{x=\varepsilon^{-1}} = 0 \quad \text{or} \quad C|_{x=x_0} = \left.\frac{\mathrm{d}C}{\mathrm{d}x}\right|_{x=x_0} = 0 \ \text{ for } \ 0 < x_0 \le \varepsilon^{-1}, \tag{B.2.1c}$$

$$C|_{x=x_n-\phi/2} = C|_{x=x_n+\phi/2}, \qquad n = 1, 2, \ldots, N;\ N \approx \varepsilon^{-1}, \tag{B.2.1d}$$

$$\left.\frac{\mathrm{d}C}{\mathrm{d}x}\right|_{x=x_n+\phi/2} - \left.\frac{\mathrm{d}C}{\mathrm{d}x}\right|_{x=x_n-\phi/2} = \mathrm{Da}. \tag{B.2.1e}$$

We also observe that letting $\phi = 0$ reduces the problem to an array of point sinks.

Substituting the multiscale expansion (2.3.1) in (B.2.1) and collecting the terms at powers of ε, we find at $O(\varepsilon^2)$:

$$pC^{(0)}_X = C^{(2)}_{xx} + C^{(0)}_{XX}, \quad 0 < X < 1, \ \ x \in (-1/2, -\phi/2) \cup (\phi/2, 1/2) \tag{B.2.2a}$$

$$C^{(2)}|_{x=-\phi/2} = C^{(2)}|_{x=\phi/2}, \quad \left.C^{(2)}_x\right|_{x=\phi/2} - \left.C^{(2)}_x\right|_{x=-\phi/2} = q, \tag{B.2.2b}$$

$$C^{(2)}|_{X=0} = 1, \quad C^{(2)}|_{X=1} = 0 \ \text{ or } \ C^{(2)}|_{X=X_0} = C^{(2)}_x|_{X=X_0} = 0, \tag{B.2.2c}$$

where $\mathrm{Pe} = \varepsilon p$, $\mathrm{Da} = \varepsilon^2 q$, $p, q = O(1)$.

Averaging (B.2.2a) over the fluid phase of the unit cell $(-\frac{1}{2} < x < \frac{\phi}{2}) \cup (-\frac{\phi}{2} < x < \frac{1}{2})$, we obtain

$$\begin{aligned}(1-\phi)\left(pC^{(0)}_X - C^{(0)}_{XX}\right) &= \int_{-1/2}^{-\phi/2} C^{(2)}_{xx}\,\mathrm{d}x + \int_{\phi/2}^{1/2} C^{(2)}_{xx}\,\mathrm{d}x = \\ &= \underbrace{C^{(2)}_x|_{x=\frac{1}{2}} - C^{(0)}_x|_{x=-\frac{1}{2}}}_{=0} - \underbrace{\left(C^{(2)}_x|_{x=\frac{\phi}{2}} - C^{(0)}_x|_{x=-\frac{\phi}{2}}\right)}_{=q},\end{aligned} \tag{B.2.3}$$

which, by using (B.2.2b) and the periodicity assumption for $C^{(2)}$ in a unit cell, reduces to

$$C^{(0)}_{XX} - pC^{(0)}_X = \frac{q}{1-\phi}, \quad 0 \le \phi < 1. \tag{B.2.4}$$

Macroscopic equation (B.2.4), subject to the boundary conditions (2.3.8b,c), generalises (2.3.8) to the case of sinks of a finite size. The effect of the sink's size (volume fraction) is therefore in modulating the net uptake rate.

B.3 Case Pe = $O(1)$: second correction estimate

Collecting the terms in (2.2.10) at $O(\varepsilon^2)$, we obtain

$$\mathrm{Pe}\left(C_x^{(2)} + C_X^{(1)}\right) = C_{xx}^{(2)} + 2\,C_{xX}^{(1)} + C_{XX}^{(0)}\,, \tag{B.3.1a}$$

$$[C^{(2)}]_{x=0} = 0, \quad [C_x^{(2)} + C_X^{(1)}]_{x=0} = 0\,, \tag{B.3.1b}$$

$$C^{(2)}|_{X=0} = 0\,, \quad C^{(2)}|_{X=1} = 0\,. \tag{B.3.1c}$$

We average equation (B.3.1a) over the unit cell $-1/2 \le x \le 1/2$ to find a macroscopic equation for $C^{(0)}$, which then be used to formulate a cell problem for $C^{(2)}$. The averaging of (B.3.1a) with the assumption of periodicity of $C^{(2)}$ and $C_x^{(2)}$ leads to

$$C_{XX}^{(0)} - \mathrm{Pe}\int_{-1/2}^{1/2} C_X^{(1)}\,\mathrm{d}\,x = [C_x^{(2)}]\big|_{x=0} - \mathrm{Pe}\,[C^{(2)}]\big|_{x=0}\,, \tag{B.3.2}$$

assuming further continuity and x-periodicity of $C_X^{(1)}$ in each unit cell (justified by the analytical solution (2.4.13) and numerical simulations) and using the jump boundary conditions (B.3.1b), we can simplify (B.3.2) to get

$$\left(1 + \mathrm{Pe}^2\,\langle b\rangle\right) C_{XX}^{(0)} = 0\,, \tag{B.3.3}$$

where we used $C^{(1)} = -b(x)\,\mathrm{Pe}\,C_X^{(0)} + a(x)\,q_1 = q_1\big(a(x)+b(x)\big)$, according to (2.4.6) and (2.4.8). The coefficient of the second derivative is the effective diffusivity coefficient $\mathrm{D_{eff}} = 1+\mathrm{Pe}^2\,\langle b(x)\rangle$, with $\langle b\rangle = \frac{1}{q_1}\,\langle C^{(1)}\rangle - \langle a\rangle$ and $\langle C^{(1)}\rangle$ given by (2.4.14). If we assume $\langle a\rangle = 0$, i.e. only $b(x)$ contributes to the average of the first correction $C^{(1)}$, and use the asymptotics $C^{(1)} \approx q_1/12$ for small Pe from (2.4.14), we can estimate the effective diffusivity as $\mathrm{D_{eff}} = 1 + \mathrm{Pe}^2\,\langle b\rangle \approx 1 + \frac{\mathrm{Pe}^2}{12}$ ($\mathrm{Pe} \ll 1$), which resembles the Taylor-Aris dispersion relation (1.4.2). This effective diffusivity becomes important in the case of non-steady advection-diffusion, e.g. when concentration C_0 at the inlet varies with time.

Providing that $\mathrm{D_{eff}}$ is a non-zero constant and substituting (B.3.3) into (B.3.1), we observe that all terms containing $C_X^{(1)}$ vanish and arrive to a unit cell problem for $C^{(2)}$:

$$\begin{aligned} &C_{xx}^{(2)} - \mathrm{Pe}\,C_x^{(2)} = 0\,,\\ &[C^{(2)}]_{x=0} = 0, \quad [C_x^{(2)}]_{x=0} = 0\,,\\ &C^{(2)}|_{X=0} = 0\,, \quad C^{(2)}|_{X=1} = 0\,, \end{aligned} \tag{B.3.4}$$

from where we have $C^{(2)}$ identically equal to zero (due to homogeneous boundary conditions both at the boundaries of a unit cell and at the global boundaries). Therefore, the second and all the successive corrections in the asymptotic series (2.3.1) vanish in this case.

B.4 Regime of large microscopic Péclet number ($\mathrm{Pe} = O(\varepsilon^{-1})$)

We consider the case of $\mathrm{Pe} = O(\varepsilon^{-1}) = \varepsilon^{-1} p_1$ and $\mathrm{Da} = O(1)$, where $p_1 = O(1)$. The original system of equations (2.2.10) takes the form:

$$p_1 (\tilde{C}_x + \varepsilon \tilde{C}_X) = \varepsilon \tilde{C}_{xx} + 2\varepsilon^2 \tilde{C}_{xX} + \varepsilon^3 \tilde{C}_{XX}, \quad 0 < x < \varepsilon^{-1}, \ 0 < X < 1, \tag{B.4.1a}$$

$$\tilde{C}|_{X=0} = 1, \quad \tilde{C}|_{X=1} = 0, \tag{B.4.1b}$$

$$\tilde{C}|_{x=n-} = \tilde{C}|_{x=n+}, \quad n = 1, 2, \ldots, N, \tag{B.4.1c}$$

$$\left[\varepsilon \tilde{C}_x + \varepsilon^2 \tilde{C}_X - p_1 \tilde{C}\right]_{x=n} = \varepsilon \mathrm{Da}. \tag{B.4.1d}$$

Note that we retain the advective flux component in (B.4.1d) since, as we show below, the continuity condition $[\tilde{C}]_{x=n}$ cannot be applied in this case due to the advective-dominated transport at the lengthscale of a single unit cell.

Substituting (2.3.1) into (B.4.1) and collecting terms in powers of ε, we find at $O(1)$:

$$\begin{aligned} &p_1 C^{(0)}_x = 0, \quad -1/2 < x < 1/2, \ 0 < X < 1, \\ &[C^{(0)}]_{x=0} = 0, \quad [p_1 C^{(0)}]_{x=0} = 0, \\ &C^{(0)}|_{X=0} = 1, \ C^{(0)}|_{X=1} = 0, \end{aligned} \tag{B.4.2}$$

which gives $C^{(0)} = C^{(0)}(X)$ for the leading-order concentration

Collecting the terms in (B.4.1) at $O(\varepsilon)$, we have

$$\begin{aligned} &p_1 \left(C^{(1)}_x + C^{(0)}_X\right) = C^{(0)}_{xx}, \\ &[C^{(1)}]_{x=0} = 0, \quad [C^{(0)}_x - p_1 C^{(1)}]_{x=0} = \mathrm{Da}, \\ &C^{(1)}|_{X=0} = 0, \ C^{(1)}|_{X=1} = 0, \end{aligned} \tag{B.4.3}$$

which reduces to

$$C^{(1)}_x = -C^{(0)}_X, \tag{B.4.4a}$$

$$[C^{(1)}]_{x=0} = 0, \qquad [C^{(1)}]_{x=0} = -\frac{\mathrm{Da}}{p_1}, \tag{B.4.4b}$$

$$C^{(1)}|_{X=0} = 0, \qquad C^{(1)}|_{X=1} = 0. \tag{B.4.4c}$$

One can see that jump boundary conditions in (B.4.4b) are mutually incompatible. We therefore assume that only total flux is continuous over the unit cell, allowing local discontinuity in the concentration profile: $[C^{(1)}]_{x=0} = -\mathrm{Da}/p_1$. Otherwise, it is possible to show that all corrections ($C^{(1)}$, $C^{(2)}$, etc.) vanish, and the solution is given by $C = 1$.

Averaging equation (B.4.4a) over the unit cell ($-1/2 < x < 1/2$) and assuming x-periodicity of $C^{(1)}$ in a unit cell, we get

$$C^{(0)}_X = [C^{(1)}]_{x=0}, \tag{B.4.5}$$

using the jump boundary conditions at the sink (B.4.4b) and macroscopic boundary conditions

(B.4.2b), we find an averaged advection-diffusion problem

$$\begin{aligned} C_X^{(0)} &= -\mathrm{Da}/p_1\,, \\ C^{(0)}|_{X=0} &= 1\,, \end{aligned} \tag{B.4.6}$$

with a solution

$$C^{(0)} = 1 - \frac{\mathrm{Da}}{p_1} X\,, \tag{B.4.7}$$

which is identical to (2.4.6) with $q_1/\mathrm{Pe} = \mathrm{Da}/p_1 = \varepsilon^{-1}\mathrm{Da}/\mathrm{Pe}$.

(B.4.4a)–(B.4.4b) provides a cell problem for the first correction:

$$\begin{aligned} C_x^{(1)} &= \mathrm{Da}/p_1\,, \quad -1/2 < x < 1/2\,, \\ [C^{(1)}]_{x=0} &= -\mathrm{Da}/p_1\,, \end{aligned} \tag{B.4.8}$$

The solution to (B.4.8) is

$$C^{(1)} = \begin{cases} \frac{\mathrm{Da}}{p_1}\left(x + \frac{1}{2}\right) + \langle C^{(1)}\rangle\,, & -1/2 \le x < 0 \\ \frac{\mathrm{Da}}{p_1}\left(x - \frac{1}{2}\right) + \langle C^{(1)}\rangle\,, & 0 \le x \le 1/2\,, \end{cases} \tag{B.4.9}$$

which coincides with cell solution (2.4.16) obtained in Section 2.4 (see regions $\mathrm{U}_2^{\mathrm{s}}$ and A^{s} in Fig. 2.2a). Solution (B.4.9) is plotted in Fig. 2.5.

We can see that $C^{(1)}$ has a discontinuous first derivative at the sinks of microstructure, and the asymptotic expansion (2.3.1) breaks down (or, equivalently, $C^{(0)}(X)$ varies over $O(\varepsilon)$ lengthscale of a few sinks) when $\mathrm{Da}/p_1 = \varepsilon^{-1}\mathrm{Da}/\mathrm{Pe} = O(\varepsilon^{-1})$, i.e. for $\mathrm{Da} \gtrsim \mathrm{Pe}$ in this case, in agreement with the results of Section 2.4.

B.5 Examples of non-periodic deterministic microstructure

Following the homogenization result (2.7.11) of Section 2.7 for the case of diffusion-dominated transport, we now consider some deterministic non-periodic distributions of sink's position x_n, described by a source term

$$f(x) = \sum_{n=1}^{N} \delta(x - x_n)\,. \tag{B.5.1}$$

Example B.1 (square-growing inter-sink distance):

The non-periodic source term of the form $f(x) = \sum_{n=1}^{N} \delta(x - n^2)$ gives $\bar{\bar{f}} = \lim_{\varepsilon\to 0} 2\varepsilon^2 \int_0^{1/\varepsilon} \lfloor\sqrt{s}\rfloor\, \mathrm{d}s$ (the number of sinks between $y = 1$ and $y = s$ is $\lfloor\sqrt{s}\rfloor$), and therefore $\bar{\bar{f}} = \lim_{\varepsilon\to 0} 2\varepsilon^2 \frac{\varepsilon^{-3/2}}{3/2} = 0$. Note, that the source term $f(x)$ of this form does not exactly satisfy (2.7.2) for all x, but it obeys the upper bound for $x \gg 1$, making an estimate $\int_0^{1/\varepsilon} \mathrm{d}s \int_0^{s} f(y)\,\mathrm{d}y \lesssim O(\varepsilon^{-2})$ possible. However, the convergence of $\bar{\bar{f}}$ is rather slow, of the order of $O(\sqrt{\varepsilon})$, so that we can expect only a smaller net effect of an array of square-distance-located sinks relative to the periodic case for

finite ε. Figure B.2(a) compares the numerical solution for the square-growing distance (solid) with the solution for the periodic sink location (dashed).

Example B.2 (exponentially-growing inter-sink distance):

The non-periodic source term of the form $f(x) = \sum_{n=1}^{N} \delta(x - (e^n - 1))$ gives $\bar{\bar{f}} = \lim_{\varepsilon \to 0} 2\varepsilon^2 \int_0^{1/\varepsilon} \lfloor \ln(s) \rfloor \, ds$ (the number of sinks between $y = 1$ and $y = s$ is $n = \lfloor \ln(s) \rfloor$), and therefore $\bar{\bar{f}} = \lim_{x \to \infty} \frac{2}{x^2} (x \ln x - x) = 0$, $x = \varepsilon^{-1}$. Although the source term of this form again does not satisfy (2.7.2) uniformly in x, we can observe that the second term on the right-hand side of (2.7.10) is of the order of $O(x \ln x)$ and therefore can be approximately balanced by the third term of the order of $O(x)$ ($x = \varepsilon^{-1}$), making the estimate $\bar{\bar{f}} \simeq 0$ correct for smaller x (larger ε) than for the square-growing distance between sinks in Example B.1. Thus, there is the vanishing net effect of an infinite inhomogeneous array of sinks of strength $O(\varepsilon^2)$ located at exponentially-growing distance from the origin (see Fig. B.2b).

Example B.3 (clustered sink distribution):

We also see from Figure B.2(a,b) that the contribution to the *perturbation of the concentration* profile over the linear drop $C = 1 - X$ of uptake-free diffusion is greater with sinks in the centre of the domain compared to sinks near the boundaries. This is explained by the fact that the diffusion-dominated transport with a single (clustered) sink of strength Nq at $X = X_0$ ($0 < X_0 < 1$), given by $C_{XX} = N\varepsilon q \, \delta(X - X_0)$, $C(X = 0) = 1$, $C(X = 1) = 0$, has the solution $[C - (1 - X)]|_{X=X_0} = -N\varepsilon q (1 - X_0) X_0$, which shows that the deviation from the sink-free diffusive linear concentration drop between the boundaries is the greatest when $X_0 = 0.5$ and tends to zero near the boundaries, as demonstrated in Figure B.2(c,d). On the other hand, if we assume a zero-flux outlet boundary condition $C_X(X = 1) = 0$, the solution to the diffusion-reaction equation at $X = X_0$ becomes $[C - 1]|_{X=X_0} = -N\varepsilon q X_0$, which reaches a minimal value (over a constant sink-free concentration) for the sink-cluster placed at the outlet ($X_0 = 1$).

Examples B.1–B.3 for the diffusion-dominated transport suggest that the "clustering" of sinks has the weakest effect on the net uptake near the inlet (Fig. B.2(b,d)), and the contribution of a cluster is maximal in the middle of the domain or at the outlet (depending on the outlet boundary condition). For diffusion-limited transport in the intervillous space of the human placenta, this might mean a greater importance of more dense villous branches close to the venous exits than to the arterial inlets, indicating no detrimental effects of the central cavity above a spiral artery (see, e.g. Fig. 1.2).

B.6 Estimate of the maximal packing density for a hard-core-type distribution

In order to identify the critical upper bound for the minimal distance d_{cr} that can be achieved in a hard-core simple sequential inhibition random process of size N, we calculate an

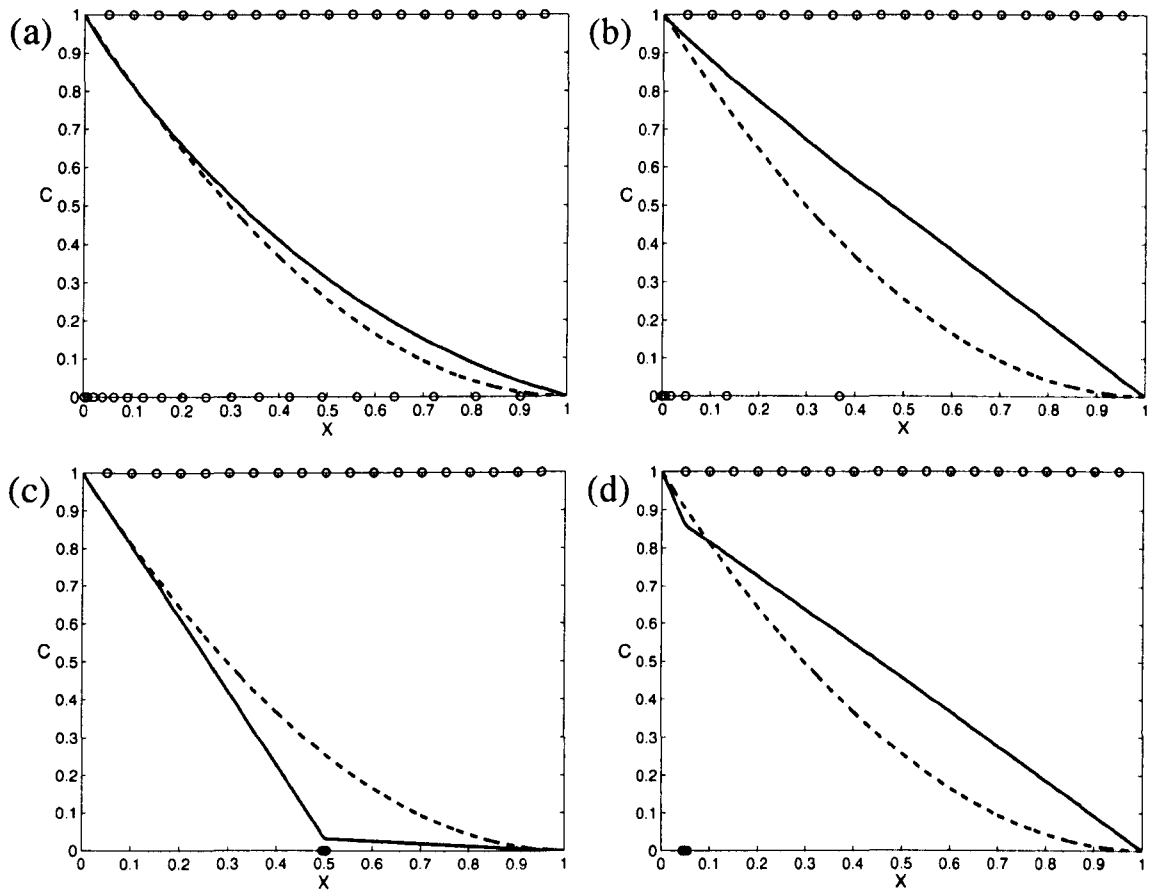

Figure B.2. The effect of different sink distributions on the concentration profile (solid line, computed for Pe $= \varepsilon^2$, Da $= 2\varepsilon^2$ on a 19-sink array (blue circles at the bottom of each diagram); $\varepsilon = 0.05$): (a) square-growing-distance array (Example B.1); (b) exponentially-growing-distance array (Example B.2); (c) a centrally positioned cluster and (d) a cluster of sinks near the inlet (Example B.3). The black dashed line indicates the reference concentration profile for a periodic array of the same size (shown as black circles on the top of each diagram).

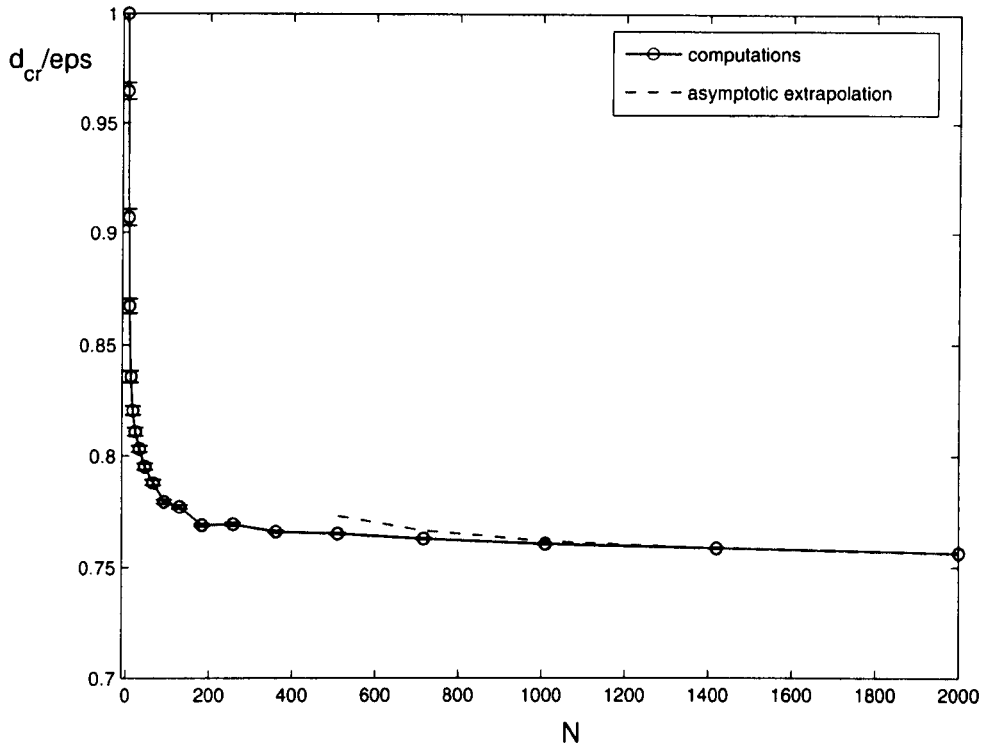

Figure B.3. Critical upper bound for the minimal distance (packing density) parameter d/ε of a hard-core point process *vs.* the number of sinks N (solid circles). Standard errors are shown with error bars, computed using an ensemble average over 500 samples for each N ($\varepsilon = 1/(N+1)$). The dashed line shows asymptotic fitting with $0.75 + 11.25/N$.

ensemble average over hard-core array realisations. Each $d_{\rm cr}$ for a given N is computed by gradually increasing d from $d = 0.7\varepsilon$, incremented in steps of $d = 0.001\varepsilon$ until no realisation of N hard-core-distributed sinks is possible.

We extrapolate numerical dependence of $d_{\rm cr}/\varepsilon$ on N by fitting to the truncated Laurent series $d \approx a_0 + a_1/N + a_2/N^2 + \ldots$ at large N, according to the following algorithm: using the last p values of $d_{\rm cr}(N)$ ($N = N_1, \ldots, N_p$) as the fitting values, and $\mathbf{a} = (a_0, a_1, \ldots, a_{p-1})$ as fitting parameters, we solve a linear system of p algebraic equations

$$\begin{pmatrix} 1 & N_1^{-1} & \ldots & N_1^{-p+1} \\ 1 & N_2^{-1} & \ldots & N_2^{-p+1} \\ \ldots & \ldots & \ldots & \ldots \\ 1 & N_p^{-1} & \ldots & N_p^{-p+1} \end{pmatrix} \mathbf{a} = \begin{pmatrix} d_{\rm cr}(N_1) \\ d_{\rm cr}(N_2) \\ \ldots \\ d_{\rm cr}(N_p) \end{pmatrix} \tag{B.6.1}$$

to find $\mathbf{a}$ and therefore an asymptote of the critical distance $d_\infty \approx a_0$.

Computations give an approximated asymptote for the critical value $d/\varepsilon \simeq 0.7430$ using five points on a logarithmic scale, which differs only in 1% from the value $d/\varepsilon \simeq 0.7508$ obtained by fitting to the last two points as shown in Fig. B.3. The results therefore tend to support the empirical upper bound $\pi/\sqrt{18}$ for the packing density [253]. This is the same density as for a cubic (or hexagonal) close packing of spheres in 3D, which is conjectured by Kepler (and is a part of the 18th Hilbert's problem [119]) to be the densest possible packing of spheres.

C A Dynamical Model of the Central Cavity in the Human Placentone

This appendix extends the static central cavity model considered in Section 6.4.5 of Chapter 6 to analyse the interaction between the deformable villous tissue and a pulsatile flow of maternal blood.

C.1 Introduction

The human placentone is defined as a single fetal cotyledon (villous tree) and corresponding maternal vessels: the supplying spiral artery in the central part and the draining decidual veins near periphery [33, 98, 237] (see Figs 1.1 and 1.2(a)).

The placentone is characterised by a spatial heterogeneity in the form of so-called "central cavity", the central portion of the fetal cotyledon that is almost devoid of villi. There is a distinct boundary formed between the less mature intermediate and the dense terminal villi branches shaped by the anchoring stem villi, which are attached to the basal plate. The intermediate and most dense portion of the fetal cotyledon, which surrounds the central cavity, is called a "mantle" of the placentone [33] (see Fig. 1.2a). The spiral artery enters the central cavity and the maternal blood is collected by the decidual veins after percolating through the mantle [98] (see Fig. C.1).

The villous tissue is compliant and therefore undergoes a periodic elastic stress due to blood flow and pressure modulation in the central cavity. The deformability of the villous tissue of the human placenta has been indirectly accounted for by Erian *et al.* [86] by introducing a

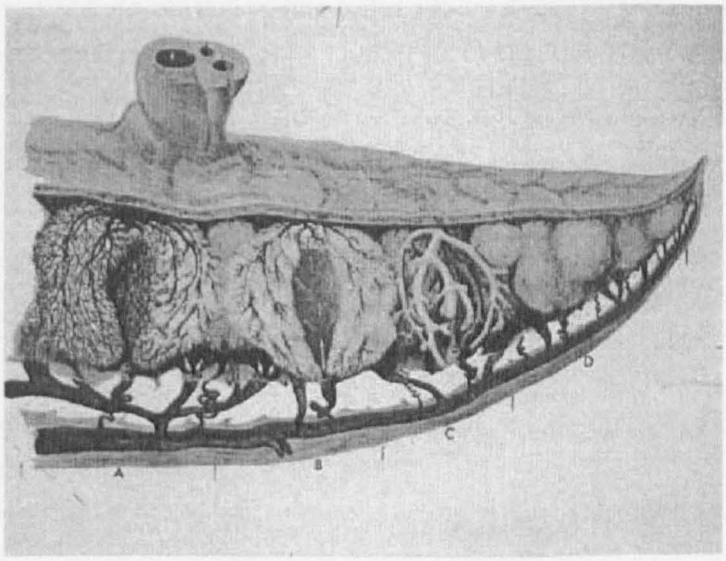

Figure C.1. A diagram of the placentone structure of the human placenta. Reproduced from [96].

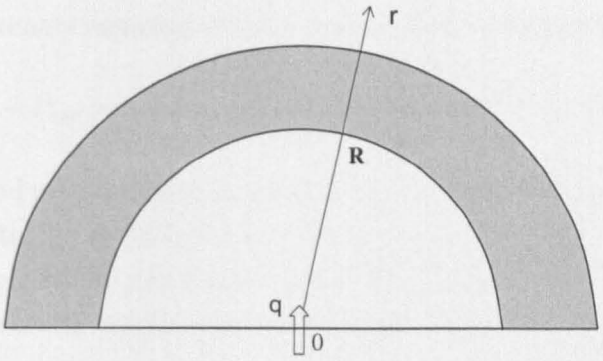

Figure C.2. A schematic hemispherical central cavity of the placentone with a periodic source of flux $q(t)$ and cavity radius $R(t)$.

flow-dependent permeability. The work by Byrne *et al.* [59] offers a more systematic framework for explicitly coupling the flow in the intervillous space with the pulsatile flow emerging from the spiral artery, where a purely elastic villous tissue and an axisymmetric flow in the central cavity are assumed.

The aim of this study is to address the impact of flow pulsatility in the spiral artery and viscoelastic properties of the villous tissue on the dynamics of the central cavity, extending the analysis of [59].

C.2 Model assumptions and problem statement

We assume the blood to be an incompressible and Newtonian fluid; flow in the central cavity is considered radial and spherically symmetric; villous tissue (the placentone mantle) is assumed viscoelastic and incompressible; and the perturbations of the cavity radius are assumed to be in the radial direction and small relative to the reference radius. The shape of the cavity (white area) is approximated as a hemisphere, as shown in Figure C.2, with a uniform blood pressure at the inner and outer boundaries of the placentone mantle (shaded area).

We consider a radial fluid motion in the polar spherical coordinates $\{r, \theta, \varphi\}$ with velocity $\mathbf{u} = u(r,t)\,\mathbf{e}_r$ in the central cavity and $\mathbf{u}_v = u_v(r,t)\,\mathbf{e}_r$ in the villous porous mantle.

The incompressibility condition gives

$$\frac{1}{r^2}\,\frac{\partial\,(r^2\,u)}{\partial\,r} = 0\,. \tag{C.2.1}$$

The blood flow through the porous mantle is described by Darcy's law

$$\frac{\partial\,P_v}{\partial\,r} = -\frac{\mu}{k}\,u_v\,, \tag{C.2.2}$$

where P_v and k are the blood pressure in the porous mantle and its permeability, and μ is the viscosity of maternal blood.

To describe the small deviations of the central cavity radius $R(t)$ from its reference value R_0,

we introduce an approximate equation of motion for a thin viscoelastic spherical shell

$$P|_{r=R} - P_{ext} = \rho_v h_0 R_{tt} + \frac{2h_0}{R_0}\sigma(R, R_t), \quad |R - R_0|/R_0 \lesssim 1, \tag{C.2.3}$$

where $P(r,t)$ is the blood pressure in the central cavity, P_{ext} is the pressure on the outer surface of the placentone mantle, $\sigma = \sigma(R, R_t)$ is a stress, described by a constitutive law for the placentone tissue, and ρ_v, h_0 are the density and reference thickness of the placentone mantle.

For a linear incompressible viscoelastic material the constitutive stress-strain law is

$$\sigma(R, R_t) = \frac{\gamma}{R_0} R_t + \frac{4E}{3}\left(\frac{R - R_0}{R_0}\right), \tag{C.2.4}$$

where E is the Young's elastic modulus and γ is the coefficient of viscosity.

We further introduce two matching relations at the interface between the maternal blood and the placentone porous mantle, based on (C.2.2) and Starling's law [242] (balancing the flow velocity and the pressure drop across the placentone mantle)

$$\frac{\mu}{k} u_v|_{r=R} \approx \frac{P|_{r=R} - P_{ext}}{h_0}, \tag{C.2.5}$$

and continuity of the flow field

$$u|_{r=R} = u_v|_{r=R} + R_t. \tag{C.2.6}$$

A flux at the spiral artery $q(t)$ provides a boundary condition to complete the problem:

$$\lim_{r\to 0} 2\pi r^2 u = q(t). \tag{C.2.7}$$

From (C.2.1) and (C.2.7) we get $u(r,t) = q(t)/2\pi r^2$, $(r > 0)$ and the kinematic matching condition (C.2.6) takes the form

$$u_v|_{r=R} = \frac{q(t)}{2\pi R^2} - R_t. \tag{C.2.8}$$

A combination of expressions (C.2.3) and (C.2.5) gives the flow velocity at the inner boundary of the porous mantle as

$$\frac{\mu}{k} u_v|_{r=R} = \rho_v R_{tt} + \frac{2}{R_0}\sigma(R, R_t). \tag{C.2.9}$$

Thus, (C.2.8) and (C.2.9) together provide an equation of motion for the radius of the central cavity

$$\rho_v R_{tt} + \frac{\mu}{k} R_t + \frac{2}{R_0}\sigma(R, R_t) = \frac{\mu}{2\pi k}\frac{q(t)}{R^2}, \tag{C.2.10}$$

which, using (C.2.4), can be rewritten as follows:

$$\rho_v R_{tt} + \left(\frac{\mu}{k} + \frac{2\gamma}{R_0^2}\right) R_t + \frac{8E}{3R_0}\left(\frac{R - R_0}{R_0}\right) = \frac{\mu}{2\pi k}\frac{q(t)}{R^2}. \tag{C.2.11}$$

Equations (C.2.10) and (C.2.11) represent a driven, damped and, in general, nonlinear

oscillator. Note that both the viscosity of the villous tissue and the inverse permeability of the placentone mantle contribute to the damping coefficient $(\mu/k + 2\gamma/R_0^2)$ in (C.2.11).

We introduce the dimensionless deviation of the radius $\eta(t) = (R - R_0)/R_0$, and equation (C.2.11) takes the form:

$$\eta_{tt} + 2\beta\,\eta_t + \omega_0^2\,\eta = \frac{f_0}{q_0}\,\frac{q(t)}{(1+\eta)^2}\,, \tag{C.2.12}$$

where $\omega_0^2 = 8E/3\rho_v R_0^2$ is the natural frequency, $\beta = (\mu/k + 2\gamma/R_0^2)/2\rho_v$ is the damping coefficient, $f_0 = \mu q_0/2\pi k\rho_v R_0^3$ is the amplitude of the driven force, and q_0 is the amplitude of the flow rate $q(t)$ in the spiral artery.

The natural frequency of the oscillator (C.2.12)

$$\omega_0^2 = \frac{8E}{3\rho_v R_0^2}\,, \tag{C.2.13}$$

together with the damping coefficient β and the characteristic frequency of the driving force ω, defines the dynamics of the central cavity.

C.3 Linear analysis of the cavity oscillations

We linearise (C.2.12) in the case of small oscillations of the central cavity $(1+\eta)^{-1} \simeq 1$, $|\eta| \ll 1$ and approximate the source of flux (from a spiral artery) with a single mode of characteristic frequency ω: $q(t) = q_0 \cos\omega t$. The governing equation (C.2.12) then becomes

$$\eta_{tt} + 2\beta\,\eta_t + \omega_0^2\,\eta = f_0 \cos\omega t\,. \tag{C.3.1}$$

The general solution to (C.3.1) is

$$\eta(t) = e^{-\beta t}\left(C_1 \cos\left(t\sqrt{\omega_0^2 - \beta^2}\right) + C_2 \sin\left(t\sqrt{\omega_0^2 - \beta^2}\right)\right) + \frac{f_0 \cos(\omega t - \alpha_0)}{\sqrt{(\omega_0^2 - \omega^2)^2 + 4\omega^2\beta^2}}\,, \tag{C.3.2}$$

where $\alpha_0 = \arctan[2\beta\omega/(\omega_0^2 - \omega^2)]$ and arbitrary constants C_1, C_2 are determined by the initial conditions.

Mechanical data for a mature normal human placenta, additional to the data of Table 6.1, are presented in Table C.1. The viscoelastic parameters for an arterial wall [61] are used to approximate the villous tissue to the nearest order of magnitude. Based on the data of Tables 6.1 and C.1, we estimate the parameters as follows: $\omega_0 \sim 10^3 - 10^4\ \mathrm{s}^{-1}$, $\omega \sim 1\ \mathrm{s}^{-1}$, $\beta \sim 10^5 - 10^6\ \mathrm{s}^{-1}$ (where the contribution of the first term μ/k is negligible over the second term due to the villous viscosity), $f_0 \sim 10^3 - 10^4\ \mathrm{s}^{-2}$, and $\tan\alpha_0 \sim 10^{-2} - 10^{-1}$. Thus, the natural oscillations are aperiodic and are promptly damped with the characteristic time $t \sim \beta^{-1}$. The solution (C.3.2) then takes a simplified form: $\eta(t) = a_0 \cos(\omega t)$, with amplitude $a_0 = f_0/\sqrt{\omega_0^4 + 4\omega^2\beta^2} \sim 10^{-3} - 10^{-2} << 1$.

Parameter	Value	Reference
Arterial flow frequency (ω)	$\simeq 80$ min^{-1}	[151]
Cavity's reference radius (R_0)	$\simeq 5 \times 10^{-3}$ m	[98]
Villous density (ρ_v)	$\simeq 10^3$ kg/m^3	[172]
Villous elasticity (E)	$\sim 10^5 - 10^6$ Pa	
Villous viscosity (γ)	$\sim 10^3 - 10^4$ Pa $\cdot$ s	
Reynolds number ($\mathrm{Re} = \frac{\rho q_0}{\mu R_0}$)	$\sim 1 - 10$	
Womersley number $\left(\alpha = R_0\sqrt{\frac{\rho\omega}{\mu}}\right)$	$\simeq 3$	
Strouhal number ($\mathrm{St} = \alpha^2 \cdot \mathrm{Re}$)	$\sim 10 - 10^2$	

Table C.1. Literature-based and calculated parameters used in the model of the central cavity. See also Table 6.1 of Chapter 6.

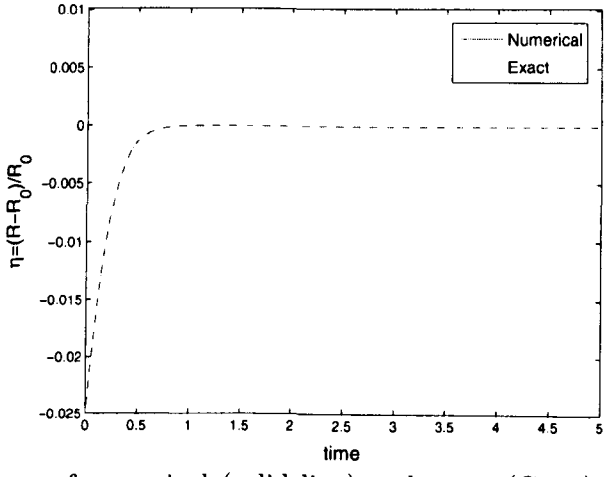

Figure C.3. Comparison of numerical (solid line) and exact (C.4.3) (dashed line) solutions to (C.4.2) for $\omega_0 = 10^3$, $\kappa = 10$, $f_0 = 0$ (plotted in dimensionless variables).

C.4 Cavity oscillations for a nonlinear-viscoelastic material

We come back to the general equation of motion (C.2.10) with a nonlinear constitutive law

$$\sigma(R, R_t) = \frac{\gamma}{R_0} R_t + \frac{4E}{3}\left[\frac{R - R_0}{R_0} + \kappa\left(\frac{R - R_0}{R_0}\right)^2\right], \tag{C.4.1}$$

where κ is the coefficient of nonlinear elasticity.

Oscillations of the central cavity is described, according to (C.2.10) and (C.4.1), as

$$\eta_{tt} + 2\beta\eta_t + \omega_0^2\left(\eta + \kappa\eta^2\right) = \frac{f_0}{q_0}\frac{q(t)}{(1+\eta)^2}\cdot \tag{C.4.2}$$

The equation (C.4.2) subject to initial radius and velocity values is solved by a second order implicit finite-difference scheme implemented in the solver `ode23t` of `MATLAB`. An exact solution

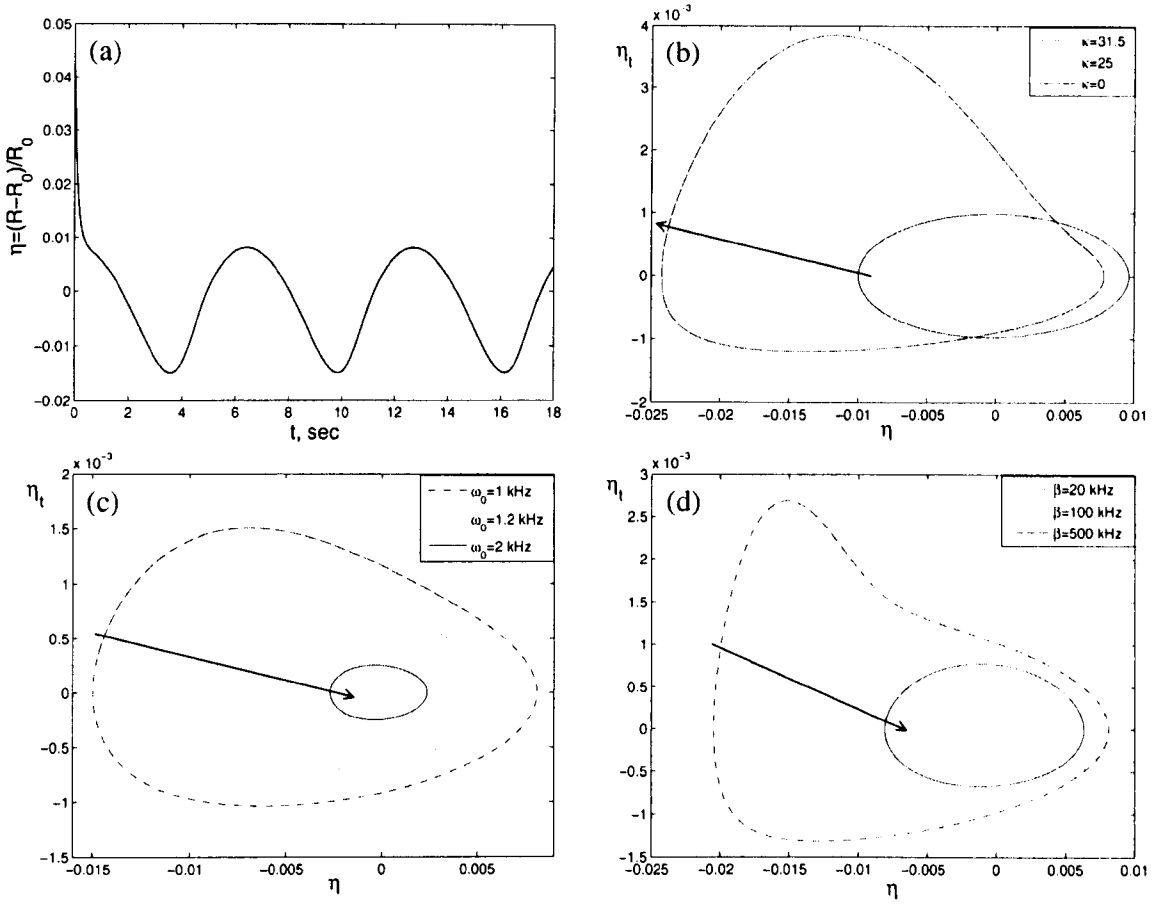

Figure C.4. (a) Typical oscillations of the central cavity described by (C.4.2) for $\beta = 10^5$ Hz, $\omega_0 = 10^3$ Hz, $\omega = 1$ Hz, $\kappa = 25$, $f_0 = 10^4$ s^{-2}, $\eta(0) = 0.05$. The parameter dependence of the flow-driven limit cycle is given in a phase plane (η, η_t) for the nonlinear elasticity coefficient κ (b), natural frequency ω_0 (c) and dissipation coefficient β (d); all the rest of parameters in (b-d) are the same as in (a). Arrows indicate the direction of increase in a parameter.

to (C.4.2) for $\beta/\omega_0 = 5\sqrt{6}/12$ and $f_0 = 0$ is [152]

$$\eta(t)_{\text{exact}} = -\frac{1}{4\kappa}\left[1 - 2\tanh\left(\tfrac{\sqrt{6}}{12}\,\omega_0 t\right) + \tanh^2\left(\tfrac{\sqrt{6}}{12}\,\omega_0 t\right)\right], \tag{C.4.3}$$

which is used for verification of the numerical solution at initial values $\eta(0) = \eta(0)_{\text{exact}}$, $\eta_t(0) = \eta_t(0)_{\text{exact}}$ (showing a very good agreement; see Fig. C.3).

A representative solution to (C.4.2) for $q/q_0 = \cos\omega t$, $\eta(0) = 0.05$, $\eta_t(0) = 0$, and the parameter values $\beta = 10^5$ Hz, $\omega_0 = 10^3$ Hz, $\kappa = 25$, $\omega = 1$ Hz, $f_0 = 10^4$ s^{-2}, is shown in Figure C.4(a). The influence of model parameters on the oscillation dynamics is presented in Figure C.4(b-d). Figure C.4(b) shows that even at a relatively large value of the nonlinear elasticity parameter κ, the deviation of the cavity radius from its equilibrium is still of the order of 1%, as it is in the linearly elastic case ($\kappa = 0$). We also conclude from Fig. C.4(c,d) that the amplitude of the cavity radius oscillations η depends much more strongly on the natural frequency ω_0 (representing the elastic properties of the villous tissue) than on the dissipation parameter β (representing a combined damping due to blood viscosity, hydraulic resistance and viscoelasticity of the placental tissue). This agrees with the prediction of the

linear model (C.3.2), giving the oscillation amplitude $f_0/\sqrt{\omega_0^4 + 4\omega^2\beta^2}$ for $\omega \ll \omega_0$.

C.5 Discussion

In this Appendix, we have derived a lumped-parameter model to describe the oscillations of the central cavity of the human placentone exposed to the pulsatile maternal blood flow from a spiral artery. We have extended the model of [59] to account for linear and weakly-nonlinear viscoelasticity of the placental tissue, and our analysis indicates the important role of villous dissipative properties in the overall model dynamics.

The Darcy flow in the villous mantle coupled with incompressible flow in the cavity and a viscoelastic constitutive law for the villous tissue give a forced non-linear oscillator for the cavity radius.

The model analysis, based on the data of mechanical villous properties and spiral artery dynamics, suggests a rapid damping of any initial perturbations and synchronisation with oscillations of the driving blood flow rate. The amplitude of the resultant cavity oscillations is small relative to the characteristic cavity radius. Therefore, the central cavity can be considered a nearly static structure separating a pool of the maternal blood from the porous medium of terminal villi, the primary site of solute exchange between the mother and the fetus.

We have shown high sensitivity of the model to the natural frequency of the villous tissue (C.2.13). Thus, for example, in the case of an abnormally low Young's modulus of the villous tissue, we might expect the cavity oscillations to become more significant. The same effect can be caused by a rise in the amplitude of systemic blood flow and pressure (e.g. in hypertensive patients).

The conclusions deduced from this model are preliminary only, because some mechanical properties of the villous tissue were extrapolated from other biological soft tissues, in view of limited or absent placental experimental data. The permeability of the placentone mantle also, in general, depends on the degree of its elastic deformation, modulating the intervillous pore size [59]. Another limitation of the model is the use of a viscoelastic thin-shell theory, neglecting the thickness of the placentone mantle which can be comparable to the cavity radius.

BIBLIOGRAPHY

[1] ABDULLAH, N.S. & DAS, D.B. (2007), Modelling nutrient transport in hollow fibre membrane bioreactor for growing bone tissue with consideration of multi-component interactions, *Chem. Eng. Sci.* 62(21): 5821–5839.

[2] ABRAMOWICZ, J.S. & SHEINER, E. (2008), Ultrasound of the placenta: A systematic approach. Part II: Functional assessment (Doppler), *Placenta* 29(11): 921–929.

[3] ACRIVOS, A., HINCH, E.J. & JEFFREY, D.J. (1980), Heat transfer to a slowly moving fluid from a dilute fixed bed of heated spheres, *J. Fluid Mech.* 101(2): 403–421.

[4] ADAMSON, S.L., LU, Y., WHITELEY, K.J., HOLMYARD, D., HEMBERGER, M., PFARRER, C. & CROSS, J.C. (2002), Interactions between trophoblast cells and the maternal and fetal circulation in the mouse placenta, *Dev. Biol.* 250(2): 358–373.

[5] AHMED, A., DUNK, C., AHMAD, S. & KHALIQ, A. (2000), Regulation of placental vascular endothelial growth factor (VEGF) and placenta growth factor (PlGF) and soluble Flt-1 by oxygen – A review, *Placenta* 21(Supplement 1): S16–S24.

[6] AIFANTIS, E.C. (1978), Towards a rational modeling for the human placenta, *Math. Biosci.* 40(3-4): 281–301.

[7] ALLAIRE, G. & RAPHAEL, A.L. (2007), Homogenization of a convection-diffusion model with reaction in a porous medium, *Comptes Rendus Mathematique* 344(8): 523–528.

[8] APLIN, J. (2000), Maternal influences on placental development, *Semin. Cell Dev. Biol.* 11(2): 115–125.

[9] ARIS, R. (1956), On the dispersion of a solute in a fluid flowing through a tube, *Proc. R. Soc. Lond. A* 235(1200): 67 77.

[10] ATHANASSIADES, A., HAMILTON, G.S. & LALA, P.K. (1998), Vascular endothelial growth factor stimulates proliferation but not migration or invasiveness in human extravillous trophoblast, *Biol. Reprod.* 59(3): 643–654.

[11] AURIAULT, J.L. & ADLER, P.M. (1995), Taylor dispersion in porous media: Analysis by multiple scale expansions, *Adv. Water Resour.* 18(4): 217–226.

[12] AURIAULT, J.L., GEINDREAU, C. & BOUTIN, C. (2005), Filtration law in porous media with poor separation of scales, *Transport in Porous Media* 60(1): 89–108.

[13] AURIAULT, J.L. & SANCHEZ-PALENCIA, E. (1977), Étude du comportement macroscopique d'un milieu poreux saturé déformable, *Journal de Mécanique* 16(4): 575 603, (in French).

[14] AVELLANEDA, M. & TORQUATO, S. (1991), Rigorous link between fluid permeability, electrical conductivity, and relaxation times for transport in porous media, *Phys. Fluids A* 3(11): 2529-2540.

[15] BABUŠKA, I. (1976), Solution of interface problems by homogenization. I, *SIAM J. Math. Anal.* 7(5): 603 634.

[16] BADDELEY, A. & JENSEN, E.B.V. (2005), *Stereology for Statisticians.* Chapman & Hall/ CRC, Boca Raton, 395 pp.

[17] BADDELEY, A. & TURNER, R. (2005), Spatstat: an R package for analyzing spatial point patterns, *J. Stat. Software* 12(6): 1–42, URL: `www.jstatsoft.org`, ISSN: 1548-7660.

[18] BADDELEY, A.J. & SILVERMAN, B.W. (1984), A cautionary example on the use of second-order methods for analyzing point patterns, *Biometrics* 40(4): 1089–1093.

[19] BAKHVALOV, N.S. (1974), Averaged characteristics of bodies with periodic structure, *Soviet Physics Doklady* 19: 650.

[20] BAKHVALOV, N.S. & PANASENKO, G.P. (1989), *Homogenisation: Averaging Processes in Periodic Media; Mathematical Problems in the Mechanics of Composite Materials.* vol. 36 of Mathematics and its applications, Kluwer Academic Publishers, Dordrecht, 366 pp.

[21] BAL, G., GARNIER, J., MOTSCH, S. & PERRIER, V. (2008), Random integrals and correctors in homogenization, *Asymptotic Analysis* 59(1): 1–26.

[22] BAL, G. & JING, W. (2010), Homogenization and corrector theory for linear transport in random media, *Discret. Contin. Dyn. Syst.* 28(4): 1311–1343.

[23] BALHOFF, M., MIKELIĆ, A. & WHEELER, M. (2009), Polynomial filtration laws for low reynolds number flows through porous media, *Transport in Porous Media* 81(1): 35–60.

[24] BANERJEE, R.K., KWON, O., VAIDYA, V.S. & BACK, L.H. (2008), Coupled oxygen transport analysis in the avascular wall of a coronary artery stenosis during angioplasty, *J. Biomech.* 41(2): 475–479.

[25] BARTELS, H. & MOLL, W. (1964), Passage of inert substances and oxygen in the human placenta, *Pflügers Arch. Eur. J. Physiol.* 280(2): 165–177.

[26] BARTH, W.H., MCCURNIN, D.C., DEE CAREY, K. & HANKINS, G.D.V. (2006), Contrast sonography, video densitometry and intervillous blood flow: A pilot project, *Placenta* 27(6-7): 719–726.

[27] BATCHELOR, G.K. (2000), *An Introduction to Fluid Dynamics.* Cambridge Mathematical Library, Cambridge University Press, 635 pp.

[28] BATCHELOR, G.K. & O'BRIEN, R.W. (1977), Thermal or electrical conduction through a granular material, *Proc. R. Soc. Lond. A* 355(1682): 313–333.

[29] BEAR, J. (1988), *Dynamics of Fluids in Porous Media.* Dover Publications, 784 pp.

[30] BEAVERS, G.S. & JOSEPH, D.D. (1967), Boundary conditions at a naturally permeable wall, *J. Fluid Mech.* 30(1): 197–207.

[31] BEES, M.A. & CROZE, O.A. (2010), Dispersion of biased swimming micro-organisms in a fluid flowing through a tube, *Proc. R. Soc. A* 466(2119): 2057–2077.

[32] BENDER, C.M. & BETTENCOURT, L.M.A. (1996), Multiple-scale analysis of the quantum anharmonic oscillator, *Phys. Rev. Lett.* 77(20): 4114–4117.

[33] BENIRSCHKE, K., KAUFMANN, P. & BAERGEN, R.N. (2006), *Pathology of the Human Placenta.* Springer, 5th edn, 1050 pp.

[34] BENSOUSSAN, A., LIONS, J.L. & PAPANICOLAOU, G. (1978), *Asymptotic Analysis for Periodic Structures.* vol. 5 of Studies in mathematics and its applications, Elsevier North-Holland, 700 pp.

[35] BENSOUSSAN, A., LIONS, J.L. & PAPANICOLAOU, G.C. (1979), Boundary layers and homogenization of transport processes, *Publ. Res. Inst. Math. Sci., Kyoto Univ.* 15: 53–157.

[36] BERDICHEVSKII, V.L. (1975), Spatial averaging of periodic structures, *Soviet Physics Doklady* 20: 334.

[37] BERGMAN, D.J. (1979), The dielectric constant of a simple cubic array of identical spheres, *J. Phys. C* 12(22): 4947–4960.

[38] BERGMAN, D.J. (1979), Dielectric constant of a two-component granular composite: A practical scheme for calculating the pole spectrum, *Phys. Rev. B* 19(4): 2359–2368.

[39] BERGMAN, D.J. (1980), Exactly solvable microscopic geometries and rigorous bounds for the complex dielectric constant of a two-component composite material, *Phys. Rev. Lett.* 44(19): 1285–1287.

[40] BERRYMAN, J.G. (2004), Comparison of two up-scaling methods in poroelasticity and its generalizations, Conference UCRL-PROC-202969, Lawrence Livermore National Laboratory (LLNL), Livermore, CA, ePublication: www.osti.gov/servlets/purl/15014045-2TXKP9/native/.

[41] BERRYMAN, J.G. (2006), Measures of microstructure to improve estimates and bounds on elastic constants and transport coefficients in heterogeneous media, *Mechanics of Materials* 38(8-10): 732–747.

[42] BIKFALVI, A. (2000), *Encyclopedic Reference of Vascular Biology & Pathology.* Springer, 372 pp.

[43] BIOT, M.A. (1941), General theory of three-dimensional consolidation, *J. Appl. Phys.* 12(2): 155–164.

[44] BOLLINI, A., HERNÁNDEZ, G., LUNA, M.B., CINARA, L. & RASIA, M. (2005), Study of intrinsic flow properties at the normal pregnancy second trimester, *Clinical Hemorheology and Microcirculation* 33(2): 155–161.

[45] BONFIGLIO, A., LEUNGCHAVAPHONGSE, K., REPETTO, R. & SIGGERS, J.H. (2010), Mathematical modeling of the circulation in the liver lobule, *J. Biomech. Eng.* 132(11): 111011.

[46] BORELL, U., FERNSTRÖM, I., OHLSON, L. & WIQVIST, N. (1965), An arteriographic study of the blood flow through the uterus and the placenta at midpregnancy, *Acta Obstet. Gynecol. Scand.* 44(1): 22–31.

[47] BOURGEAT, A. & PIATNITSKI, A. (1999), Estimates in probability of the residual between the random and the homogenized solutions of one-dimensional second-order operator, *Asymptotic Analysis* 21(3): 303–315.

[48] BOYD, J.D. & HAMILTON, W.J. (1966), Placental septa, *Cell Tissue Res.* 69(1): 613 634.

[49] BOYD, J.D. & HAMILTON, W.J. (1970), *The Human Placenta.* W.Heffer&Sons Ltd., Cambridge, 365 pp.

[50] BRENNER, H. (1980), Dispersion resulting from flow through spatially periodic porous media, *Phil. Trans. R. Soc. Lond. A* 297(1430): 81–133.

[51] BRENNER, H. & EDWARDS, D.A. (1993), *Macrotransport Processes.* Butterworth-Heinemann, Boston, 714 pp.

[52] BRINKMAN, H. (1947), A calculation of the viscous force exerted by a flowing fluid on a dense swarm of particles, *Applied Scientific Research* A1(1): 27 34.

[53] BURGER, M., CAPASSO, V. & PIZZOCCHERO, L. (2006), Mesoscale averaging of nucleation and growth models, *Multiscale Model. Simul.* 5(2): 564 592.

[54] BURRIDGE, R. & KELLER, J.B. (1981), Poroelasticity equations derived from microstructure, *J. Acoust. Soc. Am.* 70(4): 1140–1146.

[55] BURTON, G.J., JAUNIAUX, E. & CHARNOCK-JONES, D.S. (2007), Human early placental development: Potential roles of the endometrial glands, *Placenta* 28(Supplement 1): S64 S69.

[56] BURTON, G.J., JAUNIAUX, E. & WATSON, A.L. (1999), Maternal arterial connections to the placental intervillous space during the first trimester of human pregnancy: The Boyd Collection revisited, *Am. J. Obstet. Gynecol.* 181(3): 718 724.

[57] BURTON, G.J., WOODS, A.W., JAUNIAUX, E. & KINGDOM, J.C.P. (2009), Rheological and physiological consequences of conversion of the maternal spiral arteries for uteroplacental blood flow during human pregnancy, *Placenta* 30(6): 473 482.

[58] BUTLER, S.F.J. (1953), A note on Stokes's stream function for motion with a spherical boundary, *Math. Proc. Camb. Philos. Soc.* 49(1): 169–174.

[59] BYRNE, H., GOWLAND, P., JENSEN, O., MAYHEW, T., MCGUINNESS, M., PLEASE, C. & WILSON, S. (2001), Flow and transport in the placenta, In: H. Byrne, O. Jensen,

J. King & S. Waters, eds, Proceedings of the Second Mathematics-in-Medicine Study Group, University of Nottingham, pp. 11–17.

[60] BYRNE, H.M., CHAPLAIN, M.A.J., PETTET, G.J. & MCELWAIN, D.L.S. (2001), An analysis of a mathematical model of trophoblast invasion, *Appl. Math. Lett.* 14(8): 1005–1010.

[61] CANIC, S., TAMBACA, J., GUIDOBONI, G., MIKELIĆ, A., HARTLEY, C.J. & ROSENSTRAUCH, D. (2006), Modeling viscoelastic behavior of arterial walls and their interaction with pulsatile blood flow, *SIAM J. Appl. Math.* 67(1): 164–193.

[62] CAPASSO, V. (2009), Multiple scales and geometric structures: additional sources of randomness, *J. Math. Biol.* 59(1): 143–146.

[63] CAPASSO, V., MICHELETTI, A. & MORALE, D. (2008), Stochastic geometric models, and related statistical issues in tumour-induced angiogenesis, *Math. Biosci.* 214(1-2): 20–31.

[64] CARSON, D.D., BAGCHI, I., DEY, S.K., ENDERS, A.C., FAZLEABAS, A.T., LESSEY, B.A. & YOSHINAGA, K. (2000), Embryo implantation, *Dev. Biol.* 223(2): 217–237.

[65] CARTER, A.M. (1997), When is the maternal placental circulation established in man?, *Placenta* 18(1): 83–87.

[66] CARTER, A.M. (2007), Animal models of human placentation – A review, *Placenta* 28(Supplement 1): S41–S47.

[67] CARTER, A.M., ENDERS, A.C., JONES, C.J.P., MESS, A., PFARRER, C., PIJNENBORG, R. & SOMA, H. (2006), Comparative placentation and animal models: Patterns of trophoblast invasion – A workshop report, *Placenta* 27(Supplement 1): 30–33.

[68] CARTWRIGHT, J.E., HOLDEN, D.P. & WHITLEY, G.S.J. (1999), Hepatocyte growth factor regulates human trophoblast motility and invasion: a role for nitric oxide, *Br. J. Pharmacol.* 128(1): 181–189.

[69] CARTWRIGHT, J.E., KENNY, L.C., DASH, P.R., CROCKER, I.P., APLIN, J.D., BAKER, P.N. & WHITLEY, G.S.J. (2002), Trophoblast invasion of spiral arteries: a novel in vitro model, *Placenta* 23(2-3): 232–235.

[70] CASTELLUCCI, M., SCHEPE, M., SCHEFFEN, I., CELONA, A. & KAUFMANN, P. (1990), The development of the human placental villous tree, *Anat. Embryol.* 181(2): 117–128.

[71] CHAPMAN, S.J., SHIPLEY, R.J. & JAWAD, R. (2008), Multiscale modeling of fluid transport in tumors, *Bull. Math. Biol.* 70(8): 2334–2357.

[72] CHARNOCK-JONES, D.S., KAUFMANN, P. & MAYHEW, T.M. (2004), Aspects of human fetoplacental vasculogenesis and angiogenesis. I. Molecular regulation, *Placenta* 25(2-3): 103–113.

[73] CHEN, R.R., SILVA, E.A., YUEN, W.W., BROCK, A.A., FISCHBACH, C., LIN, A.S., GULDBERG, R.E. & MOONEY, D.J. (2007), Integrated approach to designing growth factor delivery systems, *FASEB J.* 21: 3896–3903.

[74] CHERNYAVSKY, I.L., JENSEN, O.E. & LEACH, L. (2010), A mathematical model of intervillous blood flow in the human placentone, *Placenta* 31(1): 44–52.

[75] CHERNYAVSKY, I.L., LEACH, L., DRYDEN, I.L. & JENSEN, O.E. (2011), Transport in the placenta: homogenizing haemodynamics in a disordered medium, *Phil. Trans. R. Soc. A* 369(1954): 4162–4182.

[76] CLARK, A., FEDERSPIEL, W., CLARK, P. & COKELET, G. (1985), Oxygen delivery from red cells, *Biophysical J.* 47(2): 171–181.

[77] COSTA, A., COSTANTINO, M. & FUMERO, R. (1992), Oxygen exchange mechanisms in the human placenta: mathematical modelling and simulation, *J. Biomed. Eng.* 14(5): 385–389.

[78] CRAVEN, C.M., ZHAO, L. & WARD, K. (2000), Lateral placental growth occurs by trophoblast cell invasion of decidual veins, *Placenta* 21(2-3): 160 169.

[79] DARCY, H.P.G. (1856), *Les Fontaines Publiques de la Ville de Dijon: Exposition et application á suivre et des formules á employer dans les questions de duistribution d'eau.* Victor Dalmont, Paris, 647 pp., (in French).

[80] DEMIR, R., KAYISLI, U.A., SEVAL, Y., CELIK-OZENCI, C., KORGUN, E.T., DEMIR-WEUSTEN, A.Y. & HUPPERTZ, B. (2004), Sequential expression of VEGF and its receptors in human placental villi during very early pregnancy: differences between placental vasculogenesis and angiogenesis., *Placenta* 25(6): 560–572.

[81] DHEIN, S. (2005), *Practical methods in cardiovascular research.* Springer, Berlin, 1010 pp.

[82] DIGGLE, P.J. (2003), *Statistical Analysis of Spatial Point Patterns.* Arnold, London, 2nd edn, 159 pp.

[83] DRYDEN, I.L. & MARDIA, K.V. (1998), *Statistical Shape Analysis.* Wiley, Chichester, 347 pp.

[84] ENDERS, A.C. & KING, B.F. (1991), Early stages of trophoblastic invasion of the maternal vascular system during implantation in the macaque and baboon, *Am. J. Anat.* 192(4): 329–346.

[85] ENE, H.I. & SÁNCHEZ-PALENCIA, E. (1975), Equations et phenomenes de surface pour l'ecoulement dans un modele de milieu poreux, *J. Mécanique* 14(1): 73 108, (in French).

[86] ERIAN, F.F., CORRSIN, S. & DAVIS, S.H. (1977), Maternal, placental blood flow: A model with velocity-dependent permeability, *J. Biomech.* 10(11-12): 807 814.

[87] ESPINOZA, J., ROMERO, R., MEE KIM, Y., KUSANOVIC, J.P., HASSAN, S., EREZ, O., GOTSCH, F., GABOR THAN, N., PAPP, Z. & JAI KIM, C. (2006), Normal and abnormal transformation of the spiral arteries during pregnancy, *J. Perinat. Med.* 34(6): 447–458.

[88] FABER, J.J. (1969), Application of the theory of heat exchangers to the transfer of inert materials in placentas, *Circ. Res.* 24(2): 221–234.

[89] FANNJIANG, A. & PAPANICOLAOU, G. (1994), Convection enhanced diffusion for periodic flows, *SIAM J. Appl. Math.* 54(2): 333–408.

[90] FANNJIANG, A. & PAPANICOLAOU, G. (1997), Convection-enhanced diffusion for random flows, *J. Stat. Phys.* 88(5/6): 1033–1076.

[91] FINN, M.D., LEACH, L., GOWLAND, P.A. & JENSEN, O.E. (2004), Hemodynamics in a lobule: a computational model, *Placenta* 25(8-9): A23, abstracts to be presented at the Placenta Association of the Americas 2004 conference/10th Meeting of the International Federation of Placenta Associations.

[92] FINN, M.D., LEACH, L., GOWLAND, P.A., WILTON, B. & JENSEN, O.E. (2004), Placental blood flow: end of year report, Tech. rep., University of Nottingham, (unpublished).

[93] FLEISCHER, A.C., APPLEBAUM, M.I. & PARSONS, A.K. (1997), *Ultrasound and the Endometrium*, Informa Healthcare, vol. 8 of Progress in Obstetric and Gynecological Sonography Series, ch. Transvaginal sonography of normal endometrium, pp. 1 16.

[94] FORCHHEIMER, P. (1901), Wasserbewegung durch Boden (Fluid motion in soil), *Z. Ver. Deutsch. Ing.* 45: 1782–1788, (in German).

[95] FRANCIS, S.T., DUNCAN, K.R., MOORE, R.J., BAKER, P.N., JOHNSON, I.R. & GOWLAND, P.A. (1998), Non-invasive mapping of placental perfusion, *The Lancet* 351(9113): 1397–1399.

[96] FREESE, U.E. (1968), The uteroplacental vascular relationship in the human, *Am. J. Obstet. Gynecol.* 101(1): 8–16.

[97] FREESE, U.E. (1971), The enigma of the maternal spiral artery and its relation to the fetal cotyledon, *Nederlands tijdschrift voor geneeskunde* 115(49): 2085 2087.

[98] FREESE, U.E. (1972), Vascular relations of placental exchange areas in primates and man, In: L. D. Longo & H. Bartels, eds, Respiratory gas exchange and blood flow in the placenta, Nat. Inst. Child Health Hum. Dev., Bethesda, Md., pp. 31 60.

[99] FREESE, U.E. & MACIOLEK, B.J. (1969), Plastoid injection studies of the uteroplacental vascular relationship in the human, *Obstet. Gynecol.* 33(2): 160 169.

[100] FRICKE, H. (1924), A mathematical treatment of the electric conductivity and capacity of disperse systems i. the electric conductivity of a suspension of homogeneous spheroids, *Phys. Rev.* 24(5): 575–587.

[101] FRICKE, H. (1955), The complex conductivity of a suspension of stratified particles of spherical or cylindrical form, *J. Phys. Chem.* 59(2): 168–170.

[102] GAYKEMA, W.P.J., HOL, W.G.J., VEREIJKEN, J.M., SOETER, N.M., BAK, H.J. & BEINTEMA, J.J. (1984), 3.2 Å structure of the copper-containing, oxygen-carrying protein *Panulirus interruptus* haemocyanin, *Nature* 309(5963): 23–29.

[103] GOLDEN, K. & PAPANICOLAOU, G. (1983), Bounds for effective parameters of heterogeneous media by analytic continuation, *Commun. Math. Phys.* 90(4): 473–491.

[104] GORDON, Z., EYTAN, O., JAFFA, A.J. & ELAD, D. (2007), Fetal blood flow in branching models of the chorionic arterial vasculature, *Annals New York Acad. Sci.* 1101(1): 250–265.

[105] GRIFFITH, L.G. & SWARTZ, M.A. (2006), Capturing complex 3D tissue physiology in vitro, *Nature Rev. Mol. Cell. Biol.* 7(3): 211–224.

[106] GRIMMETT, G.R. & STIRZAKER, D.R. (1992), *Probability and Random Processes*. Oxford science publications, Clarendon Press, 2nd edn, 541 pp.

[107] GROOME, L.J. (1991), A theoretical analysis of the effect of placental metabolism on fetal oxygenation under conditions of limited oxygen availability, *Biosystems* 26(1): 45–56.

[108] GRUENWALD, P. (1977), The development of the placental lobular pattern in the human. Review and reinterpretation of the material, *Obstet. Gynecol.* 49(6): 728–732.

[109] GUILBEAU, E.J., RENEAU, D.D. & KNISELY, M.H. (1972), The effects of placental oxygen consumption and the contractions of labor on fetal oxygen supply: A steady and unsteady state mathematical simulation, In: L. D. Longo & H. Bartels, eds, Respiratory Gas Exchange and Blood Flow in the Placenta, Nat. Inst. Child Health Hum. Dev., Bethesda, Md., pp. 297–342.

[110] HASHIN, Z. & SHTRIKMAN, S. (1962), A variational approach to the theory of the effective magnetic permeability of multiphase materials, *J. Appl. Phys.* 33(10): 3125–3131.

[111] HASHIN, Z. & SHTRIKMAN, S. (1963), A variational approach to the theory of the elastic behaviour of multiphase materials, *J. Mech. Phys. Solids* 11(2): 127–140.

[112] HASIMOTO, H. (1959), On the periodic fundamental solutions of the stokes equations and their application to viscous flow past a cubic array of spheres, *J. Fluid Mech.* 5(02): 317–328.

[113] HATA, T., TANAKA, H., NOGUCHI, J. & HATA, K. (2011), Three-dimensional ultrasound evaluation of the placenta, *Placenta* 32(2): 105–115.

[114] HAY, JR, W.W., MOLINA, R.A., DIGIACOMO, J.E. & MESCHIA, G. (1990), Model of placental glucose consumption and glucose transfer, *Am. J. Physiol. Regul. Integr. Comp. Physiol.* 258(3): R569–577.

[115] HEAZELL, A., COTTER, S.L., GALLIMORE, L.S., GREENHALGH, D., HEAZELL, A.E.P., KENNEDY, S., KLIKA, V., KRITZ, M.V., NIELSEN, P.F., PREEDY, K.F., PU, I.M., SETCHI, A., SIGGERS, J.H. & WHITTAKER, R.J. (2010), Comparing placentas from normal and abnormal pregnancies, Mathematics-in-Medicine Study Group, University of Strathclyde.

[116] HEILMANN, L., GREBNER, H., MATTHECK, C. & LUDWIG, H. (1979), Mathematical, clinical, and laboratory study of hemodynamic changes in the placental circulation, *Arch. Gynecol. Obstet.* 227(4): 303–313.

[117] HEMPSTOCK, J., BAO, Y.P., BAR-ISSAC, M., SEGAREN, N., WATSON, A.L., CHARNOCK-JONES, D.S., JAUNIAUX, E. & BURTON, G.J. (2003), Intralobular differences in antioxidant enzyme expression and activity reflect the pattern of maternal arterial bloodflow within the human placenta, *Placenta* 24(5): 517–523.

[118] HENDERSON, L.W. (1996), *Replacement of Renal Function by Dialysis*, Springer, Netherlands, ch. Biophysics of Ultrafiltration and Hemofiltration, pp. 114–145, 4th edn.

[119] HILBERT, D. (1902), Mathematical problems, *Bull. Amer. Math. Soc.* 8(10): 437–479, (lecture delivered before the International Congress of Mathematicians at Paris in 1900).

[120] HILL, A.A. & STRAUGHAN, B. (2008), Poiseuille flow in a fluid overlying a porous medium, *J. Fluid Mech.* 603(-1): 137–149.

[121] HILL, E.P., HILL, J.R., POWER, G.G. & LONGO, L.D. (1977), Carbon monoxide exchanges between the human fetus and mother: a mathematical model, *Am. J. Physiol.* 232(3): H311–323.

[122] HILL, E.P., POWER, G.G. & LONGO, L.D. (1973), A mathematical model of carbon dioxide transfer in the placenta and its interaction with oxygen, *Am. J. Physiol.* 224(2): 283–299.

[123] HIRASHIMA, M., LU, Y., BYERS, L. & ROSSANT, J. (2003), Trophoblast expression of fms-like tyrosine kinase 1 is not required for the establishment of the maternal-fetal interface in the mouse placenta., *Proc. Natl. Acad. Sci. U. S. A.* 100(26): 15637–15642.

[124] HOLMES, M.H. (1998), *Introduction to Perturbation Methods*, vol. 20 of Texts in Applied Mathematics, Springer, New York, 337 pp., corr. 2nd printing.

[125] HUPPERTZ, B., ABE, E., MURTHI, P., NAGAMATSU, T., SZUKIEWICZ, D. & SALAFIA, C. (2007), Placental angiogenesis, maternal and fetal vessels – A workshop report, *Placenta* 28(Supplement 1): S94–S96.

[126] JACKSON, M.R., MAYHEW, T.M. & BOYD, P.A. (1992), Quantitative description of the elaboration and maturation of villi from 10 weeks of gestation to term, *Placenta* 13(4): 357–370.

[127] JAIN, R.K. (1987), Transport of molecules in the tumor interstitium: A review, *Cancer Res.* 47(12): 3039–3051.

[128] JAUNIAUX, E. & GREENWOLD, N. (2003), *Fetal Cardiology*, Taylor & Francis, ch. Placental circulations, pp. 41–53.

[129] JAUNIAUX, E. & NICOLAIDES, K.H. (1996), Placental lakes, absent umbilical artery diastolic flow and poor fetal growth in early pregnancy, *Ultrasound Obstet. Gynecol.* 7(2): 141–144.

[130] KALAMKAROV, A.L., ANDRIANOV, I.V. & DANISHEVS'KYY, V.V. (2009), Asymptotic homogenization of composite materials and structures, *Appl. Mech. Rev.* 62(3): 030802–20.

[131] KAUFMANN, P., MAYHEW, T.M. & CHARNOCK-JONES, D.S. (2004), Aspects of human fetoplacental vasculogenesis and angiogenesis. II. Changes during normal pregnancy, *Placenta* 25(2-3): 114–126.

[132] KEENER, J.P. & SNEYD, J. (2001), *Mathematical Physiology*. Interdisciplinary applied mathematics, Springer, New York, 766 pp., corrected 2nd printing.

[133] KELLER, J.B. (1963), Conductivity of a medium containing a dense array of perfectly conducting spheres or cylinders or nonconducting cylinders, *J. Appl. Phys.* 34(4): 991–993.

[134] KELLER, J.B. (1964), Viscous flow through a grating or lattice of cylinders, *J. Fluid Mech.* 18(01): 94–96.

[135] KELLER, J.B. (1977), Effective behavior of heterogeneous media, In: E. W. Montroll & U. Landman, eds, Statistical Mechanics and Statistical Methods in Theory and Application, Plenum Press, New York, pp. 631–644.

[136] KELLER, J.B. (1980), Darcy's law for flow in porous media and the two-space method, In: Nonlinear partial differential equations in engineering and applied science, Marcel Dekker, New York, pp. 429–443.

[137] KELLER, J.B. (2001), Flow in random porous media, *Transport in Porous Media* 43(3): 395–406.

[138] KHALIQ, A., LI, X.F., SHAMS, M., SISI, P., ACEVEDO, C.A., WHITTLE, M.J., WEIGH, H. & AHMED, A. (1996), Localisation of placenta growth factor (PlGF) in human term placenta, *Growth Factors* 13(3): 243–250.

[139] KHONG, T.Y. (2004), Placental vascular development and neonatal outcome, *Semin. Neonatol.* 9(4): 255–263.

[140] KHONG, T.Y., TEE, J.H.C. & KELLY, A.J. (1997), Absence of innervation of the uteroplacental arteries in normal and abnormal human pregnancies, *Gynecol. Obstet. Invest.* 43(2): 89–93.

[141] KIM, H.W. & GREENBURG, A.G. (2004), Artificial oxygen carriers as red blood cell substitutes: A selected review and current status, *Artificial Organs* 28(9): 813–828.

[142] KINGDOM, J., HUPPERTZ, B., SEAWARD, G. & KAUFMANN, P. (2000), Development of the placental villous tree and its consequences for fetal growth, *Eur. J. Obstet. Gynecol. Reprod. Biol.* 92(1): 35–43.

[143] KIRSCHBAUM, T.H. & SHAPIRO, N.Z. (1969), A mathematical model of placental oxygen transfer, *J. Theor. Biol.* 25(3): 380–402.

[144] KLIMAN, H.J. (2000), Uteroplacental blood flow: The story of decidualization, menstruation, and trophoblast invasion, *Am. J. Pathol.* 157(6): 1759 1768.

[145] KNIGHT, J. (2002), Artificial wombs: An out of body experience, *Nature* 419(6903): 106–107.

[146] KOHLER, W. & PAPANICOLAOU, G.C. (1982), Bounds for the effective conductivity of random media, In: Macroscopic Properties of Disordered Media, Springer-Verlag, vol. 154 of Lecture notes in physics, pp. 111–130, proc. conf. Courant Inst., June 1981.

[147] KOLUMBÁN, J. & SOÓS, A. (2006), Homogenization with multiple scale expansion on selfsimilar structures, *Studia Universitatis Babes-Bolyai Mathematica* 51(4): 129–144.

[148] KONJE, J.C., HUPPERTZ, B., BELL, S.C., TAYLOR, D.J. & KAUFMANN, P. (2003), 3-dimensional colour power angiography for staging human placental development, *The Lancet* 362(9391): 1199–1201.

[149] KORFF, T., KRAUSS, T. & AUGUSTIN, H.G. (2004), Three-dimensional spheroidal culture of cytotrophoblast cells mimics the phenotype and differentiation of cytotrophoblasts from normal and preeclamptic pregnancies, *Exp. Cell Res.* 297(2): 415–423.

[150] KORN, G.A. & KORN, T.M. (2000), *Mathematical Handbook for Scientists and Engineers: Definitions, Theorems, and Formulas for Reference and Review.* Dover Publications, Mineola, N.Y, 1152 pp.

[151] KRAMPL, E.R., ESPINOZA-DORADO, J., LEES, C.C., MOSCOSO, G., BLAND, J.M. & CAMPBELL, S. (2001), Maternal uterine artery Doppler studies at high altitude and sea level, *Ultrasound Obstet. Gynecol.* 18(6): 578–582.

[152] KUDRYASHOV, N.A. & CHERNYAVSKY, I.L. (2008), Numerical simulation of the process of autoregulation of the arterial blood flow, *Fluid Dynamics* 43(1): 32–48.

[153] LARDNER, T.J. (1975), A model for placental oxygen exchange, *J. Biomech.* 8(2): 131–134.

[154] LASH, G.E., CARTWRIGHT, J.E., WHITLEY, G.S.J., TREW, A.J. & BAKER, P.N. (1999), The effects of angiogenic growth factors on extravillous trophoblast invasion and motility, *Placenta* 20(8): 661–667.

[155] LASH, G.E., WARREN, A.Y., UNDERWOOD, S. & BAKER, P.N. (2003), Vascular endothelial growth factor is a chemoattractant for trophoblast cells, *Placenta* 24(5): 549 556.

[156] LEACH, L., GRAY, C., STATON, S., BABAWALE, M.O., GRUCHY, A., FOSTER, C., MAYHEW, T.M. & JAMES, D.K. (2004), Vascular endothelial cadherin and β-catenin in human fetoplacental vessels of pregnancies complicated by Type 1 diabetes: associations with angiogenesis and perturbed barrier function, *Diabetologia* 47(4): 695 709.

[157] LEACH, L., LAMMIMAN, M.J., BABAWALE, M.O., HOBSON, S.A., BROMILOU, B., LOVAT, S. & SIMMONDS, M.J.R. (2000), Molecular organization of tight and adherens junctions in the human placental vascular tree, *Placenta* 21(5-6): 547 557.

[158] LEDERBERG, J. & MCCRAY, A.T. (2001), 'Ome sweet 'omics – A genealogical treasury of words, *The Scientist* 15(7): 8–9.

[159] LICK, W. (1969), Two-variable expansions and singluar perturbation problems, *SIAM J. Appl. Math.* 17(4): 815–825.

[160] LONGO, L.D. & BARTELS, H., eds (1972), *Respiratory Gas Exchange and Blood Flow in the Placenta*, International Congress of Physiological Sciences, Nat. Inst. Child Health Hum. Dev., Bethesda, Md.

[161] LOTWICK, H.W. & SILVERMAN, B.W. (1982), Methods for analysing spatial processes of several types of points, *J. R. Stat. Soc. B* 44(3): 406–413.

[162] LUKACS, E. (1975), *Stochastic Convergence.* Probability and mathematical statistics, Academic Press, New York, 2nd edn, 200 pp.

[163] LYALL, F. (2005), Priming and remodelling of human placental bed spiral arteries during pregnancy - a review, *Placenta* 26(Supplement 1): S31–S36.

[164] LYALL, F. (2006), Mechanisms regulating cytotrophoblast invasion in normal pregnancy and pre-eclampsia, *Aust. N. Z. J. Obstet. Gynaecol.* 46(4): 266–273.

[165] MADDOCKS, J.H. (2004), Bifucation theory, symmetry breaking and homogenization in continuum mechanics descriptions of DNA, In: D. Givoli, M. J. Grote & P. G. C., eds, A celebration of mathematical modeling: the Joseph B. Keller anniversary volume, Kluwer, Dordrecht, pp. 113–136.

[166] MARKOV, K.Z., TALBOT, D.R.S. & WILLIS, J.R. (1996), On stationary diffusion in heterogeneous media, *IMA J. Appl. Math.* 56(2): 133–144.

[167] MATSUNAWA, T. (1985), The exact and approximate distributions of linear combinations of selected order statistics from a uniform distribution, *Ann. Inst. Stat. Math.* 37(1): 1–16.

[168] MAURI, R. (1991), Dispersion, convection, and reaction in porous media, *Phys. Fluids A* 3(5): 743–756.

[169] MAURI, R. (1995), Heat and mass transport in random velocity fields with application to dispersion in porous media, *J. Eng. Math.* 29(1): 77–89.

[170] MAXWELL, J.C. (1873), *A Treatise on Electricity and Magnetism.* vol. 1, Clarendon press, Oxford, 365 pp.

[171] MAYHEW, T.M. (1991), The new stereological methods for interpreting functional morphology from slices of cells and organs, *Exp. Physiol.* 76(5): 639–665.

[172] MAYHEW, T.M. (1996), Patterns of villous and intervillous space growth in human placentas from normal and abnormal pregnancies, *Eur. J. Obstet. Gynecol. Reprod. Biol.* 68: 75–82.

[173] MCCARTY, P. & HORSTHEMKE, W. (1988), Effective diffusion coefficient for steady two-dimensional convective flow, *Phys. Rev. A* 37(6): 2112–2117.

[174] MCKENZIE, D.R. & MCPHEDRAN, R.C. (1977), Exact modelling of cubic lattice permittivity and conductivity, *Nature* 265(5590): 128–129.

[175] MCLAUGHLIN, D.W., PAPANICOLAOU, G.C. & PIRONNEAU, O.R. (1985), Convection of microstructure and related problems, *SIAM J. Appl. Math.* 45(5): 780–797.

[176] MCPHEDRAN, R.C. & MCKENZIE, D.R. (1978), The conductivity of lattices of spheres. I. the simple cubic lattice, *Proc. R. Soc. Lond. A* 359(1696): 45–63.

[177] MEI, C.C. & AURIAULT, J.L. (1991), The effect of weak inertia on flow through a porous medium, *J. Fluid Mech.* 222(1): 647–663.

[178] MEREDITH, R.E. & TOBIAS, C.W. (1960), Resistance to potential flow through a cubical array of spheres, *J. Appl. Phys.* 31(7): 1270–1273.

[179] METCALFE, J., BARTELS, H. & MOLL, W. (1967), Gas exchange in the pregnant uterus, *Physiol. Rev.* 47(4): 782–838.

[180] MIKELIĆ, A., DEVIGNE, V. & VAN DUIJN, C.J. (2006), Rigorous upscaling of the reactive flow through a pore, under dominant Péclet and Damköhler numbers, *SIAM J. Math. Anal.* 38(4): 1262–1287.

[181] MIKELIĆ, A. & JAGER, W. (2000), On the interface boundary condition of Beavers, Joseph, and Saffman, *SIAM J. Appl. Math.* 60(4): 1111–1127.

[182] MILNE-THOMSON, L.M. (1968), *Theoretical Hydrodynamics.* Macmillan, New York, 5th edn, 743 pp.

[183] MILTON, G.W. (1981), Bounds on the electromagnetic, elastic, and other properties of two-component composites, *Phys. Rev. Lett.* 46(8): 542–545.

[184] MOLL, W. (2003), Structure adaptation and blood flow control in the uterine arterial system after hemochorial placentation, *Eur. J. Obstet. Gynecol. Reprod. Biol.* 110(Supplement 1): S19–S27.

[185] MOLL, W., WALLENBURG, H.C.S., KASTENDIECK, E. & VOSLAR, M. (1978), The flow resistance of the spiral artery and the related intervillous space in the rhesus monkey placenta, *Pflügers Arch. Eur. J. Physiol.* 377(3): 225–228.

[186] MOORE, K.L. & PERSAUD, T.V.N. (2003), *The Developing Human: Clinically Oriented Embryology.* Saunders, Philadelphia, 7th edn, 560 pp.

[187] NIELD, D.A. & BEJAN, A. (2006), *Convection in Porous Media.* Springer, New York, 3rd edn, 640 pp.

[188] OYEN, M.L. (2010), 3D models of placental blood flow and oxygen diffusion in chorionic villi, In: Proc. 6th World Congress Biomech. 1-6 August, Singapore, p. 362.

[189] PAPADOPULOS, F., SPINELLI, M., VALENTE, S., FORONI, L., ORRICO, C., ALVIANO, F. & PASQUINELLI, G. (2007), Common tasks in microscopic and ultrastructural image analysis using imagej, *Ultrastructural Pathology* 31(6): 401–407.

[190] PARNELL, W.J. & ABRAHAMS, I.D. (2008), A new integral equation approach to elastodynamic homogenization, *Proc. R. Soc. A* 464(2094): 1461–1482.

[191] PAVLIOTIS, G.A. & STUART, A.M. (2008), *Multiscale Methods: Averaging and Homogenization.* vol. 53 of Texts in Applied Mathematics, Springer, 310 pp.

[192] PETER, M.A. (2007), Homogenisation in domains with evolving microstructure, *Comptes Rendus Mécanique* 335(7): 357–362.

[193] PIJNENBORG, R. (1998), Implantation and early placentation, *Curr. Obstet. Gynaecol.* 8(1): 8–12.

[194] PIJNENBORG, R., DIXON, G., ROBERTSON, W.B. & BROSENS, I. (1980), Trophoblastic invasion of human decidua from 8 to 18 weeks of pregnancy, *Placenta* 1(1): 3 19.

[195] PIJNENBORG, R., VERCRUYSSE, L. & HANSSENS, M. (2006), The uterine spiral arteries in human pregnancy: Facts and controversies, *Placenta* 27(9-10): 939–958.

[196] PIMENTEL, E. (1994), *Handbook of Growth Factors.* vol. II: Peptide Growth Factors, CRC Press, 384 pp.

[197] PLAISIER, M., RODRIGUES, S., WILLEMS, F., KOOLWIJK, P., VAN HINSBERGH, V.W.M. & HELMERHORST, F.M. (2007), Different degrees of vascularization and their relationship to the expression of vascular endothelial growth factor, placental growth factor, angiopoietins, and their receptors in first-trimester decidual tissues, *Fertil. Steril.* 88(1): 176–187.

[198] POLAK, J.M. & VAN NOORDEN, S. (1982), *Immunocytochemistry: Practical Applications in Pathology and Biology.* Wright-PSG, Bristol, 396 pp.

[199] POPEL, A.S. & JOHNSON, P.C. (2005), Microcirculation and hemorheology, *Annu. Rev. Fluid Mech.* 37(1): 43–69.

[200] POWER, G.G., DALE, P.S. & NELSON, P.S. (1981), Distribution of maternal and fetal blood flow within cotyledons of the sheep placenta, *Am. J. Physiol. Heart. Circ. Physiol.* 241(4): H486–496.

[201] PRAGER, S. (1961), Viscous flow through porous media, *Phys. Fluids* 4(12): 1477–1482.

[202] PRAGER, S. (1963), Interphase transfer in stationary two-phase media, *Chem. Eng. Sci.* 18(4): 227–231.

[203] PRENDERGAST, C.H., PARKER, K.H., GRAY, R., VENKATESAN, S., BANNISTER, P., CASTRO-SOARES, J., MURPHY, K.W., BEARD, R.W., REGAN, L., ROBINSON, S., STEER, P., HALLIDAY, D. & JOHNSTON, D.G. (1999), Glucose production by the human placenta in vivo, *Placenta* 20(7): 591–598.

[204] PRIES, A.R. & SECOMB, T.W. (2005), Control of blood vessel structure: insights from theoretical models, *Am. J. Physiol. Heart Circ. Physiol.* 288(3): H1010–1015.

[205] RAGAVENDRA, N. & TARANTAL, A.F. (2001), Intervillous blood flow in the third trimester gravid rhesus monkey (Macaca mulatta): Use of sonographic contrast agent and harmonic imaging, *Placenta* 22(2-3): 200–205.

[206] RAINEY, A. & MAYHEW, T.M. (2010), Volumes and numbers of intervillous pores and villous domains in placentas associated with intrauterine growth restriction and/or pre-eclampsia, *Placenta* 31(7): 602–606.

[207] RAMSEY, E.M. (1968), Uteroplacental circulation during labor, *Clin. Obstet. Gynecol.* 11(1): 78–95.

[208] RAYLEIGH, L. (1892), On the influence of obstacles arranged in rectangular order upon the properties of a medium, *Philosophical Magazine* 34(211): 481 502.

[209] RED-HORSE, K., KAPIDZIC, M., ZHOU, Y., FENG, K.T., SINGH, H. & FISHER, S.J. (2005), EPHB4 regulates chemokine-evoked trophoblast responses: a mechanism for incorporating the human placenta into the maternal circulation, *Development* 132(18): 4097–4106.

[210] REDMAN, C.W.G. (1997), Cytotrophoblasts: Masters of disguise, *Nature Medicine* 3(6): 610 611.

[211] REJNIAK, K., KLIMAN, H. & FAUCI, L. (2004), A computational model of the mechanics of growth of the villous trophoblast bilayer, *Bull. Math. Biol.* 66(2): 199–232.

[212] RENEAU, D.D., GUILBEAU, E.J. & CAMERON, J.M. (1974), A theoretical analysis of the dynamics of oxygen transport and exchange in the placental-fetal system, *Microvascular Research* 8(3): 346–361.

[213] REOMA, J.L., ROJAS, A., KIM, A.C., KHOURI, J.S., BOOTHMAN, E., BROWN, K., GROTBERG, J., COOK, K.E., BARTLETT, R.H., HIRSCHL, R.B. & MYCHALISKA, G.B. (2009), Development of an artificial placenta I: pumpless arterio-venous extracorporeal life support in a neonatal sheep model, *J. Pediatr. Surg.* 44(1): 53–59.

[214] REYNOLDS, L.P., BOROWICZ, P.P., VONNAHME, K.A., JOHNSON, M.L., GRAZUL-BILSKA, A.T., WALLACE, J.M., CATON, J.S. & REDMER, D.A. (2005), Animal models of placental angiogenesis, *Placenta* 26(10): 689–708.

[215] REYNOLDS, S.R.M. (1966), Formation of fetal cotyledons in the hemochorial placenta. A theoretical consideration of the functional implications of such an arrangement, *Am. J. Obstet. Gynecol.* 94(3): 425–439.

[216] REYNOLDS, S.R.M. (1967), Derivation of the vascular elements in the fetal cotyledon of the hemochorial placenta: A contribution to the theory of placental morphogenesis, *Anat. Rec.* 157(1): 43–46.

[217] ROOS, M.W. & SPERBER, G.O. (1997), A diffusion model of cerebral microischemia, *Experimental Neurology* 147(1): 142–150.

[218] ROSS, M.H. & PAWLINA, W. (2011), *Histology: a Text and Atlas.* Wolters Kluwer / Lippincott Williams & Wilkins, London, 6th edn, 974 pp.

[219] RUBENFELD, L.A. & KELLER, J.B. (1969), Bounds on elastic moduli of composite media, *SIAM J. Appl. Math.* 17(3): 495–510.

[220] RUBINSTEIN, J. & TORQUATO, S. (1988), Diffusion-controlled reactions: Mathematical formulation, variational principles, and rigorous bounds, *J. Chem. Phys.* 88(10): 6372–6380.

[221] RUBINSTEIN, J. & TORQUATO, S. (1989), Flow in random porous media: mathematical formulation, variational principles, and rigorous bounds, *J. Fluid Mech.* 206(1): 25–46.

[222] RUNGE, I. (1925), Zur elektrischer leitfähigkeit metallischer aggregate, *Zeitschrift für technische Physik* 6(2): 61–68, (in German).

[223] SAGUES, F. & HORSTHEMKE, W. (1986), Diffusive transport in spatially periodic hydrodynamic flows, *Phys. Rev. A* 34(5): 4136–4143.

[224] SALATHE, E.P. (1982), Mathematical modeling of oxygen transport in skeletal muscle, *Math. Biosci.* 58(2): 171–184.

[225] SALATHE, E.P. (2005), A mathematical method for determining oxygen distribution in skeletal muscle with multiple capillaries and axial diffusion, *Proc. R. Soc. A* 461(2056): 975–1004.

[226] SALATHE, E.P. & XU, Y.H. (1991), Non-linear phenomena in oxygen transport to tissue, *J. Math. Biol.* 30(2): 151–160.

[227] SÁNCHEZ-PALENCIA, E. (1980), *Non-Homogeneous Media and Vibration Theory.* vol. 127 of Lectures Notes in Physics, Springer-Verlag, Berlin, 398 pp.

[228] SANGANI, A.S. (1986), An application of an homogenization method to a model of diffusion in glassy polymers, *J. Polymer Sci. B* 24(3): 563–575.

[229] SANGANI, A.S. & ACRIVOS, A. (1982), Slow flow past periodic arrays of cylinders with application to heat transfer, *Int. J. Multiph. Flow* 8(3): 193–206.

[230] SANGANI, A.S. & ACRIVOS, A. (1983), The effective conductivity of a periodic array of spheres, *Proc. R. Soc. Lond. A* 386(1791): 263–275.

[231] SCHIESSL, B., INNES, B.A., BULMER, J.N., OTUN, H.A., CHADWICK, T.J., ROBSON, S.C. & LASH, G.E. (2009), Localization of angiogenic growth factors and their receptors in the human placental bed throughout normal human pregnancy, *Placenta* 30(1): 79–87.

[232] SCHMID-SCHÖNBEIN, H. (1988), Conceptional proposition for a specific microcirculatory problem: maternal blood flow in hemochorial multivillous placentae as percolation of a "porous medium", *Trophoblast Res.* 3: 17–38.

[233] SCHMIDT, W.O. & KURJAK, A. (2005), *Color Doppler Sonography in Gynecology and Obstetrics.* Thieme, 405 pp.

[234] SCHRÖDER, H.J. (1982), Fluid shift across the placenta: III. application of a computer model of passive placental transfer, *Placenta* 3(4): 349–357.

[235] SCHUHMANN, R., KRAUS, H., BORST, R. & GEIER, G. (1976), Regionally different activity of enzymes within placentones of human term-placentas, *Arch. Gynecol. Obstet.* 220(3): 209–226.

[236] SCHUHMANN, R. & WEHLER, V. (1971), Histologische Unterschiede an Placentazotten innerhalb der materno-fetalen Strömungseinheit, *Arch. Gynecol. Obstet.* 210(4): 425–439, (in German).

[237] SCHUHMANN, R.A. (1982), Placentone structure of the human placenta, In: P. Kaufmann & B. King, eds, Structural and Functional Organization of the Placenta, Karger, no. 22 In Bibliotheca Anatomica, pp. 46–57.

[238] SENGERS, B.G., PLEASE, C.P. & LEWIS, R.M. (2010), Computational modelling of amino acid transfer interactions in the placenta, *Exp. Physiol.* 95: 829–840.

[239] SHAH, C.B. & YORTSOS, Y.C. (1995), Aspects of flow of power-law fluids in porous media, *AIChE Journal* 41(5): 1099–1112.

[240] SHAPIRO, M. & BRENNER, H. (1988), Dispersion of a chemically reactive solute in a spatially periodic model of a porous medium, *Chem. Eng. Sci.* 43(3): 551–571.

[241] SHAW, G.B. (1903), *Man and superman: a comedy and a philosophy.* Constable, Westminster, 244 pp.

[242] SHIPLEY, R.J. & CHAPMAN, S.J. (2010), Multiscale modelling of fluid and drug transport in vascular tumours, *Bull. Math. Biol.* 72: 1464–1491.

[243] SHORE, V.H., WANG, T.H., WANG, C.L., TORRY, R.J., CAUDLE, M.R. & TORRY, D.S. (1997), Vascular endothelial growth factor, placenta growth factor and their receptors in isolated human trophoblast, *Placenta* 18(8): 657–665.

[244] SHOWALTER, R.E. (2000), Diffusion in poro-elastic media, *J. Math. Anal. Appl.* 251(1): 310–340.

[245] SIKLOSI, M., JENSEN, OLIVER, E., TEW, RICHARD, H. & LOGG, A. (2008), Multiscale modeling of the acoustic properties of lung parenchyma, *ESAIM: Proc.* 23: 78–97.

[246] SIMPSON, N.A.B., NIMROD, C.A. & VERMETTE, R.D. (1998), Doppler evidence of intervillous flow in the embryonic period, *J. Maternal-Fetal Invest.* 8(1): 11–16.

[247] SINGH, K.M. & TANAKA, M. (2000), Analytical integration of weakly singular integrals in boundary element analysis of Helmholtz and advection-diffusion equations, *Comput. Methods Appl. Mech. Eng.* 189(2): 625–640.

[248] SMITH, C.J., WILSON, S.K. & DUFFY, B.R. (2005), Mathematical modelling of blood flow in the placenta, *Placenta* 26(8-9): A77, abstracts for the forthcoming European Placenta Group meeting in Glasgow.

[249] SOGHOMONIANS, A., BARAKAT, A.I., THIRKILL, T.L., BLANKENSHIP, T.N. & DOUGLAS, G.C. (2002), Effect of shear stress on migration and integrin expression in macaque trophoblast cells, *Biochim. Biophys. Acta - Mol. Cell Res.* 1589(3): 233–246.

[250] SPRAGUE, B., CHESLER, N.C. & MAGNESS, R.R. (2010), Shear stress regulation of nitric oxide production in uterine and placental artery endothelial cells: experimental studies and hemodynamic models of shear stresses on endothelial cells, *Int. J. Dev. Biol.* 54(2-3): 331–339.

[251] STEDMAN, T.L. (2006), *Stedman's Medical Dictionary.* Lippincott Williams & Wilkins, Philadelphia, 28th edn, 2162 pp.

[252] STEVEN, D. & MORRISS, G. (1975), *Comparative placentation: Essays in structure and function*, Monographs for Students of Medicine, Academic Press, London, ch. Development of the Foetal Membranes, pp. 58–86.

[253] STOYAN, D., KENDALL, W.S. & MECKE, J. (1995), *Stochastic Geometry and its Applications.* UMI, Ann Arbor, MI, 2nd edn, 436 pp.

[254] SWABB, E.A., WEI, J. & GULLINO, P.M. (1974), Diffusion and convection in normal and neoplastic tissues, *Cancer Res.* 34(10): 2814–2822.

[255] TALBERT, D. & SEBIRE, N.J. (2004), The dynamic placenta: I. hypothetical model of a placental mechanism matching local fetal blood flow to local intervillus oxygen delivery, *Med. Hypotheses* 62(4): 511–519.

[256] TALBOT, D.R.S. & WILLIS, J.R. (1984), The overall sink strength of an inhomogeneous lossy medium. Part I: self-consistent estimates, *Mechanics of Materials* 3(3): 171–181.

[257] TAYLOR, C.C., DRYDEN, I.L. & FARNOOSH, R. (2001), The K-function for nearly regular point processes, *Biometrics* 57(1): 224–231.

[258] TAYLOR, G. (1953), Dispersion of soluble matter in solvent flowing slowly through a tube, *Proc. R. Soc. Lond. A* 219(1137): 186–203.

[259] TAYLOR, G. (1954), Conditions under which dispersion of a solute in a stream of solvent can be used to measure molecular diffusion, *Proc. R. Soc. Lond. A* 225(1163): 473–477.

[260] TORQUATO, S. (1991), Random heterogeneous media: Microstructure and improved bounds on effective properties, *Appl. Mech. Rev.* 44(2): 37–76.

[261] TORQUATO, S. (2006), *Random Heterogeneous Materials: Microstructure and Macroscopic Properties.* vol. 16 of Interdisciplinary Applied Mathematics, Springer, New York, 701 pp., corr. 2nd printing.

[262] TRAVKIN, V.S. & CATTON, I. (2001), Transport phenomena in heterogeneous media based on volume averaging theory, In: J. P. Hartnett, T. F. Irvine & Y. I. Cho, eds, Advances in heat transfer, Academic Press, vol. 34, pp. 1–144.

[263] VALENTIN, L., SLADKEVICIUS, P., LAURINI, R., SODERBERG, H. & MARSAL, K. (1996), Uteroplacental and luteal circulation in normal first-trimester pregnancies: Doppler ultrasonographic and morphologic study, *Am. J. Obstet. Gynecol.* 174(2): 768–775.

[264] WANG, W. & SANGANI, A.S. (1997), Nusselt number for flow perpendicular to arrays of cylinders in the limit of small Reynolds and large Péclet numbers, *Phys. Fluids* 9(6): 1529–1539.

[265] WANIEWSKI, J. (2006), Mathematical modeling of fluid and solute transport in hemodialysis and peritoneal dialysis, *Journal of Membrane Science* 274(1-2): 24–37.

[266] WEISS, J.L., MALONE, F.D., EMIG, D., BALL, R.H., NYBERG, D.A., COMSTOCK, C.H., SAADE, G., EDDLEMAN, K., CARTER, S.M., CRAIGO, S.D., CARR, S.R. & D'ALTON, M.E. (2004), Obesity, obstetric complications and cesarean delivery rate – A population-based screening study, *Am. J. Obstet. Gynecol.* 190(4): 1091–1097.

[267] WEISS, P. (1944), On hydrodynamical images. Arbitrary irrotational flow disturbed by a sphere, *Math. Proc. Camb. Philos. Soc.* 40(3): 259–261.

[268] WHITAKER, S. (1967), Diffusion and dispersion in porous media, *AIChE Journal* 13(3): 420–427.

[269] WHITAKER, S. (1996), The Forchheimer equation: A theoretical development, *Transport in Porous Media* 25(1): 27–61.

[270] WHITAKER, S. (1999), *The Method of Volume Averaging.* Kluwer Academic Publishers, Dordrecht, 219 pp.

[271] WHITELEY, J.P., GAVAGHAN, D.J. & HAHN, C.E.W. (2002), Mathematical modelling of oxygen transport to tissue, *J. Math. Biol.* 44(6): 503–522.

[272] WIGGLESWORTH, J.S. (1967), Vascular organization of the human placenta, *Nature* 216(5120): 1120–1121.

[273] WILBUR, W.J., POWER, G.G. & LONGO, L.D. (1978), Water exchange in the placenta: a mathematical model, *Am J Physiol Regul Integr Comp Physiol* 235(3): R181–199.

[274] WILKIN, P. (1954), Contribution to the study of the fetal placental circulation, *Gynécol. et Obstet.* 53: 239–263, (in French).

[275] WOOD, B.D., QUINTARD, M. & WHITAKER, S. (2002), Calculation of effective diffusivities for biofilms and tissues, *Biotechnol. Bioeng.* 77(5): 495–516.

[276] WOOD, B.D. & WHITAKER, S. (2000), Multi-species diffusion and reaction in biofilms and cellular media, *Chem. Eng. Sci.* 55(17): 3397–3418.

[277] XIA, Q., SALAFIA, C. & MORGAN, S. (2010), Optimal transport and the placenta, Tech. rep., Los Alamos National Laboratory, (IEEE Visual Communications and Image Processing, Huang Shan, An Hui, China, 11-14 July).

[278] YANIV, S., ELAD, D., JAFFA, A.J. & EYTAN, O. (2003), Biofluid aspects of embryo transfer, *Ann. Biomed. Eng.* 31(10): 1255–1262.

[279] YEOM, J., AGONAFER, D.D., HAN, J.H. & SHANNON, M.A. (2009), Low Reynolds number flow across an array of cylindrical microposts in a microchannel and figure-of-merit analysis of micropost-filled microreactors, *J. Micromech. Microeng.* 19(6): 065025–35.

[280] YU, B. (2008), Analysis of flow in fractal porous media, *Appl. Mech. Rev.* 61(5): 050801–19.

[281] ZAKRZEWSKA, M., KROWARSCH, D., WIEDLOCHA, A., OLSNES, S. & OTLEWSKI, J. (2005), Highly stable mutants of human fibroblast growth factor-1 exhibit prolonged biological action, *J. Mol. Biol.* 352(4): 860–875.

[282] ZHIKOV, V.V., KOZLOV, S.M., OLEINIK, O.A. & NGOAN, K.T. (1979), Averaging and G-convergence of differential operators, *Rus. Math. Surv.* 34(5): 69–147.

[283] ZOLOTAREV, P.P. & RADUSHKEVICH, L.V. (1968), The equations for dynamic sorption in an undeformed porous medium, *Doklady Phys. Chem.* 182: 643–646.